

University of Alberta

**Exploring Atomic Force Microscopy To Probe Charge Transport Through
Molecular Films And For The Development Of
Combinatorial Force Microscopy**

by

Roderick A. Chisholm

A thesis submitted to the Faculty of Graduate Studies and Research
in partial fulfillment of the requirements for the degree of

Doctor of Philosophy

Chemistry

©Roderick A. Chisholm

Spring 2011

Edmonton, Alberta

Permission is hereby granted to the University of Alberta Libraries to reproduce single copies of this thesis and to lend or sell such copies for private, scholarly or scientific research purposes only. Where the thesis is converted to, or otherwise made available in digital form, the University of Alberta will advise potential users of the thesis of these terms.

The author reserves all other publication and other rights in association with the copyright in the thesis and, except as herein before provided, neither the thesis nor any substantial portion thereof may be printed or otherwise reproduced in any material form whatsoever without the author's prior written permission.

Examining Committee

Mark McDermott, Department of Chemistry, University of Alberta

Richard McCreery, Department of Chemistry, University of Alberta

Jon Veinot, Department of Chemistry, University of Alberta

Jed Harrison, Department of Chemistry, University of Alberta

Michael Brett, Electrical and Computer Engineering, University of Alberta

Daniel Frisbie, Department of Chemical Engineering and Material Science,
University of Minnesota

ABSTRACT

Since the invention of the atomic force microscope (AFM), this technology has had profound implications in the study of material science and molecular biology. The ability to visualize and perform quantitative analysis of the nanoscale properties of surfaces has provided great insights into these nanoscale landscapes. The present dissertation manuscript exploits this technology for the measurement of charge transport through molecular films and the development of combinatorial force microscopy.

Firstly, this work probed, for the first time, charge transport through molecular films derived from diazonium salts grafted to carbon electrodes using conductive atomic force microscopy. We found the charge transport properties of a molecular junction are dependent upon the chemical structure of the molecular film. We also investigated the effect of molecular film compression and deformation has on charge transport. In this, we observed increases in current densities associated with increases in applied load to the molecular film. Furthering these initial findings, PPF/NAB/Cu molecular junctions were fabricated having junction sizes ranging between micro-scale and nanoscale. The charge transport experiments reveal an agreement of electron transport properties between the metal deposited PPF/NAB/Cu junction and a PPF/NAB/Cu AFM tip junction at an applied load of approximately 60nN. This form of molecular layer charge transport control may potentially open new horizons for integration of molecular films into the microelectronics industry.

This dissertation manuscript also describes the development of the quantitative interrogation opposing chemical libraries involved in combinatorial inverted atomic force microscopy. Tipless cantilever's were patterned with chemically modified nanorods. These modified nanorods were then used as chemical identifiers during a combinatorial force microscopy experiment and for the first time 16 interactions were monitored within one experiment in a continuous medium. Thus, providing excellent for the validation that combi-AFM is a truly quantitative high-throughput technology.

ACKNOWLEDGMENTS

I would like to thank my Research supervisors Dr. Mark McDermott and Dr. John-Bruce Green for their guidance, supervision and patience throughout my years of graduate school. I would also like to extend my appreciation for originally introducing me to surface science research and in particular to the atomic force microscope. My gratitude is owed to all my lab mates throughout the years for all the great times and discussions. I would like to thank a collaborator Doug Gish for the preparation of GLAD films and helpful discussions. I would like to thank Adam Bergren for his useful discussions and aid during my work with molecular layers. My gratitude is extended to the department of Chemistry's glassware, machine and electronics shops. Without your services and recommendations my research would be greatly hindered. I would like to thank the professional services of George Braybrook of the scanning electron microscope facilities of Earth and Biological Sciences. I would like to thank my supervisory committee members – Dr. Rick McCreery, Dr. Jon Veinot, Dr. Jed Harrison and Dr. Michael Brett – for their guidance and direction throughout the years. I would also like to extend my appreciation to my adopted family Rob and Cate for the many dinners, discussions and good times. Your friendship is cherished.

Finally, to my beloved wife and partner Ashley. Your unwavering love and commitment is a constant reminder of life itself. I will forever remain indebted to you. Thanks Ash.

Table of Contents

Abstract -----	i
Acknowledgements -----	iii
Table of Contents -----	iv
List of Abbreviations -----	x
List of Symbols -----	xv
List of Figures -----	xvi
List of Tables -----	xxxii

Chapter One

Introduction

1.1 Imaging of Nanoscience -----	1
1.2 Scanning Probe Microscopy -----	2
1.3 Atomic Force Microscopy -----	3
1.4 Contact Mode -----	6
1.5 Tapping Mode -----	8
1.6 Force Curves -----	11
1.7 Chemical Force Microscopy -----	15
1.8 Inverted Atomic Force Microscopy (i-AFM) -----	16
1.9 Conductive Atomic Force Microscopy (c-AFM) -----	22
1.10 Molecular Electronics -----	22
1.11 Grafting Aryl films derived from Diazonium salts -----	26
1.12 Dissertation Objectives -----	28

Chapter Two

Characterization of Aryl Films Derived from Diazonium Salts on Carbon

Electrodes Using Conductive Atomic Force Microscopy

2.1	Introduction -----	42
2.2	Experimental -----	47
	Preparation of diazonium salts -----	47
	Preparation of Pyrolysed Photoresist Films (PPF) -----	48
	Surface Modification -----	49
	X-ray Photoelectron Spectroscopy -----	49
	Atomic Force Microscopy -----	50
2.3	Results and Discussion -----	51
	Electrochemical Surface Modification -----	51
	Charge Transport Investigations -----	59
	Effects of applied load on charge transport investigations -----	62
	Contact Area Consideration -----	64
	Distance Dependence consideration -----	67
	Molecular Layer Rearrangement Consideration -----	69
2.4	Conclusions -----	70

Chapter Three

Top contact formation and scalability of ppf/NAB/Cu junctions

3.1	Introduction -----	79
3.2	Experimental -----	85

	Preparation of diazonium salts -----	87
	Preparation of pyrolyzed photoresist (PPF) -----	85
	Surface derivatization -----	86
	Microsized Cu junction Fabrication -----	87
	AFM tip Characterization -----	87
	Charge Transport investigations -----	88
3.3	Results and Discussion -----	90
	Characterization of PPF/NAB/Cu Junctions -----	90
	C-AFM Charge Transport Investigations -----	91
3.4	Conclusions -----	107

Chapter Four

A Surface-enhanced Raman Scattering Study into the Coupling of Aryl Films Derived from Diazonium Salts to Gold Electrodes

4.1	Introduction -----	111
4.2	Experimental -----	119
	Glancing Angle Deposition Film Fabrication -----	119
	Surface Modification -----	120
	Characterization of Au GLAD films -----	121
4.3	Results and Discussion -----	122
	Glancing Angle Deposition Films Fabrication -----	122
	Preliminary Study of AU GLAD films for SERS -----	122

Existence of Nitrogen Species within Diazonium salt derived Aryl Films-----	128
X-ray Photoelectron Spectroscopy Characterization-----	128
Characterization of Aryl Films by SERS-----	132
Potential Step Deposition of BA Films Derived from Diazonium Salts-----	139
4.4 Conclusions-----	147

Chapter Five

Patterning of cantilevers with functionalized nanoparticles for combinatorial atomic force microscopy

5.1 Introduction-----	153
5.2 Experimental-----	159
Nanorod modification-----	159
Tip array modification-----	159
Cantilever modification-----	160
Nanorod Characterization-----	161
Atomic force microscopy-----	162
5.3 Results and Discussion-----	162
Characterization of Nanorods-----	163
Immobilization of Chemically Modified Nanorods-----	168
Combinatorial Atomic Force Microscopy-----	172
5.4 Conclusions-----	176

Chapter Six

Tip characterization for inverted atomic force microscopy

6.1	Introduction -----	180
6.2	Experimental -----	183
	Chemicals and Materials -----	183
	Tip Array -----	183
	Colloidal gold tip characterization -----	184
	SEM tip characterization -----	185
	Evaporated niobium tip characterization -----	185
	Cantilevers for force measurements -----	186
	Cantilever force constant determination -----	186
	Force measurements -----	187
	Contact angle measurements -----	187
6.3	Results and Discussion -----	187
	Contact Angle Discussion -----	189
	Scanning Electron Microscopy Characterization -----	191
	Colloidal Gold Characterization -----	196
	Blind Reconstruction Characterization -----	202
6.4	Conclusions -----	209

Chapter Seven

Conclusions & Future Work

7.1	Overall Conclusions-----	213
7.2	Future Work-----	215
	Ongoing Investigations of Charge Transport Through Molecular Layers-----	215
	Future Prospects for Combinatorial Atomic Force Microscopy-----	219

Appendix

8.1	Igor Pro Routine for Analysis of Force Curves-----	222
------------	-----------------------------------------------------------	------------

List of Abbreviations

Amine	aminoundecanethiol
APDMES	aminopropyldimethylethoxysilane
ATP	aminothiophenol
AFM	atomic force microscopy
BA	benzoic acid
BP	biphenyl
Combi-AFM	combinatorial atomic force microscopy
c-AFM	conductive atomic force microscopy
Cu	copper
I	current
J	current density
DNA	Deoxyribonucleic acid
DMS	dimethyloctadecylchlorosilane
Methyl	dodecanethiol
e-beam	electron beam
eV	electron volts

GaAs	Gallium arsenide
GLAD	glancing angle deposition
Au	gold
HT	high throughput
HOMO	highest occupied molecular orbital
HF	hydrofluoric acid
IRRAS	Infrared reflection adsorption spectroscopy
i-AFM	inverted atomic force microscopy
JKR	Johnton-Kendal-Joberts
LUMO	lowest unoccupied molecular orbital
MUA	mercaptoundecanoic acid
Acid	mercaptoundecanoic acid
Alcohol	mercaptoundecanol
BA-thiol	4-mercaptobenzoic acid
μm	micrometers
mJ	milliJoules
nm	nanometer

nN	nanonewton
NSOM	near-field scanning optical microscopy
Nb	niobium
NAB	nitroazobenzene
NB	nitrobenzene
NB-thiol	nitrobenzene thiol
N	nitrogen
Pd	palladium
Pt	platinum
MBD	p-mercaptanitrobenzene
MBA	p-mercaptobenzoic acid
PDMS	Poly(dimethylsiloxane)
PPF	pyrolyzed photoresist films
SECM	scanning electrochemical microscopy
SEM	scanning electron microscopy
Si	silicon

SPM	scanning probe microscopy
SThM	scanning thermal microscopy
SPIP	scanning probe imaging processor
STM	scanning tunneling microscopy
Ag	silver
SERS	surface-enhanced Raman scattering
TOF SIMS	time-of-flight secondary ion mass spectrometry
TEM	transmission electron microscopy
V	voltage
cm⁻¹	wavenumber
XPS	x-ray photoelectronspectroscopy

List of Symbols

Θ	angle
P	applied load
R_t	calculated tip radius
a	contact radius
I	current
$^{\circ}$	degree
d	distance
R_{eff}	effective tip radius
F	force
h	height
γ_L	interfacial surface energy's of the liquid interface
γ_S	interfacial surface energy's of the solid interface
γ_{SL}	interfacial surface energy's of the solid-liquid interface
R_p	particle half width
h_p	particle height
R	tip radius

β tunneling factor constant

w width

W_{ad} work of adhesion

Table of Figures

Figure 1.1 Cartoon illustration of constant height(a) and constant current(b) feedback modes commonly employed during STM operation.

Figure 1.2 Illustration of a typical experimental setup of an AFM in which the sample is scanned with respect to the AFM tip and cantilever's response is monitored by the optical response of a laser beam reflected off the backside of the cantilever.

Figure 1.3 Constant force feedback employed during operation of contact mode AFM. The feedback mechanism adjusts the z-piezo distance to maintain constant force between the AFM tip and sample.

Figure 1.4 Torsional deflections in the cantilever, attributed to friction appear as a deflection in the horizontal direction in the split photodetector. Cantilever response under no frictional force (a) and with frictional force (b)

Figure 1.5 Amplitude feedback employed during operation of tapping mode AFM. The feedback mechanism adjusts the z-piezo distance to maintain constant amplitude.

Figure 1.6 Illustration depiction of a force curve data collected by bring the AFM tip in and out of contact with a surface. The force curve collected during approach is depicted in blue while the retract force curve is depicted in red.

Figure 1.7 Illustration of the JRK contact mechanical model, where R is the radius of the sphere and a is the contact radius between the sphere and surface.

Figure 1.8 Illustration of the i-AFM design demonstrating a tipless cantilever being imaged by substrate supported AFM tips.

Figure 1.9 Schematic of the fabrication process involved to produce and liberate substrate supported inverted AFM tips.

Figure 1.10 Cartoon representations of molecular junction formation by the mercury drop (a), metal deposition of the top contact (b), nanogap (c) and scanning probe (d) methods.

Figure 1.11 Schematic depicting the proposed mechanism of aryl-group attachment onto a carbon electrode.

Figure 1.12 Proposed attachment mechanism for multilayer formation. The proton in the coupling reaction has been included for clarity.

Figure 2.1 Schematic depicting the proposed mechanism of aryl-group attachment onto a carbon electrode.

Figure 2.2 Cyclic voltammograms collected during the deposition of nitroazobenzene (1a) and biphenyl (1b) from their corresponding diazonium salts to PPF.

Figure 2.3 High-resolution XPS spectra, of the nitrogen 1s region, for the NAB and BP modified PPF substrates

Figure 2.4 High resolution XPS spectra of the carbon 2s region of the NAB, BP and bare PPF substrates

Figure 2.6 Topographic AFM images after scratching experiments (a) biphenyl modified PPF (b), nitroazobenzene modified PPF and (c) unmodified PPF. The height difference between the corresponding 250nm^2 areas were used to determine the molecular layer's thickness.

Figure 2.6 A cartoon representation of the resultant layer formation for biphenyl (a) and nitroazobenzene (b) modified PPF.

Figure 2.7 IV curves for NAB and BP collected with an applied force of 100nN within a hexadecane environment.

Figure 2.8 Schematic representation of NAB forming a quinoid structure at positive tip biases.

Figure 2.9 C-AFM IV curves of BP (a) and NAB (b) molecular layers grafted to PPF collected at increasing applied loads.

Figure 2.10 Topographic image of evaporated Nb (a) used to calculate a 3D model of the c-AFM tip (b)

Figure 2.11 Calculated JV curves for measuring charge transport through (a) PPF/BP/Pt and (b) PPF/NAB/Pt molecular junctions at various applied loads.

Figure 2.12 Calculated JV curves for (a) BP and (b) NAB compensated for distance dependence during molecular layer compression.

Figure 3.1 Cartoon representation of a molecular junction. In this a molecule is sandwiched between two conducting metals. This setup allows for charge to be passed through the central molecule.

Figure 3.2 Experimental setups of charge transfer experiments that monitor electron transfer through a monolayer on gold. In (a) electron transfer through an ensemble of molecules is measured using a conduction AFM probe. In (b) the concentration of conducting molecules immobilized on the surface has been decreased such that only charge being passed through a single molecule is being investigated.

Figure 3.2c Gold coated STM tip is lowered into contact forming a molecular junction in the presence of conducting molecules and charge transport through the molecule is measured. The junction is then broken by withdrawing the STM tip. This process is repeated thereby enabling a large number of charge transport measurements to be collected.

Figure 3.4 Illustration of ppf/NAB/Cu experiment setup. Charge transport studies through microsized junctions occurred by placing Cu coated AFM tip in contact with microsized Cu pad. Charge transport investigations on the nanometer size regime occurred by positioning the Cu AFM tip in contact with the bare NAB molecular layer.

Figure 3.5 (a) Tapping mode AFM topography image of patterned e-beam evaporated Cu pads on NAB molecular layer. (b) Topography line trace of patterned Cu pads, area of interest is indicated by red line in topography image.

Figure 3.6 Scanning electron microscopy image of patterned e-beam evaporated Cu island pads, through a 2000 mesh(a) and 400 mesh(b) TEM grid, on a NAB molecular layer supported by ppf. The area of the bright squares was used to assess the contact area of the PPF/NAB/Cu molecular junction.

Figure 3.7 Overlay of 5 JV curves collected on individual PPF/NAB/Cu molecular junction having a contact area of $\sim 64 \text{ nm}^2$ and $\sim 1600 \text{ nm}^2$.

Figure 3.8 Overlay of 16 JV curves collected on 16 different PPF/NAB/Cu molecular junctions having a contact area of $\sim 64 \text{ nm}^2$.

Figure 3.9 IV curves collected using a Cu coated AFM tip as the top contact in the PPF/NAB/Cu molecular junction. In this the applied load was increased between 0 nN and 154 nN, at which point an Ohmic response was observed.

Figure 3.10 Topographic image of evaporated Nb (a) used to calculate a 3D model of the c-AFM tip using blind reconstruction methods (b)

Figure 3.11 JV curves collected using a Cu coated AFM tip as the top contact in the PPF/NAB/Cu molecular junction. In this the applied load was increased between 0 nN and 154 nN, at which point an Ohmic response was observed.

Figure 3.12a JV curve and corresponding Simmons's tunneling model fit of data collected on a 1600 \AA^2 PPF/NAB/Cu molecular junction. The raw data was fit between -0.49V and + 0.40V.

Figure 3.12b Plot of $\ln(I/V^2)$ versus $1/V$ used to determine V_{trans} of the 1600 \AA^2 PPF/NAB/Cu molecular junction fit in Figure 3.12a. V_{trans} was determined to be -0.49V and + 0.40V.

Figure 3.13b JV curve and corresponding Simmons's tunneling model fit of data collected on a PPF/NAB/Cu c-AFM tip molecular junction having an applied load of approximately 10 nN. The raw data was fit between -0.91V and + 0.78V.

Figure 3.13b Plot of $\ln(I/V^2)$ versus $1/V$ used to determine V_{trans} of the PPF/NAB/Cu c-AFM molecular junction at applied load of approximately 10nN fit in Figure 3.12a. V_{trans} was determined to be -0.91V and + 0.78V

Figure 4.1 Proposed mechanism of attachment of aryl films derived from corresponding diazonium salts.

Figure 4.2 Proposed attachment mechanism for multilayer formation. The proton in the coupling reaction has been included for clarity.

Figure 4.3 Cartoon depiction of the fabrication of GLAD films.

Figure 4.4 Rayleigh and Raman scattering energy diagram, adapted from reference³²

Figure 4.5 Scanning electron micrographs of gold GLAD films demonstrating surface morphology (a) and side profile (b) of gold pillars.

Figure 4.6 Raman spectra of NB-thiol collected on planar evaporated gold (a) and Au GLAD film (b)

Figure 4.7a Overlay of three hundred Raman spectra collected on a single sample

Figure 4.7b Raman spectra collected from five separate sample substrates.

Figure 4.8 XPS high-resolution spectra of Au4f region of nitroazobenzene, nitrobenzene, nitrobenzene thiol, 4-benzoic acid and 4-mercaptobenzoic acid immobilized onto gold GLAD film electrodes.

Figure 4.9 XPS high-resolution spectra of N1s region of nitroazobenzene, nitrobenzene, nitrobenzene thiol, 4-benzoic acid and 4-mercaptobenzoic acid immobilized onto gold GLAD film electrodes.

Figure 4.10 Infrared reflection adsorption spectroscopy (IRRAS) spectrum of an NAB on planar gold substrate.

Figure 4.11 Raman spectra of nitroazobenzene grafted to gold GLAD film electrodes and planar evaporated gold electrode. Spectra offset for clarity.

Figure 4.12a Raman spectra of nitrobenzene and nitrobenzene thiol grafted to gold GLAD film electrodes. Spectra offset for clarity.

Figure 4.12b Raman spectra of 4-benzoic acid, BA, and 4-mercaptobenzoic acid thiol, BA thiol, grafted to gold GLAD film electrodes. Spectra offset for clarity.

Figure 4.13 XPS spectra of electrolysis deposition of 4-benzoic acid modified gold GLAD film at various voltage depositions -10mV, -100mV, -200mV, -500mV and -1000mV. Spectra offset for clarity.

Figure 4.14 XPS high-resolution spectra of Au4f region of electrolysis deposition of 4-benzoic acid modified gold GLAD film at various voltage depositions -100mV, -200mV, -600mV and -1000mV

Figure 4.15 SERS spectra of electrolysis deposition of 4-benzoic acid modified gold GLAD film at various voltage depositions. Arrow indicates increasingly negative potential starting at 0V and decreasing in -200mV steps. Spectra offset for clarity.

Figure 4.16 A plot of the 1450cm^{-1} peak height versus deposition potentials results, indicating multi-layer formation under highly negative biases.

Figure 4.17 Proposed mechanism for multilayer formation involving azo coupling.

Figure 4.18 Illustration depicting non-uniform multilayer structure of molecular layer

Figure 5.1 Micrographs of tip arrays: This optical micrograph (A) shows the arrangement of tips in the tip array when in use with tipless cantilevers. The index markers provide unique location identifiers for each of the 10's of thousands of substrate supported tips.

Figure 5.2 Cartoon representing the concept of nanoparticle based combinatorial AFM. The nanorods 1-4 and the tips a-d are each chemically modified with distinct chemistries, and the interaction measurements between each of the 16 combinations may be measured.

Figure 5.3 Scanning electron micrograph of gold nanorods demonstrating length dispersion within a given batch. Scale bar represent 10 μm .

Figure 5.4 Scanning electron micrograph of gold/silver barcoded nanorods. The visual contrast in materials may be used as an identifier of nanorod modification chemistry.

Figure 5.5 Reflection optical micrographs of 4 different gold/silver barcoded nanorods illuminated by blue light. The visual contrast due to reflective property differences between gold and silver may be used as an identifier of nanorod modification chemistry.

Figure 5.6 Optical micrographs of nanorod modified cantilevers representative of solution phase deposition of (A) uncoded and (B) coded nanorods, as well as manual deposition of (C) uncoded and (D) coded nanorods. The oscillatory pattern is due to optical interference through the PDMS film used for adhesion.

Figure 5.7 Raman spectra and corresponding optical micrographs of nanorods modified with (MBA) p-mercaptobenzoic acid, (MNB) p-mercaptanitrobenzene, (BT) benzenethiol and (ATP) p-aminothiophenol. The dotted rectangles enclose the regions illuminated by the diode laser and correspond to the samples for the Raman spectra.

Figure 5.8 (A) Inverted tapping AFM topography image and (B) corresponding histograms of four chemically different tips octadecanethiol (methyl), aminoundecanethiol (amine), mercaptoundecanol (alcohol), mercaptoundecanoic acid (acid), interacting with four chemically different nanorods benzenethiol (BT), p-aminothiophenol (ATP), p-mercaptanitrobenzene (MNB), and p-mercaptobenzoic acid (MBA) immobilized onto a PDMS cantilever. The scale bar represents 50 measurements

Figure 6.1 A. Force curves in water between octadecyl modified tip and cantilever for a “dull” tip, shown in blue and a “sharp” tip shown in red. B Histograms of the measured pull-off forces from the force curves. Insets are expanded views of the two histograms.

Figure 6.2 Typical images collected during contact angle measurements using water (a), diiodomethane (b) and ethanleneglycol (c) on an octadecyl modified silicon wafer.

Figure 6.3 Scanning electron micrograph of AFM tip before (a) and after (b) exposure to a 5kV electron beam for 1 minute.

Figure 6.4 Scanning electron micrographs of tips. These SEM images (A) and (B) show a tip representative of a sharp tip array imaged along the x and y

directions respectively. The insets include superimposed circles to determine tip radii. The SEM images (C) and (D) show similar results from a tip representative of a dull tip array. The plot in (E) is the exported data that corresponds to the apparent tip edge, and this curve was used to calculate the curvature at the apex of the tip.

Figure 6.5 Plot of pull-off force as a function of effective tip radius calculated from SEM images. The data points are the mean values of measured pull-off force and determined tip radius. The error bars are the standard deviation of the mean for each parameter. The solid line is the linear least squares fit of the data. The slope of this line was used to determine the work of adhesion of the system to be $28.7 \pm 1.9 \text{ mJ/m}^2$.

Figure 6.6 Inverted tapping mode AFM topography image of a group of colloidal gold particles on a cantilever imaged with the sharp and dull tips shown in Figure 1B and 1C. Cross-sectional profiles below each image correspond to the line drawn on the image.

Figure 6.7 Geometric models of the methods used to calculate an inverted AFM tip's radius based on imaging colloidal gold nanoparticles. (a) corresponds to calculating the tip's radius using the width at half max in the topography image, and (b) corresponds to calculating the tip's radius using height information within the first 1nm of the tip's apex.

Figure 6.8 This plot of the adhesion versus tip radius is a result of different inverted AFM tips where the tip radii were calculated using the method given in figure 6.7a. The error bars represent standard deviations of the mean values and the solid line is the linear least squares regression through the data which was used to calculate the work of adhesion of the system to be $28.4 \pm 3.3 \text{ mJ/m}^2$.

Figure 6.9 This plot of the adhesion versus tip radius is a result of different inverted AFM tips where the tip radii were calculated using the method given in figure 6.7b. The error bars represent standard deviations of the mean values and the solid line is the linear least squares regression through the data which was used to calculate the work of adhesion of the system to be $29.3 \pm 2.4 \text{ mJ/m}^2$.

Figure 6.10 Blind reconstruction of the tip shape using a MATLAB routine. (a) Inverted tapping mode image of a niobium coated cantilever showing the local maxima that were used for reconstructing the tip shape. (b) Tip shape generated by blind reconstruction process. (c) Cross sectional traces along the x (red-open diamonds) and y (blue-filled diamonds) axes are shown. The solid lines represent polynomial fits used to determine the radius of curvature along each direction and at the apex.

Figure 6.11 This plot of the adhesion versus tip radius is a result of different inverted AFM tips where the tip radii were calculated using blind reconstruction algorithms. The error bars represent standard deviations of the mean values and the solid line is the linear least squares regression through the data, which was used to calculate the work of adhesion of the system to be $30.9 \pm 1.7 \text{ mJ/m}^2$.

Figure 7.1 Overlay of five IV curves of a Au/0.5NAB(0.5C12-thio)/Au-tip molecular junction.

Figure 7.2 Overlay of five IV curves of a Au/C12-thio/Au-tip molecular junction.

List of Tables

Table 3.1 List of parameters determined from the Simmons tunneling fits of $1600\mu\text{m}^2$ PPF/NAB/Cu molecular junction and PPF/NAB/Cu c-AFM molecular junctions at various applied loads.

Table 4.1 Raman band assignments for nitroazobenzene molecular layer grafted to a gold GLAD film.

Table 4.2 Raman band assignments for nitrobenzene, NB, and nitrobenzene thiol, NB thiol, grafted to a gold GLAD film.

Table 4.2 Raman band assignments for 4-benzoic acid, BA, and 4-mercaptobenzoic acid thiol, BA thiol, grafted to a gold GLAD film.

Table 5.1 Summary of peaks positions for the MBA, MNB, BT and ATP Raman active reporters.

Table 6.1 Summary of determined work of adhesion mean values and corresponding uncertainty for the different characterization methods.

Chapter I

Introduction

1.1 Imaging Nanoscience

The 1986 publication of “Engines of creation”, by K.E. Drexler,¹ demonstrates the societal impact an emerging field of science can have on the minds of the public. In this novel Drexler describes the scientific field of nanotechnology and the future implications it may have. Nanotechnology refers to the study and fabrication of matter on the nanometer scale (1×10^{-9} m). This genre of science is often referred to as a modern or new science. However, nanoscience is not very new at all. Most molecular biology processes occur at this length scale. This perception of nanoscience as being modern is based upon that fact that technology was not available to visualize into this size regime until the mid 20th century. An adage borrowed from Confucianism states “a picture is worth ten thousand words”, or as in the case for the field of nanoscience, pictures allowed scientists to peer into a new world.

The first glimpse into this new world occurred in the early 1930's with the development of electron microscopy.² Conventional light microscopy intrinsically has a resolution, R , of half the wavelength of light, λ , being used to observe the sample.

$$R = \lambda/2 \qquad 1.1$$

When considering visible light, this limitation is approximately 200 nm. The electrons used in electron microscopy have wavelengths shorter than that of visible light, thereby decreasing the resolution of electron microscopy into the

nanoscale regime. The two most common electron microscopy methods are transmission electron microscopy (TEM) and scanning electron microscopy (SEM).^{3,4}

1.2 Scanning Probe Microscopy

One drawback in electron microscopy is the limitation of visualization of morphological architecture which includes an ensemble of molecules. Ideally knowing the exact location, functionality and chemical properties of all molecules on a surface would provide great insights. At present, no single analytical technique exists that can obtain all of this information simultaneously. One avenue being developed in pursuit of this goal is scanning probe microscopy (SPM).

SPM is generally defined as the use of a sharp probe to image a surface. This field encompasses a wide variety of techniques; scanning tunneling microscopy (STM),^{5,6} atomic force microscopy (AFM),⁷⁻⁹ near-field scanning optical microscopy (NSOM),^{10,11} scanning thermal microscopy (SThM)¹² and scanning electrochemical microscopy (SECM)¹³⁻¹⁵ and all their subset derivatives. This field was born with the inception of scanning tunneling microscopy (STM) in 1981 for which Binnig and Rohrer were awarded the Nobel Prize in 1986.^{5,6} STM, and almost all SPM techniques, achieve sub-angstrom positioning by using piezoelectric materials to control the tip position relative to the sample. This class of materials expands or contracts when exposed to an electric field. The sub-

angstrom displacement of piezoelectric material deformation gives STM the ability to image at the same length scale.

In STM, the tunneling current is measured between a conducting probe and sample in one of two possible modes of feedback, constant height or constant current. A depiction of each of these feedback modes is shown in Figure 1.1. In constant height feedback, the STM probe follows the topography of the sample at a constant height and monitors the tunneling current at a given potential bias. In constant current feedback, the tunneling current is kept constant at a given potential bias and the distance between the STM probe and sample is varied. In both of these modes of feedback the image collected is a combination of electronic properties of the probe and sample and samples are limited to be conducting material.

1.3 Atomic Force Microscopy

Atomic force microscopy (AFM) was developed to overcome the STM intrinsic limitation of solely being able to interrogate conductive materials.⁷⁻⁹ The feedback mechanism of AFM relies on deflection of a cantilever. An illustration of a typical AFM is given in Figure 1.2. Piezoelectric actuators are used to obtain the required nanoscale positioning. The piezoelectric tube bends and expands to position the mounted sample. The sample is interrogated by a tip that is mounted on a cantilever. AFM tips and cantilevers are typically made by microfabrication of silicon or silicon nitride. The interaction between the AFM tip and sample are recorded as the cantilever's response.

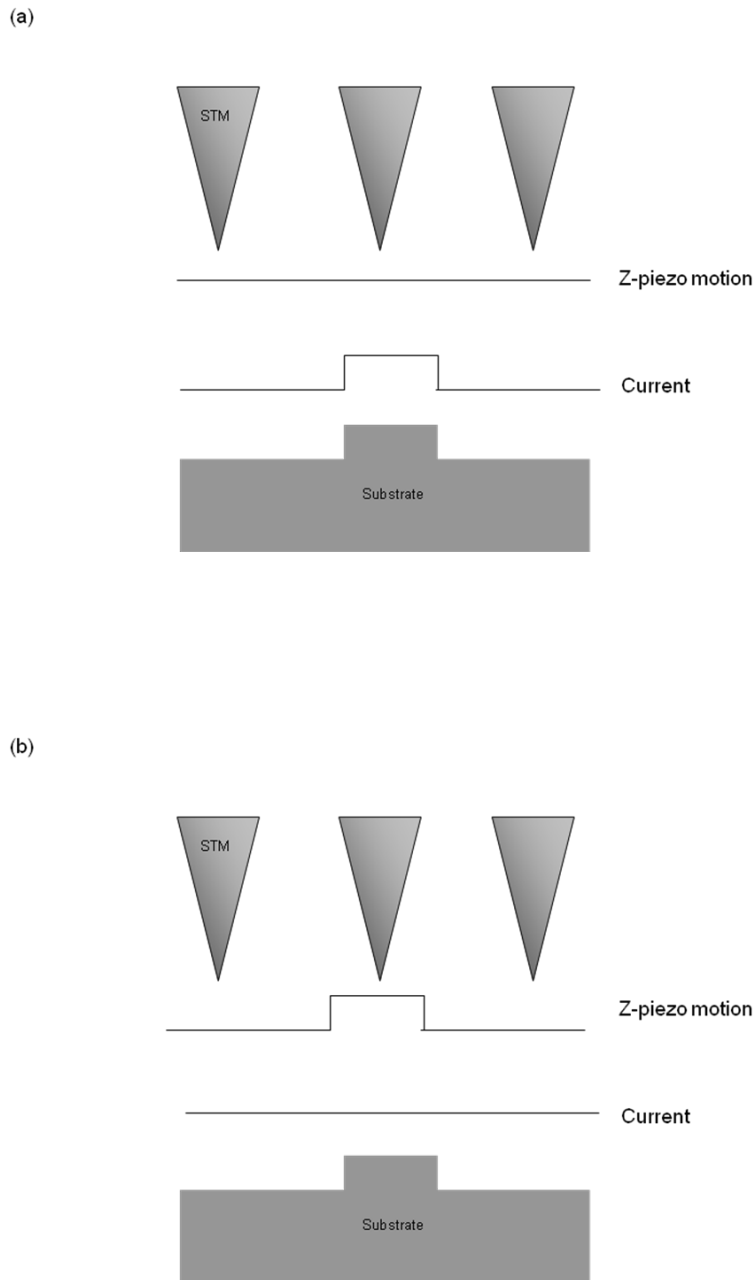


Figure 1.1 Cartoon illustration of constant height(a) and constant current(b) feedback modes commonly employed during STM operation.

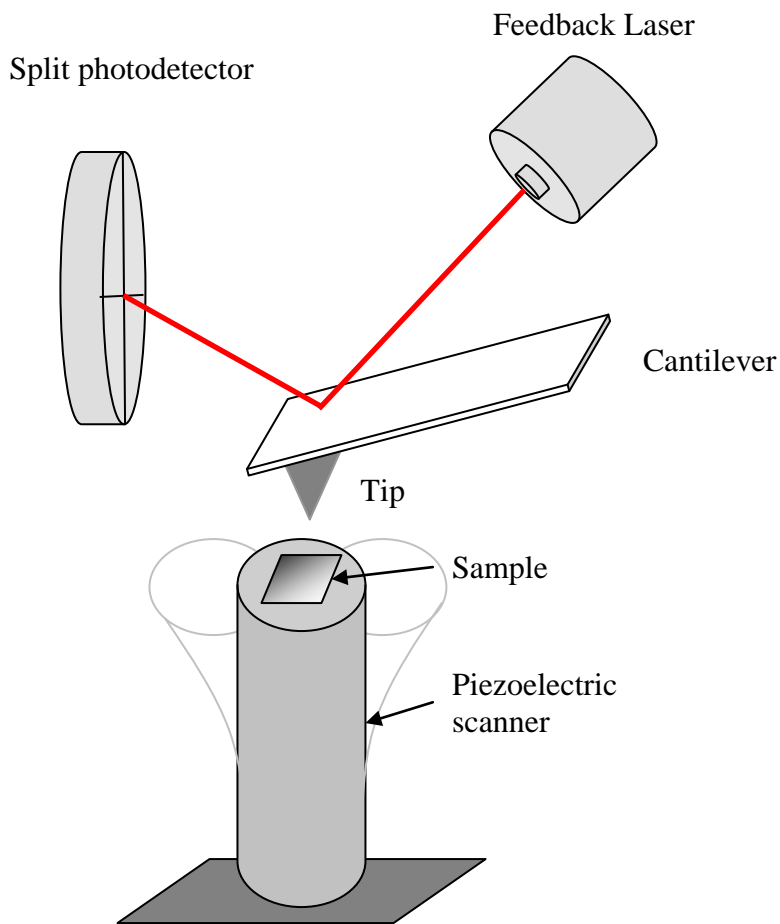


Figure 1.2 Illustration of a typical experimental setup of an AFM in which the sample is scanned with respect to the AFM tip and cantilever's response is monitored by the optical response of a laser beam reflected off the backside of the cantilever.

Originally the cantilever's response was monitored by an STM in constant height feedback positioned on the backside of the AFM cantilever.⁹ As the AFM cantilever is deflected, the STM would respond and provide monitoring of the AFM cantilever response to the tip-sample interactions. Due to the experimental complexities, this mode of monitoring a cantilever's response has largely been abandoned and replaced by monitoring a laser beam reflected off the back surface of the cantilever.¹⁶ In this method, a laser beam is reflected off the back surface of the cantilever and onto a split photodetector. As the cantilever bends, in response to the tip-sample interactions, the position of the reflected laser beam moves on the split photodetector. The difference in light intensity in the different quadrants of the split photodetector will change and is used to monitor the cantilever response to the tip-sample interactions.

1.4 Contact Mode

The two most common imaging modes used in the AFM are contact and tapping. In contact mode the tip is held at a constant force or constant height on the sample while the sample is rastered. The tip is then rastered over the surface and topography changes are registered. A cartoon depicting the feedback during contact mode operation of the AFM is provided in figure 1.3.

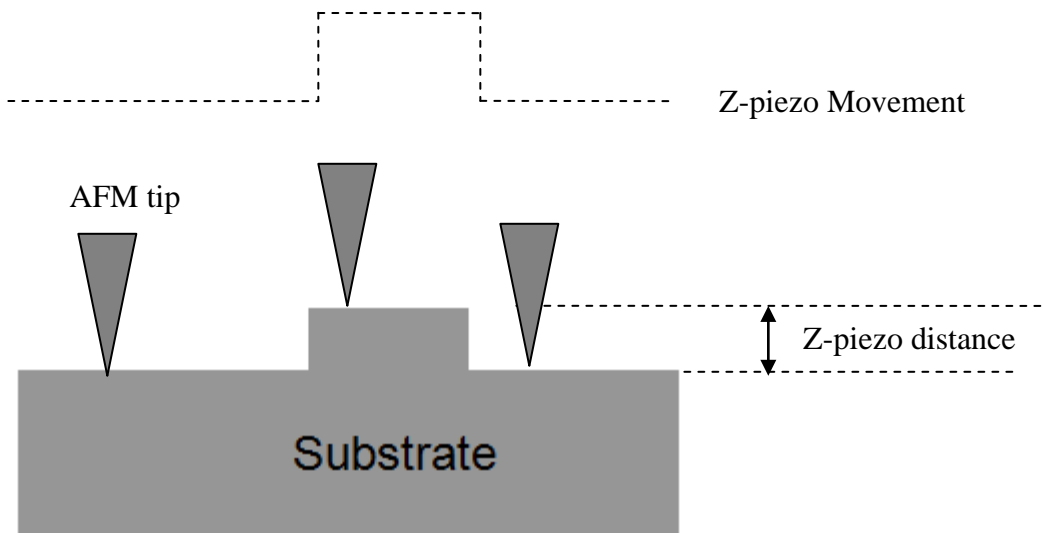


Figure 1.3 Constant force feedback employed during operation of contact mode AFM. The feedback mechanism adjusts the z-piezo distance to maintain constant force between the AFM tip and sample.

While the tip is being translated across the surface, the tip also experiences lateral forces. In contact operation the frictional forces cause lateral torsion in the cantilever causing the laser beam to deflect in the x-direction of the split photodetector, as seen in Figure 1.4. The difference in photodetector from the left and right is interpreted as friction. It has been found that friction signals can distinguish between different function groups on a surface.^{17, 18}

1.5 Tapping Mode

The lateral forces present during contact mode imaging give rise to difficulties when imaging delicate samples.¹⁹ In many situations these lateral forces are large enough to damage the sample. Intermittent contact (tapping) mode was developed to overcome this limitation.¹⁹ In tapping mode, the tip is brought into contact with the sample, and withdrawn before moving to the next measurement location. This is achieved by oscillating the cantilever at its resonant frequency with a sinusoidal wave. A cartoon depiction of this is provided in Figure 1.5. On each cycle of oscillation, the tip intermittently contacts the surface, thereby avoiding lateral drag. In this mode of operation the amplitude of oscillation is monitored for the feedback. Upon encountering an asperity on the surface, the amplitude of oscillation will decrease. To maintain constant amplitude, the piezo must adjust the tip-sample distance accordingly, which is registered as a topography change. Since the cantilever is vibrated with a sinusoidal wave, the wave contains both amplitude and phase information. The phase of oscillation contains a large

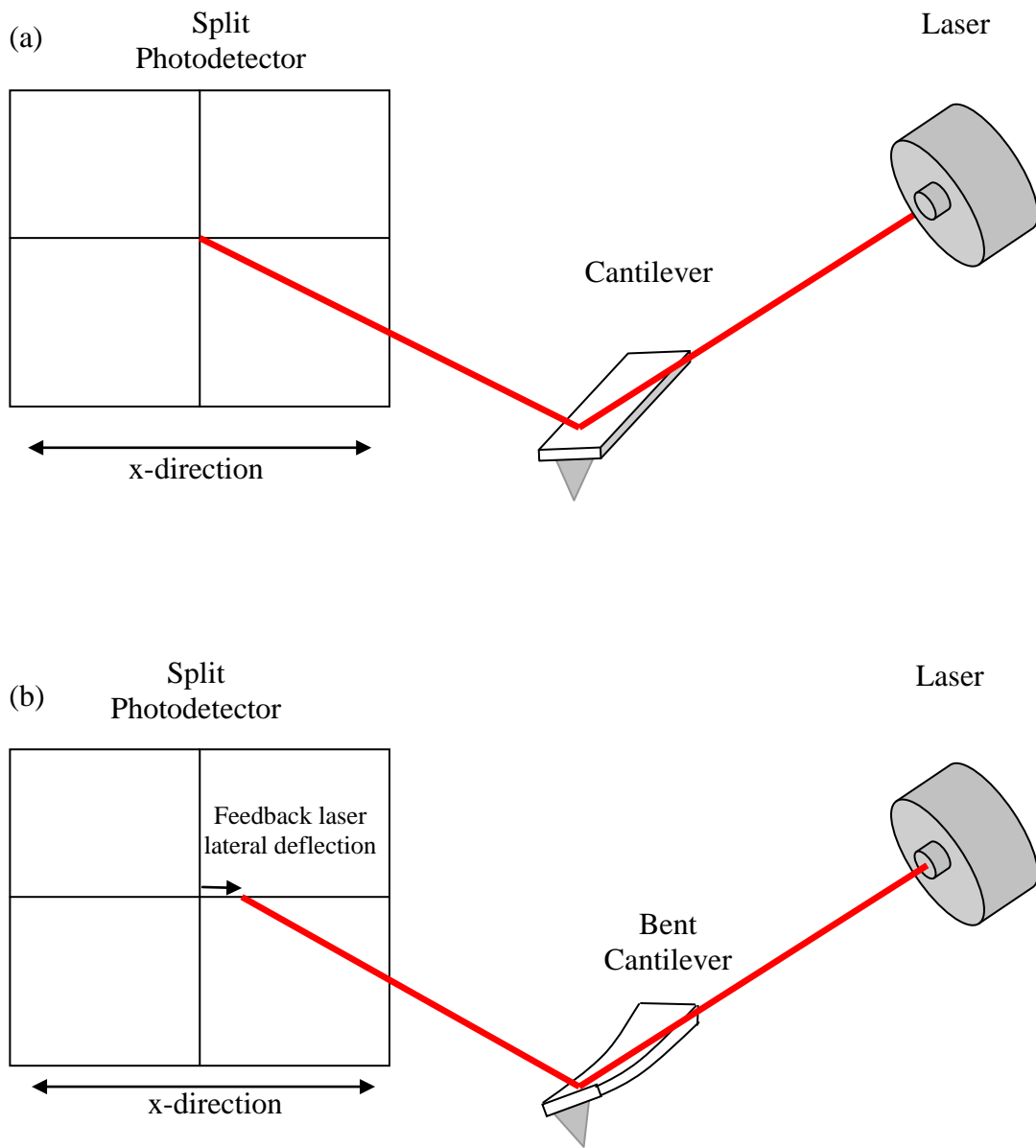


Figure 1.4 Torsional deflections in the cantilever, attributed to friction appear as a deflection in the horizontal direction in the split photodetector. Cantilever response under no frictional force (a) and with frictional force (b)

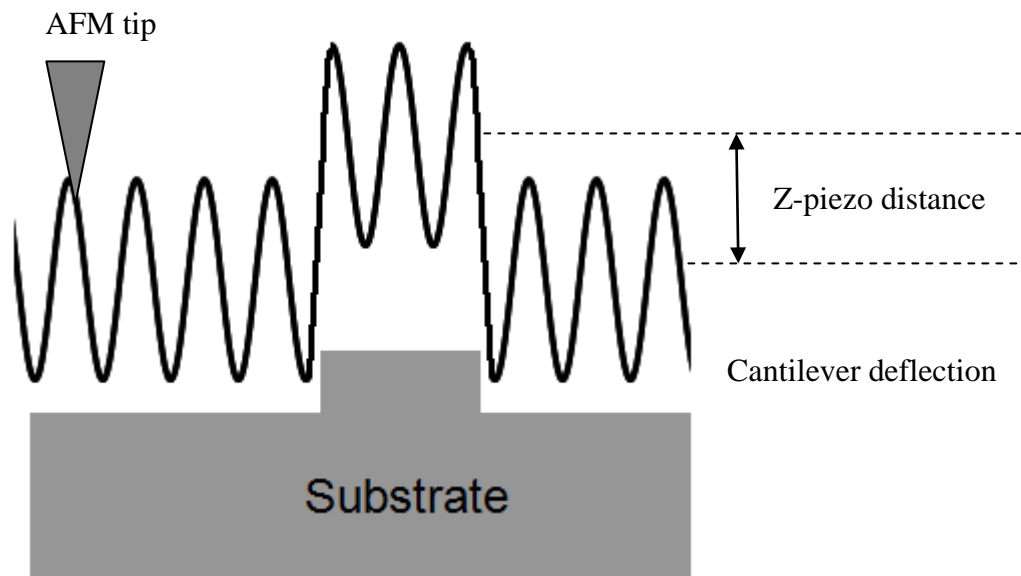


Figure 1.5 Amplitude feedback employed during operation of tapping mode AFM. The feedback mechanism adjusts the z-piezo distance to maintain constant amplitude.

amount of information. When encountering a height asperity the amplitude of oscillation decreases, creating a phase shift. Sample compressibility and adhesive properties can also cause a phase shift. Researchers have demonstrated that phase information can distinguish between chemical functional groups based on a surface.²⁰

1.6 Force Curves

Since the inception of AFM, these microscopes have been used to study interaction forces between two substrates.^{17, 21-23} This field is conventionally known as force spectroscopy and it has taken on many forms. The AFM can measure the interaction forces of extremely small numbers of molecules and at the lower limit single molecule interaction forces can be monitored.^{22, 24} Generally, a force spectroscopy experiment is performed by bringing the AFM tip in and out of contact with a surface. The cantilever deflection is monitored as a function of distance traveled by the piezo and a force curve is generated. An example force curve is given in Figure 1.6.

During the approach, the tip experiences attractive forces from the sample. When the tip is away from the sample, these forces are weak and little to no cantilever deflection is detected. Upon decreasing the separation distances, the attractive forces become large enough to overcome the cantilever's stiffness and the tip snaps into contact with the surface. Once in contact the cantilever will continue to deflect linearly with further piezo displacement.

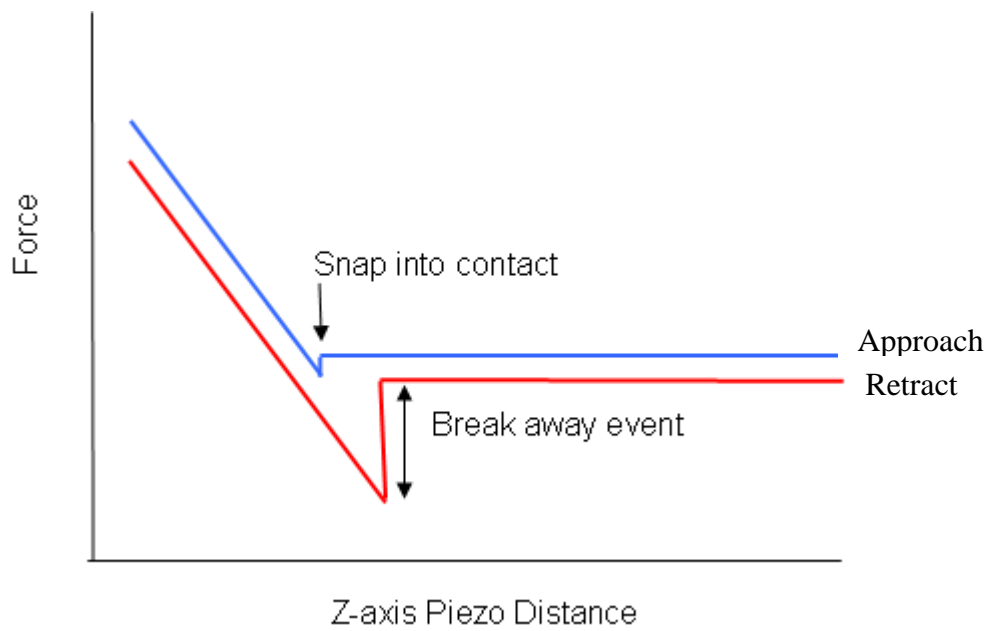


Figure 1.6 Illustration depiction of a force curve data collected by bring the AFM tip in and out of contact with a surface. The force curve collected during approach is depicted in blue while the retract force curve is depicted in red.

The detector response may be used to determine the sensitivity of the cantilever. When retracting the tip from the surface it is common for the tip to be withdrawn further than the location of the snap in. This is attributed to adhesive forces “holding on to” the tip. Once the cantilever stiffness is greater than these adhesive forces the tip will be released from the surface. This discontinuity in the force curve is referred to as the pull off force and is used, in AFM measurements, as a measure of the adhesive force.

The Johnson-Kendall-Roberts (JKR) model is commonly used to understand these events and quantify these pull off forces.²⁵ An illustration of the geometric depiction of this model is provided in Figure 1.7. The JKR model assumes elastic deformation of the probe and surface. Upon pulling away the tip, the JKR model predicts the two surfaces will continue to interact, even past the point of initial contact, this is referred to as adhesion. The JKR model predicts the adhesive force to separate a sphere, having a radius R , from a flat plane is given by;²⁵

$$F=3/2\pi W_{ad} R \quad (1.1)$$

where W_{ad} is the change in free energy required to separate two surfaces within a medium or more commonly the work of adhesion. Commonly W_{ad} is determined by the AFM by measuring the pull-off force, F , between the AFM tip and R is the radius of the tip. The JKR model predicts a contact radius, a , given by^{21, 25}

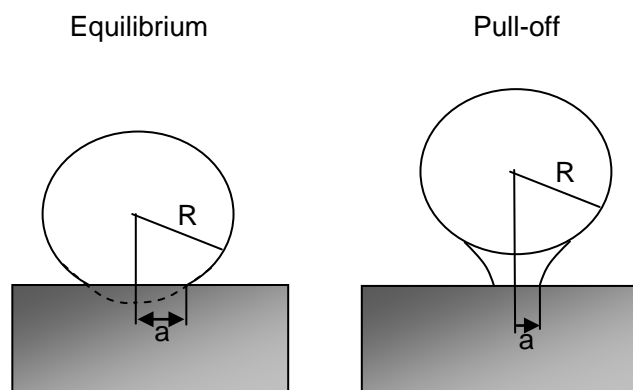


Figure 1.7 Illustration of the JRK contact mechanical model, where R is the radius of the sphere and a is the contact radius between the sphere and surface.

$$a^3 = RP_0/K \quad (1.2)$$

where

$$P_0 = P + 3\pi W_{ad}R + (6\pi W_{ad}RP + 3\pi W_{ad}R)^{1/2} \quad (1.3)$$

P is the initial applied load between the probe and sample, and K is the cantilever's spring constant, assuming the cantilever is less rigid than the underlying surface. Thus the JKR model can be used to estimate the work of adhesion and contact area for a given force between a tip and a surface.

1.7 Chemical Force Microscopy

Chemical force microscopy refers to the application of force microscopy to distinguish between chemical species on a surface.^{21, 26, 27} This can be achieved using a variety of methods, the most common of these being friction imaging, phase imaging, or adhesion measurements. For all these methods, small differences in the AFM probe and sample interactions are monitored. This usually begins by immobilizing a chemical layer onto the AFM tip to ensure chemical homogeneity. Typical immobilization procedures employ adsorption of thiol molecules onto a gold coated AFM tip.^{21, 26} The sample is subsequently interrogated by the modified AFM probe and the small chemical differences are monitored providing chemical information about the surface.

Lieber and coworkers demonstrated that monitoring the friction signal of the AFM when imaging patterned regions of CH₃ or COOH terminated thiols a

contrast could be observed for the varying surface functionality.²⁷ The friction images provided predictable contrast that agreed well with the position of the functional groups on the surface. The friction image contrast is attributed to adhesive differences between the modified tip and the CH₃ or COOH patterns. The resolution of this method of chemical recognition is highly dependent on the AFM probe size. As such, researchers have been developing smaller probe sizes to provide maximum resolution.²⁸ McDermott and coworkers later found that phase imaging during tapping mode AFM provides contrast that agrees with chemical composition of the surface.²⁰ In this work they found differences in the phase image corresponding to CH₃ or COOH terminated layers. It is believed that the contrast mechanism for these chemical recognition methods is attributed to adhesive differences between the chemical functionalities.

1.8 Inverted Atomic Force Microscopy (i-AFM)

Most force spectroscopy experiments monitor a small number of interactions in highly controlled environments.²¹⁻²⁴ These low numbers of molecular interactions, in a given experiment, are largely attributed to the bottleneck created by using the conventional AFM tip-cantilever setup. It is relatively simple to pattern a chemical library of tens of thousands of different molecules on substrates. However one tip-cantilever combination at a time is used to investigate each molecular interaction at a time. To increase the throughput available to AFM experiments microfabrication of cantilever arrays has been developed.^{11, 29-32} Each cantilever could be monitored, enabling vast

amount of interactions to be measured simultaneously. An example of this has been the development of the millipede atomic force microscope.¹¹ In this concept, 1024 cantilevers were fabricated in a 3mm x 3mm area for imprinting data storage.

True high-throughput AFM is still eluding the scientific community. One potential candidate to circumvent these issues has been the development of inverted atomic force microscopy (i-AFM).^{18, 33, 34} In this inverted design, the sample is located on the end of a tipless cantilever and is interrogated by any one of the tens of thousands of substrate-supported tips located on a microfabricated tip array. Figure 1.8 is an illustration of the i-AFM design.

Substrate supported tip arrays are fabricated by conventional microfabrication techniques, as shown in Figure 1.9. An initial template pattern is fabricated on a silicon wafer using photoresist. The unexposed photoresist is removed leaving behind a patterned silicon wafer. Reactive ion etching is used to etch silicon pillars, in the positions of the patterned photoresist. Following this a protective silicon oxide layer is formed using thermal oxide methods and a substrate supported silicon tip is protected by a silicon oxide layer. Prior to use, the silicon oxide layer is removed using hydrofluoric acid, leaving behind a substrate supported silicon tip.

Tips are generally arranged in a square array with a 25 μm pitch, each having a unique location identifier. In this arrangement a 1 cm^2 tip array will have 81,000 available tips. Tip arrays have been modified via microcontact printing, robotic spotting as well as microfluidics.^{35-37,33} The substrate supported

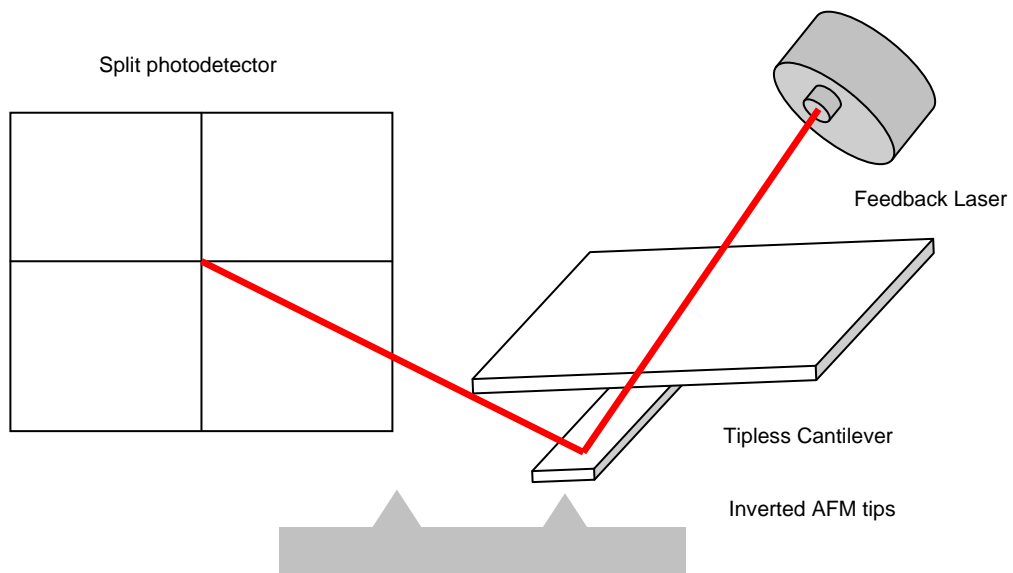


Figure 1.8 Illustration of the i-AFM design demonstrating a tipless cantilever being imaged by substrate supported AFM tips.

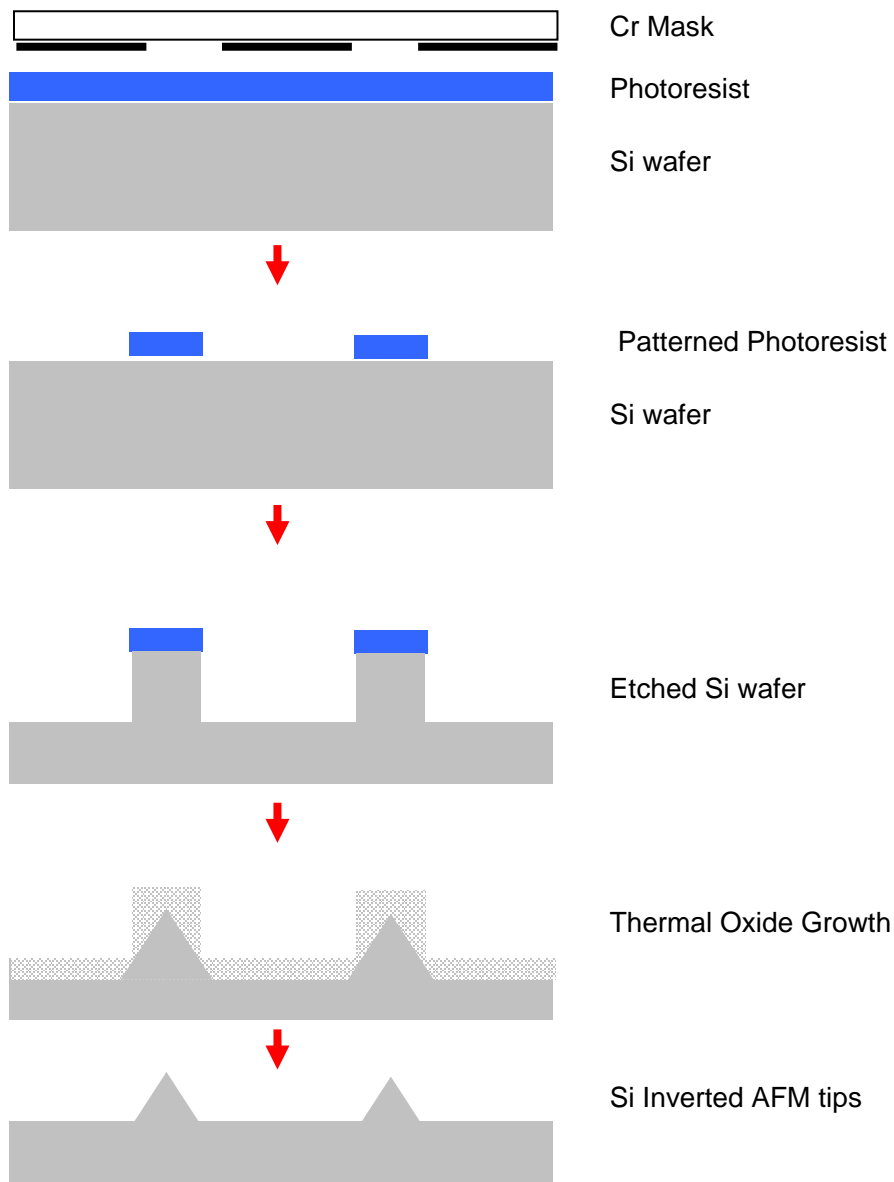


Figure 1.9 Schematic of the fabrication process involved to produce and liberate substrate supported inverted AFM tips.

tips are then further used to interrogate a sample that has been mounted onto a tipless cantilever.³⁸ Commercial tipless cantilevers are typically 20-40 μm wide, and these smaller dimensions have restricted patterning to more complex methods such as dip pen nanolithography, carefully controlled microcontact printing and nanoparticle patterning.^{35-37,33}

The strengths of i-AFM arise from the redundancy and large number of available tips to interrogate a cantilever supported sample. A very common obstacle when performing an AFM experiment is the tip changing shape from usage or contamination. In the conventional AFM design, one would have to disassemble the experiment and start over. i-AFM avoids this, allowing the user to simply move to a new tip and the experiment may continue. With respect to high-throughput chemical force microscopy this redundancy in tips can include potentially large numbers of combinations of interactions from a moderate number of molecular library elements.

1.9 Conductive AFM

Conducting atomic force microscopy (c-AFM) can be used to probe the electrical properties of the sample. Generally, the AFM tip is coated with a metal and a potential bias is applied between the tip and sample and the current response is recorded. Due to the small size of the AFM tip, electrical properties on the nanometer size regime are investigated. Data can be collected in a variety of ways. A constant potential bias can be applied and the sample can be imaged. In this form the current response at different locations on the surface will be

monitored. The result is a current image of the surface that can be correlated to height or friction images. Another mode of interrogation occurs by keeping the tip –sample position constant and varying the potential bias, while monitoring the current response, thereby collecting a current/voltage (IV) curve. Due to the reliable constant force feedback, intrinsic to the AFM, IV curves can be collected at a variety of forces, thereby monitoring electrical response of a material to an applied load.

1.10 Molecular Electronics

One of the first reports of synthetically tailoring a molecule's structure for electronic properties was published in 1974 by Avimar and Ratner.³⁹ In this work they designed a molecule that contained electron donating and accepting functional groups and would present rectification properties when electronically interrogated. This important modeling work showed the promise of using molecular systems to control current flow and laid the foundation for a field of study known as “molecular electronics”.

The heart of functionality of these devices is movement of charge through the molecular component. A molecule is immobilized between two electrodes forming what is referred to as a molecular junction. Typically the molecule is first immobilized onto the bottom electrode. This immobilization process may occur in a variety of ways. Initially electrodes were modified by the physical adsorption of molecules or polymers.^{40, 41} Control of molecular orientation was initially achieved by Langmuir-Blodgett films, and shortly after by silanization and aldehyde reactions to chemically modify the lower electrode of a molecular

junction.⁴²⁻⁴⁵ However, the vast majority of lower electrode surface modification contain the thiol-gold linkage.^{23, 46-48} The reason for this extensive usage is that thiols are well known to form a highly dense, well ordered monolayer on the gold surface.^{49, 50} The molecular orientation, layer thickness, interaction with the lower electrode and packing geometry are well controlled.

Once the molecule is immobilized on the lower electrode typically the top contact electrode is fabricated, completing the molecular junction. Cartoon depictions of common molecular junctions are provided in Figure 1.10. Initially, mercury drop electrodes were used as top contacts to investigate charge transport through molecule layers (Figure 1.10a).⁵¹⁻⁵⁹ Another commonly used means of fabricating top contact electrodes is photolithographic or shadow mask techniques, (Figure 1.10b). The metal top contact is deposited onto the molecular layer through a pattern.⁶⁰⁻⁶² This method is very useful, as it directly incorporates microelectronic technology into the fabrication process. Both the mercury drop and metal deposited molecular junctions commonly have contact areas from centimeters to tens of micrometer contact areas⁶².

With the decreasing size of electrical components, researchers have been devising means to fabricate devices that involve extremely small ensembles of molecules. This can be achieved in a variety of different ways, for instance fabricated nanogaps^{19, 63-65}. In this setup nanofabricated

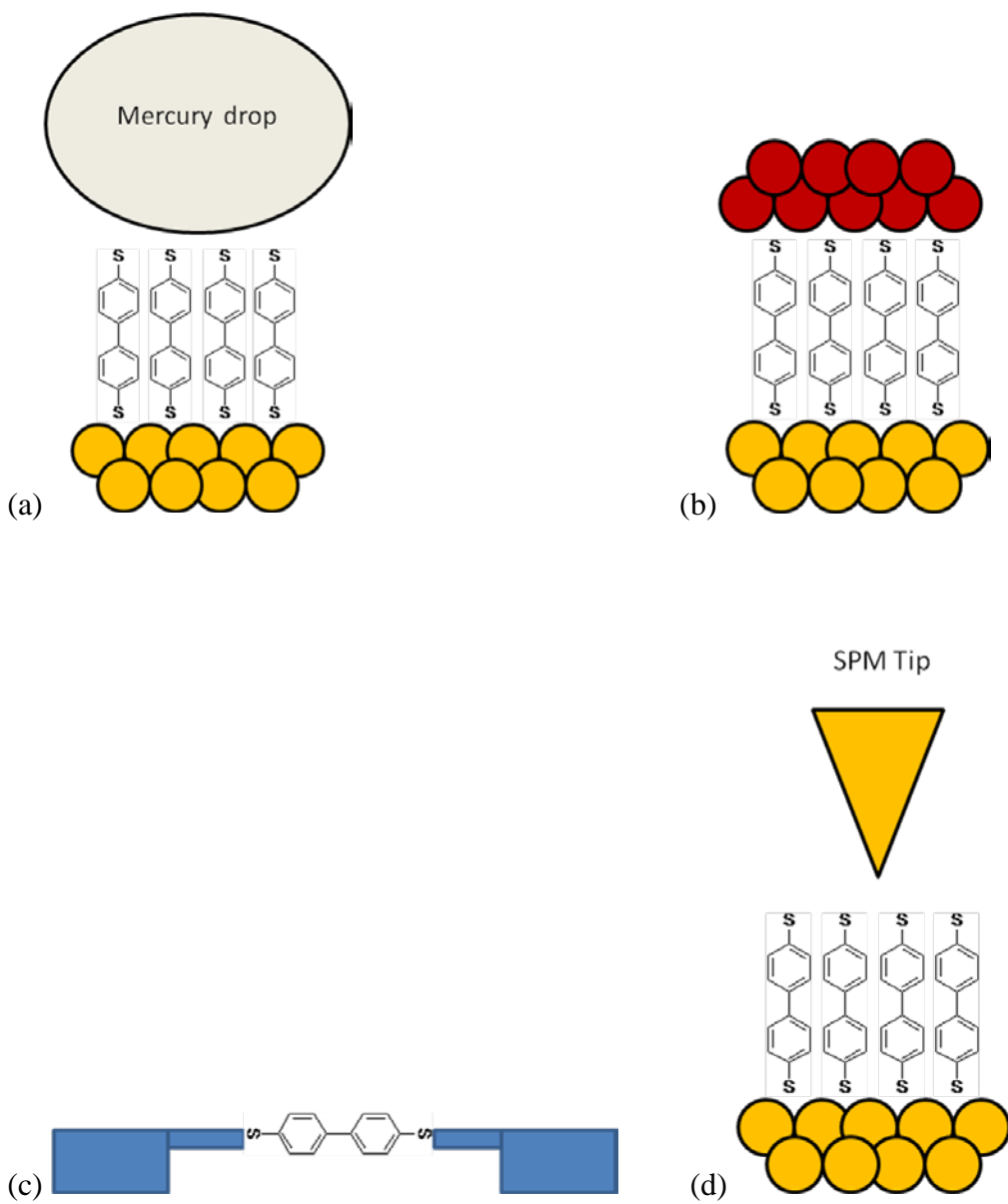


Figure 1.10 Cartoon representations of molecular junction formation by the mercury drop (a), metal deposition of the top contact (b), nanogap (c) and scanning probe (d) methods.

electrodes are used to bridge low numbers of molecules (Figure 1.10c). A variety of nanoelectrode materials have been used, including doped silicon, metals, or carbon nanotubes. However, a great amount of time and expertise is needed to generate such devices.

Due to the small probe size used in scanning probe techniques, scanning probe techniques have shown promise in molecular electronic measurements (figure 1.10d).^{23, 48, 66-68} Using these methods, charge transport studies are conducted on small ensembles of molecules. Most notable are the investigations using the scanning tunneling microscope (STM)^{23, 48, 66-68}. In these types of experiments the STM tip is used as the top contact in the molecular junction and the electronic properties of the immobilized molecules are probed. Despite charge transfer investigations occurring on proposed single molecules a large degree of irreproducibility is observed during these single molecule experiments. To overcome this uncertainty Tao and coworkers devised a statistical means to collecting and analyzing charge transport results.²³ In this approach, a gold – molecule – gold junction is repeatedly formed and broken. This is referred to as a break junction. A gold scanning tunneling microscope (STM) tip is brought in and out of contact with a gold surface in a solution of thiol molecules. A bridge of gold atoms forms between the two electrodes and at the moment of separation a molecule may drift between the gap, forming a molecular junction. The number of molecules involved in the junction will vary between each measurement, however the results are quantized and information concerning single molecule junctions may be obtained.

Similarly, conducting atomic force microscopy (c-AFM) can be used to probe the charge transport properties of extremely small ensembles of molecules.^{23, 46, 47, 69-73} Intrinsically, due to probe size, c-AFM usually involves a larger ensemble of molecules than the STM. However with low concentration of immobilized conduction molecules, the c-AFM probe will only interact with one conducting molecule at a time, thereby forming a single molecule molecular junction.⁷⁴ One advantage c-AFM has over STM experiments is that the force applied can be controlled. Frisbie and coworker found a molecular layer film will compress and deform upon subjection to increased forces.⁷¹

1.11 Grafting Aryl films derived from diazonium salts

Much of the work in this thesis involves the interrogation of aryl films derived from diazonium salts. Pinson and coworkers were the first to show that electrochemical reduction of nitrobenzene diazonium salt at a glassy carbon electrode results in a tightly bound layer of nitrobenzene on the electrode surface.⁷⁵ The mechanism they proposed is shown in Figure 1.11.

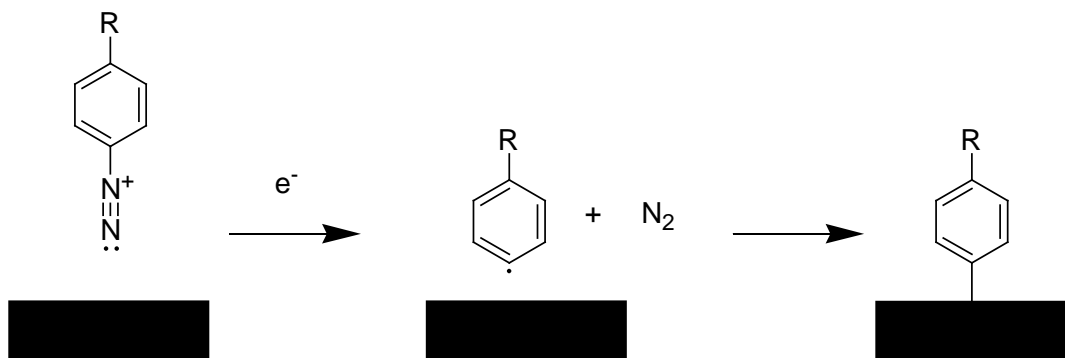


Figure 1.11 Schematic depicting the proposed mechanism of aryl-group attachment onto a carbon electrode. Adapted from reference⁷⁵

Electrochemical reduction of a diazonium salt results in the corresponding aryl radical. Being highly reactive, the radical combines with an electron from the carbon surface forming a covalent bond. Since this initial discovery, researchers have used this process to modify a wide variety of substrates.^{23, 76, 77} Diazonium salts have also demonstrated the tendency to spontaneously react with a surface, thereby avoiding the need for electrochemical equipment and allowing for complex surfaces to be modified.^{78, 79} In-situ methods for immobilizing aryl films have been developed. For these methods, the generation and further reduction of the diazonium salt occurs in the same solution, thus avoiding the need for purification steps of the diazonium salt precursor.^{80, 81}

It is the flexibility of covalently modifying a diverse range of electrodes that gives diazonium salts a unique advantage. It was later found that due to the aggressive nature of radical attachment multilayers can form. Aryl-radicals in solution may attach to the pre-existing layer, creating a branched layer structure.⁸²

Recently, x-ray photoelectron spectroscopy (XPS) studies have indicated the presence of nitrogen within aryl layers which should contain no nitrogen atoms.⁸³ This observation has been attributed to a wide variety of sources, ranging from azide radicals forming in solution which may attach to the surface^{84, 85}; to azo-coupling reactions⁸⁶; to reduction of nitro groups, to quite simply contamination within the XPS vacuum chamber⁸⁷.

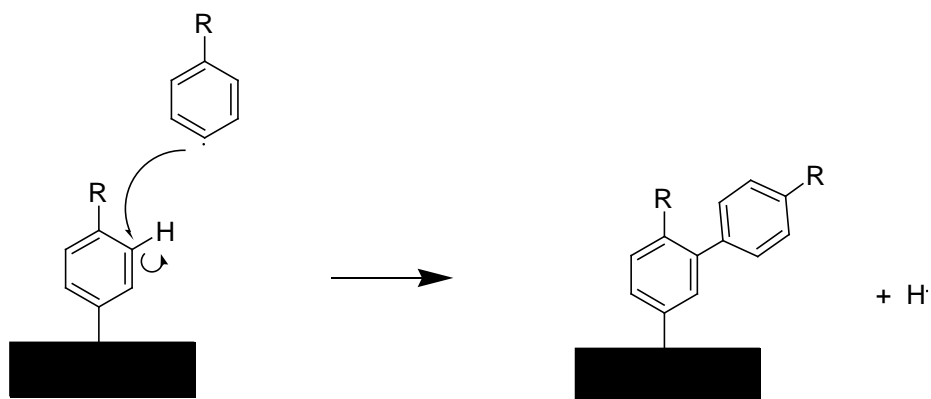


Figure 1.12 Proposed attachment mechanism for multilayer formation. The proton in the coupling reaction has been included for clarity.

McCreery and coworkers have used the diazonium salt attachment method to form molecular junctions. They have attached a variety of aryl films to carbon electrodes and observed differences in charge transport attributed to chemical differences and molecular layer thickness.^{36, 88-92} They also found that the material and formation of the top contact plays an important role in observed electron transport.⁹¹⁻⁹³

1.12 Thesis Objectives

The objective of this thesis is to exploit the nanoscale positioning and force sensitivity of atomic force microscopy to interrogate chemically modified surfaces. Chapters 2 and 3 explore the use of conductive AFM to simultaneously vary the applied load and measure charge transport through aryl films derived from diazonium salts. The aim of these investigations was to develop a methodology to investigate scalability of such junctions and to better understand top contact formation during metal deposition. The aim of Chapter 4 is to provide the first vibrational spectroscopic evidence into the mechanism of attachment and growth of aryl films derived from diazonium salts. Chapters 5 and 6 address the inherent bottle-neck of conventional AFM force spectroscopy and explores the methodology to circumvent this issue via the use of inverted atomic force microscopy.

References

1. Drexler, K. E., *Engines of Creation, The Coming Era of Nanotechnology*. Anchor Books: 1986.
2. von Borries, B.; Ruska, E., The electron microscope and its application. *Deutsche Medizinische Wochenschrift* **1935**, 79, 519-524.
3. Erni, R.; Rossell, M. D.; Kisielowski, C.; Dahmen, U., Atomic-Resolution Imaging with a Sub-50-pm Electron Probe. *Physical Review Letters* **2009**, 102, (9).
4. Smith, K. C. A.; Oatley, C. W., The Scanning Electron Microscope and Its Fields of Application. *British Journal of Applied Physics* **1955**, 6, (11), 391-399.
5. Binnig, G.; Rohrer, H.; Gerber, C.; Weibel, E., Tunneling through a Controllable Vacuum Gap. *Applied Physics Letters* **1982**, 40, (2), 178-180.
6. Binnig, G.; Rohrer, H.; Gerber, C.; Weibel, E., Surface Studies by Scanning Tunneling Microscopy. *Physical Review Letters* **1982**, 49, (1), 57-61.
7. Binnig, G.; Gerber, C.; Stoll, E.; Albrecht, T. R.; Quate, C. F., Atomic Resolution with Atomic Force Microscope. *Europhysics Letters* **1987**, 3, (12), 1281-1286.
8. Binnig, G.; Gerber, C.; Stoll, E.; Albrecht, T. R.; Quate, C. F., Atomic Resolution with Atomic Force Microscope. *Surface Science* **1987**, 189, 1-6.
9. Binnig, G.; Quate, C. F.; Gerber, C., Atomic Force Microscope. *Physical Review Letters* **1986**, 56, (9), 930-933.

10. Betzig, E.; Lewis, A.; Harootunian, A.; Isaacson, M.; Kratschmer, E., Near-Field Scanning Optical Microscopy (Nsm) - Development and Biophysical Applications. *Biophysical Journal* **1986**, 49, (1), 269-279.
11. Durig, U.; Pohl, D. W.; Rohner, F., Near-Field Optical-Scanning Microscopy. *Journal of Applied Physics* **1986**, 59, (10), 3318-3327.
12. Williams, C. C.; Wickramasinghe, H. K., Scanning Thermal Profiler. *Applied Physics Letters* **1986**, 49, (23), 1587-1589.
13. Kwak, J.; Bard, A. J., Scanning Electrochemical Microscopy - Theory of the Feedback Mode. *Analytical Chemistry* **1989**, 61, (11), 1221-1227.
14. Engstrom, R. C.; Pharr, C. M., Scanning Electrochemical Microscopy. *Analytical Chemistry* **1989**, 61, (19), A1099-&.
15. Husser, O. E.; Craston, D. H.; Bard, A. J., Scanning Electrochemical Microscopy - High-Resolution Deposition and Etching of Metals. *Journal of the Electrochemical Society* **1989**, 136, (11), 3222-3229.
16. Meyer, G.; Amer, N. M., Novel Optical Approach to Atomic Force Microscopy. *Applied Physics Letters* **1988**, 53, (12), 1045-1047.
17. Meyer, G.; Amer, N. M., Simultaneous Measurement of Lateral and Normal Forces with an Optical-Beam-Deflection Atomic Force Microscope. *Applied Physics Letters* **1990**, 57, (20), 2089-2091.
18. McDermott, M. T.; Green, J. B. D.; Porter, M. D., Scanning force microscopic exploration of the lubrication capabilities of n-alkanethiolate monolayers chemisorbed at gold Structural basis of microscopic friction and wear. *Langmuir* **1997**, 13, (9), 2504-2510.

19. Putman, C. A. J.; Vanderwerf, K. O.; Degrooth, B. G.; Vanhulst, N. F.; Greve, J., Tapping Mode Atomic-Force Microscopy in Liquid. *Applied Physics Letters* **1994**, 64, (18), 2454-2456.
20. Finot, M. O.; McDermott, M. T., High-resolution chemical mapping of surface bound functional groups with tapping-mode scanning force microscopy. *Journal of the American Chemical Society* **1997**, 119, (36), 8564-8565.
21. Vezenov, D. V.; Noy, A.; Ashby, P., Chemical force microscopy: probing chemical origin of interfacial forces and adhesion. *Journal of Adhesion Science and Technology* **2005**, 19, (3-5), 313-364.
22. Li, H. B.; Rief, M.; Oesterhelt, F.; Gaub, H. E.; Zhang, X.; Shen, J. C., Single-molecule force spectroscopy on polysaccharides by AFM - nanomechanical fingerprint of alpha-(1,4)-linked polysaccharides. *Chemical Physics Letters* **1999**, 305, (3-4), 197-201.
23. Allen, S.; Chen, X.; Davies, J.; Davies, M. C.; Dawkes, A. C.; Edwards, J. C.; Roberts, C. J.; Tendler, S. J. B.; Williams, P. M., The application of force microscopy to immunodiagnostic systems imaging and biomolecular adhesion measurements. *Applied Physics a-Materials Science & Processing* **1998**, 66, S255-S261.
24. Pierres, A.; Benoliel, A. M.; Bongrand, P., Studying receptor-mediated cell adhesion at the single molecule level. *Cell Adhesion and Communication* **1998**, 5, (5), 375-395.

25. Johnson, K. L.; Kendall, K.; Roberts, A. D., Surface Energy and Contact of Elastic Solids. *Proceedings of the Royal Society of London Series a-Mathematical and Physical Sciences* **1971**, 324, (1558), 301-&.
26. Noy, A.; Vezenov, D. V.; Lieber, C. M., Chemical force microscopy. *Annual Review of Materials Science* **1997**, 27, 381-421.
27. Frisbie, C. D.; Rozsnyai, L. F.; Noy, A.; Wrighton, M. S.; Lieber, C. M., Functional-Group Imaging by Chemical Force Microscopy. *Science* **1994**, 265, (5181), 2071-2074.
28. Hafner, J. H.; Cheung, C. L.; Woolley, A. T.; Lieber, C. M., Structural and functional imaging with carbon nanotube AFM probes. *Progress in Biophysics & Molecular Biology* **2001**, 77, (1), 73-110.
29. Minne, S. C.; Yaralioglu, G.; Manalis, S. R.; Adams, J. D.; Zesch, J.; Atalar, A.; Quate, C. F., Automated parallel high-speed atomic force microscopy. *Applied Physics Letters* **1998**, 72, (18), 2340-2342.
30. Saya, D.; Fukushima, K.; Toshiyoshi, H.; Hashiguchi, G.; Fujita, H.; Kawakatsu, H., Fabrication of single-crystal Si cantilever array. *Sensors and Actuators a-Physical* **2002**, 95, (2-3), 281-287.
31. Kakushima, K.; Watanabe, T.; Shimamoto, K.; Gouda, T.; Ataka, M.; Mimura, H.; Isono, Y.; Hashiguchi, G.; Mihara, Y.; Fujita, H., Atomic force microscope cantilever array for parallel lithography of quantum devices. *Japanese Journal of Applied Physics Part 1-Regular Papers Brief Communications & Review Papers* **2004**, 43, (6B), 4041-4044.

32. Kawakatsu, H.; Saya, D.; Kato, A.; Fukushima, K.; Toshiyoshi, H.; Fujita, H., Millions of cantilevers for atomic force microscopy. *Review of Scientific Instruments* **2002**, 73, (3), 1188-1192.
33. Chisholm, R. A.; Qiu, W.; Green, J. B. D., Patterning of cantilevers with functionalized nanoparticles for combinatorial atomic force microscopy. *Langmuir* **2007**, 23, (15), 7891-7894.
34. Chan, S. S. F.; Green, J. B. D., Tapping mode imaging and measurements with an inverted atomic force microscope. *Langmuir* **2006**, 22, (15), 6701-6706.
35. Piner, R. D.; Zhu, J.; Xu, F.; Hong, S. H.; Mirkin, C. A., "Dip-pen" nanolithography. *Science* **1999**, 283, (5402), 661-663.
36. McCreery, R. L.; Wu, J.; Kalakodimi, R. P., Electron transport and redox reactions in carbon-based molecular electronic junctions. *Physical Chemistry Chemical Physics* **2006**, 8, (22), 2572-2590.
37. Quist, A. P.; Pavlovic, E.; Oscarsson, S., Recent advances in microcontact printing. *Analytical and Bioanalytical Chemistry* **2005**, 381, (3), 591-600.
38. Mabry, J. C.; Yau, T.; Yap, H. W.; Green, J. B. D., Developments for inverted atomic force microscopy. *Ultramicroscopy* **2002**, 91, (1-4), 73-82.
39. Aviram, A.; Ratner, M. A., Molecular Rectifiers. *Chemical Physics Letters* **1974**, 29, (2), 277-283.
40. Hoshino, S., Diffusion and Electric Conductance in Polymer Solutions. *International Chemical Engineering* **1970**, 10, (4), 678-&.

41. Chudleigh, P. W., Mechanism of Charge-Transfer to a Polymer Surface by a Conducting Liquid Contact. *Journal of Applied Physics* **1976**, 47, (10), 4475-4483.
42. Shikin, S. A.; Berzina, T. S.; Sotnikov, P. S.; Troitsky, V. I.; Neilands, O. Y.; Pukitis, G. G.; Khodorkovsky, V. Y., Preparation and Electrical-Properties of Conducting Langmuir-Blodgett-Films of Hexadecylbis (Ethylenedithio)-Ttf and Hexadecyl-Tcnq Mixture. *Biologicheskije Membrany* **1990**, 7, (10), 1111-1117.
43. Lopinski, G., Organics on silicon; single molecules, nanostructures and monolayers. *International Journal of Nanotechnology* **2008**, 5, (9-12), 1247-1267.
44. Kirczenow, G.; Piva, P. G.; Wolkow, R. A., Linear chains of styrene and methylstyrene molecules and their heterojunctions on silicon: Theory and experiment. *Physical Review B* **2005**, 72, (24).
45. Dogel, I. A.; Dogel, S. A.; Pitters, J. L.; DiLabio, G. A.; Wolko, R. A., Chemical methods for the hydrogen termination of silicon dangling bonds. *Chemical Physics Letters* **2007**, 448, (4-6), 237-242.
46. Beebe, J. M.; Kim, B.; Frisbie, C. D.; Kushmerick, J. G., Measuring relative barrier heights in molecular electronic junctions with transition voltage spectroscopy. *Acs Nano* **2008**, 2, (5), 827-832.
47. Engelkes, V. B.; Frisbie, C. D., Simultaneous nanoindentation and electron tunneling through alkanethiol self-assembled monolayers. *Journal of Physical Chemistry B* **2006**, 110, (20), 10011-10020.

48. Shewchuk, D. M.; McDermott, M. T., Comparison of Diazonium Salt Derived and Thiol Derived Nitrobenzene Layers on Gold. *Langmuir* **2009**, *25*, (8), 4556-4563.
49. Walczak, M. M.; Popenoe, D. D.; Deinhammer, R. S.; Lamp, B. D.; Chung, C. K.; Porter, M. D., Reductive Desorption of Alkanethiolate Monolayers at Gold - a Measure of Surface Coverage. *Langmuir* **1991**, *7*, (11), 2687-2693.
50. Zhong, C. J.; Brush, R. C.; Anderegg, J.; Porter, M. D., Organosulfur monolayers at gold surfaces: Reexamination of the case for sulfide adsorption and implications to the formation of monolayers from thiols and disulfides. *Langmuir* **1999**, *15*, (2), 518-525.
51. Mann, B.; Kuhn, H., Tunneling through Fatty Acid Salt Monolayers. *Journal of Applied Physics* **1971**, *42*, (11), 4398-&.
52. Ranganathan, S.; Steidel, I.; Anariba, F.; McCreery, R. L., Covalently bonded organic monolayers on a carbon substrate: A new paradigm for molecular electronics. *Nano Letters* **2001**, *1*, (9), 491-494.
53. Holmlin, R. E.; Haag, R.; Chabynyc, M. L.; Ismagilov, R. F.; Cohen, A. E.; Terfort, A.; Rampi, M. A.; Whitesides, G. M., Electron transport through thin organic films in metal-insulator-metal junctions based on self-assembled monolayers. *Journal of the American Chemical Society* **2001**, *123*, (21), 5075-5085.
54. Solak, A. O.; Ranganathan, S.; Itoh, T.; McCreery, R. L., A mechanism for conductance switching in carbon-based molecular electronic junctions. *Electrochemical and Solid State Letters* **2002**, *5*, (8), E43-E46.

55. Liu, Y. J.; Yu, H. Z., Alkyl monolayer-passivated metal-semiconductor diodes: Molecular tunability and electron transport. *Chemphyschem* **2002**, 3, (9), 799-+.
56. Grave, C.; Tran, E.; Samori, P.; Whitesides, G. M.; Rampi, M. A., Correlating electrical properties and molecular structure of SAMs organized between two metal surfaces. *Synthetic Metals* **2004**, 147, (1-3), 11-18.
57. Tran, E.; Grave, C.; Whitesides, G. A.; Rampi, M. A., Controlling the electron transfer mechanism in metal-molecules-metal junctions. *Electrochimica Acta* **2005**, 50, (25-26), 4850-4856.
58. Tran, E.; Duati, M.; Whitesides, G. M.; Rampi, M. A., Gating current flowing through molecules in metal-molecules-metal junctions. *Faraday Discussions* **2006**, 131, 197-203.
59. Tran, E.; Duati, M.; Ferri, V.; Mullen, K.; Zharnikov, M.; Whitesides, G. M.; Rampi, M. A., Experimental approaches for controlling current flowing through metal-molecules-metal junctions. *Advanced Materials* **2006**, 18, (10), 1323-1328.
60. McCarty, G. S., Molecular lithography for wafer-scale fabrication of molecular junctions. *Nano Letters* **2004**, 4, (8), 1391-1394.
61. Chang, S. C.; Li, Z. Y.; Lau, C. N.; Larade, B.; Williams, R. S., Investigation of a model molecular-electronic rectifier with an evaporated Ti-metal top contact. *Applied Physics Letters* **2003**, 83, (15), 3198-3200.

62. Akkerman, H. B.; Blom, P. W. M.; de Leeuw, D. M.; de Boer, B., Towards molecular electronics with large-area molecular junctions. *Nature* **2006**, 441, (7089), 69-72.
63. Morpurgo, A. F.; Marcus, C. M.; Robinson, D. B., Controlled fabrication of metallic electrodes with atomic separation. *Applied Physics Letters* **1999**, 74, (14), 2084-2086.
64. Johnston, D. E.; Strachan, D. R.; Johnson, A. T. C., Parallel fabrication of nanogap electrodes. *Nano Letters* **2007**, 7, (9), 2774-2777.
65. Mahapatro, A. K.; Ying, J. W.; Ren, T.; Janes, D. B., Electronic transport through ruthenium-based redox-active molecules in metal-molecule-metal nanogap junctions. *Nano Letters* **2008**, 8, (8), 2131-2136.
66. Gittins, D. I.; Bethell, D.; Schiffrin, D. J.; Nichols, R. J., A nanometre-scale electronic switch consisting of a metal cluster and redox-addressable groups. *Nature* **2000**, 408, (6808), 67-69.
67. Bumm, L. A.; Arnold, J. J.; Dunbar, T. D.; Allara, D. L.; Weiss, P. S., Electron transfer through organic molecules. *Journal of Physical Chemistry B* **1999**, 103, (38), 8122-8127.
68. Guisinger, N. P.; Yoder, N. L.; Hersam, M. C., Probing charge transport at the single-molecule level on silicon by using cryogenic ultra-high vacuum scanning tunneling microscopy. *Proceedings of the National Academy of Sciences of the United States of America* **2005**, 102, (25), 8838-8843.

69. Cui, X. D.; Zarate, X.; Tomfohr, J.; Sankey, O. F.; Primak, A.; Moore, A. L.; Moore, T. A.; Gust, D.; Harris, G.; Lindsay, S. M., Making electrical contacts to molecular monolayers. *Nanotechnology* **2002**, 13, (1), 5-14.
70. Loiacono, M. J.; Granstrom, E. L.; Frisbie, C. D., Investigation of charge transport in thin, doped sexithiophene crystals by conducting probe atomic force microscopy. *Journal of Physical Chemistry B* **1998**, 102, (10), 1679-1688.
71. Wold, D. J.; Frisbie, C. D., Fabrication and characterization of metal-molecule-metal junctions by conducting probe atomic force microscopy. *Journal of the American Chemical Society* **2001**, 123, (23), 5549-5556.
72. Tivanski, A. V.; Bemis, J. E.; Akhremitchev, B. B.; Liu, H. Y.; Walker, G. C., Adhesion forces in conducting probe atomic force microscopy. *Langmuir* **2003**, 19, (6), 1929-1934.
73. Tivanski, A. V.; Walker, G. C., Ferrocenylundecanethiol self-assembled monolayer charging correlates with negative differential resistance measured by conducting probe atomic force microscopy. *Journal of the American Chemical Society* **2005**, 127, (20), 7647-7653.
74. Ramachandran, G. K.; Tomfohr, J. K.; Li, J.; Sankey, O. F.; Zarate, X.; Primak, A.; Terazono, Y.; Moore, T. A.; Moore, A. L.; Gust, D.; Nagahara, L. A.; Lindsay, S. M., Electron transport properties of a carotene molecule in a metal-(single molecule)-metal junction. *Journal of Physical Chemistry B* **2003**, 107, (25), 6162-6169.
75. Bourdillon, C.; Delamar, M.; Demaille, C.; Hitmi, R.; Moiroux, J.; Pinson, J., Immobilization of Glucose-Oxidase on a Carbon Surface Derivatized by

Electrochemical Reduction of Diazonium Salts. *Journal of Electroanalytical Chemistry* **1992**, 336, (1-2), 113-123.

76. Stewart, M. P.; Tour, J. M.; Kosynkin, D. V.; Allara, D. L.; Dirk, S. M.; Maya, F. M., Reactions of oligo(phenylene ethynylene) diazonium salts with Si, GaAs, and Pd surfaces. *Abstracts of Papers of the American Chemical Society* **2003**, 225, 2-INOR.

77. Bernard, M. C.; Chausse, A.; Cabet-Deliry, E.; Chehimi, M. M.; Pinson, J.; Podvorica, F.; Vautrin-UI, C., Organic layers bonded to industrial, coinage, and noble metals through electrochemical reduction of aryldiazonium salts. *Chemistry of Materials* **2003**, 15, (18), 3450-3462.

78. Combellas, C.; Kanoufi, F.; Pinson, J.; Podvorica, F. I., Time-of-flight secondary ion mass spectroscopy characterization of the covalent bonding between a carbon surface and aryl groups. *Langmuir* **2005**, 21, (1), 280-286.

79. Adenier, A.; Barre, N.; Cabet-Deliry, E.; Chausse, A.; Griveau, S.; Mercier, F.; Pinson, J.; Vautrin-UI, C., Study of the spontaneous formation of organic layers on carbon and metal surfaces from diazonium salts. *Surface Science* **2006**, 600, (21), 4801-4812.

80. Baranton, S.; Belanger, D., Electrochemical derivatization of carbon surface by reduction of in situ generated diazonium cations. *Journal of Physical Chemistry B* **2005**, 109, (51), 24401-24410.

81. Lyskawa, J.; Belanger, D., Direct modification of a gold electrode with aminophenyl groups by electrochemical reduction of in situ generated

aminophenyl monodiazonium cations. *Chemistry of Materials* **2006**, 18, (20), 4755-4763.

82. Kariuki, J. K.; McDermott, M. T., Formation of multilayers on glassy carbon electrodes via the reduction of diazonium salts. *Langmuir* **2001**, 17, (19), 5947-5951.

83. Laforgue, A.; Addou, T.; Belanger, D., Characterization of the deposition of organic molecules at the surface of gold by the electrochemical reduction of aryl diazonium cations. *Langmuir* **2005**, 21, (15), 6855-6865.

84. Saby, C.; Ortiz, B.; Champagne, G. Y.; Belanger, D., Electrochemical modification of glassy carbon electrode using aromatic diazonium salts .1. Blocking effect of 4-nitrophenyl and 4-carboxyphenyl groups. *Langmuir* **1997**, 13, (25), 6805-6813.

85. Doppelt, P.; Hallais, G.; Pinson, J.; Podvorica, F.; Verneyre, S., Surface modification of conducting substrates. Existence of azo bonds in the structure of organic layers obtained from diazonium salts. *Chemistry of Materials* **2007**, 19, (18), 4570-4575.

86. Hurley, B. L.; McCreery, R. L., Covalent bonding of organic molecules to Cu and Al alloy 2024 T3 surfaces via diazonium ion reduction. *Journal of the Electrochemical Society* **2004**, 151, (5), B252-B259.

87. deVilleneuve, C. H.; Pinson, J.; Bernard, M. C.; Allongue, P., Electrochemical formation of close-packed phenyl layers on Si(111). *Journal of Physical Chemistry B* **1997**, 101, (14), 2415-2420.

88. Anariba, F.; McCreery, R. L., Electronic conductance behavior of carbon-based molecular junctions with conjugated structures. *Journal of Physical Chemistry B* **2002**, 106, (40), 10355-10362.
89. Anariba, F.; Steach, J. K.; McCreery, R. L., Strong effects of molecular structure on electron transport in carbon/molecule/copper electronic junctions. *Journal of Physical Chemistry B* **2005**, 109, (22), 11163-11172.
90. Bergren, A. J.; Harris, K. D.; Deng, F. J.; McCreery, R. L., Molecular electronics using diazonium-derived adlayers on carbon with Cu top contacts: critical analysis of metal oxides and filaments. *Journal of Physics-Condensed Matter* **2008**, 20, (37).
91. Kalakodimi, R. P.; Nowak, A. M.; McCreery, R. L., Carbon/molecule/metal and carbon/molecule/metal oxide molecular electronic junctions. *Chemistry of Materials* **2005**, 17, (20), 4939-4948.
92. McCreery, R. L.; Viswanathan, U.; Kalakodimi, R. P.; Nowak, A. M., Carbon/molecule/metal molecular electronic junctions: the importance of "contacts". *Faraday Discussions* **2006**, 131, 33-43.
93. McCreery, R. L., Molecular electronic junctions. *Chemistry of Materials* **2004**, 16, (23), 4477-4496.

Chapter II

Characterization of Aryl Films Derived from Diazonium Salts on Carbon Electrodes Using Conductive Atomic Force Microscopy

2.1 Introduction

The shrinking size of electronic devices is motivated by the promise of enhanced performance (e.g. storage density and speed). Molecular electronics is an approach to device fabrication that involves the incorporation of molecules into electronic devices. One of the first documented reports, suggesting integration of molecular components into electronic devices was published by Herwald and Angello in 1960.¹ An excerpt from this contains, “The trend in electronics circuit construction is toward microminiaturization and molecular electronics”. Furthering this idea, Moore developed a law which predicts the number of electric components in a microprocessor to double every year.² Based upon this trend, and the ever-increasing drive for increased number electronic components, the need for miniaturization is quite apparent. One can envision decreasing the size of an electronic device to its smallest possible limit. The overall electronic properties of such a device would be governed by a single molecule. This would enable the electronic tailoring of a device by conventional organic synthesis. This integration of molecular components, with a wide variety of possible structures and properties, into existing silicon-based microelectronics may lead to new and/or improved functionality.

The functionality of molecular devices is based upon the movement of charge through the molecular component. To form a molecular junction a molecule or molecular layer is first immobilized onto a bottom electrode. This immobilization process may occur in a variety of ways. Initially, electrodes were modified by the physical adsorption of molecules or polymers.^{3,4} Control of molecular orientation in such films is quite difficult and Langmuir-Blodgett films were later used to provide a higher degree of control.⁵ Silanization and aldehyde reactions have also shown to be quite successful in the covalent attachment of molecular structures to the lower electrode, giving rise to great insights into charge transport through molecules.⁶⁻⁸ However, the vast majority of lower electrode modification involves the thiol-gold linkage.⁹⁻¹² The reason for this extensive usage is that thiols are known to form highly dense, well-ordered monolayers on the gold surface.^{13,14} By this approach, the molecular orientation, layer thickness, interaction with the lower electrode and packing geometry are well controlled. From a molecular electronics view point, this degree of molecular control has many benefits, in a field plagued by a high degree of uncertainty.¹⁵ However, the shortcoming in this modification process is that thiols are limited for attachment to metals and the linkage is non-covalent in nature. Thereby lateral movement and displacement of thiol molecules may occur. Also the non-covalent thiol-gold bond does not have a high degree of electronic coupling, thus creating an energy barrier that must be overcome before electron transport may occur.

Another molecular adsorption mechanism being explored to circumvent these issues posed by the thiol-gold bond is the covalent attachment of aryl groups by the reduction of diazonium salts. Pioneered by Pinson and coworkers in 1992, it was found that the electrochemical reduction of nitrobenzene diazonium salt forms an aryl layer on a carbon working electrode.¹⁶ The mechanism they proposed is shown in Figure 2.1.

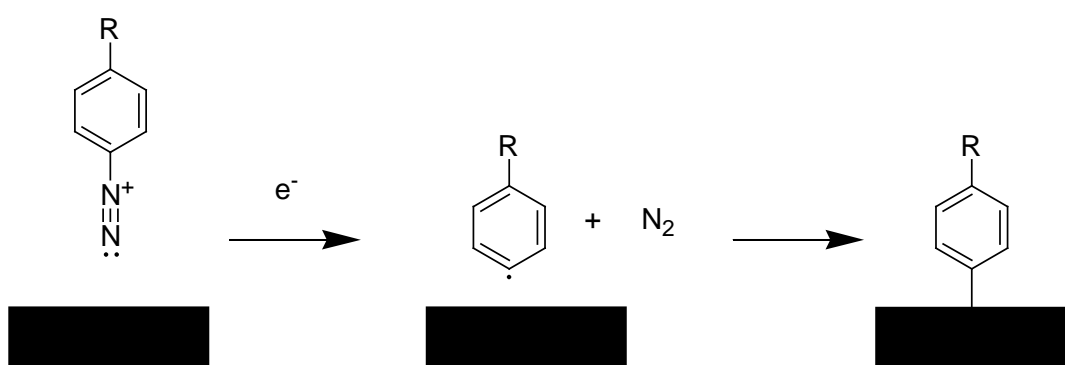


Figure 2.1 Schematic depicting the proposed mechanism of aryl-group attachment onto a carbon electrode. Adapted from reference ¹⁶

The electrochemical reduction of the diazonium cation forms an aryl radical. The highly reactive radical combines with an electron from the carbon surface, thereby forming an aryl film. Since this initial discovery researchers have used this process to modify a wide variety of substrates, such as Si, Pd, Fe, GaAs, as well as coinage and noble metals.¹⁷⁻¹⁹ It is this flexibility of covalently modifying a diverse range of electrodes that gives this process a unique advantage. It was later found that due to the aggressive nature of radical attachment multilayers can form. Aryl-radicals in solution may attach to the pre-

existing layer, creating a branched layer structure.²⁰ More on this topic will be discussed in chapter 4. The present work in chapters 2 and 3 uses this original modification scheme in Figure 2.1 to prepare molecular films on conducting carbon.

When preparing a charge transport device a contact must be fabricated on the top of the molecule or molecular film. The first experiments to measure electronic properties through monolayers involved mercury drop electrodes as top contacts.^{21,22} Mercury drops have been used extensively to study charge transport through molecular junctions for their high degree of reproducibly forming similar contact areas and ease of generating a clean electrode surface.²²⁻²⁹ Junction contact areas using mercury droplets as top contact electrodes are usually on the order of a few square millimeters.²² Another commonly used means of forming top contact electrodes is metal deposition of the top contact directly onto the immobilized molecules.³⁰⁻³² This method is very useful, as it directly incorporates microelectronic technology into the fabrication process, making the transition from silicon-based electronics to organic based easier. These junctions commonly have a range of contact areas from centimeters to micrometer contact areas.³²

McCreery and coworkers have utilized the photolithographic patterning process in the study of charge transport through covalently grafted aryl films to carbon substrates.^{15,33-35} Photolithographic patterning allowed the study of top contact formation effects on charge transport. They found that the charge transport through a nitroazobenzene layer grafted to a carbon film is influenced by the electronic properties of the top electrode.^{33,35}

With the decreasing size of electrical components researchers have been devising means to fabricate devices that involve extremely small ensembles of molecules. This can be achieved in a variety of different ways. Fabricated nanogaps, in which nanofabricated electrodes are used to bridge low numbers of molecules.³⁶⁻³⁹ A variety of nanoelectrode materials have been used, including, doped silicon, metals, or carbon nanotubes. However, a great amount of time and expertise is needed to generate such devices.

Scanning probe techniques inherently have a small contact area between the probe and surface. This has led to scanning probe techniques investigating charge transport through small ensembles of molecules.^{9,11,12,40-50} Most notable are investigations using the scanning tunneling microscope (STM)^{12,40-44}. In these types of experiments the STM tip is used as the top contact in the molecular junction and the electronic properties of the immobilized molecules are probed. Due to the very nature of electron tunneling involved in the STM, single molecule charge transport experiments can be conducted. Similarly, conducting atomic force microscopy (c-AFM) can be used to probe the charge transport properties of extremely small ensembles of molecules^{9,11,45-50}. Due to probe size, c-AFM usually involves a larger ensemble of molecules than the STM. However with immobilization of low densities of conduction molecules, charge transport through single molecule can be conducted using the c-AFM. One advantage c-AFM has over STM experiments is that the force applied can be controlled.⁴⁸ This feature allows for investigations of intermolecular interactions, top contact

formation, film compressibility, and film deformation influences on charge transport.

In this work, we apply c-AFM to investigate the effects of applied load on electron transport through diazonium salt derived aryl films on flat carbon. Similar systems have been studied by McCreery and coworkers using metal deposition during formation of the top contact.^{33-35,51} The molecular layers chosen were biphenyl and nitroazobenzene molecular layers grafted to proylzed photoresist films (PPF). The present study is the first time c-AFM has been used to study charge transport through a diazonium salt derived molecular junction. This work sheds light onto the true nano-scale landscape of charge transport in these layers and provides the experimental framework to compare the c-AFM results with experiments involving larger ensembles of molecules.

2.2 Experimental

Preparation of diazonium salts

Biphenyl and nitroazobenzene diazonium salts were synthesized according to the Starkey method⁵². In short, the amine precursors [Sigma Aldrich] were reacted with sodium nitrite, added drop wise, in the presence of tetrafluoroboric acid [48% Sigma Aldrich]. 10mL of acetonitrile [Sigma Aldrich] was used to aid solubility of amine precursors. During the entire reaction all solutions were consistently below 2°C to avoid diazonium degradation. The resulting diazonium salts were isolated by recrystallization by addition of ether, then dried in a

rotoevaporator immersed in ice/water at 0°C. The isolated diazonium salts were stored below 0°C, in the dark and over desiccant.

Preparation of Pyrolysed Photoresist Films (PPF)

Silicon wafers were diced into 1.5cm x 1.5cm squares, cleaned with soap, tap water, distilled water, followed by immersion in freshly prepared piranha solution. Piranha was prepared by mixing 1 part 30% hydrogen peroxide (EMD, ACS certified) with 3 parts concentrated sulfuric acid (EMD, ACS certified). *Extreme care should be taken during piranha use due to its violent reactions with organic molecules.* Following piranha cleaning the Si wafers were rinsed with copious amounts of 0.2µm filtered 18MΩ·cm water (Barnstead-Thermolyne, Nanopure water filtration unit) followed by drying via an argon stream within a Terra Universal Whisper Flow Benchtop clean hood. Once dried the PPF layer was prepared in a similar manner as previously reported⁵³ In short, one layer of AZ4330 photoresist was spin coated initially at a rate of 500rpm for 20sec followed by 2000rpm for 20 sec and finally 3000rpm for 40sec. The coated samples were immediately placed in an oven at 110°C for solvent drying for 20 minutes. Following the solvent drying step the coated samples were placed in a tube furnace and the environmental atmosphere was purged with forming gas [N₂ with 5%H₂] for 20 minutes. The samples were then heated, under constant flow of forming gas, to 1000°C and held for 1 hour. The samples were then cooled to room temperature to enable handling. Upon removal from the tube furnace the

PPF samples were immediately placed in a vacuum, over desiccant and stored until use.

Surface Modification

Surface derivatization of PPF occurred by initially cleaning the substrates vigorously using 3 successive sonications in isopropanol (Sigma Aldrich) which has been filtered through activated carbon. The PPF substrates were then rinsed with copious amounts of 0.2 μ m filtered 18M Ω ·cm water followed by drying with a gentle stream of argon. Derivatization of the PPF substrates with aryl films occurred by electrochemical reduction of the diazonium salts (1mM in acetonitrile) within a three-probe electrochemical cell in the presence of tetrabutylammonium tetrafluoroborate electrolyte (Sigma Aldrich). The cell consisted of a Ag/AgNO₃ reference electrode and a platinum mesh as a counter electrode. Using a Pine biopotentiostat, the voltage was ramped at a rate of 200mV/s while monitoring the resulting current. The modified samples were removed and rinsed with copious amounts of acetonitrile, 0.2 μ m filtered 18M Ω ·cm water, followed by drying with a stream of Argon.

X-ray Photoelectron Spectroscopy

X-ray photoelectron spectroscopy was performed using an Axis 165 X-ray Photoelectron Spectrometer (Kratos Analytical). All spectra were collected at room temperature and the pressure was always below 10⁻⁹ torr. Survey spectra were collected between 100 and 1000 eV with a resolution of 2 eV. High-

resolution spectra were collected for the carbon and nitrogen regions of the spectra at a resolution of 0.1 eV.

Atomic Force Microscopy

Current/voltage (I/V) curves were acquired in hexadecane (Sigma Aldrich) using an Asylum MFP-3D atomic force microscope equipped with an Orca conductive probe module. All conductive probes were Platinum coated and purchased from Nanosensors. To ensure constant applied force during IV curves the AFM was operated in deflection feedback and curves were collected at a rate of 1Hz. The applied force applied during I/V curves was adjusted using the setpoint voltage. Force curves were acquired under a potential bias between the conductive probe and the sample. This enabled monitoring the current response during molecular layer compression and relaxation. Force curves were acquired at a rate of 1Hz with a ramp size of 500 nm.

AFM scratching experiments were conducted by initially imaging a 1 μm x 1 μm square of the molecular layer film in contact mode AFM under an applied load of 600 nN. Feedback was switched to amplitude and a tapping mode image was collected for a 5 μm x 5 μm square including where the initial scratching occurred. Cantilever force constants were determined using the thermal calibration method⁵⁴ available within the Asylum AFM software.

Tips were characterized by employing blind reconstruction algorithms to reconstruct a three-dimensional model of the AFM tip's apex^{55,56}. In short, four topographic images were collected at various locations and scan angles of an

evaporated niobium substrate. Due to the relatively high degree of sharp features of the evaporated Nb crystallites, the substrate is in fact imaging the c-AFM tip. The evaporated niobium substrate was kindly donated by Aurora Nanodevices Inc. The topographic images were recorded at a scan rate of 0.5Hz, and scan size of 500 nm. To ensure adequate resolution of the reconstructed tip model, a resolution of 512x512 was used. Scanning Probe Imaging Processor (SPIP) was used to generate a 3D model of the c-AFM tip's geometry. Upon constructing a three-dimensional model of the tip's apex, the first 1nm of the tip's apex was fit to a parabola to determine the radius of curvature. This process occurred for the four topographic images to determine an average and standard deviation of the tip's radius of curvature.

2.3 Results and Discussion

The present work outlines the challenges when investigating charge transport through molecular layers and proposes characterization methods to minimize uncertainty when interpreting the data. By utilizing the c-AFM to investigate charge transport, molecular layer mechanical properties of biphenyl and nitroazobenzene films grafted to pyrolysed photoresist are simultaneously investigated.

Electrochemical Surface Modification

Surface modification of the clean PPF substrates occurred by linearly sweeping the voltage, within an electrochemical cell containing aryl-diazonium

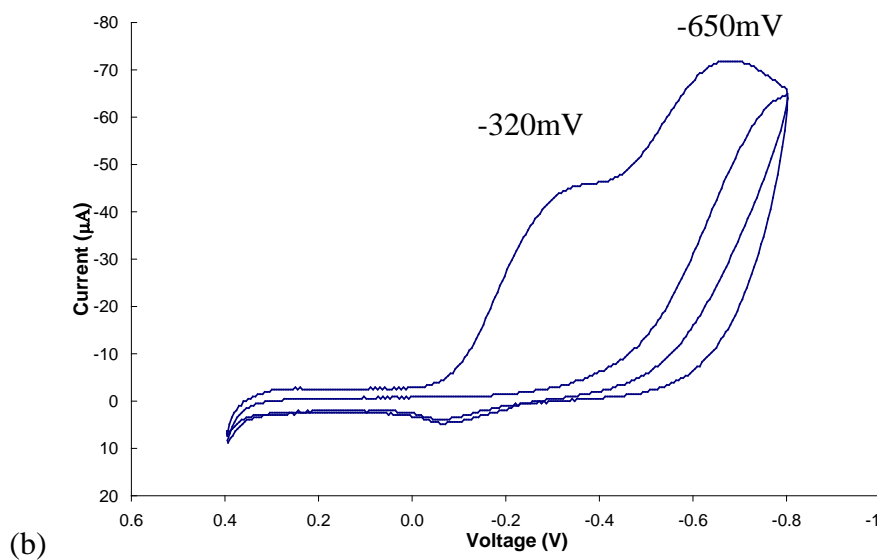
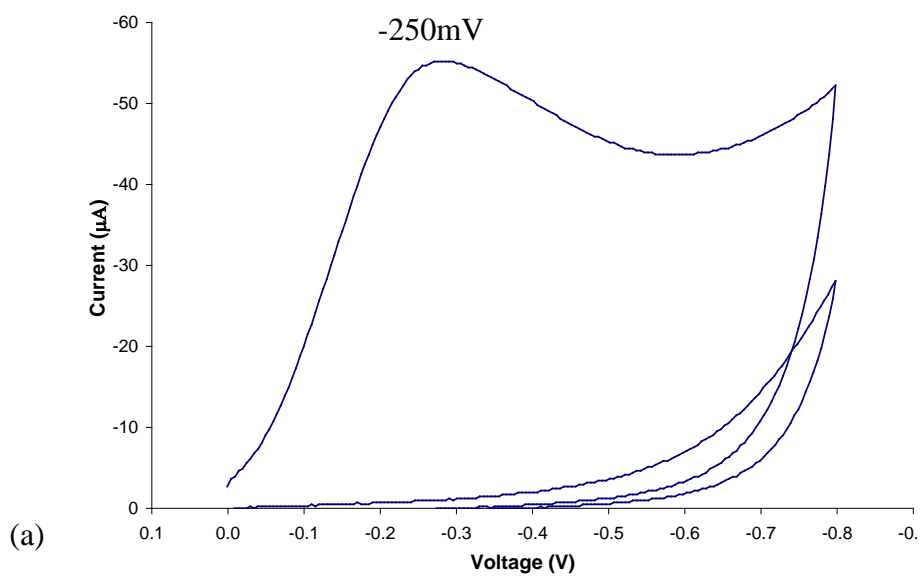


Figure 2.2 Cyclic voltammograms collected during the deposition of nitroazobenzene (1a) and biphenyl (1b) from their corresponding diazonium salts to PPF.

salts, while monitoring the resulting current. Figure 2.2 contains the cyclic voltammograms obtained from the reduction of (a) nitroazobenzene and (b) biphenyl diazonium salts. The reduction peak apparent on the initial scan, and the disappearance of this peak on subsequent scans indicates the reduction of the diazonium cations and molecular layer formation. The potential for peak current is -250mV for NAB, and BP contains two reduction peaks at -320mV and -650mV . The presence of two reductive peaks has been observed by other researchers on similar systems and has been attributed to a variety of sources.⁵⁷⁻⁶⁰

X-ray photoelectron spectroscopy (XPS) was used to characterize the resulting aryl films. Figure 2.3 contains the high-resolution XPS spectra, of the nitrogen 1s region for the NAB and BP modified ppf substrates. Two prominent N peaks are observed for the nitroazobenzene-modified PPF at 400eV and 406eV . Elsewhere these peaks have been attributed to the azo and nitro functionalities within the NAB structure respectively.^{33,61} It is interesting to note a small peak is also observed from the BP modified PPF substrate, although it should contain no nitrogen. It has been proposed that this observation is due to azo-coupling of the diazonium to either the substrate or within the multilayer.⁶¹⁻⁶⁴

Figure 2.4 contains the carbon 2s region of the NAB, BP and bare ppf substrates. A prominent peak at 284.5 eV is apparent for all the substrates and attributed to the underlying carbon of the ppf substrate. Note that the NAB peak is suppressed and broadened. This is indicative of a rather thick NAB molecular

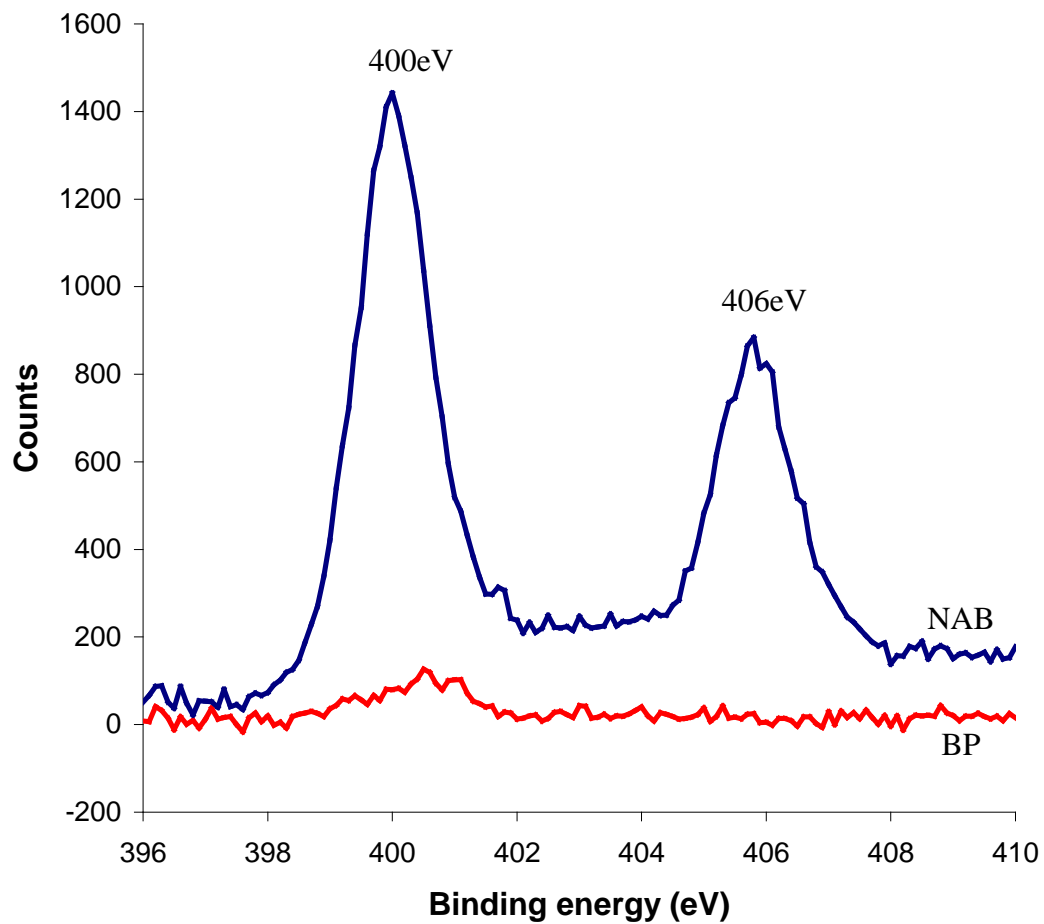


Figure 2.3 High-resolution XPS spectra, of the nitrogen 1s region, for the NAB and BP modified PPF substrates

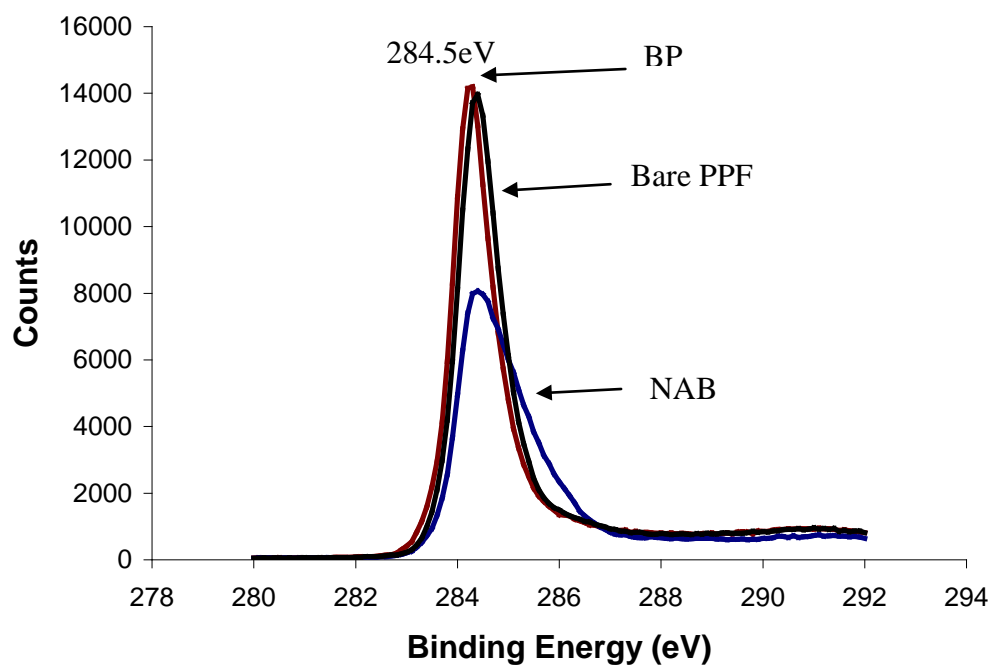


Figure 2.4 High resolution XPS spectra of the carbon 2s region of the NAB, BP and bare PPF substrates

layer that significantly suppresses the XPS signal from the underlying substrate. The peak broadening is accredited to the increased number carbon environments within the NAB layer, associated with the carbons near the azo and nitro groups. The carbon XPS signal of the BP layer is similar to that of bare PPF, hence it is difficult to distinguish the BP layer from the substrate.

The molecular layer thicknesses were assessed using AFM scratching. In this experiment a large normal force is applied to the substrate during contact mode imaging. This provides a lateral force great enough to scratch away the molecular layer. Care should be taken to increase the normal force large enough to remove the entire molecular layer without damaging or removing the underlying PPF substrate. The AFM mode of operation is then changed to tapping mode and the image size increased.

Figure 2.5 contains topographic images of AFM scratching for (A), biphenyl, (B) nitroazobenzene and (C) unmodified PPF. The image of the unmodified PPF shows no evidence of scratching verifying the applied force is below the threshold of causing damage to the underling PPF substrate. The image also reveals a roughness of ≈ 0.3 nm rms for PPF, which is comparable with previous reports.^{34,53} The molecular layer thickness for the biphenyl and nitroazobenzene modified PPF were measured from the images by calculating the z-axis step height difference between two 250 nm^2 areas within and outside the scratched area, as indicated by the squares in the topographic images of Figure 2.5. This method provides an average height difference between the two areas.

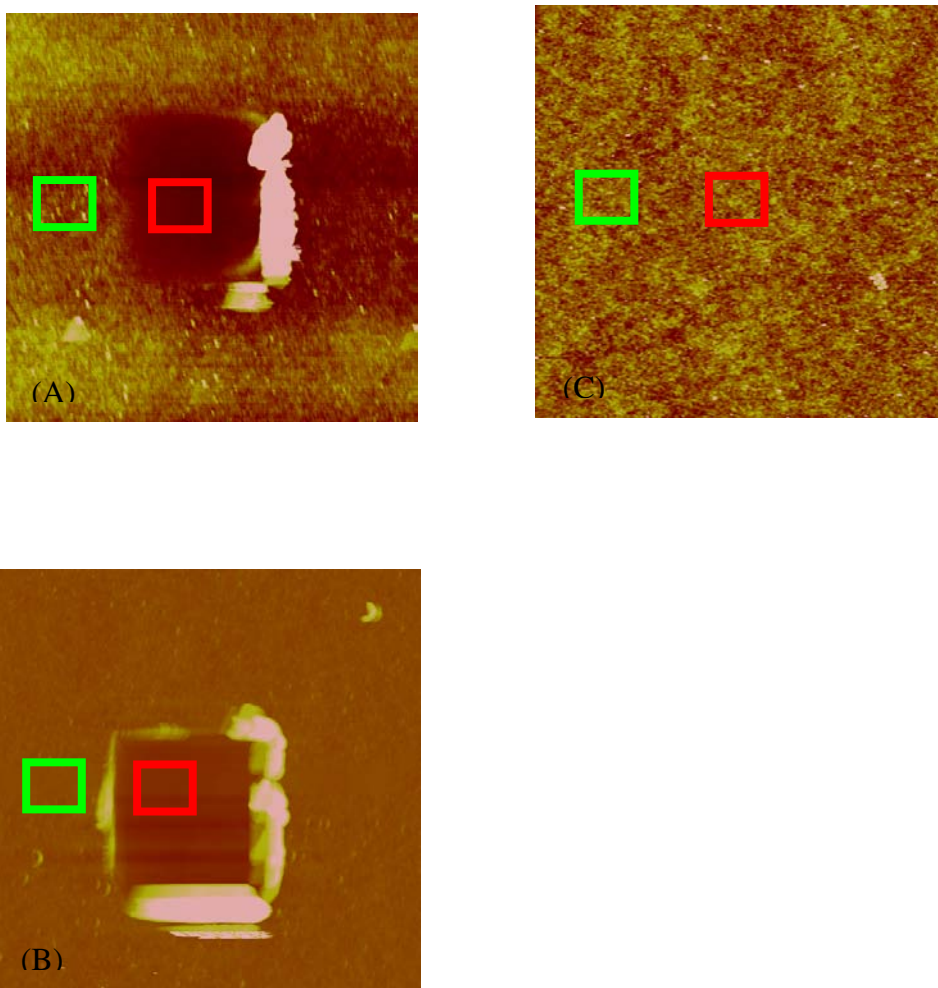


Figure 2.6 Topographic AFM images after scratching experiments (A) biphenyl modified PPF (B), nitroazobenzene modified PPF and (C) unmodified PPF. The height difference between the corresponding 250nm^2 areas were used to determine the molecular layer's thickness.

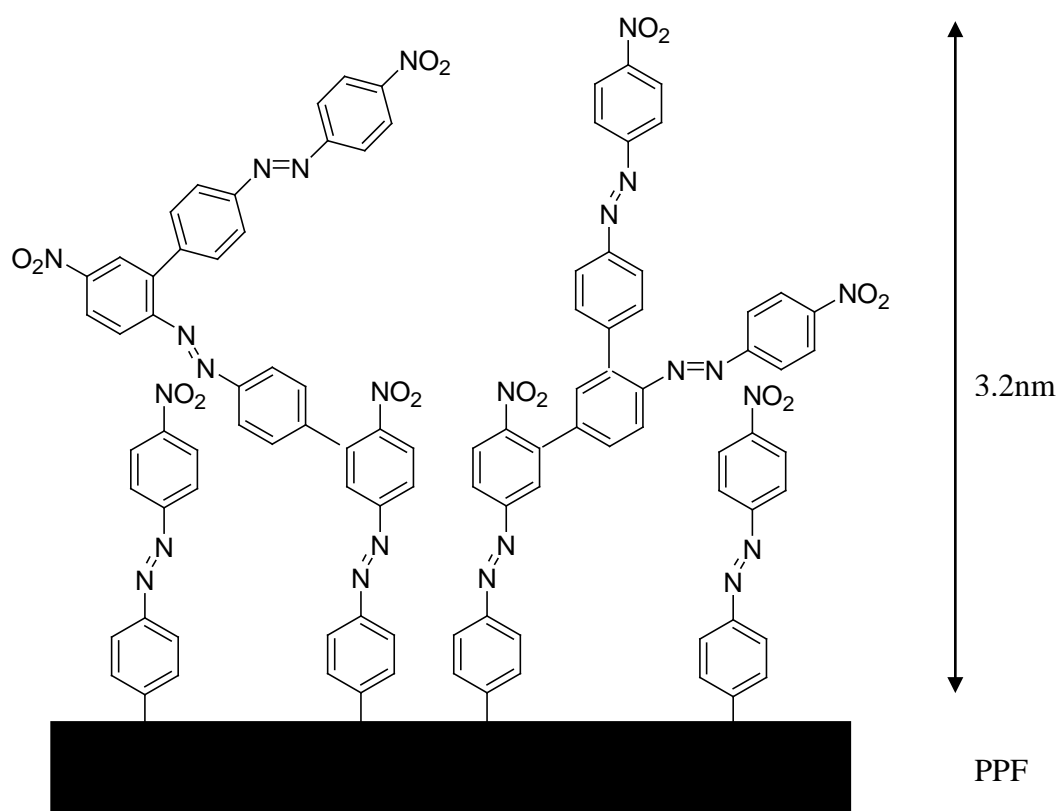


Figure 2.6 Illustrated representation of the resulting multilayer formation of a nitroazobenzene modified PPF.

The molecular layer thicknesses were determined to be 0.8 nm and 3.2 nm for the biphenyl and nitroazobenzene modified surfaces respectively. These values indicate that BP layer is close to that expected for a BP monolayer and nitroazobenzene modification is three times as thick as expected.³⁴ Observations of this difference in thickness is believed to be attributed to multilayer formation of the nitroazobenzene layer.^{20,34} These thickness values suggest that under these conditions, reduction of nitroazobenzene diazonium salt is much more likely to form multilayers than during the reduction of biphenyl diazonium salt on PPF. Figure 2.6 is an illustration representation of the resulting multilayer formation of a nitroazobenzene modified PPF.

Charge Transport Investigations

Conductive atomic force microscopy (c-AFM) was used to investigate charge transport through BP and NAB molecular layers. Current/voltage (I/V) curves were collected on the modified substrates by sweeping the voltage bias between the conductive tip and substrate while monitoring the current. Figure 2.7 contains IV curves for NAB and BP collected with an applied force of 100 nN within a hexadecane environment. The bias voltages are tip versus sample. Some important features in the IV curves are apparent and require further discussion. The IV curves appear in Figure 2.7 appear to be non-Ohmic. This suggests that indeed modification of PPF with a molecular layer drastically changes the charge transport between the tip and surface.

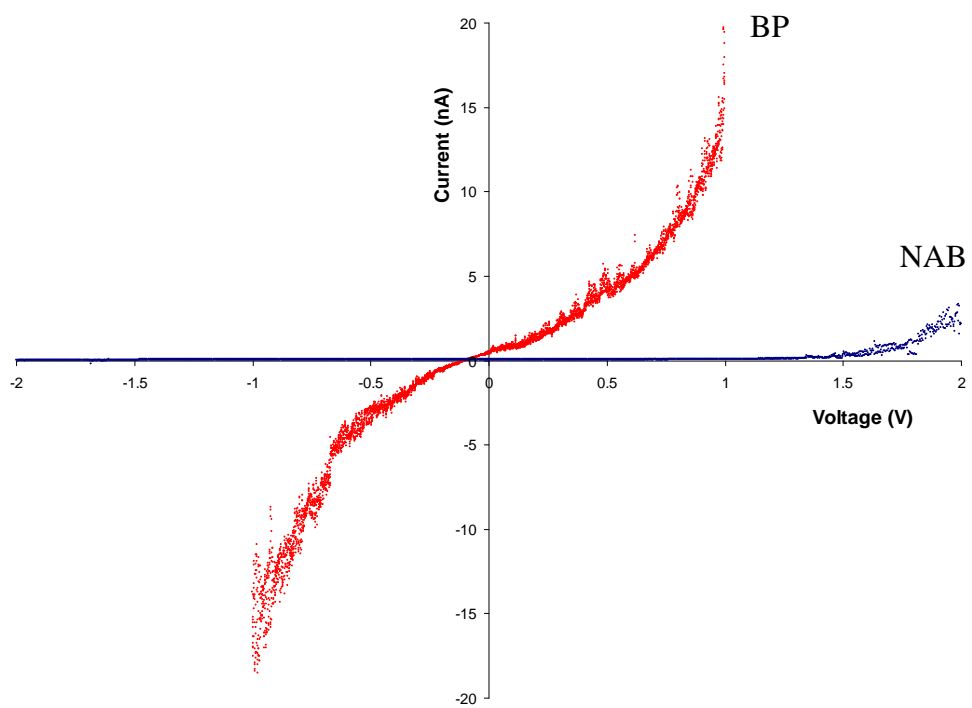


Figure 2.7 IV curves for NAB and BP collected with an applied force of 100nN within a hexadecane environment.

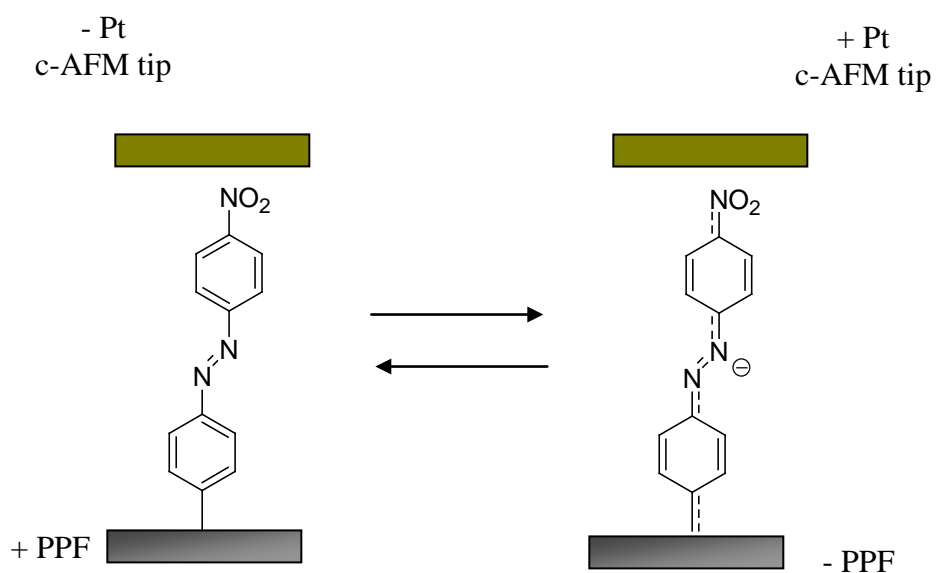


Figure 2.8 Schematic representation of NAB forming a quinoid structure at positive tip biases.

It is also interesting to note the differences between the IV curves collected on the BP and NAB molecular layers. The current through the BP layer measured higher than that collected on the NAB layer. The lower current may be attributed to the thicker molecular layer of NAB.

However thickness alone cannot account for the shape of the IV curves. The BP modified ppf displays a symmetric IV curve, while the NAB modified PPF shows rectification. The rectification of the NAB IV curve was calculated to be factor of 5 at +2V to -2V. Experiments on larger junctions have also demonstrated rectifying IV characteristics in similar junctions^{33,65}. Researchers have suggested this phenomenon may be attributed to quinoid formation within the NAB layer at positive tip biases, thereby changing the ability of the electron to move between the molecular layer and the conducting probe.^{33,65,66} Figure 2.8 contains a representation of NAB forming a quinoid structure at positive tip biases.

Effects of applied load on charge transport investigations

Further investigations of the charge transport through these molecular layers were conducted by collecting IV curves at various applied forces. Figure 2.9 contains IV curves of BP (a) and NAB (b) molecular layers grafted to PPF collected at increasing applied loads. Note that the IV curves, collected at different forces, do not overlap and the current increases with applied load. This

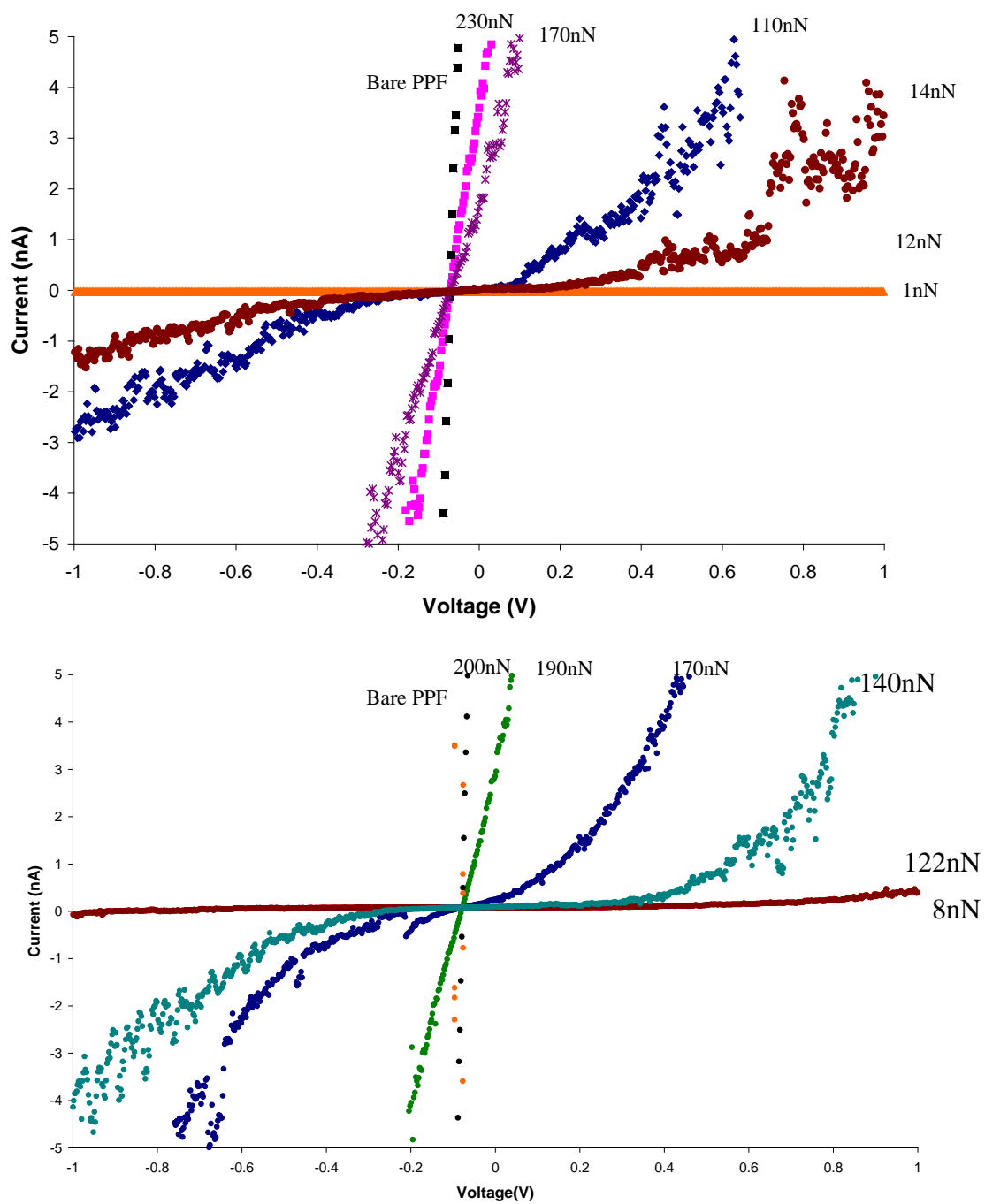


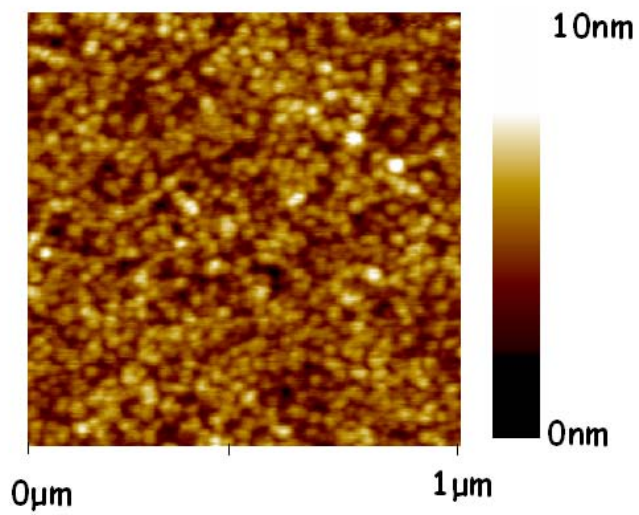
Figure 2.9 C-AFM IV curves of BP (a) and NAB (b) molecular layers grafted to PPF collected at increasing applied loads.

observation may be attributed to a variety of sources; 1) increased contact area between the conducting probe and molecular layer, 2) decreased distance between the PPF substrate and conducting probe, and 3) changes in the intramolecular interactions and/or arrangement within the molecular film. The contribution of each of the source, to the observations noted for the increased current upon greater applied loads, will be discussed further

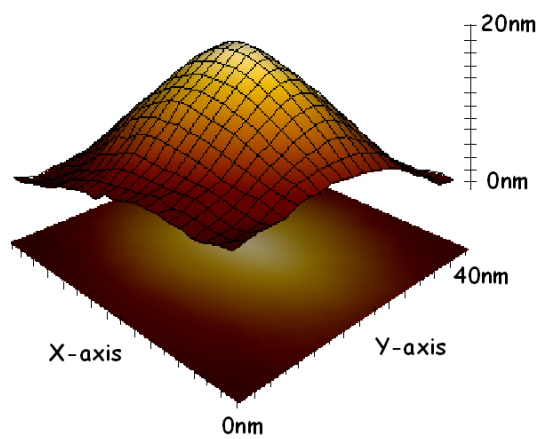
Contact Area Consideration

The determination of contact area in c-AFM experiments requires knowledge of the tip shape and some estimation of contact mechanics. Fortunately, these problems are intrinsic to AFM operation itself and methods have been developed to determine tip geometry. These methods include deconvolution of the tip's geometry from images of known shapes,⁶⁷ direct imaging using high resolution scanning electron microscopy⁶⁸ and blind reconstruction methods from images of unknown geometries.^{55,56} In the blind reconstruction methods a 3-D model of the tip's shape is created from the topographic data of the sharpest features within an image. An in-depth discussion for all of these techniques can be found in Chapter 6.

Based upon the findings in Chapter 6, blind reconstruction was chosen as the tip characterization method. This method yields lower uncertainties and minimal tip damage, as compared to the other methods. A typical topographic image of an evaporated Nb film and the 3-D reconstructed tip geometry is given

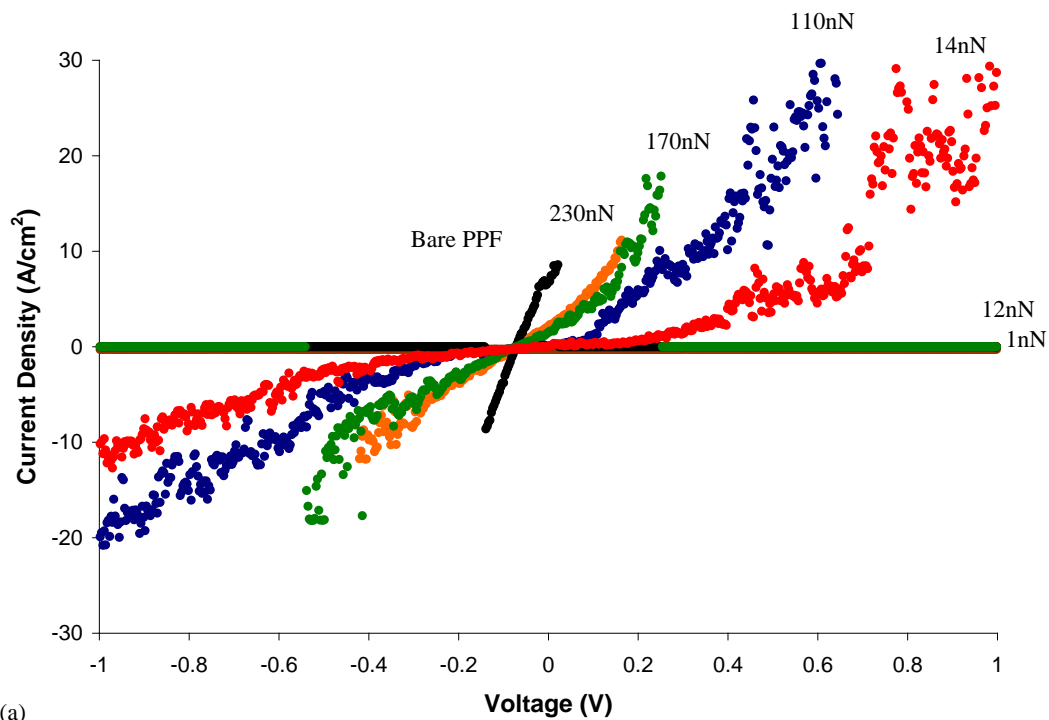


(a)

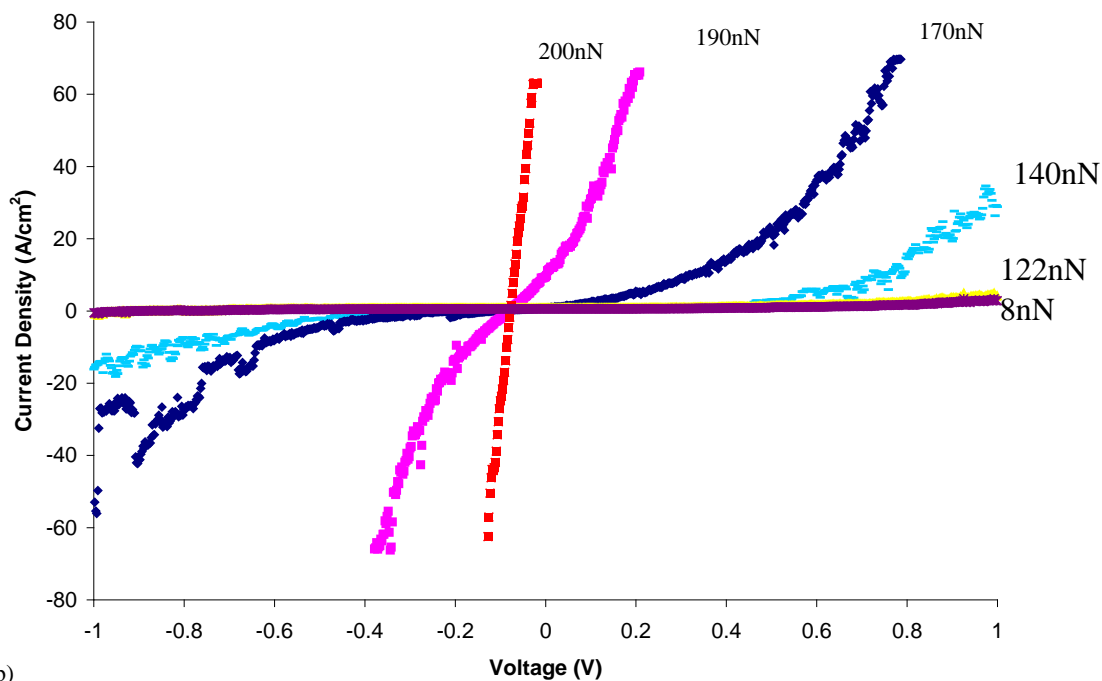


(b)

Figure 2.10 Topographic image of evaporated Nb (a) used to calculated a 3D model of the c-AFM tip (b)



(a)



(b)

Figure 2.11 Calculated JV curves for measuring charge transport through (a) PPF/BP/Pt and (b) PPF/NAB/Pt molecular junctions at various applied loads.

in Figure 2.10. By fitting the first 1 nm from the apex of the tip to a parabola, a tip radius of $35 \text{ nm} \pm 3 \text{ nm}$ was determined. Using the calculated tip radius, the calibrated spring constant, and applied load, the Johnson-Kendall-Robert's (JKR) theory⁶⁹ was used to determine the contact area between the c-AFM tip and the molecular layers. The contact area for each of the applied forces was used to determine current densities (J). The resultant JV curves are presented in Figure 2.11. It is noted that each force yields a distinct JV curve with little overlap between curves. This suggests that contact area changes alone cannot describe the increasing current trend we observe in Figure 2.9 otherwise all of the JV curves would overlap.

Distance Dependence consideration

Higher applied tip-sample forces can result in molecular layer compression and a decreased distance between the PPF substrate and the conducting probe. If electron tunneling is the sole source of charge transport observed in the IV curves, the current, I, would be dependent upon distance, d, by equation 2.2,^{15,34}

$$I = I_0 e^{-\beta d} \quad (2.2)$$

where β is defined as the tunneling factor constant. β is dependent upon the material the electron is tunneling through and is determined experimentally by varying the thickness of the molecular layer and measuring the current at a constant voltage. McCreery and coworkers have measured β for PPF/NAB/Cu junctions by systematically varying the thickness of the NAB layer and measuring

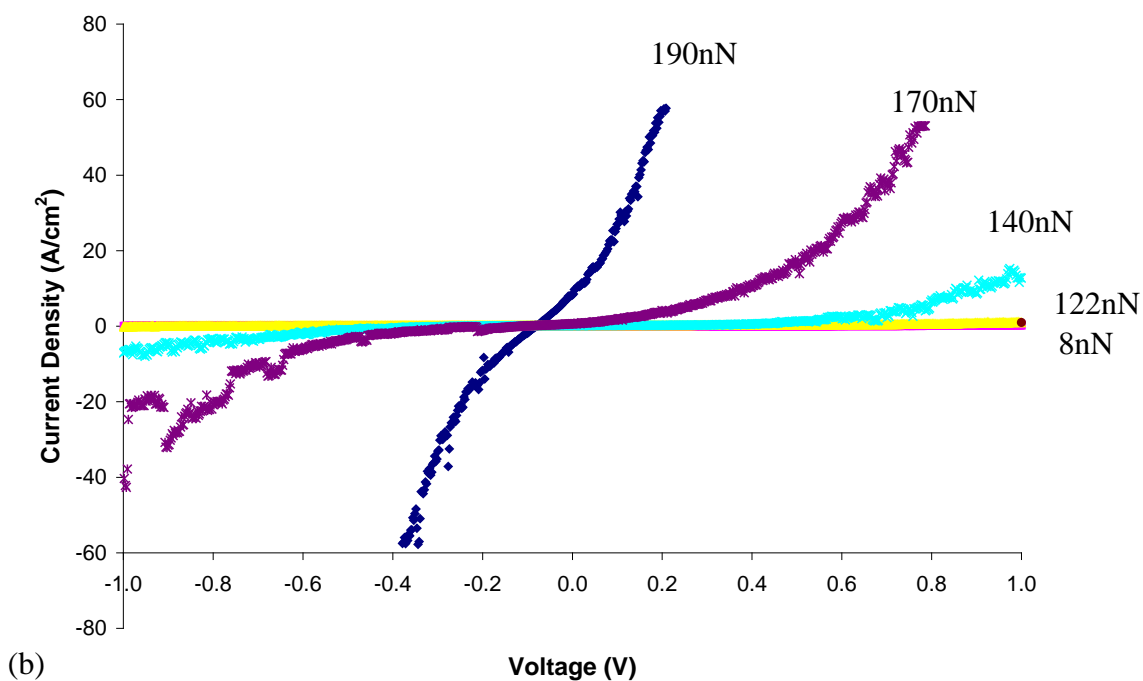
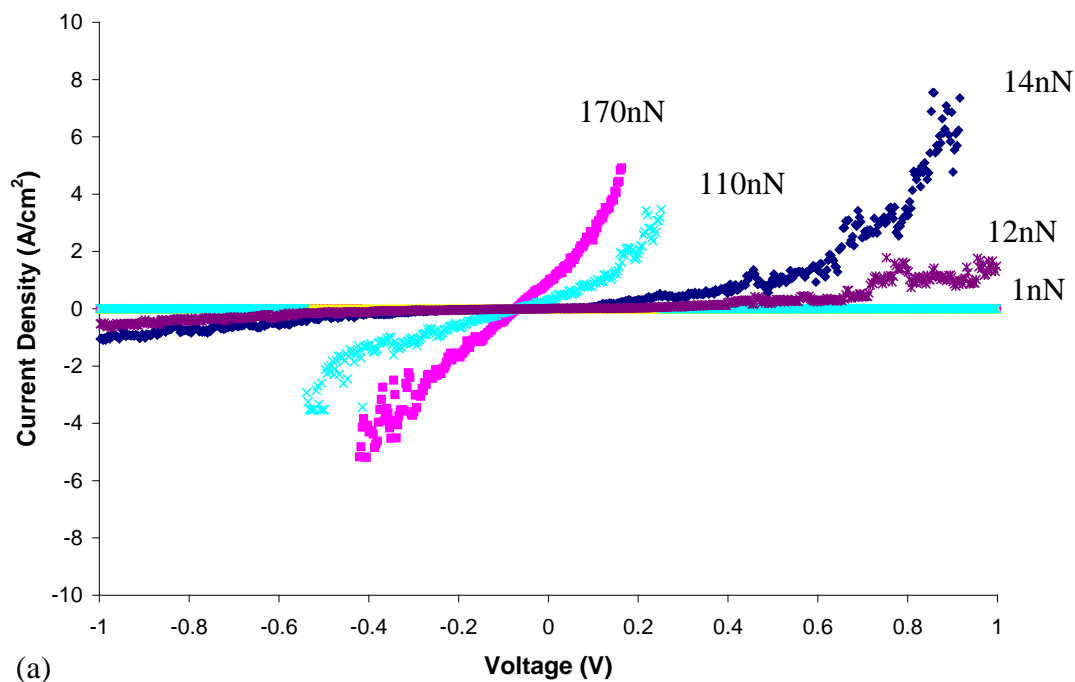


Figure 2.12 Calculated JV curves for (a) BP and (b) NAB compensated for distance dependence during molecular layer compression.

the current at +0.5V for the various thicknesses. β was determined to be 0.21 A^{-1} .^{15,34} This β can be used as an estimation to correct for changes in the tip-sample distance while under applied loads. This correction is performed by assuming the force at which an Ohmic response occurs when the conducting probe is in direct contact with the underlining PPF substrate. This direct contact is set as $d = 0 \text{ nm}$. It is further assumed that the molecular layer is less stiff than the stiffness of the cantilever, therefore separation between the PPF and probe is reliant on the cantilever's sensitivity. Equation 2.2 was then used to correct for the distance dependence associated with the observed current. Figure 2.12 shows the resulting JV curves as a function of applied force. The JV curves at different forces again do not overlap, suggesting other factors must be contributing to the observed JV characteristics.

Molecular Layer Rearrangement Consideration

The final factor that will be discussed as a possible contribution to the increased current as a function of force is the effects of molecular layer rearrangement under increasingly greater loads. It is well known that molecular layers may rearrange under applied loads.⁴⁸ Under increasing applied loads a tip induced defect site may form. This deformation allows for the top contact of the c-AFM tip to be closer to the PPF electrode, thereby increasing electron tunneling in relation to equation 2.2 and discussed in the previous section. This deformation of a molecular film and its effects on charge transport have been previously reported for alkyl thiol monolayers.⁴⁸ However, the applied load induced

transition from rectifying to non-rectifying charge transport has not been previously observed. Under low applied loads electron tunneling appears to occur through the barriers associated with the molecular structures of the film and the metal contacts. The JV curves display slight rectifying characteristics, having a rectifying ratio at +1V and -1V ranging between 2 and 5.

The observations of a change in tunneling mechanism, allows for the conclusion that the interface between the probe and molecule is extremely important for interpretation of charge transport experiments. In the region of lower applied loads, the electronic properties appear to be dependent upon molecular structure within the molecular layer. Applying greater loads may thereby change the molecular structure of the layer. The molecule will compress, molecular bonds will rotate and bonds become strained. These structural changes will led to changes the tunneling energy barriers associated with the molecular layer. All of these effects manifest as changes in JV curves that cannot be directed related to junction size or tip-sample distance considerations.

2.4 Conclusions

Conducting atomic force microscopy provides a unique platform for probing charge transport through molecular layers. It was found that chemical structure and net film formation influence charge transport properties through molecular layers derived from diazonium salts. To aid in comparison studies the current densities must be accurately calculated, thereby requiring an accurate measurement of contact area between the conducting probe and surface. It was

found that applied force between the conducting probe and molecular layer drastically influences electron transport, which cannot be fully understood by changes in contact area. These results outline the methodology to allow for comparison between c-AFM investigations and macro-sized contact area studies. These results also suggest that to achieve the true molecular tailoring sought after by the molecular electronics field one must consider film alteration during top contact formation and this adds yet another variable that must be controlled to achieve meaningful results.

References

- (1) Herwald, S. W.; Angello, S. J. *Science* **1960**, *132*, 1127-1133.
- (2) Moore, G. E. *Proceedings of the Ieee* **1998**, *86*, 82-85.
- (3) Hoshino, S. *International Chemical Engineering* **1970**, *10*, 678-&.
- (4) Chudleigh, P. W. *Journal of Applied Physics* **1976**, *47*, 4475-4483.
- (5) Shikin, S. A.; Berzina, T. S.; Sotnikov, P. S.; Troitsky, V. I.; Neilands, O. Y.; Pukitis, G. G.; Khodorkovsky, V. Y. *Biologicheskije Membrany* **1990**, *7*, 1111-1117.
- (6) Lopinski, G. *International Journal of Nanotechnology* **2008**, *5*, 1247-1267.
- (7) Kirczenow, G.; Piva, P. G.; Wolkow, R. A. *Physical Review B* **2005**, *72*.
- (8) Dogel, I. A.; Dogel, S. A.; Pitters, J. L.; DiLabio, G. A.; Wolkow, R. A. *Chemical Physics Letters* **2007**, *448*, 237-242.
- (9) Beebe, J. M.; Kim, B.; Gadzuk, J. W.; Frisbie, C. D.; Kushmerick, J. G. *Physical Review Letters* **2006**, *97*.
- (10) Chen, F.; Li, X. L.; Hihath, J.; Huang, Z. F.; Tao, N. J. *Journal of the American Chemical Society* **2006**, *128*, 15874-15881.
- (11) Engelkes, V. B.; Beebe, J. M.; Frisbie, C. D. *Journal of the American Chemical Society* **2004**, *126*, 14287-14296.
- (12) He, J.; Sankey, O.; Lee, M.; Tao, N. J.; Li, X. L.; Lindsay, S. *Faraday Discussions* **2006**, *131*, 145-154.

- (13) Walczak, M. M.; Popenoe, D. D.; Deinhammer, R. S.; Lamp, B. D.; Chung, C. K.; Porter, M. D. *Langmuir* **1991**, *7*, 2687-2693.
- (14) Zhong, C. J.; Brush, R. C.; Anderegg, J.; Porter, M. D. *Langmuir* **1999**, *15*, 518-525.
- (15) Akkerman, H. B.; de Boer, B. *Journal of Physics-Condensed Matter* **2008**, *20*.
- (16) Delamar, M.; Hitmi, R.; Pinson, J.; Saveant, J. M. *Journal of the American Chemical Society* **1992**, *114*, 5883-5884.
- (17) Stewart, M. P.; Tour, J. M.; Kosynkin, D. V.; Allara, D. L.; Dirk, S. M.; Maya, F. M. *Abstracts of Papers of the American Chemical Society* **2003**, 225, 2-INOR.
- (18) Chen, B.; Lu, M.; Flatt, A. K.; Maya, F.; Tour, J. M. *Chemistry of Materials* **2008**, *20*, 61-64.
- (19) Bernard, M. C.; Chausse, A.; Cabet-Deliry, E.; Chehimi, M. M.; Pinson, J.; Podvorica, F.; Vautrin-UI, C. *Chemistry of Materials* **2003**, *15*, 3450-3462.
- (20) Kariuki, J. K.; McDermott, M. T. *Langmuir* **2001**, *17*, 5947-5951.
- (21) Mann, B.; Kuhn, H. *Journal of Applied Physics* **1971**, *42*, 4398-&.
- (22) Ranganathan, S.; Steidel, I.; Anariba, F.; McCreery, R. L. *Nano Letters* **2001**, *1*, 491-494.
- (23) Holmlin, R. E.; Haag, R.; Chabinye, M. L.; Ismagilov, R. F.; Cohen, A. E.; Terfort, A.; Rampi, M. A.; Whitesides, G. M. *Journal of the American Chemical Society* **2001**, *123*, 5075-5085.

- (24) Solak, A. O.; Ranganathan, S.; Itoh, T.; McCreery, R. L. *Electrochemical and Solid State Letters* **2002**, *5*, E43-E46.
- (25) Liu, Y. J.; Yu, H. Z. *Chemphyschem* **2002**, *3*, 799-+.
- (26) Grave, C.; Tran, E.; Samori, P.; Whitesides, G. M.; Rampi, M. A. *Synthetic Metals* **2004**, *147*, 11-18.
- (27) Tran, E.; Grave, C.; Whitesides, G. A.; Rampi, M. A. *Electrochimica Acta* **2005**, *50*, 4850-4856.
- (28) Tran, E.; Duati, M.; Whitesides, G. M.; Rampi, M. A. *Faraday Discussions* **2006**, *131*, 197-203.
- (29) Tran, E.; Duati, M.; Ferri, V.; Mullen, K.; Zharnikov, M.; Whitesides, G. M.; Rampi, M. A. *Advanced Materials* **2006**, *18*, 1323-1328.
- (30) McCarty, G. S. *Nano Letters* **2004**, *4*, 1391-1394.
- (31) Chang, S. C.; Li, Z. Y.; Lau, C. N.; Larade, B.; Williams, R. S. *Applied Physics Letters* **2003**, *83*, 3198-3200.
- (32) Akkerman, H. B.; Blom, P. W. M.; de Leeuw, D. M.; de Boer, B. *Nature* **2006**, *441*, 69-72.
- (33) McCreery, R. L.; Viswanathan, U.; Kalakodimi, R. P.; Nowak, A. *M. Faraday Discussions* **2006**, *131*, 33-43.
- (34) Anariba, F.; Steach, J. K.; McCreery, R. L. *Journal of Physical Chemistry B* **2005**, *109*, 11163-11172.
- (35) Bergren, A. J.; Harris, K. D.; Deng, F. J.; McCreery, R. L. *Journal of Physics-Condensed Matter* **2008**, *20*.

- (36) Morpurgo, A. F.; Marcus, C. M.; Robinson, D. B. *Applied Physics Letters* **1999**, *74*, 2084-2086.
- (37) Hu, W. P.; Jiang, J.; Nakashima, H.; Luo, Y.; Kashimura, Y.; Chen, K. Q.; Shuai, Z.; Furukawa, K.; Lu, W.; Liu, Y. Q.; Zhu, D. B.; Torimitsu, K. *Physical Review Letters* **2006**, *96*.
- (38) Johnston, D. E.; Strachan, D. R.; Johnson, A. T. C. *Nano Letters* **2007**, *7*, 2774-2777.
- (39) Mahapatro, A. K.; Ying, J. W.; Ren, T.; Janes, D. B. *Nano Letters* **2008**, *8*, 2131-2136.
- (40) Chen, F.; Tao, N. J. *Accounts of Chemical Research* **2009**, *42*, 429-438.
- (41) Gittins, D. I.; Bethell, D.; Schiffrin, D. J.; Nichols, R. J. *Nature* **2000**, *408*, 67-69.
- (42) Bumm, L. A.; Arnold, J. J.; Dunbar, T. D.; Allara, D. L.; Weiss, P. S. *Journal of Physical Chemistry B* **1999**, *103*, 8122-8127.
- (43) Guisinger, N. P.; Yoder, N. L.; Hersam, M. C. *Proceedings of the National Academy of Sciences of the United States of America* **2005**, *102*, 8838-8843.
- (44) He, J.; Chen, F.; Lindsay, S.; Nuckolls, C. *Applied Physics Letters* **2007**, *90*.
- (45) Chen, F.; Huang, Z. F.; Tao, N. J. *Applied Physics Letters* **2007**, *91*.

- (46) Cui, X. D.; Zarate, X.; Tomfohr, J.; Sankey, O. F.; Primak, A.; Moore, A. L.; Moore, T. A.; Gust, D.; Harris, G.; Lindsay, S. M. *Nanotechnology* **2002**, *13*, 5-14.
- (47) Loiacono, M. J.; Granstrom, E. L.; Frisbie, C. D. *Journal of Physical Chemistry B* **1998**, *102*, 1679-1688.
- (48) Wold, D. J.; Frisbie, C. D. *Journal of the American Chemical Society* **2001**, *123*, 5549-5556.
- (49) Tivanski, A. V.; Bemis, J. E.; Akhremitchev, B. B.; Liu, H. Y.; Walker, G. C. *Langmuir* **2003**, *19*, 1929-1934.
- (50) Tivanski, A. V.; Walker, G. C. *Journal of the American Chemical Society* **2005**, *127*, 7647-7653.
- (51) Solak, A. O.; Eichorst, L. R.; Clark, W. J.; McCreery, R. L. *Analytical Chemistry* **2003**, *75*, 296-305.
- (52) Dunker, M. F. W.; Starkey, E. B.; Jenkins, G. L. *Journal of the American Chemical Society* **1936**, *58*, 2308-2309.
- (53) Ranganathan, S.; McCreery, R. L. *Analytical Chemistry* **2001**, *73*, 893-900.
- (54) Hutter, J. L.; Bechhoefer, J. *Review of Scientific Instruments* **1993**, *64*, 1868-1873.
- (55) Sheng, S.; Czajkowsky, D. M.; Shao, Z. *Journal of Microscopy-Oxford* **1999**, *196*, 1-5.
- (56) Bonnet, N.; Dongmo, S.; Vautrot, P.; Troyon, M. *Microscopy Microanalysis Microstructures* **1994**, *5*, 477-487.

- (57) Andrieux, C. P.; Pinson, J. *Journal of the American Chemical Society* **2003**, *125*, 14801-14806.
- (58) Baranton, S.; Belanger, D. *Journal of Physical Chemistry B* **2005**, *109*, 24401-24410.
- (59) Benedetto, A.; Balog, M.; Viel, P.; Le Derf, F.; Salle, M.; Palacin, S. *Electrochimica Acta* **2008**, *53*, 7117-7122.
- (60) Brooksby, P. A.; Downard, A. J. *Langmuir* **2004**, *20*, 5038-5045.
- (61) Toupin, M.; Belanger, D. *Journal of Physical Chemistry C* **2007**, *111*, 5394-5401.
- (62) Doppelt, P.; Hallais, G.; Pinson, J.; Podvorica, F.; Verneyre, S. *Chemistry of Materials* **2007**, *19*, 4570-4575.
- (63) Hurley, B. L.; McCreery, R. L. *Journal of the Electrochemical Society* **2004**, *151*, B252-B259.
- (64) Saby, C.; Ortiz, B.; Champagne, G. Y.; Belanger, D. *Langmuir* **1997**, *13*, 6805-6813.
- (65) McCreery, R.; Dieringer, J.; Solak, A. O.; Snyder, B.; Nowak, A. M.; McGovern, W. R.; DuVall, S. *Journal of the American Chemical Society* **2003**, *125*, 10748-10758.
- (66) Itoh, T.; McCreery, R. L. *Journal of the American Chemical Society* **2002**, *124*, 10894-10902.
- (67) Ramirez-Aguilar, K. A.; Rowlen, K. L. *Langmuir* **1998**, *14*, 2562-2566.
- (68) Chan, S. S. F.; Green, J. B. D. *Langmuir* **2006**, *22*, 6701-6706.

(69) Johnson, K. L.; Kendall, K.; Roberts, A. D. *Proceedings of the Royal Society of London Series a-Mathematical and Physical Sciences* **1971**, 324, 301-&.

Chapter III

Top contact formation and scalability of PPF/NAB/Cu junctions

3.1 Introduction

The ever increasing need for miniaturization of electrical components has been fed by the promise of increased performance. One can imagine decreasing the size of an electronic device until it is only the size of a single molecule. In 1960, Herwald and Angello suggested that the trend in the electronics industry is towards miniaturization and the integration of molecular components into electronic devices.¹ The electronic properties of such devices could be tailored by synthetic strategies, opening new frontiers for the industry. One of the first reports of tailoring a molecule for electronic properties was published in 1974 by Avimar and Ratner.² In this work they designed a molecule that contained electron donating and accepting functional groups which should permit electron flow only in one direction through the molecule. The integration of these tailored molecular components with a wide variety of possible structures and properties into existing microelectronics may ultimately lead to new and/or improved functionality.

The investigation of electron transport through molecules requires that the molecule be linked between two electrodes. This is defined as a molecular junction and is depicted in Figure 3.1. The most prevalent means of immobilizing molecules between electrodes involves the thiol-gold linkage. The molecule contains a thiol functional group that spontaneously adsorbs to gold electrodes.³⁻⁶

This immobilization process has many advantages. Highly dense, well-ordered monolayers are readily formed on gold surfaces.⁷ Thus the molecular orientation, packing geometry, and interaction with electrodes are well controlled.

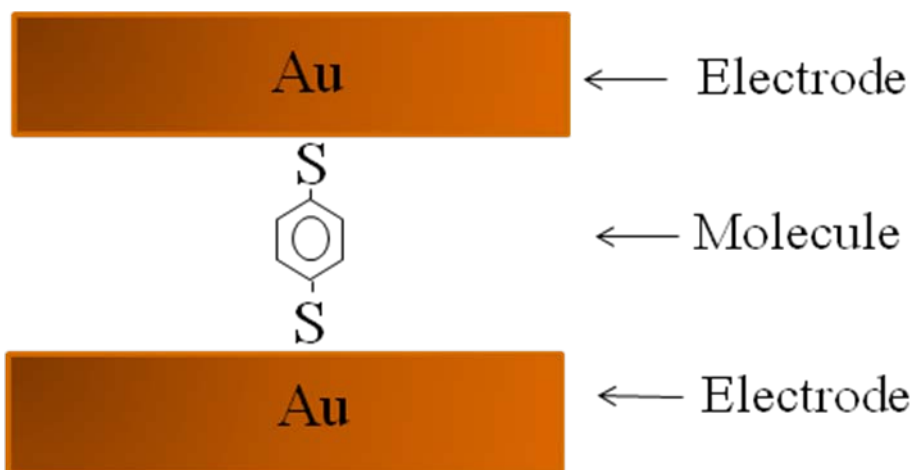


Figure 3.1 Cartoon representation of a molecular junction. In this a molecule is sandwiched between two conducting metals. This setup allows for charge to be passed through the central molecule.

Due to the small probe size intrinsic to scanning probe techniques, scanning probe microscopy has been used to investigate charge transport through small ensembles of molecules.^{3,5,8-14} Atomic force microscopy (AFM) has been used to study charge transport through a variety of thiol monolayers on gold.^{3,5,11-14} A metal AFM probe is used as a top contact to the molecules immobilized onto the gold surface. A depiction of this experimental set-up is given Figure 3.2 a. The probe thus interrogates electron transport through a small ensemble of molecules. An advantage of this technique is that the applied force can be

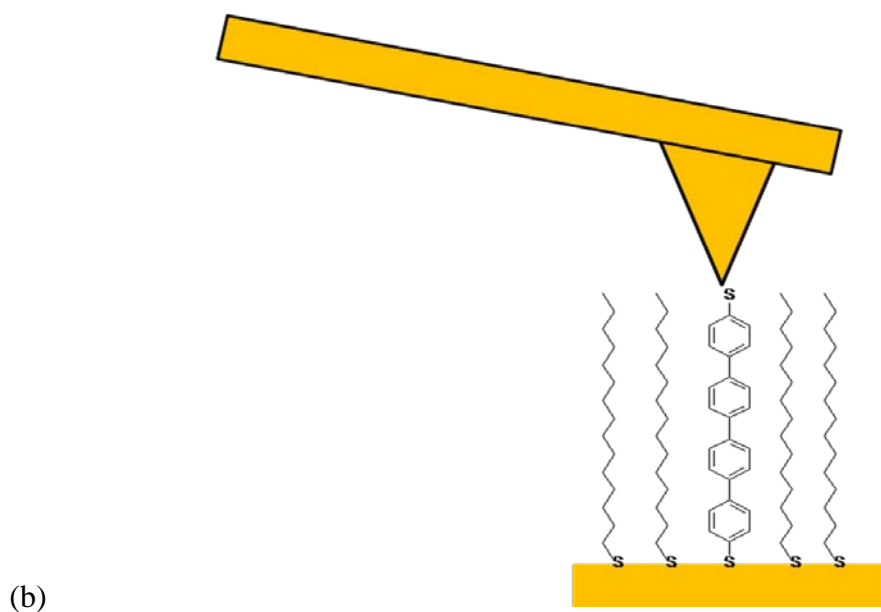
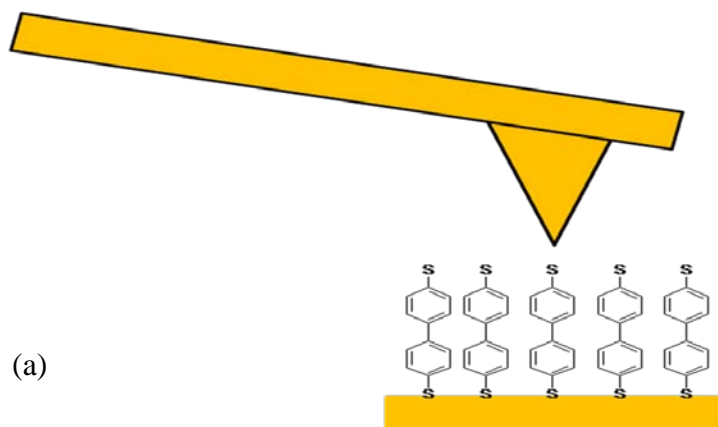


Figure 3.2 Experimental setups of charge transfer experiments that monitor electron transfer through a monolayer on gold. In (a) electron transfer through an ensemble of molecules is measured using a conduction AFM probe. In (b) the concentration of conducting molecules immobilized on the surface has been decreased such that only charge being passed through a single molecule is being investigated.

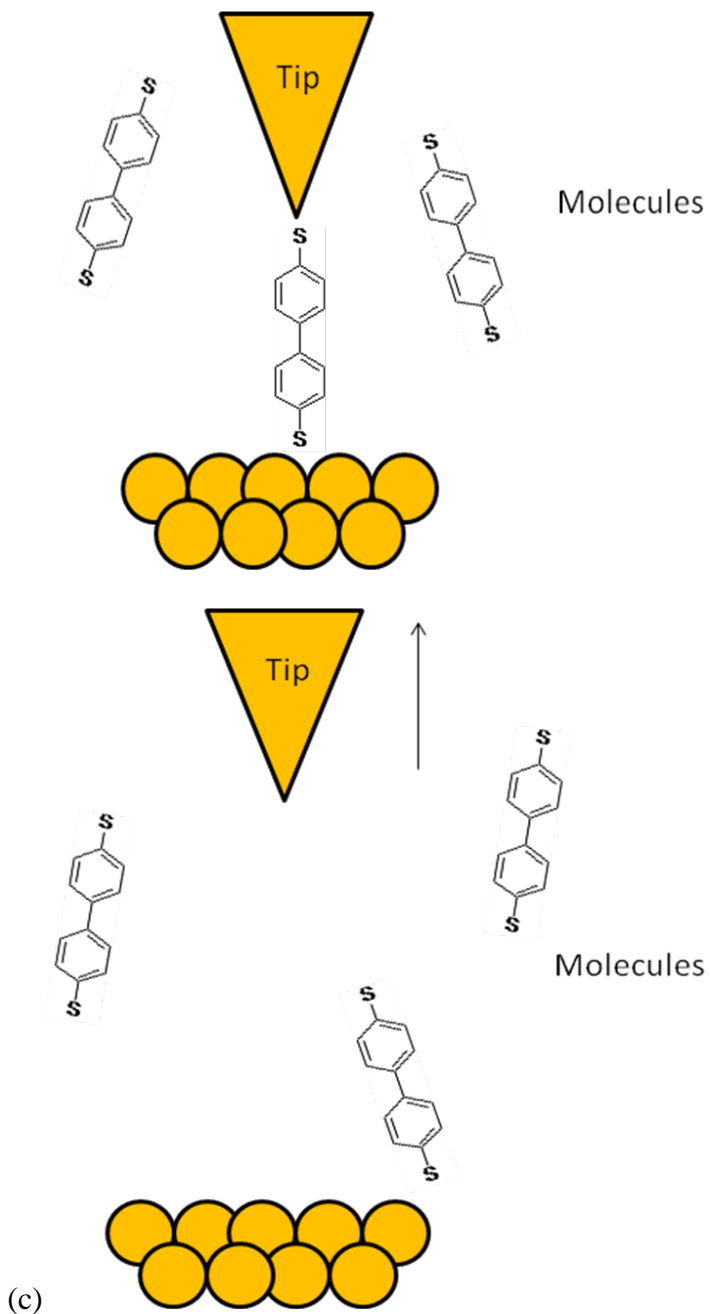


Figure 3.2c Gold coated STM tip is lowered into contact forming a molecular junction in the presence of conducting molecules and charge transport through the molecule is measured. The junction is then broken by withdrawing the STM tip. This process is repeated thereby enabling a large number of charge transport measurements to be collected.

controlled and the effects of molecular layer compression may be investigated.¹¹ Also by using mixed monolayers the surface concentration of “conducting” molecules can be decreased so that at any given time the probe is interrogating only one molecule, as depicted in Figure 3.2b.¹⁵ However, even with careful control, there is quite a bit of variability in experimental results. Tao and coworkers devised a method to repeatedly form and break a molecular junction using a scanning tunneling microscope (STM).^{8,16} In this approach a gold – molecule – gold junction is repeatedly formed and broken, creating a break junction and depicted in Figure 3.2c. A gold scanning tunneling microscope tip is brought in and out of contact with a gold surface in a solution of thiol molecules. The number of molecules involved in the junction will vary in each experiment, however, the results are quantized and information concerning single molecule junctions may be obtained.

Despite these advances, the formation and measurement of molecular junctions has been burdened by irreproducibility and uncertainty. A recent review has even stated that resistance per molecule can vary 8 orders of magnitude.¹⁷ Potentially, some of the uncertainty in measurements may be due to the drawbacks of the thiol gold linkage. The thiol-gold linkage is non-covalent in nature and the molecules may laterally diffuse or be removed from the surface. This immobilization process is also limited to metal junctions.

One avenue being explored to circumvent these issues is the grafting of diazonium salt derived aryl layers. Originally pioneered by Pinson and coworkers in 1992, they found that upon the electrochemical reduction of nitrobenzene

diazonium salt, a carbon working electrode could be modified.¹⁸ Later it was found that diazonium salts can be used to modify Au, Cu, Ag, Pt as well as Si, Pd, Fe, GaAs.²⁰⁻²² It is this flexibility of modifying a diverse range of substrates that gives this process a unique advantage. The procedure for diazonium modification of metals is similar to that of carbon modification, described in section 1.11

McCreery and coworkers have used the diazonium salt attachment method to form molecular junctions. They have shown charge transport in macro-size molecular junctions can vary, but with control of molecular layer and top contact formation, this irreproducibility can be decreased.^{23,24} In this work they found the thickness of the nitroazobenzene (NAB) molecular layer could drastically affect the magnitude of electron transport through a PPF/NAB/Cu junction.²³ They also found that top contact formation plays an important role in observed electron transport.²³ By increasing the pressure during top contact fabrication of PPF/NAB/Cu junction they observed a decrease in electron transport.

The present chapter addresses the lack of reproducibility between micro and nanoscale measurements. A comparison of charge transport through microscale and nanoscale PPF/NAB/Cu molecular junctions was made by performing c-AFM investigates on a PPF/NAB layer right beside a micro-sized PPF/NAB/Cu junction. This work addresses scalability of molecular junctions as well as considering top contact formation in PPF/NAB/Cu junctions.

3.2 Experimental

Preparation of nitroazobenzene diazonium salts

Nitroazobenzene diazonium salt were synthesized according to the Starkey method.²⁵ The amine precursor [Sigma Aldrich] were reacted with sodium nitrite, added drop wise, in the presence of tetrafluoroboric acid [48% Sigma Aldrich]. 10mL of acetonitrile [Sigma Aldrich] was used to aid solubility of amine precursor. During the entire reaction all solutions were kept below 2°C to avoid diazonium degradation. The resulting diazonium salt was isolated by recrystallization upon addition of ether and dried in an ice bath cold rotoevaporator. Once isolated the nitroazobenzene diazonium salt was stored below 0°C, in the dark, and over desiccant.

Preparation of pyrolyzed photoresist (PPF)

Silicon wafers were diced into 1.5cm x 1.5cm squares, cleaned with soap, tap water, distilled water, followed by emersion in freshly prepared piranha solution. Piranha was prepared by mixing 1 part 30% hydrogen peroxide (EMD, ACS certified) with 3 parts concentrated sulfuric acid (EMD, ACS certified). *Extreme care should be taken during piranha use due to its violent exothermal nature.* Following piranha cleaning the Si wafers were rinsed with copious amounts of 0.2µm filtered 18MΩ·cm water (Barnstead-Thermolyne, Nanopure water filtration unit) followed by drying via an argon stream within a Terra Universal Whisper flow Benchtop clean hood. One layer of AZ4330 photoresist was spin coated onto the dried Si wafer initially at a rate of 500rpm for 20sec

followed by 2000rpm for 20 sec and finally 3000rpm for 40sec. The coated samples were immediately placed in an oven at 110°C for solvent drying for 20 minutes. Following the solvent drying step the coated samples were placed in a tube furnace and the environmental atmosphere was purged with forming gas [N₂ with 5%H₂] for 20 minutes. The samples were then heated, under constant flow of forming gas, to 1000°C and held for 1 hour. The samples were then cooled to room temperature to enable handling. Upon removal from the tube furnace the PPF samples were immediately placed in a vacuum over desiccant and stored until use.

Surface derivatization

Surface derivatization of PPF occurred by initially cleaning the substrates vigorously using 3 successive ultrasonic bath treatments in isopropanol which had been filtered through activated carbon. The PPF substrates were then rinsed with copious amounts of with 0.2µm filtered 18MΩ·cm water followed by drying by a gentle stream of argon. Derivatization of the PPF substrates with aryl films was accomplished by electrochemical reduction of the diazonium salts (1mM in acetonitrile) within a three-probe electrochemical cell in the presence of tetrabutylammoniumtetrafluoroborate electrolyte (Sigma Aldrich). The cell consisted of a Ag/AgNO₃ reference electrode and a platinum mesh as a counter electrode. Using a Pine biopotentiostat, the voltage was ramped at a rate of 200 mV/s while monitoring the resulting current. The modified samples were

removed and rinsed with copious amounts of acetonitrile, 0.2 μm filtered 18 M Ω -cm water, followed by drying with a stream of Argon.

Micro-sized Cu junction Fabrication

65 μm^2 and 1600 μm^2 PPF/NAB/Cu junctions were fabricated by e-beam evaporation of 45nm of Cu through a 2000 and 400 mesh TEM grids respectively. This was followed by evaporation of 5nm of gold to minimize oxidization of the Cu. All metal evaporation occurred in an e-beam evaporator at a base pressure of no greater than 10^{-6} Torr during deposition. Removal of the TEM grid left behind, 65 μm^2 and 400 μm^2 Cu island PPF/NAB/Cu junctions were left behind. The PPF/NAB/Cu junctions were then characterized using a Hitachi HF 3300 scanning electron microscope. Figure 3.4 is a depiction of the experimental set-up used to investigate top contact formation and scalability in conventional PPF/NAB/Cu devices. This work was in collaboration with Adam J. Bergren and Richard L. McCreery. With the interest of reproducing similar junctions as Bergren et. al. recently reported,²³ Bergren kindly prepared the NAB molecular layers on PPF and deposited the copper.

AFM tip Characterization

The conductive probes were fabricated by coating conventional Si AFM probes (Olympus) with 50nm of electron beam evaporated Cu. An e-beam evaporator was used with a pressure of no greater than 10^{-6} Torr during Cu deposition. Characterization of the Cu coated AFM tip occurred by scanning

electron microscopy and deconvolution of the tip's geometry using a blind reconstruction method as discussed in Chapter 6. In short this occurred by collection of topographical images of evaporated niobium films. These images were then processed to create a geometric envelope of the tip using SPIP software package.

Charge Transport investigations

Current/voltage (I/V) curves were acquired in air using an Asylum MFP-3D atomic force microscope equipped with an Orca conductive probe module. To ensure constant applied force during IV curves the AFM was operated in deflection feedback and curves were collected at a rate of 1Hz. The applied force applied during I/V curves was adjusted using the setpoint voltage. Cantilever force constants were calculated using the thermal method²⁶ available within the Asylum AFM software. Current/voltage (I/V) curves using the Cu coated AFM tips as the top contact were collected using the Orca conductive probe module and self contained Asylum MFP-3D software. IV curves on the $65 \mu\text{m}^2$ and $1600 \mu\text{m}^2$ Cu island junctions occurred by placing a Cu coated AFM in contact with the Cu island. This formed an Ohmic electrical contact between the Cu island and Cu-AFM probe. The voltage was then ramped between the Cu-AFM probe and PPF using a Gramry potentiostat. The IV curves were collected in the Gramry electrochemical software.

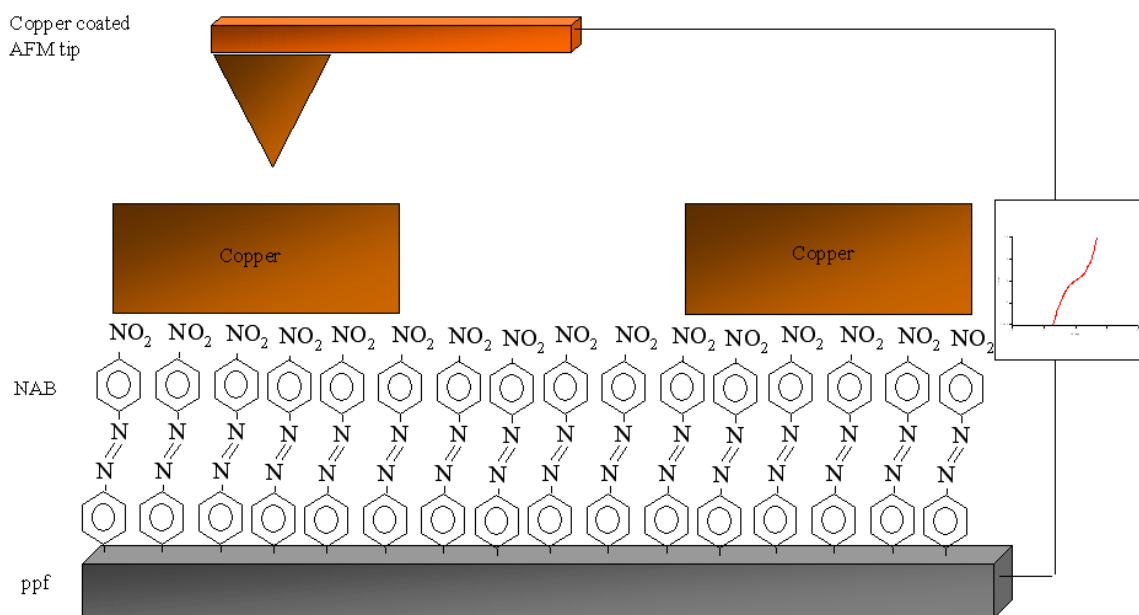


Figure 3.4 Illustration of PPF/NAB/Cu experiment setup. Charge transport studies through micro-sized junctions occurred by placing Cu coated AFM tip in contact with micro-sized Cu pad. Charge transport investigations on the nanometer size regime occurred by positioning the Cu AFM tip in contact with the bare NAB molecular layer.

3.3 Results and Discussion

Characterization of PPF/NAB/Cu Junctions

Chapter 2 consisted of charge transfer experiments conducted using a Pt AFM tip as the top contact in the molecular junction. The work described in this chapter aims to directly study the effect of junction size on the I/V characteristics of molecular junctions. We thus used Cu coated AFM tips to interrogate PPF/NAB/Cu junctions. Figure 3.5 contains a tapping mode topographic AFM image and representative cross-sectional profile of the Cu island junctions supported on the NAB molecular film. The topographic image reveals the geometry of the Cu patterned sample. By performing cross sectional profiles the size of the Cu patterned islands was determined to be $8.1\ \mu\text{m} \times 8.1\ \mu\text{m}$ when evaporated through a $6\ \mu\text{m}$ hole TEM grid (2000 mesh) and $43\ \mu\text{m} \times 43\ \mu\text{m}$ using a $45\ \mu\text{m}$ hole TEM grid (400 mesh). The spacing between the 2000 mesh and 400 mesh Cu islands were measured to be $3.1\ \mu\text{m}$ and $20\ \mu\text{m}$, respectively. The Cu island thickness was measured to be 32 nm and 35 nm for the 2000 mesh and 400 mesh devices, respectively.

Scanning electron micrographs were also collected for Cu patterned devices to measure contact areas. The results for the 2000 mesh and 400 mesh grids are shown in Figures 3.6a and 3.6b, respectively. Three sample areas were collected to measure junction uniformity. The scanning electron micrographs reveal excellent junction size uniformity over large distances on the substrate. 30 Cu junctions were measured for each sample giving an averaged contact area of $65\ \mu\text{m}^2$ and $1600\ \mu\text{m}^2$ for the 2000 mesh and 400 mesh TEM grids respectively.

C-AFM Charge Transport Investigations

Having confidence in contact areas and uniformity of junctions, a Cu coated AFM tip was brought into Ohmic contact to one of the Cu islands and IV curves were collected. The geometric size of the Cu islands found by SEM was used to calculate the current density, J . Figure 3.7 contains five JV curves on individual junctions of $65 \mu\text{m}^2$ and $1600 \mu\text{m}^2$ in size. The Cu coated tip was withdrawn and engaged for each JV at a different location on the Cu island. The plots exhibit current densities at +0.5V of $0.7 \pm 0.1 \text{ Acm}^{-2}$ and $0.2 \pm 0.1 \text{ Acm}^{-2}$. The slight difference in measured current densities may be attributed to not accurately knowing the contact area for this specific junction.

A set of 16 JV curves was collected on 16 different $8.3\mu\text{m} \times 8.3\mu\text{m}$ Cu junctions to assess inter-junction reproducibility. The results are presented in Figure 3.8. 14 out of 16 junctions produced JV curves that overlay each other reasonably well. Excluding the two outlier JV curves, the current density at +0.5V and +1V was determined to be $0.7 \pm 0.7 \text{ Acm}^{-2}$ and $1.6 \pm 1.4 \text{ Acm}^{-2}$. These current densities are slightly larger than those previously reported by Bergren et. al.²³ In this previous work, the authors measured JV curves on junctions with significantly larger contact areas of 0.0025cm^2 . The measured average current density they found was 0.21 Acm^{-2} at +0.5V. They also noticed differences in inter-junction reproducibility, where current densities could be as large as 1.4 Acm^{-2} at +0.5V. The agreement between the "macro" junctions and the current "micro" junctions is reasonable, and implies that similar phenomena control the current magnitudes. It is interesting to note that electron transfer is

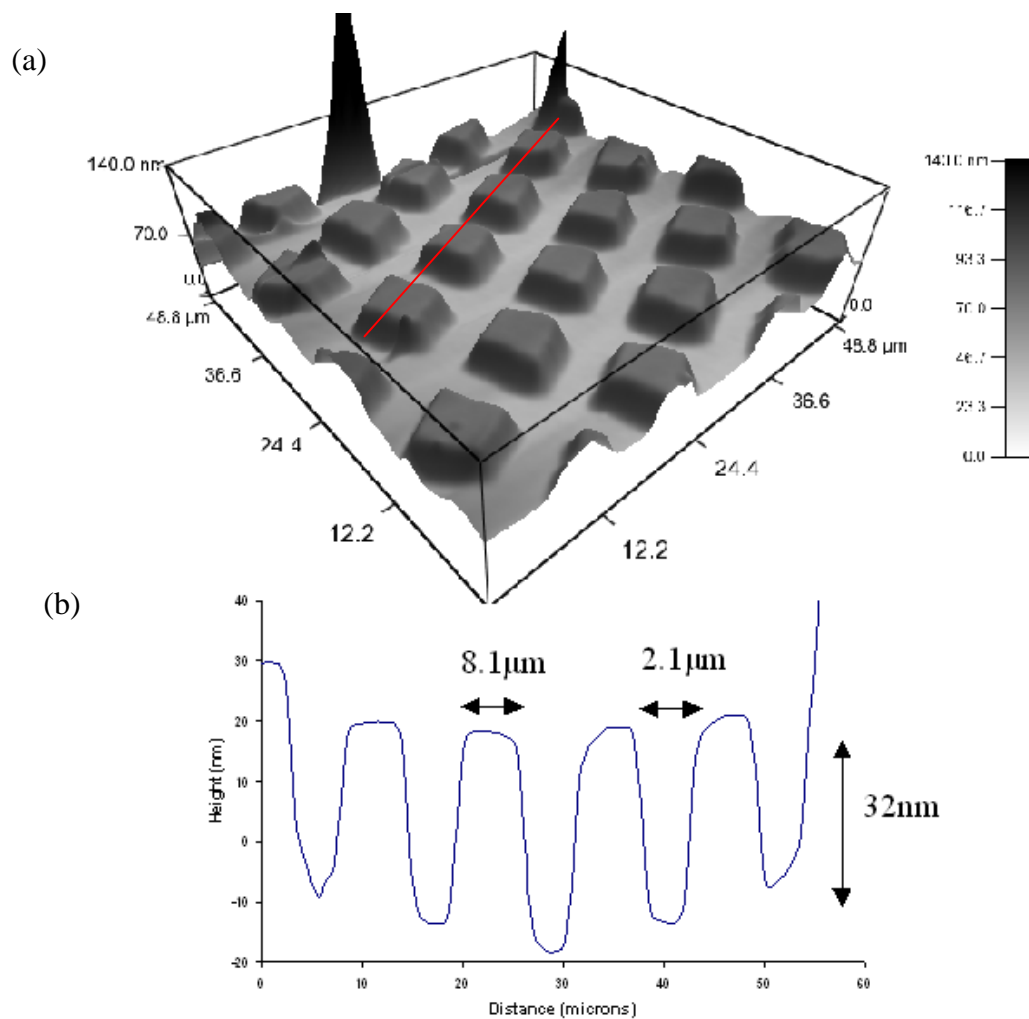


Figure 3.5 (a) Tapping mode AFM topography image of patterned e-beam evaporated Cu pads on NAB molecular layer. (b) Topography line trace of patterned Cu pads, area of interest is indicated by red line in topography image.

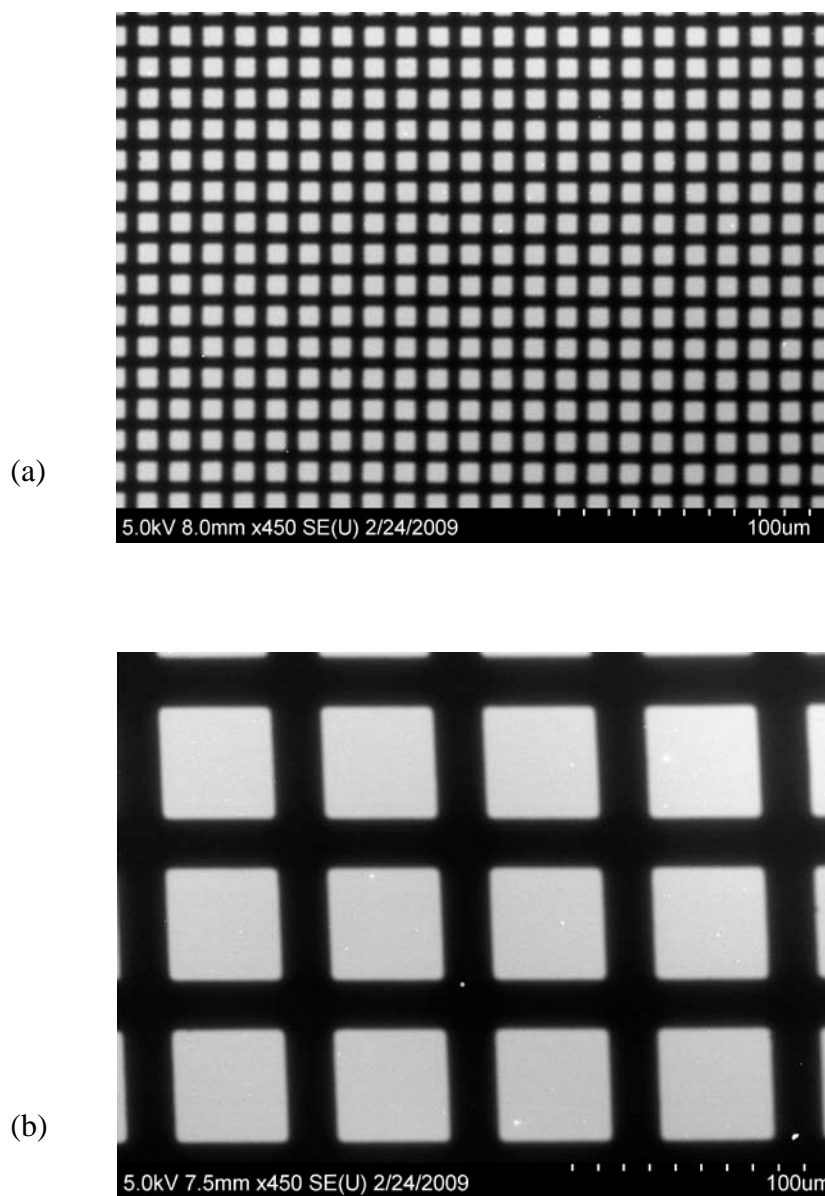


Figure 3.6 Scanning electron microscopy image of patterned e-beam evaporated Cu island pads, through a 2000 mesh(a) and 400 mesh(b) TEM grid, on a NAB molecular layer supported by PPF. The area of the bright squares was used to assess the contact area of the PPF/NAB/Cu molecular junction.

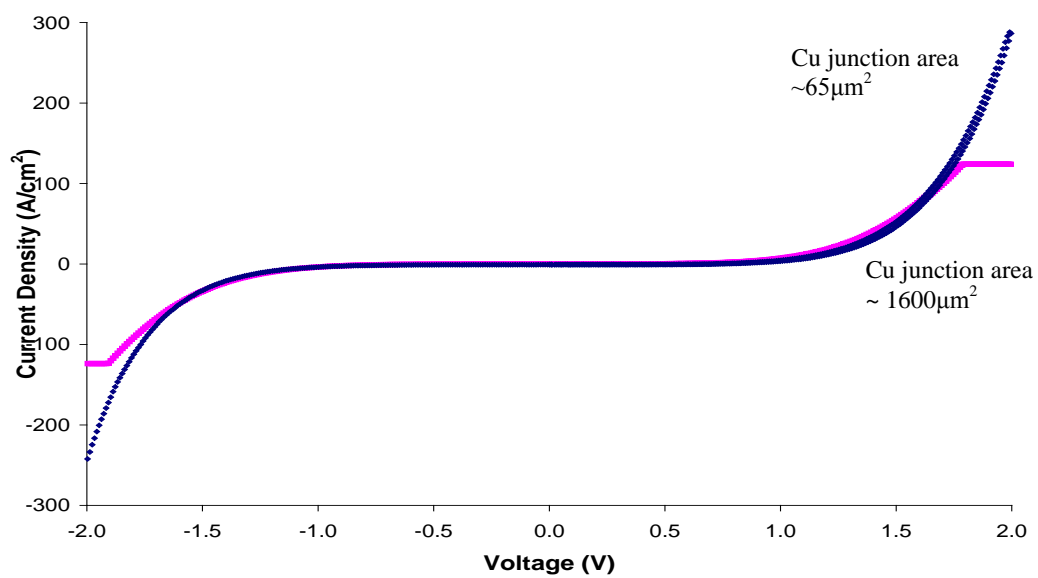


Figure 3.7 Overlay of 5 JV curves for each area collected on individual PPF/NAB/Cu molecular junction having a contact area of $\sim 64\ \mu\text{m}^2$ and $\sim 1600\ \mu\text{m}^2$.

non-Ohmic and no appreciable rectification is observed. The lack of rectification observed in the JV curves could suggest differences in electronic coupling between the NAB molecules and the Cu electrode and the NAB molecules and Pt c-AFM top electrode's in Chapter 2. Junctions using the Cu coated AFM tip as the top contact were probed to investigate the effect of junction size. The junctions were formed adjacent to a Cu pad on the same samples to ensure that the same NAB/PPF layer was being probed. Figure 3.9 contains IV curves collected by c-AFM under a variety of applied loads. The observed current increases as the applied load exerted on the cantilever is increased. This can be attributed to an increase in contact area, and molecular layer compression/deformation at the larger forces as described in Chapter 2.

The effect of junction size can be explored by directly comparing the I/V characteristics of the Cu pad/NAB/PPF junctions and the AFM tip/NAB/PPF junctions. This comparison requires normalization for the contact area to construct plots of current density (J) vs voltage. For the micro-sized Cu island junctions it is a simple calculation in which the measured current is divided by the area of the island. Calculation of the current density curves collected using the Cu coated tips requires consideration of changes in contact area due to increases in applied load. The Johnson-Kendall-Robert's (JKR) contact mechanical theory was applied to determine contact area between the Cu coated AFM tips and the NAB layer.²⁷ The tip radius was determined by blind reconstruction methods in which topographic data is used to create a 3-D model of the tip's geometry.^{28,29} A topographic image of evaporated niobium and the reconstructed tip model of the

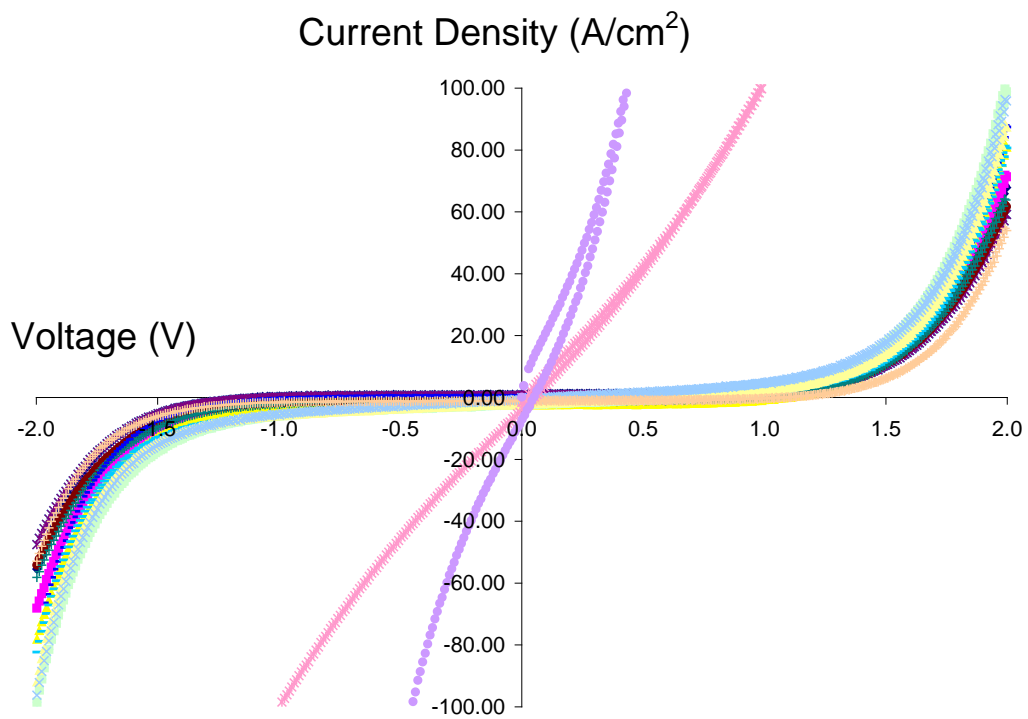


Figure 3.8 Overlay of 16 JV curves collected on 16 different PPF/NAB/Cu molecular junctions having a contact area of $\sim 64 \mu\text{m}^2$.

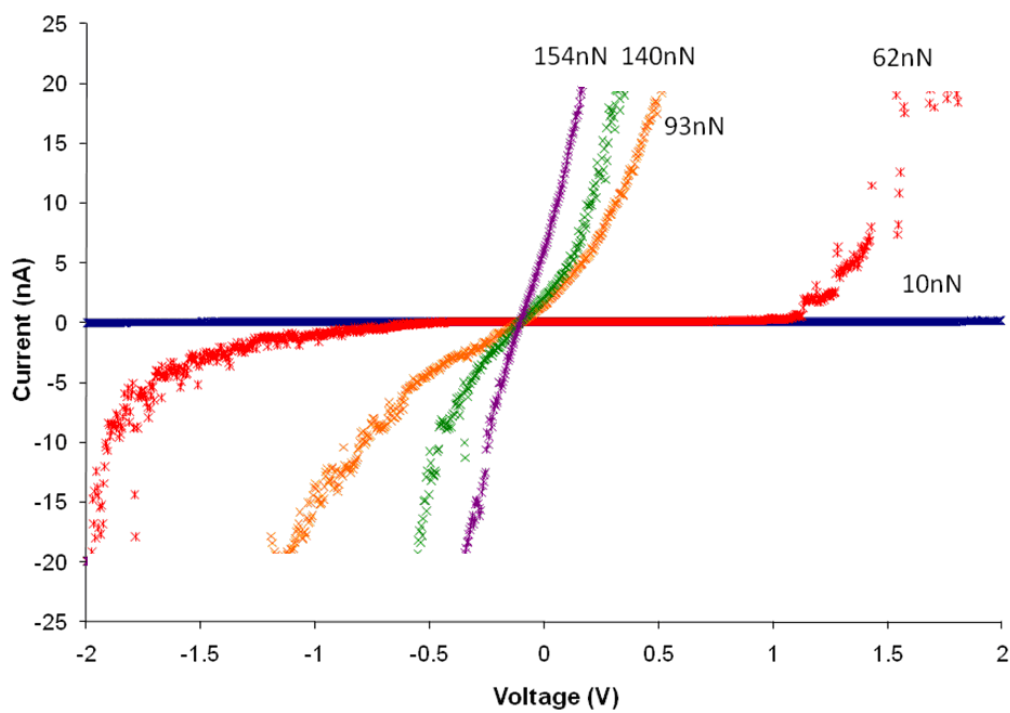


Figure 3.9 IV curves collected using a Cu coated AFM tip as the top contact in the PPF/NAB/Cu molecular junction. The applied load was increased between 0 nN and 154 nN, at which point an Ohmic response was observed.

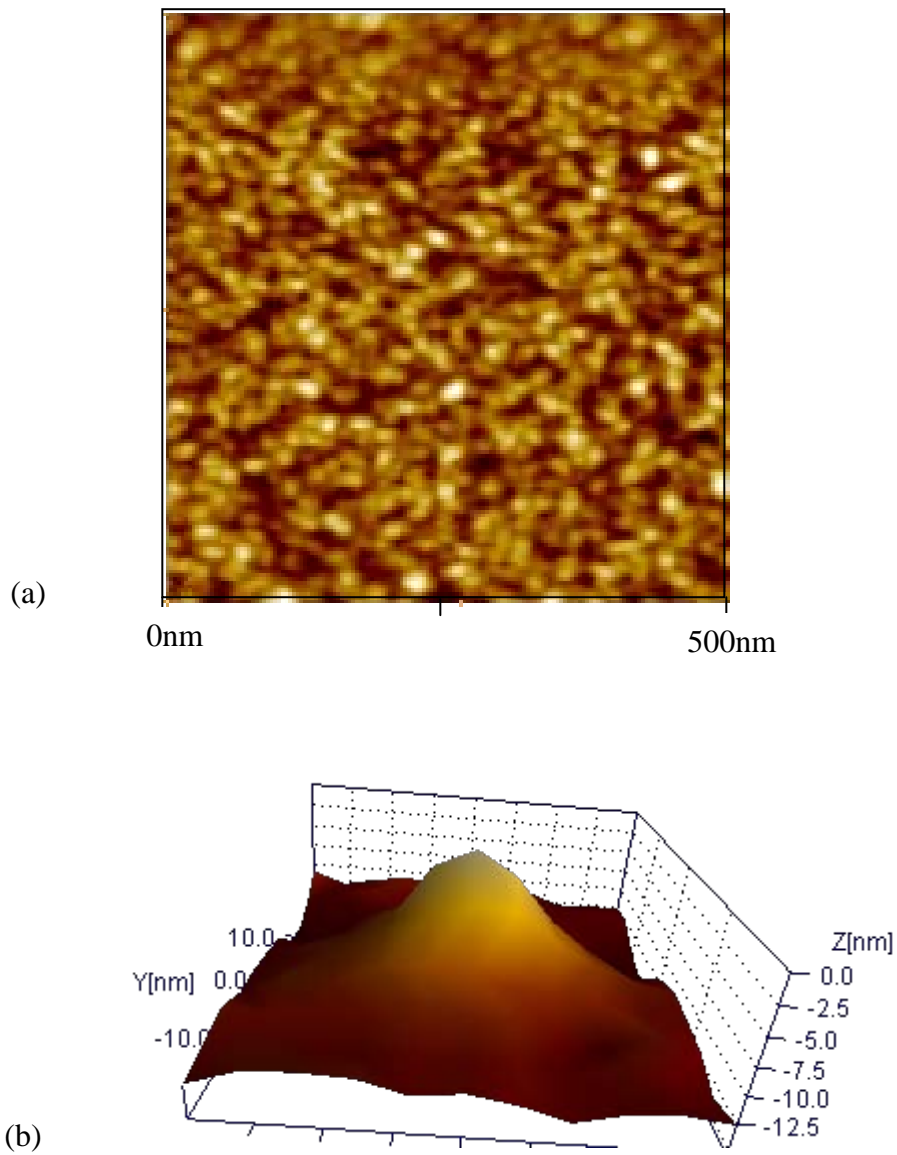


Figure 3.10 Topographic image of evaporated Nb (a) used to calculate a 3D model of the c-AFM tip using blind reconstruction methods (b)

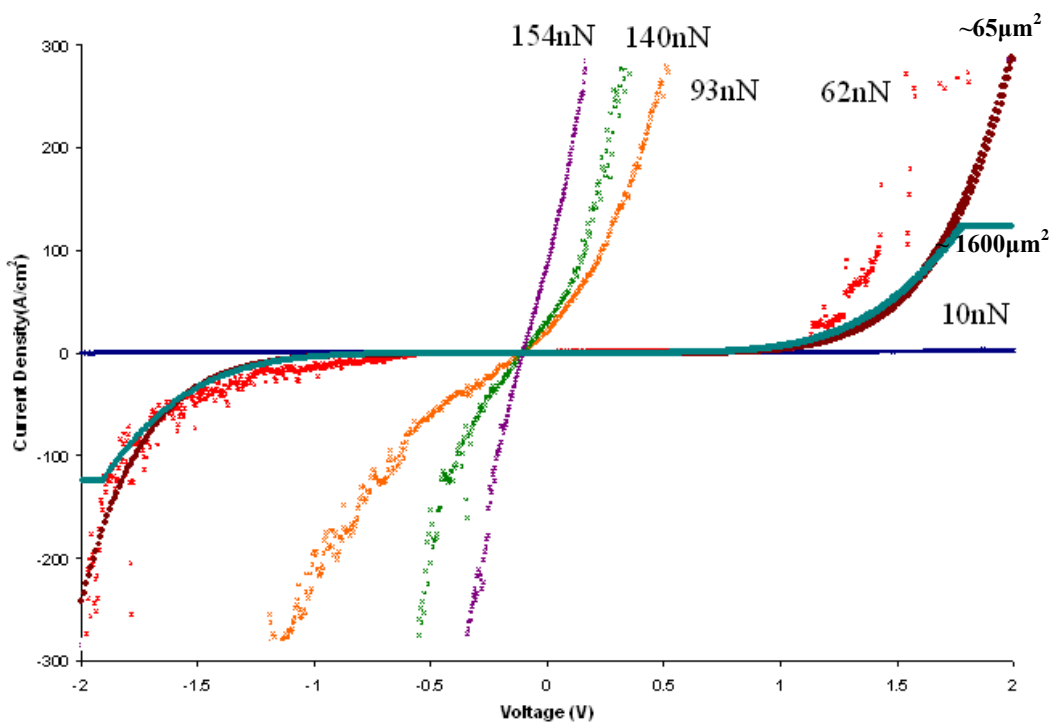


Figure 3.11 JV curves collected using a Cu coated AFM tip as the top contact in the PPF/NAB/Cu molecular junction. The applied load was increased between 0 nN and 154 nN, at which point an Ohmic response was observed.

Cu coated AFM tip are given in Figure 3.10. The tip radius of the probe used in the charge transport experiments was determined to be $11 \text{ nm} \pm 3 \text{ nm}$. The tip radius of 11 nm was used in equation 3.1 to determine the contact area between the probe and NAB layer at various applied loads. The contact areas between the Cu coated AFM tip and NAB surface were used to determine the current densities for each applied load and are plotted in Figure 3.11. From Figure 3.11 we notice that the JV curves at increasing applied loads do not overlap. This suggests that contact area is not the sole contributor to the increase in measured current upon for larger applied loads.

As previously described in Chapter 2, JV curves not overlapping are associated with molecular layer compression and deformation induced by greater applied loads.¹¹ Figure 3.11 also shows that the JV curves associated with the micro-sized Cu island junctions agree well with the results of the JV curve representation of the $\sim 60 \text{ nN}$ applied force, having a current density at $+0.5 \text{ V}$ and $+1.0 \text{ V}$ of $0.4 \pm 0.2 \text{ A cm}^{-2}$ and $1.6 \pm 0.2 \text{ A cm}^{-2}$ respectively. The micro-sized Cu island junctions had current densities at $+0.5 \text{ V}$ of $0.7 \pm 0.1 \text{ A cm}^{-2}$ and $0.2 \pm 0.1 \text{ A cm}^{-2}$ for the $65 \mu\text{m}^2$ and the $1600 \mu\text{m}^2$ junctions respectively. This agreement is quite remarkable given a recent review has demonstrated that there can be a 10^8 magnitude of variability in these values when scaling from micron size to small ensembles of molecules investigated in scanning probe techniques.¹⁷ A great deal of this variability may be attributed to the influences that the experimental tools have on the outcome of observations. This agreement in charge transport values

may be attributed to performing both the macro-sized and nano-sized IV curves on the same sample. This limits possible sample-to-sample variability.

It is interesting to note the applied force of ~60 nN where the AFM tip/NAB/PPF JV data agrees well with the micro-sized Cu junctions. This suggests that the underlying NAB layer in the micro-sized Cu junctions may be a similar junction as the AFM tip/NAB/PPF JV at ~60 nN. To better understand this phenomenon the JV curves were fit with a common tunneling theory used to interpret molecular junctions.^{24,30,31} Figures 3.12 and 3.13 are representative JV curves of Cu island junctions and Cu coated AFM junctions respectively fit to the Simmons tunneling model.³⁰ A complete list of tunneling barriers and effective electron masses determined from the fits are provided in Table 3.1. The fit range for each JV curve fit was determined by finding the transition voltage, V_{trans} , in which electron transport changes from direct tunneling to field emission.³¹ V_{trans} can be estimated from a plot of $\ln(I/V^2)$ versus $1/V$. Plots of $\ln(I/V^2)$ versus $1/V$ used to determine Figures 3.12 and 3.13 V_{trans} are provided in Figures 3.12b and Figure 3.13b. The entire JV curve for the PPF/NAB/Cu c-AFM tip at applied loads of 93 nN and 140 nN were fit due to the absence of V_{trans} . From these fits we find the barrier height and effective electron mass, e^- mass, determined for the $1600 \mu\text{m}^2$ PPF/NAB/Cu molecular junction is in good agreement with the values determined for a PPF/NAB/Cu c-AFM tip molecular junction at an applied load of 62 nN. The V_{trans} from the $1600 \mu\text{m}^2$ PPF/NAB/Cu molecular junction PPF/NAB/Cu c-AFM tip molecular junction at an applied load of 62nN are similar to those reported for similar junction, having a $V_{\text{trans}} = 0.45 \pm 0.08\text{V}$.²³

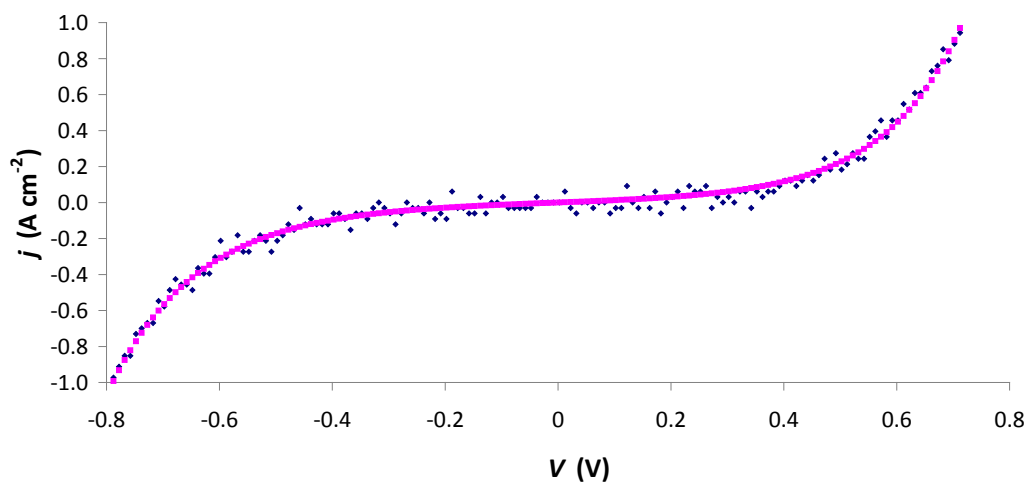


Figure 3.12a JV curve and corresponding Simmon's tunneling model fit of data collected on a $1600\mu\text{m}^2$ PPF/NAB/Cu molecular junction. The raw data was fit between -0.49V and $+0.40\text{V}$.

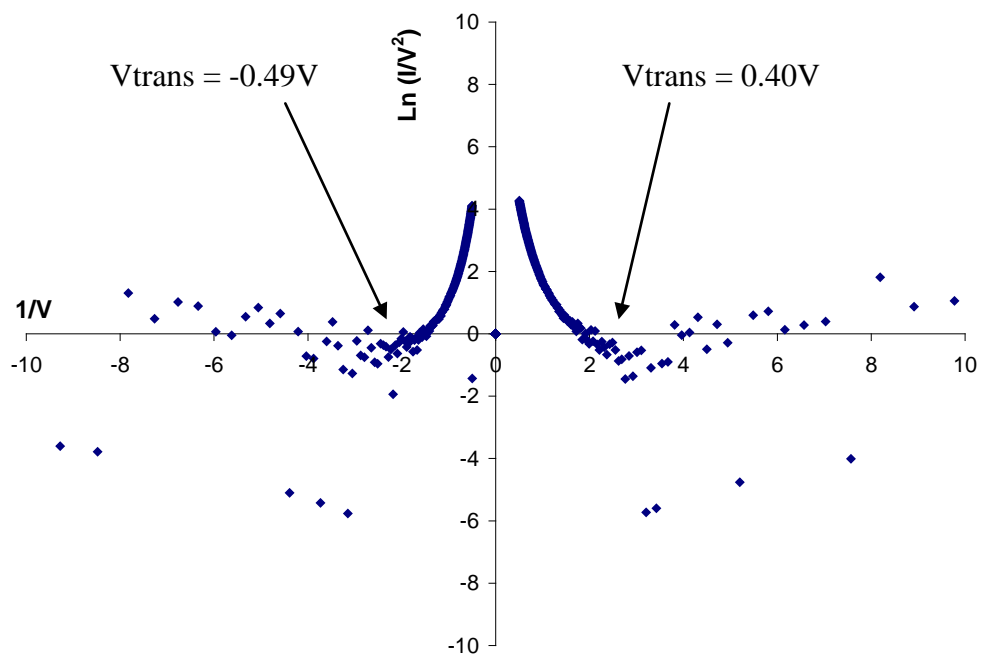


Figure 3.12b Plot of $\text{Ln}(I/V^2)$ versus $1/V$ used to determine V_{trans} of the $1600\mu\text{m}^2$ PPF/NAB/Cu molecular junction fit in Figure 3.12a. V_{trans} was determined to be -0.49V and $+0.40\text{V}$. The large scatter for $1/V > 3$ is due to digitization noise for the small currents involved.

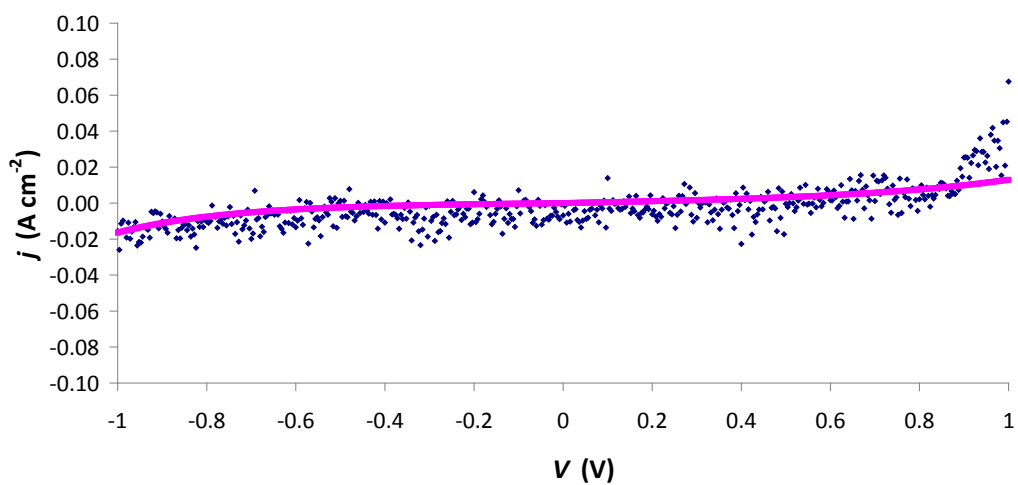


Figure 3.13b JV curve and corresponding Simmon's tunneling model fit of data collected on a PPF/NAB/Cu c-AFM tip molecular junction having an applied load of approximately 10 nN. The raw data was fit between -0.91V and + 0.78V.

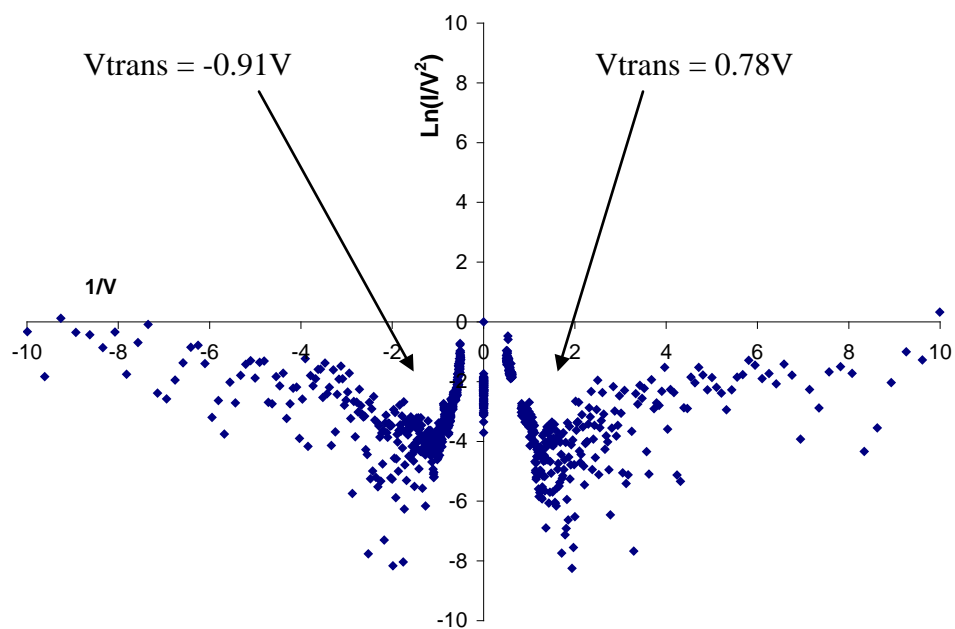


Figure 3.13b Plot of $\text{Ln}(I/V^2)$ versus $1/V$ used to determine V_{trans} of the PPF/NAB/Cu c-AFM molecular junction at applied load of approximately 10nN fit in Figure 3.12a. V_{trans} was determined to be -0.91V and + 0.78V

Junction	Barrier, Φ	e^- mass	Fit Range
$1600\mu\text{m}^2$	1.5eV	0.11	-0.49V to 0.40V
10nN c-AFM	1.0eV	0.13	-0.91 to 0.78V
62nN c-AFM	1.4eV	0.12	-0.45V to 0.65V
93nN c-AFM	1.8eV	0.09	Entire curve
140nN c-AFM	1.2eV	0.08	Entire Curve

Table 3.1 List of parameters determined from the Simmons tunneling fits of $1600\mu\text{m}^2$ PPF/NAB/Cu molecular junction and PPF/NAB/Cu c-AFM molecular junctions at various applied loads.

This suggests that the electron transport involved in the micro-sized PPF/NAB/Cu molecular junctions is similar to that observed in the PPF/NAB/Cu c-AFM tip molecular junction at an applied load of 62 nN, suggesting a similar molecular junction and charge transport is occurring within these two junction size regimes.

3.4 Conclusions

In conclusions we have demonstrated for the first time a means of fabrication of PPF/NAB/Cu junctions to probe the top contact formation and scalability of such junctions from microns to nanoscale regimes. The charge transport behavior was found to scale with junction size from the micro-scale regime into the nanoscale regime. The JV characteristics of the micro-sized PPF/NAB/Cu island junctions agree well with the JV characteristics of the PPF/NAB/Cu probe under an applied load of ~60 nN. These results demonstrate a high degree of agreement when scaling from micron sized molecular junctions to the nanoscale size regime, which may potentially lead to new applications within the microelectronics industry.

References

- (1) Herwald, S. W.; Angello, S. J. *Science* **1960**, *132*, 1127-1133.
- (2) Aviram, A.; Ratner, M. A. *Chemical Physics Letters* **1974**, *29*, 277-283.
- (3) Beebe, J. M.; Kim, B.; Frisbie, C. D.; Kushmerick, J. G. *Acs Nano* **2008**, *2*, 827-832.
- (4) Chen, F.; Li, X. L.; Hihath, J.; Huang, Z. F.; Tao, N. J. *Journal of the American Chemical Society* **2006**, *128*, 15874-15881.
- (5) Engelkes, V. B.; Beebe, J. M.; Frisbie, C. D. *Journal of the American Chemical Society* **2004**, *126*, 14287-14296.
- (6) Hu, W. P.; Jiang, J.; Nakashima, H.; Luo, Y.; Kashimura, Y.; Chen, K. Q.; Shuai, Z.; Furukawa, K.; Lu, W.; Liu, Y. Q.; Zhu, D. B.; Torimitsu, K. *Physical Review Letters* **2006**, *96*.
- (7) Walczak, M. M.; Popenoe, D. D.; Deinhammer, R. S.; Lamp, B. D.; Chung, C. K.; Porter, M. D. *Langmuir* **1991**, *7*, 2687-2693.
- (8) Chen, F.; Tao, N. J. *Accounts of Chemical Research* **2009**, *42*, 429-438.
- (9) Gittins, D. I.; Bethell, D.; Schiffrin, D. J.; Nichols, R. J. *Nature* **2000**, *408*, 67-69.
- (10) Bumm, L. A.; Arnold, J. J.; Dunbar, T. D.; Allara, D. L.; Weiss, P. S. *Journal of Physical Chemistry B* **1999**, *103*, 8122-8127.

- (11) Wold, D. J.; Frisbie, C. D. *Journal of the American Chemical Society* **2001**, *123*, 5549-5556.
- (12) Loiacono, M. J.; Granstrom, E. L.; Frisbie, C. D. *Journal of Physical Chemistry B* **1998**, *102*, 1679-1688.
- (13) Tivanski, A. V.; Bemis, J. E.; Akhremitchev, B. B.; Liu, H. Y.; Walker, G. C. *Langmuir* **2003**, *19*, 1929-1934.
- (14) Tivanski, A. V.; Walker, G. C. *Journal of the American Chemical Society* **2005**, *127*, 7647-7653.
- (15) Ramachandran, G. K.; Tomfohr, J. K.; Li, J.; Sankey, O. F.; Zarate, X.; Primak, A.; Terazono, Y.; Moore, T. A.; Moore, A. L.; Gust, D.; Nagahara, L. A.; Lindsay, S. M. *Journal of Physical Chemistry B* **2003**, *107*, 6162-6169.
- (16) Chen, F.; Huang, Z. F.; Tao, N. J. *Applied Physics Letters* **2007**, *91*.
- (17) Akkerman, H. B.; de Boer, B. *Journal of Physics-Condensed Matter* **2008**, *20*.
- (18) Bourdillon, C.; Delamar, M.; Demaille, C.; Hitmi, R.; Moiroux, J.; Pinson, J. *Journal of Electroanalytical Chemistry* **1992**, *336*, 113-123.
- (19) Kariuki, J. K.; McDermott, M. T. *Langmuir* **2001**, *17*, 5947-5951.
- (20) Stewart, M. P.; Tour, J. M.; Kosynkin, D. V.; Allara, D. L.; Dirk, S. M.; Maya, F. M. *Abstracts of Papers of the American Chemical Society* **2003**, *225*, 2-INOR.
- (21) Chen, B.; Lu, M.; Flatt, A. K.; Maya, F.; Tour, J. M. *Chemistry of Materials* **2008**, *20*, 61-64.

- (22) Bernard, M. C.; Chausse, A.; Cabet-Deliry, E.; Chehimi, M. M.; Pinson, J.; Podvorica, F.; Vautrin-UI, C. *Chemistry of Materials* **2003**, *15*, 3450-3462.
- (23) Bergren, A. J.; Harris, K. D.; Deng, F. J.; McCreery, R. L. *Journal of Physics-Condensed Matter* **2008**, *20*.
- (24) McCreery, R. L. *Chemistry of Materials* **2004**, *16*, 4477-4496.
- (25) Dunker, M. F. W.; Starkey, E. B.; Jenkins, G. L. *Journal of the American Chemical Society* **1936**, *58*, 2308-2309.
- (26) Hutter, J. L.; Bechhoefer, J. *Review of Scientific Instruments* **1993**, *64*, 1868-1873.
- (27) Johnson, K. L.; Kendall, K.; Roberts, A. D. *Proceedings of the Royal Society of London Series a-Mathematical and Physical Sciences* **1971**, *324*, 301-&.
- (28) Sheng, S.; Czajkowsky, D. M.; Shao, Z. *Journal of Microscopy-Oxford* **1999**, *196*, 1-5.
- (29) Bonnet, N.; Dongmo, S.; Vautrot, P.; Troyon, M. *Microscopy Microanalysis Microstructures* **1994**, *5*, 477-487.
- (30) Simmons, J. G. *Journal of Applied Physics* **1963**, *34*, 1793-&.
- (31) Beebe, J. M.; Kim, B.; Gadzuk, J. W.; Frisbie, C. D.; Kushmerick, J. G. *Physical Review Letters* **2006**, *97*.

Chapter IV

A Surface-enhanced Raman Scattering Study into the Coupling of Aryl Films Derived from Diazonium Salts to Gold Electrodes

4.1 Introduction

Since Pinson's initial discovery of the ability to graft aryl films to carbon surfaces by electrochemical reduction of diazonium salts,¹ a wide variety of surfaces have been modified.²⁻⁶ Aryl groups derived from diazonium salts have been grafted to Si, GaAs, Pd, as well as coinage and noble metals.^{2,4} These early experiments involved the electrochemical reduction of the diazonium salt, typically in a three electrode electrochemical cell. Since then diazonium salts have also demonstrated the tendency to spontaneously react with a surface.^{7,8} In-situ methods for immobilizing aryl films have been developed avoiding the need for purification steps of the diazonium salt precursor.⁹⁻¹¹ Thus giving another added ease of use and flexibility of this grafting procedure. This modification process has been exploited for a wide range of applications including molecular electronics¹²⁻¹⁵, protein immobilization^{1,16-19}, oligopeptide immobilization²⁰, and DNA detection.^{17,18}

The original attachment mechanism Pinson proposed is given in Figure 4.1 and is as follows;

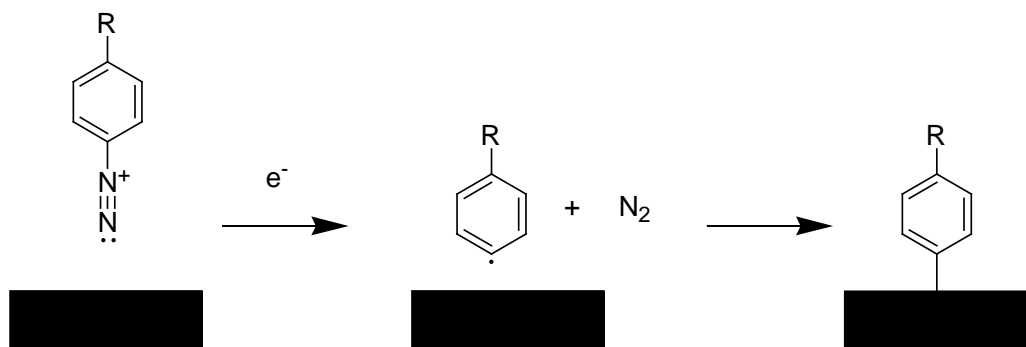


Figure 4.1 Proposed mechanism of attachment of aryl films derived from corresponding diazonium salts.

Upon electrochemical reduction of the aryl-diazonium, an aryl radical is formed. This then reacts with a surface forming an aryl modified surface.²¹ Shortly following this report it was found that the radical attachment process is so aggressive that it rarely ceases upon the formation of a monolayer. Rather successive aryl-radicals attach onto the aryl film thereby forming a much thicker layer than previously believed.²² The mechanism of multilayer growth is depicted in figure 4.2. Aryl radicals form and attach to a substrate as in Figure 4.1. This is followed by subsequent attachment of secondary aryl radicals, formed by the reduction process, propagating multilayer formation and growth.²²

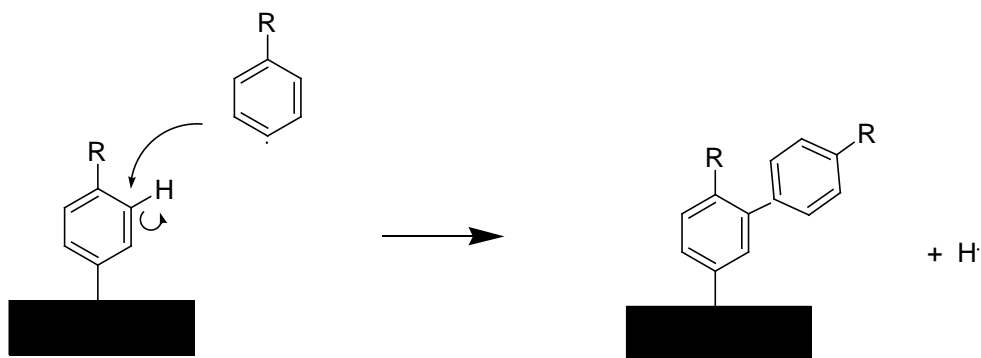


Figure 4.2 Proposed attachment mechanism for multilayer formation. The proton in the coupling reaction has been included for clarity.

Despite the wealth of investigations and device applications, the nature of attachment and subsequent multilayer growth of aryl films remains unclear. X-ray photoelectron spectroscopy (XPS) studies have indicated the presence of nitrogen within aryl layers that should contain no nitrogen.³ This observation has been attributed to a wide variety of sources, ranging from azide radicals forming in solution which may attach to the surface^{23,24}; to azo-coupling reactions²⁵; to reduction of nitro groups from the electron beam of the XPS,⁵ or quite simply contamination within the XPS vacuum chamber.⁵ The reason for this wide array of possible explanations for the appearance of nitrogen is that XPS is limited to observing the oxidation state of atoms, and inherently not chemical structure. Recently Pinson and coworkers addressed this issue by the use of time-of-flight secondary ion mass spectrometry (TOF SIMS).⁷ In this work, aryl films derived from diazonium salts were grafted to a carbon substrate. Interrogation of these

film using TOF SIMS found the presence of a -N=N- bound between phenyl groups.⁷

The present work is complementary to Pinson's findings, in which we investigate the existence of nitrogen within molecular layers electrodes using vibrational spectroscopy. Gold was chosen as the electrode for these investigations for its potential to provide surface enhancement in vibrational spectroscopy. Molecular layers grafted to gold have recently been characterized using infrared reflection adsorption spectroscopy.²⁶ However, the infrared signal for an azide stretch is weak, limiting characterization of this phenomenon to other vibrational spectroscopy tools. For this reason, we chose to characterize the existence of nitrogen functional groups within molecular layers using Raman spectroscopy and thereby providing the first vibrational spectroscopy evidence for azide coupling during multilayer growth.

Due to the intrinsically low signals involved in Raman spectroscopy we chose to graft the molecular layers to a gold electrode which possessed nanostructures that would provide surface enhancement. Recently glancing angle deposition (GLAD) films have demonstrated the ability of providing a local electromagnetic field enhancement required for Raman enhancement.^{27,28} In short, GLAD films are fabricated using metal deposition at which the flux of material bombards the substrate at large glancing angles. Figure 4.3 contains a cartoon depiction of the fabrication of GLAD films. Typically these angles are $>70^\circ$. Initially metal nucleation sites form on the substrate. Upon further deposition of metal these nucleation sites shadow the area opposite the metal flux, thereby only

the exposed nucleation sites receive the incoming metal, causing the nucleation sites to grow into pillars, further shadowing the area opposite the flux.

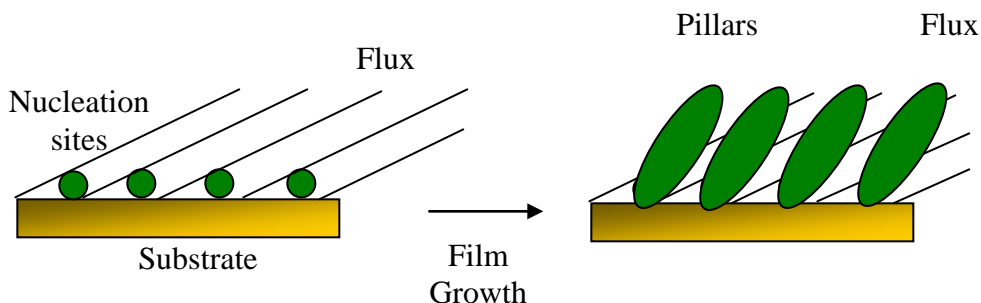


Figure 4.3 Cartoon depiction of the fabrication of GLAD films.

By controlling the angle of impinging flux and substrate rotation many different GLAD film morphologies can be fabricated for a wide range of applications.²⁹⁻³¹ To better understand how GLAD films provide Raman enhancement we must first have a fundamental understanding of Raman scattering.

The vast majority of light scattered undergoes elastic scattering where no energy transitions occur.³² The photons of the scattered beam have the same energy of those in the incident beam. This is known as Rayleigh scattering. However, roughly 1 in every 10^7 scattered photons undergo inelastic scattering.³² An energy transformation occurs and the scattered photons are of different energy than the incident photons. This is referred to as Raman scattering, named after the discoverer and Nobel laureate Sir Chandrasekhara Venkata Raman.^{33,34} The differences between these forms of scattering can be seen in the energy diagram given in figure 4.4.

The incident beam of photons excites a ground state molecule into an excited virtual state. In Rayleigh scattering the molecule relaxes into its initial ground state and no energy is lost or gained in the scattered photon. In Raman scattering, the molecule relaxes into a different vibrational ground state. This creates a change in energy of the scattered photon. If energy is lost it is referred to as a Stokes shift and if energy is gained it is called an anti-Stokes shift. These energy shifts are equal to the infrared absorption energies for the same vibrations. Although dependant on the same vibrational modes of a molecule, infrared absorption and Raman scattering are sensitive to different vibrational mechanisms. Infrared absorption requires a dipole change in the molecular bond, where Raman scattering is sensitive to changes in polarizability within a bond. Due to these differences, infrared absorption and Raman scattering are complementary techniques.

Due to the low occurrence of a Raman scattered photon, Raman signals are relatively weak. However, it was found that the intensity of Raman scattering could be increased with the use of metal structures and surfaces. It is generally accepted that this signal enhancement occurs by two mechanisms; 1) a chemical effect where the interaction with the metal enhances charge transfer thereby aiding the polarizability of a molecular bond and 2) an electromagnetic effect where the metal structure provides an increased local electromagnetic field thereby increasing the Raman intensity. This increase in Raman scattering intensity is known as surface-enhanced Raman scattering (SERS).

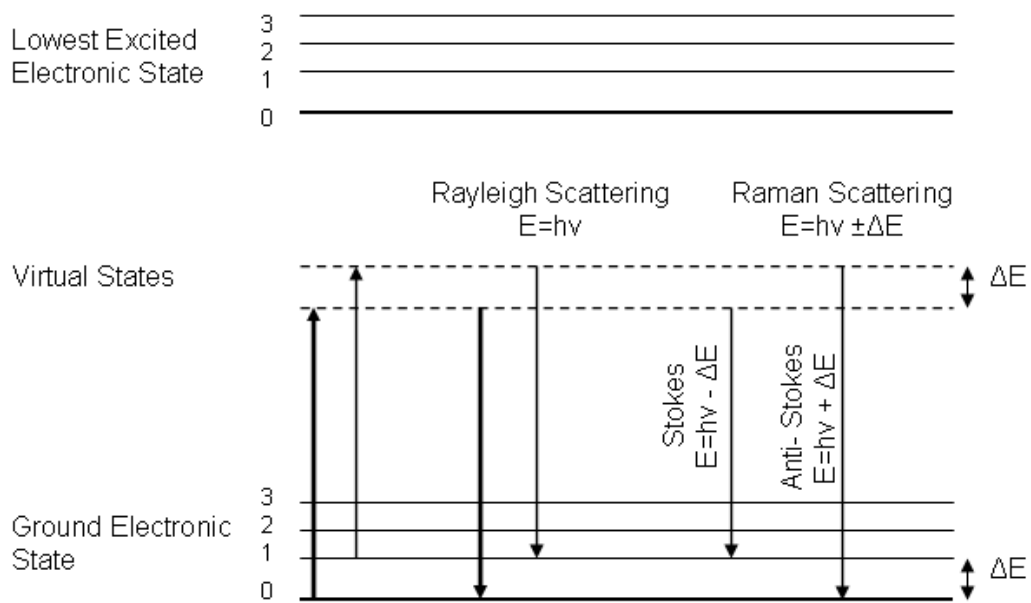


Figure 4.4 Rayleigh and Raman scattering energy diagram, adapted from reference³²

SERS was discovered in 1974 by McQuillan and coworkers.³⁵ They found that upon immobilization of pyridine onto a silver surface increased the Raman signal.³⁵ Later Van Duyne and coworkers found that upon roughening a silver electrode this Raman enhancement could be greatly increased.³⁶ Since then researchers have developed many different metal surfaces in pursuit of the ideal Raman enhancement.³⁷⁻⁴³ However due to the lack of control at the nanoscale of these metal structures this field has been plagued by irreproducibility in signal enhancement.

Recently GLAD films fabricated from electron beam evaporated silver have reported enhancement factors upwards of 10^6 .⁴⁴ It is speculated that GLAD films achieve this enhancement by providing nanometer scale metal structures that aid in enhancing the local electromagnetic fields. Initially trans-1,2-bis-4-pyridyl-ethane was used as a proof of principle Raman active reporter demonstrating that indeed Ag GLAD films provide surface enhancement.⁴⁵ These films also provided a sample to sample reproducibility of 15%, which is lower than using roughened metal surfaces or metal nanoparticles as SERS substrates.⁴⁵ The use of Ag GLAD films has now been extended to the detection of viruses and bacteria, discriminating between the different types and strains of pathogens, as well as discrimination between mRNA patterns.^{27,44,46-48} In the current chapter gold GLAD films are explored as electrodes for the electrochemical deposition of aryl films derived from corresponding diazonium salts. The SERS spectra of diazonium salt derived layers were analyzed for the presence of an azide stretch,

providing insight into the existence of nitrogen moieties within these molecular layers.

4.2 Experimental

Glancing Angle Deposition Film Fabrication

Preparation of gold GLAD films began by first immersing 1cm x 1cm Si wafers into freshly prepared piranha. Piranha was prepared by mixing 1 part 30% hydrogen peroxide (EMD, ACS certified) with 3 parts concentrated sulfuric acid (EMD, ACS certified). *Care should be taken during piranha use due to its violent exothermal nature.* Following piranha cleaning the Si wafers were rinsed with copious amounts of 0.2 μ m filtered 18M Ω -cm water (Barnstead-Thermolyne, Nanopure water filtration unit) followed by drying via an argon stream. A \approx 5nm Chromium layer was initially deposited on the polished side of the Si wafer followed by a \approx 5nm Gold layer. The sample stage was then tilted until an angle of 86 degrees was achieved, between the source and sample normal. Evaporation of gold continued until a 360-370 nm layer was formed. The base pressure of the vacuum chamber was 2.5×10^{-7} Torr prior to evaporation and deposition pressure was $\approx 5 \times 10^{-6}$ Torr with a deposition rate of 5 A/sec. Fabrication of the gold GLAD films was conducted by Douglas Gish of the Michael Brett research group.

Surface Modification

Prior to surface modification of the GLAD films, possible contaminants were removed by a gentle rinsing in 2-propanol (Sigma Aldrich) (0.2 μ m filtered within activated carbon), and then 0.2 μ m filtered 18M Ω ·cm water, followed by drying with a gentle stream of argon. 4-benzoic acid, nitroazobenzene and nitrobenzene diazonium salts were prepared by the Starkey method⁴⁹ in which the amine precursors (Sigma Aldrich) were reacted with 1mM solution sodium nitrite (Sigma Aldrich) in tetrafluoroboric acid (Sigma Aldrich). The resulting diazonium salts were then recrystallized and stored in the dark at 2°C until use.

Aryl films, derived from corresponding diazonium salts, were grafted to gold electrodes by ramping the voltage bias between the surface and a Ag/Ag⁺ reference electrode at a rate of 100mV/s in the presence of a 5mM solution of aryl-diazonium salt / 0.1M tetrabutylammonium tetrafluoroborate electrolyte (Sigma Aldrich). This process was controlled by a (Pine) potentiostat and employed a platinum mesh as a counter electrode.

The reduction of diazonium salts at fixed potentials occurred by the rapid injection of benzoic acid diazonium salt into the electrochemical cell containing a solution of tetrabutylammonium tetrafluoroborate electrolyte in acetonitrile while holding the potential between the GLAD film and counter electrode at a fixed voltage for 10 minutes. The final solution concentrations were 5mM solution of 4-benzoic acid diazonium salt / 0.1M tetrabutylammonium tetrafluoroborate electrolyte. All solutions were prepared in acetonitrile and purged for 20 minutes with Argon prior to use in an attempt to reduce the presence of oxygen.

Thiol modified surfaces were prepared by immersing a clean GLAD film in a 1mM solution of 4-mercaptobenzoic acid in ethanol for 4 hours followed by a gentle rinsing with ethanol and dried with a stream of argon. Upon modification with diazonium salts, the gold GLAD films were gently rinsed with 0.2 μ m filtered 18M Ω ·cm water and dried under an argon flow.

Characterization of Au GLAD films

Morphological top down and cross-sectional scanning electron micrographs of the gold GLAD films were collected by a Hitachi HF 3300 SEM. Raman spectra of freshly prepared GLAD film surface modification were collected using a Renishaw inVia Raman microscope equipped with an inverted microscope. Spectra were obtained using a 785nm laser and a 20 times magnification objective. Each sample was exposed to 5% of a 30-mW 785nm laser light while the spectra were being collected from 100-3200 cm⁻¹ at 1-second exposures. Band intensities showed no appreciable decrease upon repeated spectra collection. X-ray photoelectron spectroscopy was obtained using an Axis 165 X-ray Photoelectron Spectrometer (Kratos Analytical). All spectra were collected at room temperature and the pressure was always below 10⁻⁹ torr. The survey spectra were collected between 100eV and 1000eV with a resolution of 2eV. High-resolution spectra were collected for the gold and nitrogen regions of the spectra at a resolution of 0.1eV.

4.3 Results and Discussion

Glancing Angle Deposition Films Fabrication

Recently, silver GLAD films have been shown to enhance the Raman signal of an analyte by a factor of 10^6 .⁴⁴ Using similar methodology, gold GLAD films were used as electrodes to study the grafting of aryl cations. The formation and growth of GLAD films has been well documented elsewhere.²⁹⁻³¹ Figure 4.5 shows scanning electron micrographs of a typical gold GLAD film used in this study. Figure 4.5a depicts the top profile of the substrate showing the highly dense, pillared morphology of the GLAD films. The cross section of the cleaved GLAD film, Figure 4.5b, demonstrates that the pillars are tilted and a thickness of approximately 360 nm. It can also be noted that the thickness is relatively uniform. It is suggested that this dense packing of nano-structures could produce a significant increase in Raman intensity.⁴⁴

Preliminary Study of AU GLAD films for SERS

To assess the SERS activity of these Au GLAD films, initial studies were conducted using nitrobenzene thiol (NB-thiol). Thiols are known to form densely packed monolayers on Au and the nitrobenzene group exhibits a large Raman cross section.^{12,50-52} NB-thiol was immobilized onto the AU GLAD film and Raman spectra recorded. Figure 4.6 contains the Raman spectra of NB-thiol of planar evaporated gold and Au GLAD films. From the increase in Raman

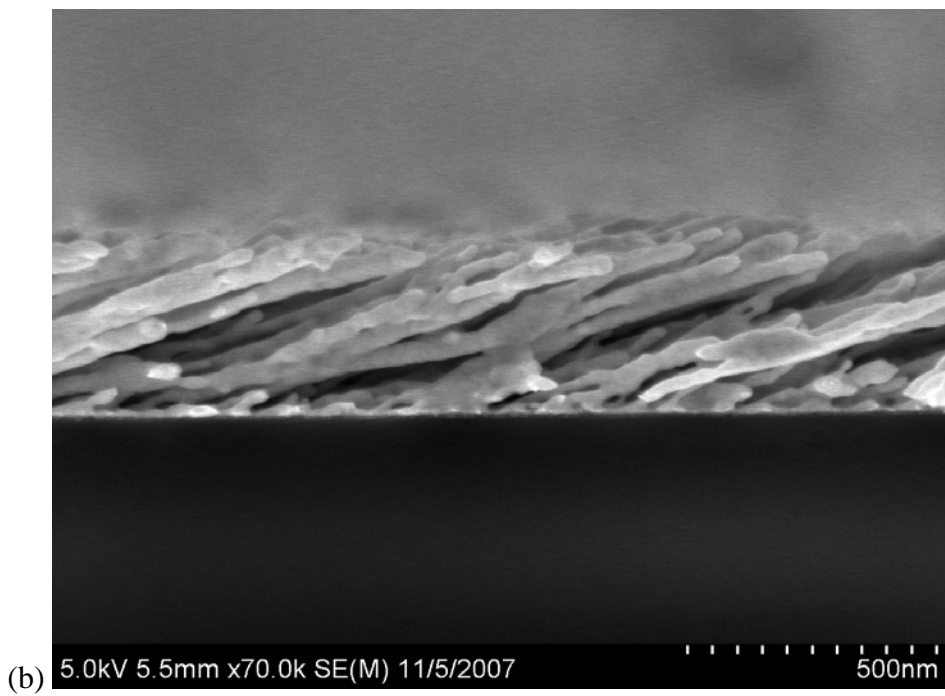
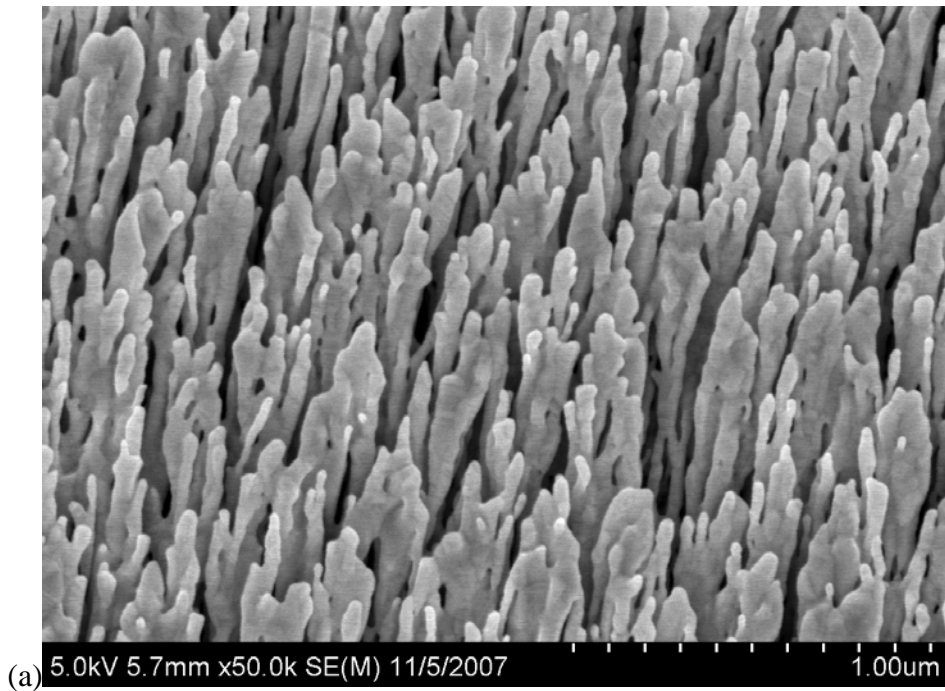


Figure 4.5 Scanning electron micrographs of gold GLAD films demonstrating surface morphology (a) and side profile (b) of gold pillars.

intensity observed in the spectra collected on the Au GLAD film it is apparent that the metallic structures provide surface enhancement.

To assess the applicability of Au GLAD films to be used as reproducible SERS substrates, three hundred Raman spectra were collected over the surface area of the sample substrate modified with NB-thiol. The influence of sample-to-sample variability was investigated by collecting Raman spectra from five separate sample substrates. Figure 4.7a contains an overlay of three hundred Raman spectra collected on a single sample and Figure 4.7b contains Raman spectra collected from five separate sample substrates.

The intensity of the symmetric nitro-stretch at 1350 cm^{-1} was used as a diagnostic for Raman signal reproducibility and surface enhancement of the Au-GLAD films. The reproducibility of the Raman signal intensity within a single sample was determined to be 5% *rsd*, and the sample-to-sample variability was determined to be 7% *rsd*. These values are lower than the 15% values reported of GLAD films being used as SERS substrates in literature.^{44,45} The enhancement factor of the Au-GLAD film was determined to be 3×10^5 , which is slightly lower than those previously reported.^{44,45} This observation is likely attributed to the use of gold as the metal nanostructure surface, rather than silver. Gold substrates commonly provide lower enhancement than their silver counterparts.⁵³⁻⁵⁵

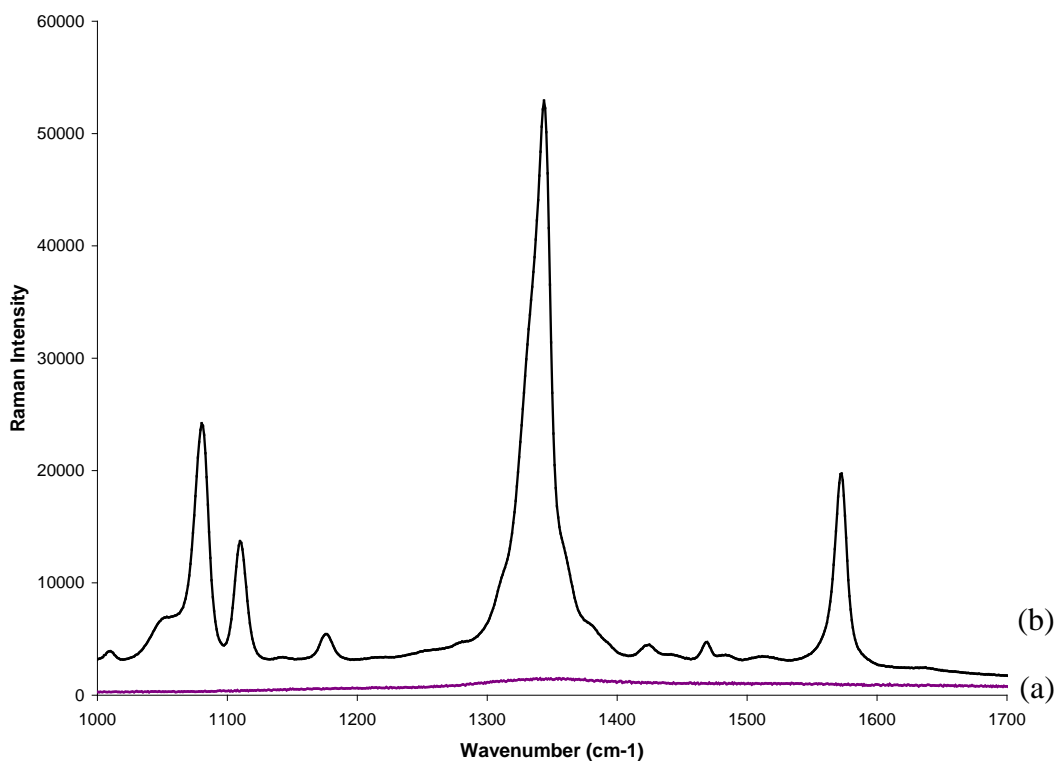


Figure 4.6 Raman spectra of NB-thiol collected on planar evaporated gold (a) and Au GLAD film (b)

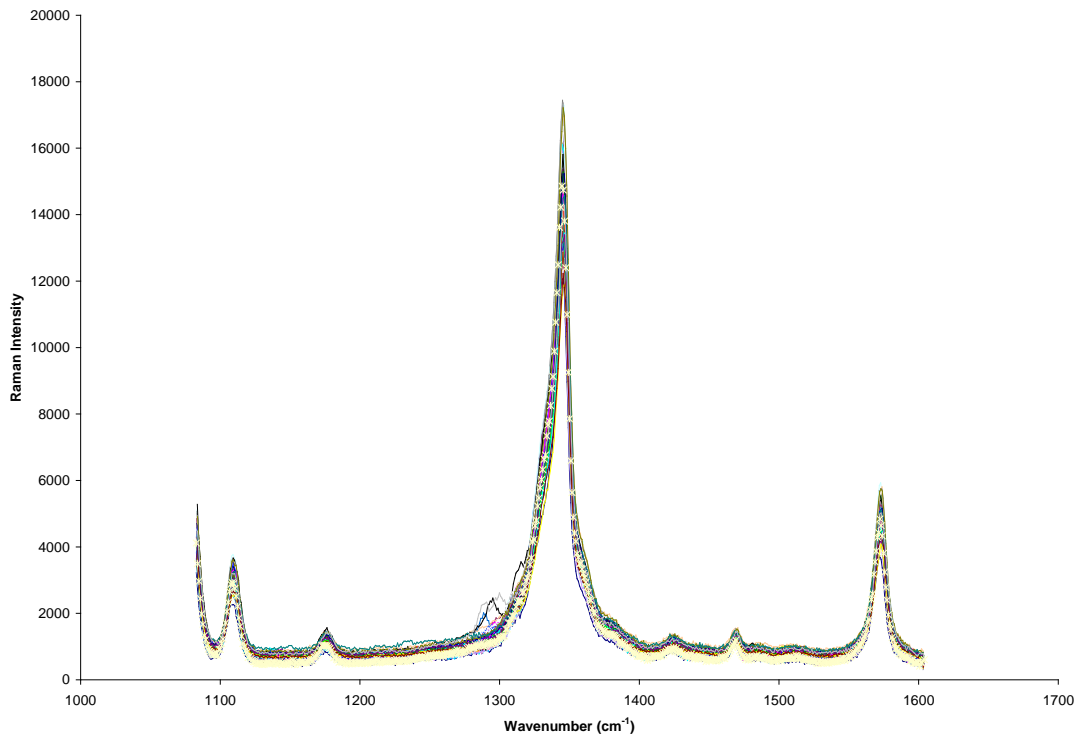


Figure 4.7a Overlay of three hundred Raman spectra collected on a single sample

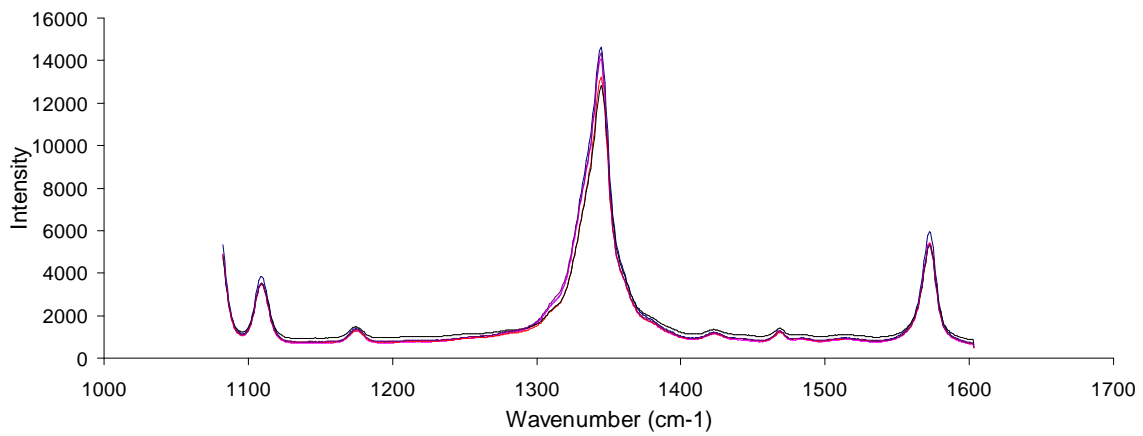


Figure 4.7b Raman spectra collected from five separate sample substrates.

Existence of Nitrogen Species within Diazonium salt derived Aryl Films

X-ray Photoelectron Spectroscopy Characterization

X-ray photoelectron spectroscopy (XPS) was used to assess surface modification of the gold electrodes. The high-resolution spectra of this Au4f region presented in Figure 4.8 reveals that the aryl films diminish the intensity of the Au4f peaks. It has been noted elsewhere that this decrease in Au4f7/2 XPS signal is due to the shielding of the underlying gold by the molecular layer.^{56,57} Upon closer examination it is revealed that the peaks are not diminished equally for each species. The least suppressed peaks correspond to the thio-derivatized aryl layers attaching to the gold. It should be noted that the shielding effect is most prevalent in the spectra of the nitroazobenzene-modified surface. This trend may be due to the heightened tendency of diazonium salt derived layers to form multilayers, which has been previously well documented.¹²

Upon surface modification, peaks appear in the N 1s region, which further indicates modification has occurred. Figure 4.9 contains the high-resolution spectra of the N1s region before and after surface modification. The energy peak at 400 eV has been attributed to a reduced nitrogen species, possibly an azo or amine.^{58,59} The 406eV peak commonly attributed to nitro linkages.^{58,59} As expected each of these peaks can easily be seen for the nitroazobenzene layer and a peak at 406eV can be seen in the spectra for the nitrobenzene modified gold.

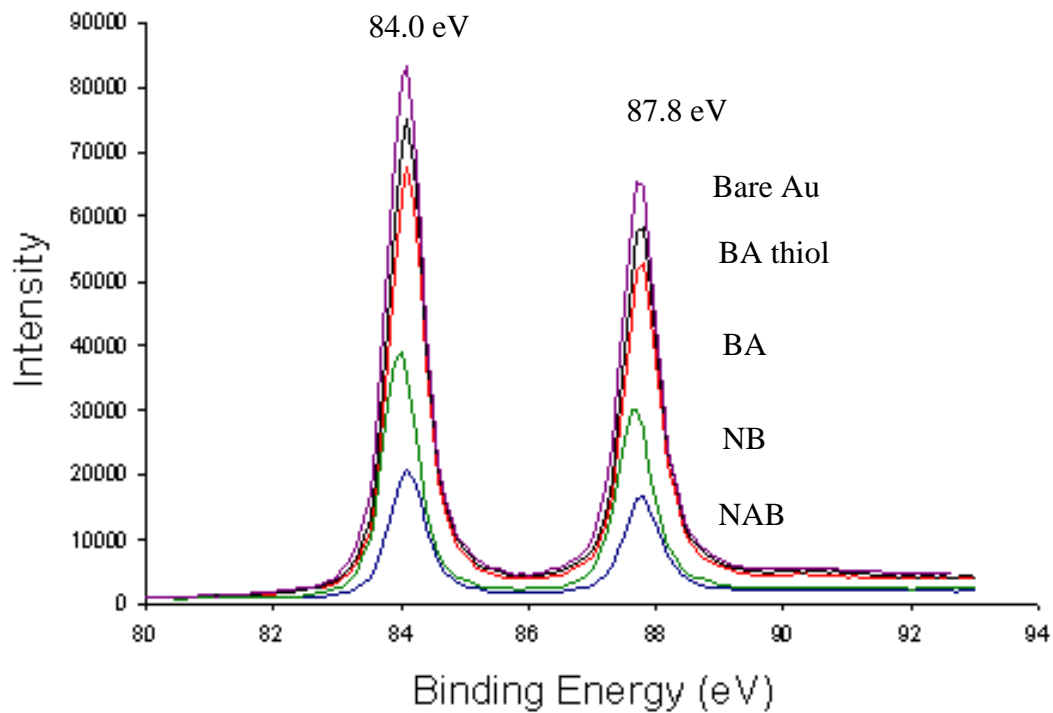


Figure 4.8 XPS high-resolution spectra of Au4f region of nitroazobenzene, nitrobenzene, nitrobenzene thiol, 4-benzoic acid and 4-mercaptobenzoic acid immobilized onto gold GLAD film electrodes.

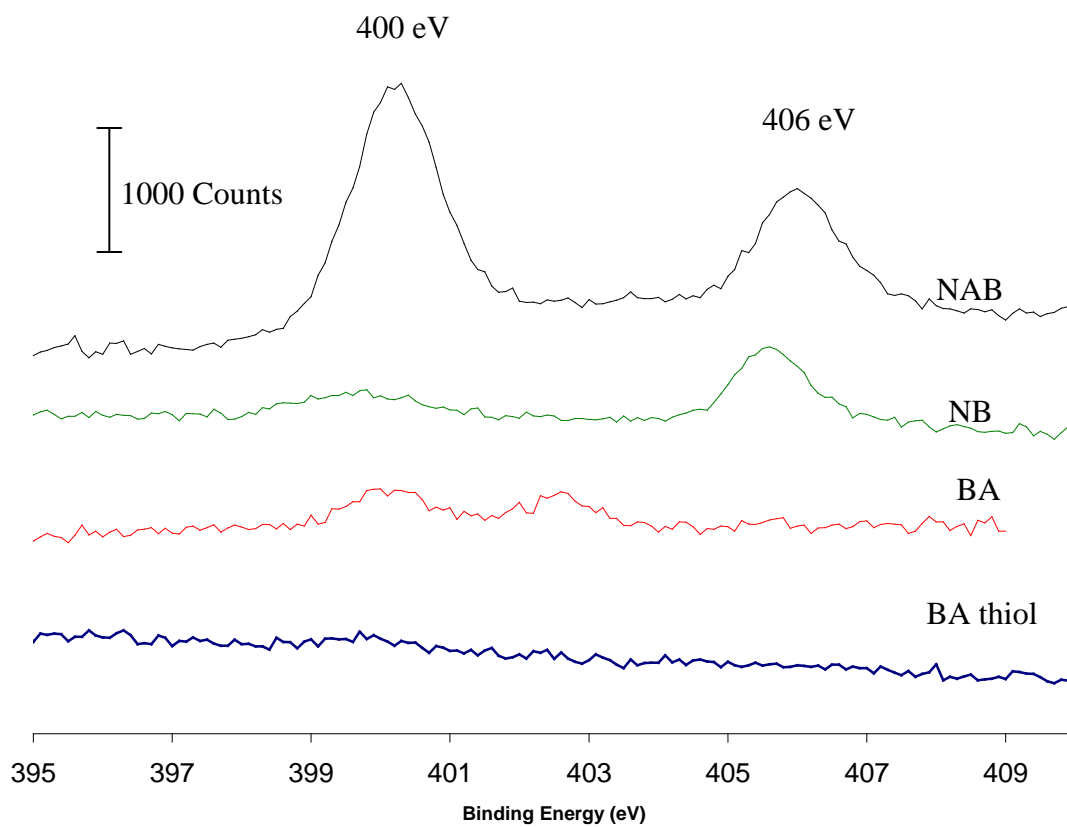


Figure 4.9 XPS high-resolution spectra of N1s region of nitroazobenzene, nitrobenzene, nitrobenzene thiol, 4-benzoic acid and 4-mercaptobenzoic acid immobilized onto gold GLAD film electrodes.

The XPS spectrum of the N 1s region of the benzoic acid layer also contains two small peaks at 402 eV and 400 eV. Each of these peaks is consistent with the presence of a reduced nitrogen species within the BA molecular layer.³ This observation is consistent with previous results. However, the source of this phenomenon remains unclear and has been proposed to be caused from a variety of sources; the formation of azide-radicals within solution,^{23,24} or azo coupling reactions, or a reduction of nitro functional groups upon exposure to the electron beam, or quite simply caused by contamination.⁵

To further probe for the existence of azo linkages we chose to investigate the structure of diazonium salt derived layers using vibrational spectroscopy. Figure 4.10 contains an infrared reflection adsorption spectroscopy (IRRAS) spectrum of an NAB aryl film on a planar gold electrode. The vibrational energy where one would expect an azo (N=N) stretch is at 1450 cm^{-1} . Due to the weak infrared signature of the azo stretch, this band is not easily observed using IRRAS; we therefore choose to study this phenomenon using SERS.

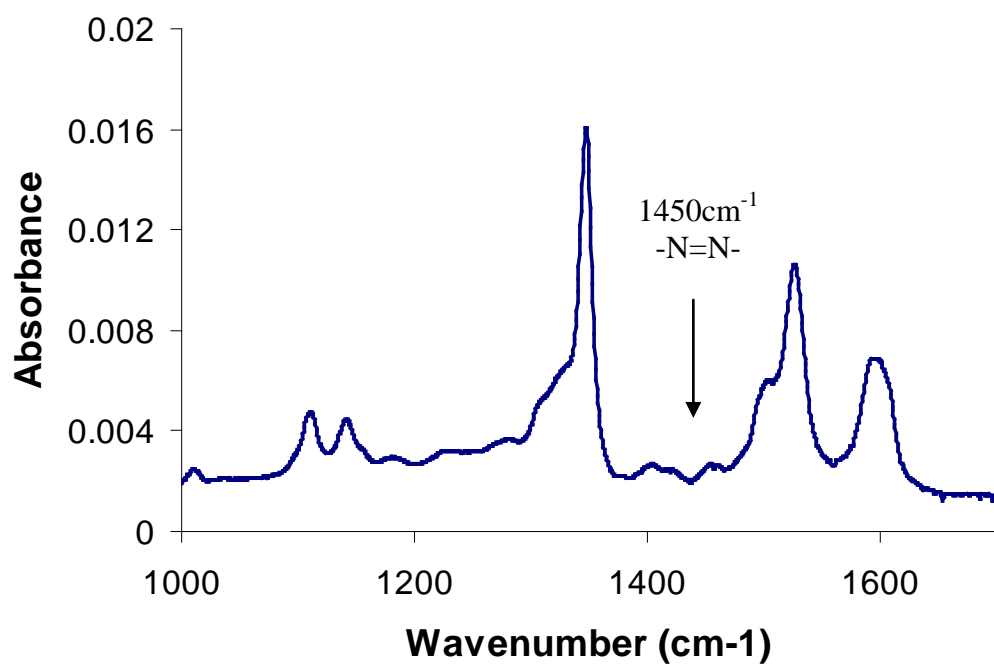


Figure 4.10 Infrared reflection adsorption spectroscopy (IRRAS) spectrum of an NAB on planar gold substrate.

Characterization of Aryl Films by SERS

The high reproducibility observed for the GLAD films provides a reliable platform for SERS structural characterization of diazonium salt derived aryl films. Figure 4.11 contains the Raman spectrum of electrochemically deposited NAB on a Au GLAD film and on a planar Au substrate. Raman bands characteristic of NAB are clearly observed in the spectrum from the GLAD film, while no bands were observed on the planar Au under the spectroscopic conditions employed here. This is due to the SERS effect provided by the GLAD films. The observed bands can be assigned based on previous Raman explorations of NAB films and these assignments are listed in Table 4.1. Of particular note are the bands at 1445 cm^{-1} and 1138 cm^{-1} which are assigned to the N=N stretch and the phenyl-NN stretch, respectively.

Figure 4.12 contains Raman spectra of diazonium salt derived NB (Figure 4.12a) and BA (Figure 4.12b) on GLAD films. The spectra of the analogous thiol monolayers are also presented for comparison. The major striking feature in Figure 4.16 is the much greater intensities observed for the thiol monolayers. The reason for the higher observed intensities for the thiol monolayers relative to the diazonium salt derived layers is currently unknown. Possible explanations include a higher packing density near the GLAD films surface for the thiolate monolayers and different interactions involved in the binding of each film to the surface. Further investigations are needed to explore this observation.

Band assignments for the diazonium salt derived NB and BA films are given in Tables 4.2 and 4.3. Apparent in both spectra are bands assigned to the

azo N=N stretch and the phenyl-NN stretch. These bands are especially unexpected in the spectrum for BA, as that aryl group contains no nitrogen species. This observation correlates with the XPS results discussed above that indicate the presence of nitrogen containing species in the BA film. Note that the IRRAS spectra from all diazonium films do not exhibit a band at 2300cm^{-1} that would be diagnostic of unreacted diazonium moiety. We attribute the bands in the SERS for BA at 1445cm^{-1} and 1134cm^{-1} to be due to azide functionalities in the film structure. Further exploration of this is presented below.

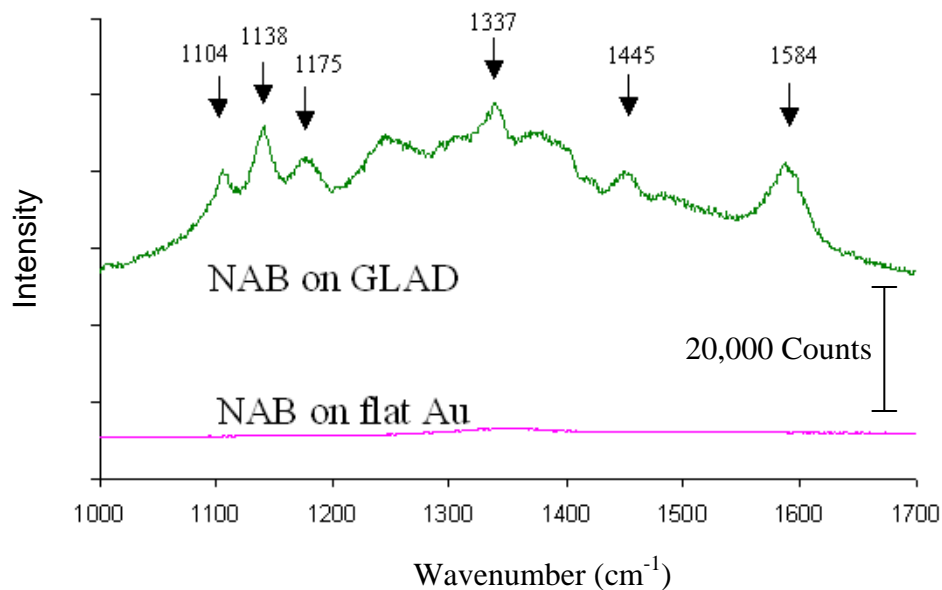


Figure 4.11 Raman spectra of nitroazobenzene grafted to gold GLAD film electrodes and planar evaporated gold electrode. Spectra offset for clarity.

Assignment	Band (cm ⁻¹)
C=C ring stretch	1584
N=N stretch	1445
NO ₂ stretch	1337
CH bend	1175
Phenyl-NN stretch	1138
Phenyl- NO ₂ stretch	1104

Table 4.1 Raman band assignments for nitroazobenzene molecular layer grafted to a gold GLAD film.

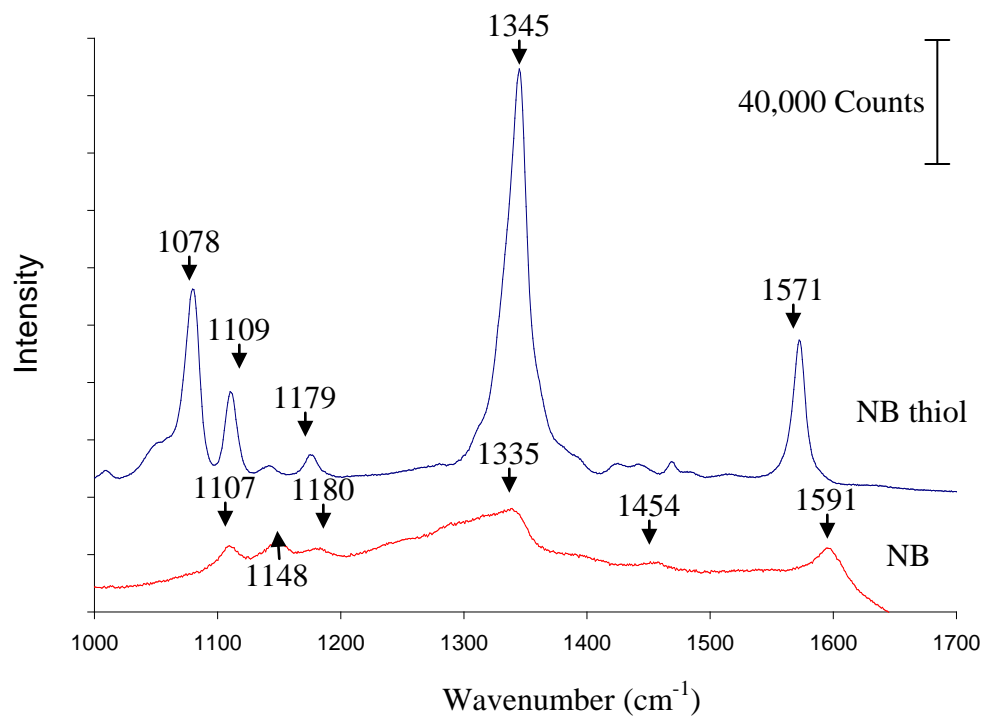


Figure 4.12a Raman spectra of nitrobenzene and nitrobenzene thiol grafted to gold GLAD film electrodes. Spectra offset for clarity.

Molecule	Assignment	Band (cm ⁻¹)
Nitrobenzene	C=C ring stretch	1591
	N=N stretch	1454
	NO ₂ stretch	1345
	CH bend	1180
	Phenyl-NN stretch	1148
	Phenyl- NO ₂ stretch	1107
Nitrobenzene thiol	C=C ring stretch	1571
	NO ₂ stretch	1345
	CH bend	1179
	Phenyl- NO ₂ stretch	1109
	CS stretch	1078

Table 4.2 Raman band assignments for nitrobenzene, NB, and nitrobenzene thiol, NB thiol, grafted to a gold GLAD film.

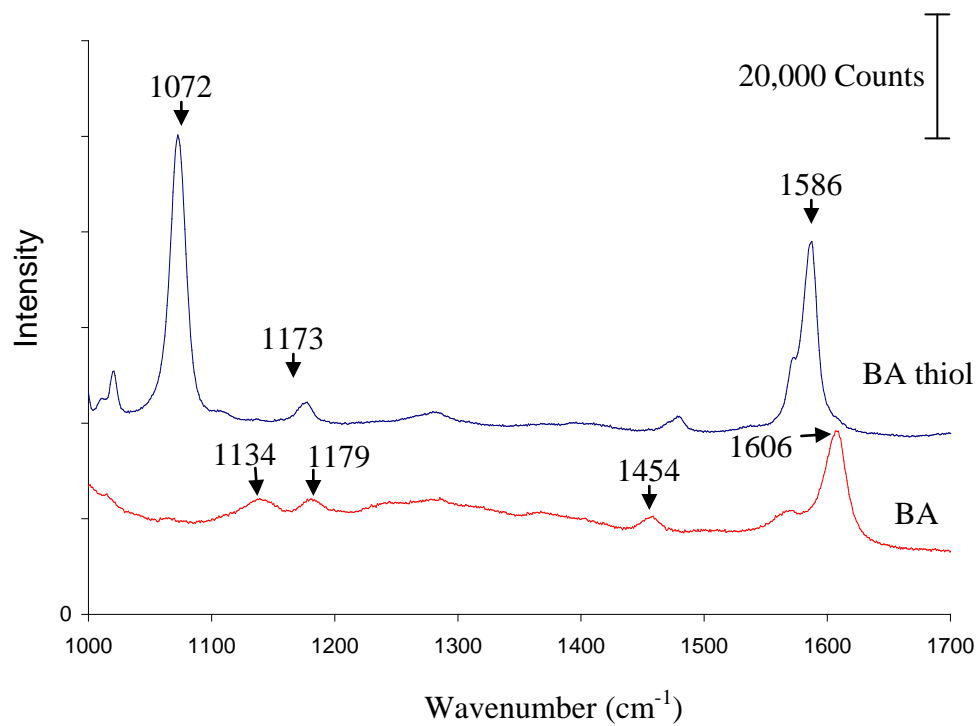


Figure 4.12b Raman spectra of 4-benzoic acid, BA, and 4-mercaptobenzoic acid thiol, BA thiol, grafted to gold GLAD film electrodes. Spectra offset for clarity.

Molecule	Assignment	Band (cm ⁻¹)
Benzoic Acid	C=C ring stretch	1606
	N=N stretch	1454
	CH bend	1179
	Phenyl-NN stretch	1134
Benzoic Acid thiol	C=C ring stretch	1586
	CH bend	1179
	CS stretch	1072

Table 4.2 Raman band assignments for 4-benzoic acid, BA, and 4-mercaptobenzoic acid thiol, BA thiol, grafted to a gold GLAD film.

Potential Step Deposition of BA Films Derived from Diazonium Salts

To further investigate and understand the formation of the azide-moiety, benzoic acid aryl films were grafted onto gold GLAD films under a constant applied voltage, ranging from 0 mV to -1000 mV with respect to a Ag/Ag⁺ reference electrode. Benzoic acid was chosen due to its lack of nitrogen containing functional groups, as well as for its potential for molecular biology immobilization applications being explored in our group. Figure 4.13 contains high-resolution XPS spectra of the N1s region of the BA modified substrates deposited at various potentials.

Two small peaks at 400 eV and 402 eV are observed for the benzoic acid modified gold. For more negative deposition potentials the peak at 400 eV grows, indicating an increase in the surface density of the azide moiety. Also interestingly, Figure 4.14 reveals that as more negative biases are used during the deposition process, a decrease is observed for the Au4f peaks.

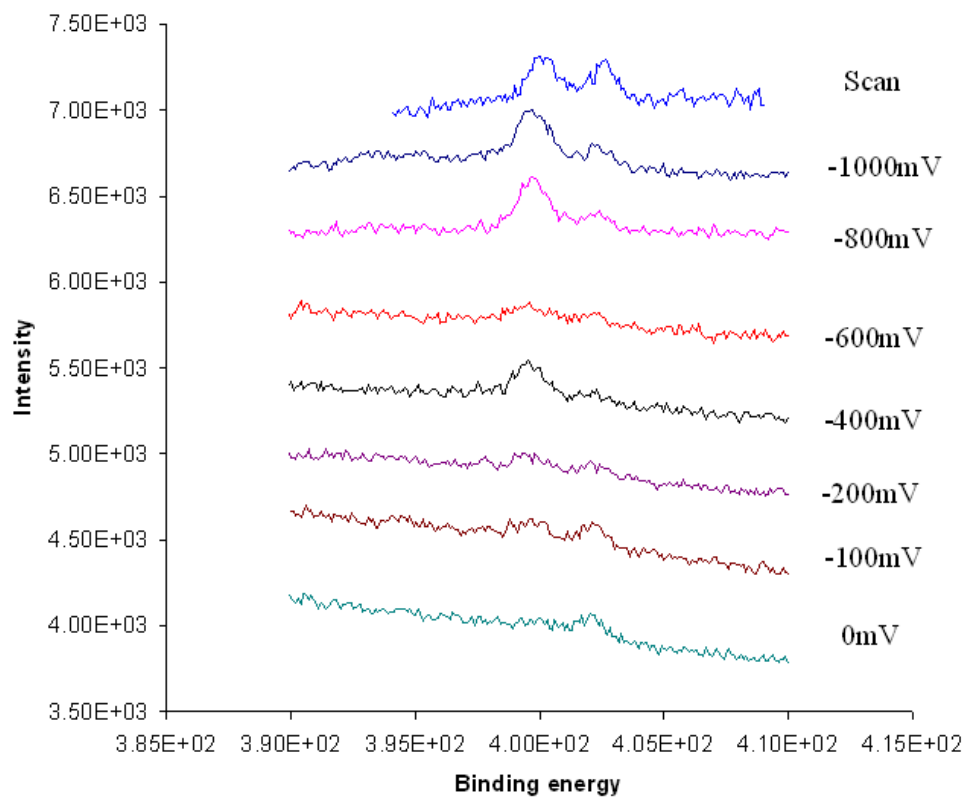


Figure 4.13 XPS spectra of electrolysis deposition of 4-benzoic acid modified gold GLAD film at various voltage depositions -10mV, -100mV, -200mV, -500mV and -1000mV. Spectra offset for clarity.

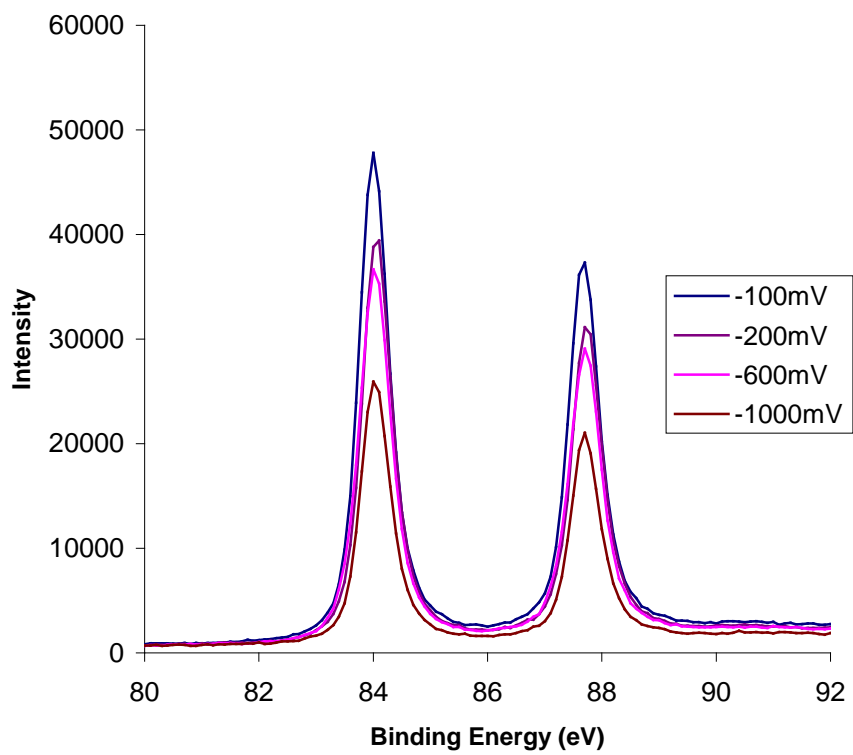


Figure 4.14 XPS high-resolution spectra of Au4f region of electrolysis deposition of 4-benzoic acid modified gold GLAD film at various voltage depositions -100mV, -200mV, -600mV and -1000mV

The increase in Au4f signal shielding suggests that under increasingly negative deposition conditions, multilayer formation is promoted, which also correlates with an increase of the density of the azide moiety. An estimation of the surface coverage, based upon the attenuation of the Au4f peaks^{5,60,61}, finds that for depositions that have little to no azide functionality present, monolayer or submonolayer coverage is achieved. As the deposition conditions use increasingly negative potentials the molecular layer becomes thicker, as well as containing a higher occurrence of azo coupling.

SERS spectra of BA films on gold GLAD films were collected and are shown in Figure 4.15. An increase in the intensity of the bands at 1454 cm^{-1} and 1134 cm^{-1} with deposition potential is observed. A plot of the 1450 cm^{-1} peak height versus deposition potential is provided for clarity in Figure 4.16. Recall that these Raman bands are diagnostic of azo groups in the film. Thus, at potential biases below -100 mV , essentially no azide functionalities are detected. Upon further negative biases the density of the azide functionality increases, which is consistent with the XPS data. This suggests that the occurrence of the azide functionality and resultant structure of the layer is strongly dependent upon the applied biases that the diazonium is exposed to.

The growth of the aromatic ring-breathing peak at 1600 cm^{-1} suggests that more material is deposited as the potential biases are more negative. This observation is in agreement with the previous XPS results.

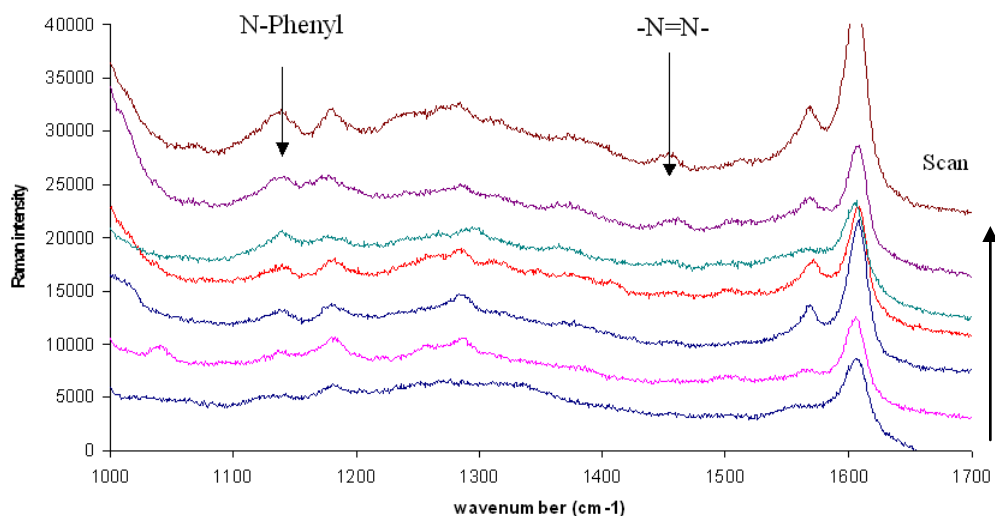


Figure 4.15 SERS spectra of electrolysis deposition of 4-benzoic acid modified gold GLAD film at various voltage depositions. Arrow indicates increasingly negative potential starting at 0V and decreasing in -200mV steps. Spectra offset for clarity.

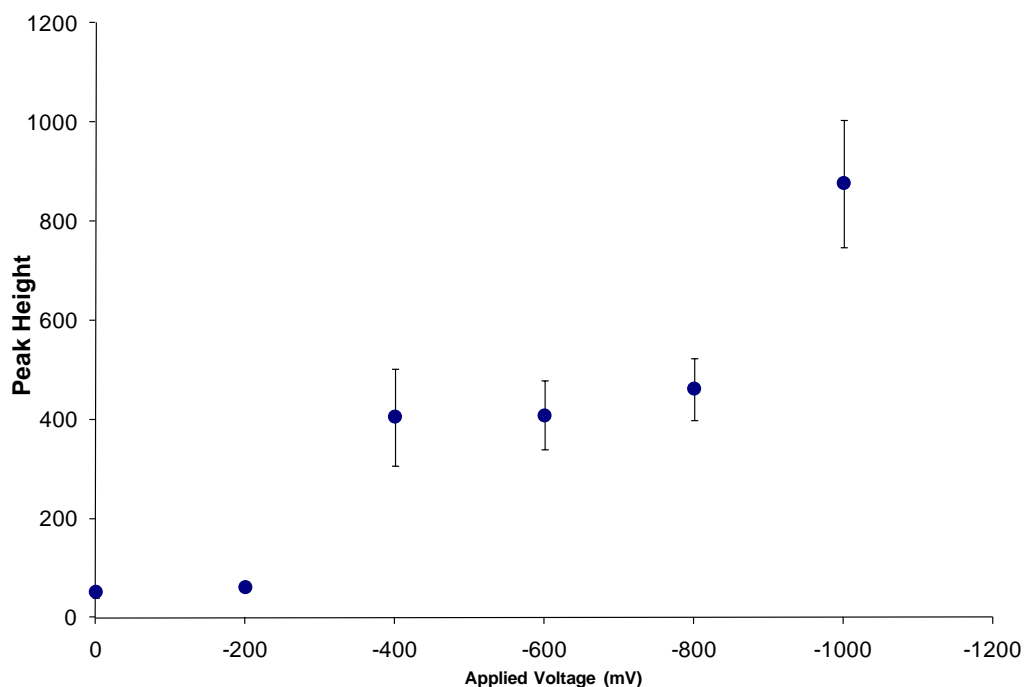


Figure 4.16 A plot of the 1450cm^{-1} peak height versus deposition potentials results, indicating multi-layer formation under highly negative biases.

The XPS and SERS results presented above suggest that the density of azo groups in the film increase as the film grows thicker. Belanger and coworkers proposed that aryl-azide radicals form during electrochemical deposition.^{23,24} However, an aryl-azide radical would tend to decompose forming the aryl-radical and dinitrogen. We believe that the appearance of the azo functionality is due to a coupling reaction involving the diazonium group. This coupling reaction would follow a typical electrophilic aromatic substitution mechanism, presented in Figure 4.17 and form a highly branched, non-uniform molecular layer similar to that presented in Figure 4.18.⁶²

Due to the large degree of electronic coupling between the electrode substrate and diazonium salt derived aryl film, electrons from the substrate can be injected into the molecular layer. These delocalized electrons would create a negative charge at the surface that may preferentially attract the positively charged species of the diazonium cation. The diazonium cation would be attracted into proximity to further react the modified surface creating multilayered structures. Further negative deposition potentials would attract more diazonium cations, thereby increasing the number of electrophilic aromatic substitution reactions. This phenomenon may increase the density of azo groups within the molecular layer, as the film grows under increasingly negative deposition conditions.

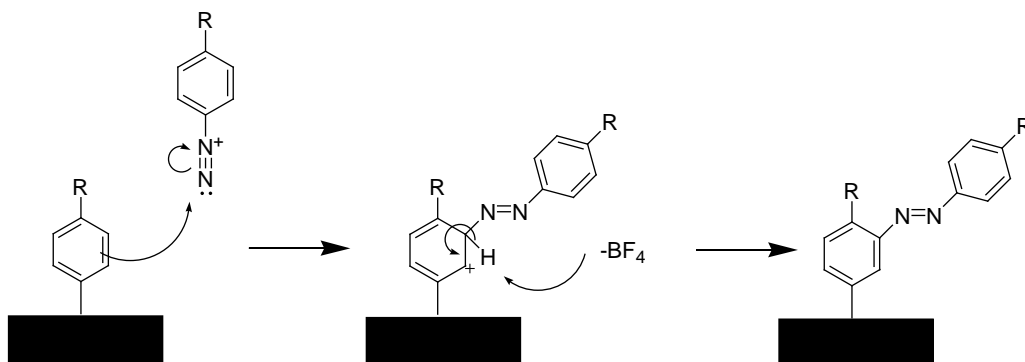


Figure 4.17 Proposed mechanism for multilayer formation involving azo coupling.

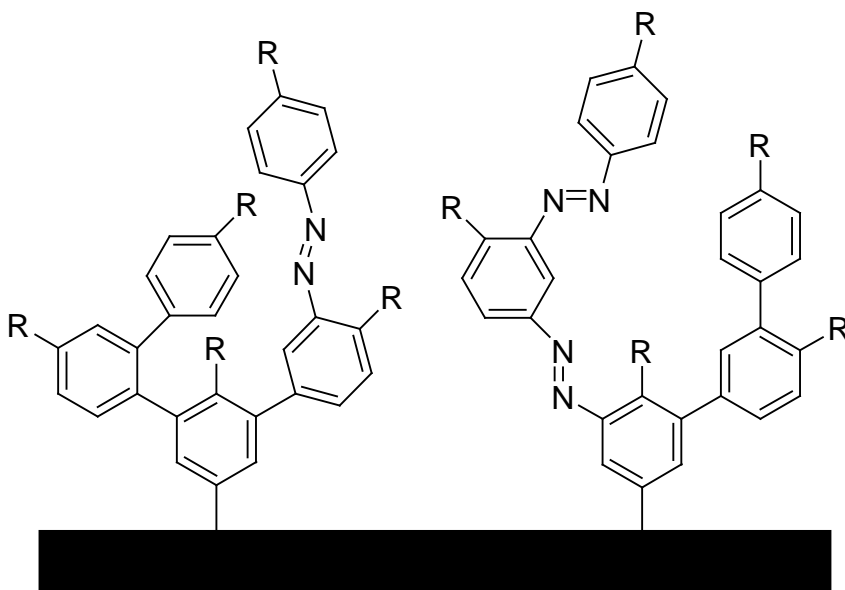


Figure 4.18 Illustration depicting non-uniform multilayer structure of molecular layer.

4.4 Conclusions

Gold GLAD films were used as SERS substrates supporting grafted aryl films derived from diazonium salts. The attachment chemistry of these aryl films were monitored by XPS and Raman spectra. The spectra indicate the presence of an azide functionality, and our results on benzoic acid derived films suggest that under low deposition bias conditions the density of the azide moiety can be minimized. Upon increasingly negative biases the occurrence of the azide moiety increases. This suggests that under gentle deposition conditions the aryl films are much more homogeneous with respect to attachment functionalities and multi-layer formation, both of which are of utmost importance concerning molecular electronic and molecular biology applications.

References

- (1) Bourdillon, C.; Delamar, M.; Demaille, C.; Hitmi, R.; Moiroux, J.; Pinson, J. *Journal of Electroanalytical Chemistry* **1992**, *336*, 113-123.
- (2) Stewart, M. P.; Tour, J. M.; Kosynkin, D. V.; Allara, D. L.; Dirk, S. M.; Maya, F. M. *Abstracts of Papers of the American Chemical Society* **2003**, *225*, U7-U7.
- (3) Laforgue, A.; Addou, T.; Belanger, D. *Langmuir* **2005**, *21*, 6855-6865.
- (4) Bernard, M. C.; Chausse, A.; Cabet-Deliry, E.; Chehimi, M. M.; Pinson, J.; Podvorica, F.; Vautrin-UI, C. *Chemistry of Materials* **2003**, *15*, 3450-3462.
- (5) deVilleneuve, C. H.; Pinson, J.; Bernard, M. C.; Allongue, P. *Journal of Physical Chemistry B* **1997**, *101*, 2415-2420.
- (6) Chausse, A.; Chehimi, M. M.; Karsi, N.; Pinson, J.; Podvorica, F.; Vautrin-UI, C. *Chemistry of Materials* **2002**, *14*, 392-400.
- (7) Combellas, C.; Kanoufi, F.; Pinson, J.; Podvorica, F. I. *Langmuir* **2005**, *21*, 280-286.
- (8) Adenier, A.; Barre, N.; Cabet-Deliry, E.; Chausse, A.; Griveau, S.; Mercier, F.; Pinson, J.; Vautrin-UI, C. *Surface Science* **2006**, *600*, 4801-4812.
- (9) Baranton, S.; Belanger, D. *Journal of Physical Chemistry B* **2005**, *109*, 24401-24410.

- (10) Baranton, S.; Lyskawa, J.; Belanger, D. *Abstracts of Papers of the American Chemical Society* **2006**, 231.
- (11) Lyskawa, J.; Belanger, D. *Chemistry of Materials* **2006**, 18, 4755-4763.
- (12) Anariba, F.; Viswanathan, U.; Bocian, D. F.; McCreery, R. L. *Analytical Chemistry* **2006**, 78, 3104-3112.
- (13) Nowak, A. M.; McCreery, R. L. *Analytical Chemistry* **2004**, 76, 1089-1097.
- (14) Bergren, A. J.; Harris, K. D.; Deng, F. J.; McCreery, R. L. *Journal of Physics-Condensed Matter* **2008**, 20.
- (15) Wang, W.; Lee, T.; Kamdar, M.; Reed, M. A.; Stewart, M. P.; Hwang, J. J.; Tour, J. M. In *Molecular Electronics Iii*; New York Acad Sciences: New York, 2003; Vol. 1006, p 36-47.
- (16) Polsky, R.; Harper, J. C.; Dirk, S. M.; Arango, D. C.; Wheeler, D. R.; Brozik, S. M. *Langmuir* **2007**, 23, 364-366.
- (17) Polsky, R.; Harper, J. C.; Wheeler, D. R.; Dirk, S. M.; Arango, D. C.; Brozik, S. M. *Biosensors & Bioelectronics* **2008**, 23, 757-764.
- (18) Polsky, R.; Harper, J. C.; Wheeler, D. R.; Brozik, S. M. *Electroanalysis* **2008**, 20, 671-679.
- (19) Harper, J. C.; Polsky, R.; Wheeler, D. R.; Dirk, S. M.; Brozik, S. M. *Langmuir* **2007**, 23, 8285-8287.
- (20) Liu, G. Z.; Bocking, T.; Gooding, J. J. *Journal of Electroanalytical Chemistry* **2007**, 600, 335-344.

- (21) Delamar, M.; Hitmi, R.; Pinson, J.; Saveant, J. M. *Journal of the American Chemical Society* **1992**, *114*, 5883-5884.
- (22) Kariuki, J. K.; McDermott, M. T. *Langmuir* **2001**, *17*, 5947-5951.
- (23) Saby, C.; Ortiz, B.; Champagne, G. Y.; Belanger, D. *Langmuir* **1997**, *13*, 6805-6813.
- (24) Doppelt, P.; Hallais, G.; Pinson, J.; Podvorica, F.; Verneyre, S. *Chemistry of Materials* **2007**, *19*, 4570-4575.
- (25) Hurley, B. L.; McCreery, R. L. *Journal of the Electrochemical Society* **2004**, *151*, B252-B259.
- (26) Shewchuk, D. M.; McDermott, M. T. *Langmuir* **2009**, *25*, 4556-4563.
- (27) Shanmukh, S.; Jones, L.; Zhao, Y. P.; Driskell, J. D.; Tripp, R. A.; Dluhy, R. A. *Analytical and Bioanalytical Chemistry* **2008**, *390*, 1551-1555.
- (28) Tripp, R. A.; Dluhy, R. A.; Zhao, Y. P. *Nano Today* **2008**, *3*, 31-37.
- (29) Robbie, K.; Brett, M. J. *Journal of Vacuum Science & Technology a-Vacuum Surfaces and Films* **1997**, *15*, 1460-1465.
- (30) Robbie, K.; Brett, M. J.; Lakhtakia, A. *Nature* **1996**, *384*, 616-616.
- (31) Robbie, K.; Hnatiw, A. J. P.; Brett, M. J.; MacDonald, R. I.; McMullin, J. N. *Electronics Letters* **1997**, *33*, 1213-1214.
- (32) Skoog D.A., H. F. J., Nieman T.A. **1998**, 429-444
- (33) Raman, C. V.; Krishnan, K. S. *Nature* **1928**, *121*, 501-502.

- (34) Raman, C. V.; Krishnan, K. S. *Proceedings of the Royal Society of London Series a-Containing Papers of a Mathematical and Physical Character* **1928**, *122*, 23-35.
- (35) Fleischm.M; Hendra, P. J.; McQuillan.A j *Chemical Physics Letters* **1974**, *26*, 163-166.
- (36) Jeanmaire, D. L.; Vanduyne, R. P. *Journal of Electroanalytical Chemistry* **1977**, *84*, 1-20.
- (37) Anema, J. R.; Brolo, A. G.; Marthandam, P.; Gordon, R. *Journal of Physical Chemistry C* **2008**, *112*, 17051-17055.
- (38) Beermann, J.; Novikov, S. M.; Leosson, K.; Bozhevolnyi, S. I. *Optics Express* **2009**, *17*, 12698-12705.
- (39) Fan, M. K.; Brolo, A. G. *Chemphyschem* **2008**, *9*, 1899-1907.
- (40) Kahl, M.; Voges, E.; Kostrewa, S.; Viets, C.; Hill, W. *Sensors and Actuators B-Chemical* **1998**, *51*, 285-291.
- (41) Lin, X. M.; Cui, Y.; Xu, Y. H.; Ren, B.; Tian, Z. Q. *Analytical and Bioanalytical Chemistry* **2009**, *394*, 1729-1745.
- (42) Lombardi, J. R.; Birke, R. L. *Accounts of Chemical Research* **2009**, *42*, 734-742.
- (43) Yeo, B. S.; Stadler, J.; Schmid, T.; Zenobi, R.; Zhang, W. H. *Chemical Physics Letters* **2009**, *472*, 1-13.
- (44) Driskell, J. D.; Shanmukh, S.; Liu, Y. J.; Hennigan, S.; Jones, L.; Zhao, Y. P.; Dluhy, R. A.; Krause, D. C.; Tripp, R. A. *Ieee Sensors Journal* **2008**, *8*, 863-870.

- (45) Chaney, S. B.; Shanmukh, S.; Dluhy, R. A.; Zhao, Y. P. *Applied Physics Letters* **2005**, *87*.
- (46) Zhao, Y. P.; Li, S. H.; Chaney, S. B.; Shanmukh, S.; Fan, J. G.; Dluhy, R. A.; Kisaalita, W. *Journal of Electronic Materials* **2006**, *35*, 846-851.
- (47) Driskell, J. D.; Seto, A. G.; Jones, L. P.; Jokela, S.; Dluhy, R. A.; Zhao, Y. P.; Tripp, R. A. *Biosensors & Bioelectronics* **2008**, *24*, 917-922.
- (48) Shanmukh, S.; Jones, L.; Driskell, J.; Zhao, Y. P.; Dluhy, R.; Tripp, R. A. *Nano Letters* **2006**, *6*, 2630-2636.
- (49) Dunker, M. F. W.; Starkey, E. B.; Jenkins, G. L. *Journal of the American Chemical Society* **1936**, *58*, 2308-2309.
- (50) Abdelsalam, M. E. *Central European Journal of Chemistry* **2009**, *7*, 446-453.
- (51) Shin, K. S.; Park, C. S.; Kang, W.; Kim, K. *Chemistry Letters* **2008**, *37*, 180-181.
- (52) Liang, H. H.; Tian, H.; McCreery, R. L. *Applied Spectroscopy* **2007**, *61*, 613-620.
- (53) Holze, R. 1988, p 45-58.
- (54) Holze, R. *Electrochimica Acta* **1990**, *35*, 1037-1044.
- (55) Pockrand, I. *Journal of Electron Spectroscopy and Related Phenomena* **1983**, *29*, 357-362.
- (56) Laibinis, P. E.; Fox, M. A.; Folkers, J. P.; Whitesides, G. M. *Langmuir* **1991**, *7*, 3167-3173.

- (57) Laibinis, P. E.; Whitesides, G. M.; Allara, D. L.; Tao, Y. T.; Parikh, A. N.; Nuzzo, R. G. *Journal of the American Chemical Society* **1991**, *113*, 7152-7167.
- (58) Itoh, T.; McCreery, R. L. *Journal of the American Chemical Society* **2002**, *124*, 10894-10902.
- (59) Solak, A. O.; Eichorst, L. R.; Clark, W. J.; McCreery, R. L. *Analytical Chemistry* **2003**, *75*, 296-305.
- (60) Chamoulaud, G.; Belanger, D. *Journal of Physical Chemistry C* **2007**, *111*, 7501-7507.
- (61) Bain, C. D.; Whitesides, G. M. *Journal of Physical Chemistry* **1989**, *93*, 1670-1673.
- (62) Graham Solomons, T. W.; Fryhle, C. B. **1998**.

Chapter V

Patterning of cantilevers with functionalized nanoparticles for combinatorial atomic force microscopy*

5.1 Introduction

Development of a technique to become high throughput (HT) invariably precedes an explosion of new information, and often this wealth of information enables revolutionary new levels of understanding. This trend is especially evident when considering the impact that HT molecular biology and bioanalytical techniques have had on medicine and society. These HT techniques typically operate at high speed and are set up to automatically process numerous samples (usually with some degree of parallelism) resulting in a rapid and high level of productivity. Single-molecule force-measuring instrumentation provide a new level of insight into molecular interactions, and to date these methods have been largely limited to small numbers of interactions under controlled conditions and with a high degree of experienced oversight. Atomic force microscopy, AFM, and other single-molecule force-measurement tools are in a different class when compared to “traditional” HT techniques. In many traditional HT methods, hundreds of thousands of discrete systems that can be characterized within a day, and while some manifestations of HT AFM could in principle be capable of those throughputs, the current state of the art for force measurement is not there yet.

*A form of this chapter has been published as Chisholm, R. A.; Qiu, W.; Green, J. B. D. *Langmuir* **2007**, *23*, 7891-7894

One avenue being explored is the microfabrication of cantilever arrays¹⁻⁵. In this design the deflection of each cantilever can be monitored enabling the measurement of numerous interactions simultaneously. This design could also be used for nanoscale patterning over a large area. One example developed by IBM is the millipede atomic force microscope.³ In this concept, 1024 cantilevers were fabricated in a 3mm x 3mm area for imprinting data storage.

Another means of increasing the throughput of AFM is simply increasing the speed at which a sample can be interrogated. This may be achieved by increasing the speed of the two dimensional scan axis⁶⁻⁸ to achieve fast image acquisition or as in the case of force spectroscopy by varying the cantilever drive signal to achieve rapid force measurements as collected during pulsed force mode.⁹

However, successful HT AFM based force measurements will require more than just high-speed. It will also require a platform for measuring a large number of interactions. High speed and force resolution can both be attained via small cantilevers,¹⁰ and the patterning of surfaces can produce libraries of molecules, which can be probed by an AFM tip. This mode of HT AFM force measurements would be a viable possibility if it were not for the bottleneck posed by the single AFM tip. One platform currently being explored for potential application to HT force measurements is combinatorial AFM, or combi-AFM, which is based on an inverted AFM design.^{11, 12} In this inverted design, the sample is located on the end of a tipless cantilever and is interrogated by any one of the

tens of thousands of substrate-supported tips located on a microfabricated tip array.

The strengths of inverted AFM arise from the redundancy and large number of available tips, and combi-AFM extends this redundancy to include potentially large numbers of combinations of interactions from a moderate number of molecular library elements. Initial efforts to create combi-AFM focused on the development of inverted AFM and various styles of tip arrays.^{12, 13} Although the first tip arrays were designed to contain tips with a range of tip radii,¹² later developments were aimed at increasing tip uniformity.¹⁴ While many of the tip arrays are opaque silicon, Bottomley and coworkers¹³ have created transparent tip arrays, which would be appropriate for simultaneous fluorescence and force measurements.

A typical inverted AFM design in our lab is shown in the optical micrograph presented in Figure 5.1. Each dark spot in Figure 5.1 is a substrate supported AFM tip. Typically the tips are arranged in a square array with a 25 μm pitch and each tip is ~4 μm tall with a radius of curvature of ~20nm. These dimensions are compatible with conventional patterning methodologies, and tip arrays have been successfully modified via microcontact printing,¹⁴ robotic spotting as well as microfluidics. In this inverted format 10's to 100's of thousands of AFM tips are readily available for interrogating a tipless cantilever supported sample. Commercial tipless cantilevers are typically 20-40 μm wide, and these smaller dimensions have restricted patterning to more complex methods

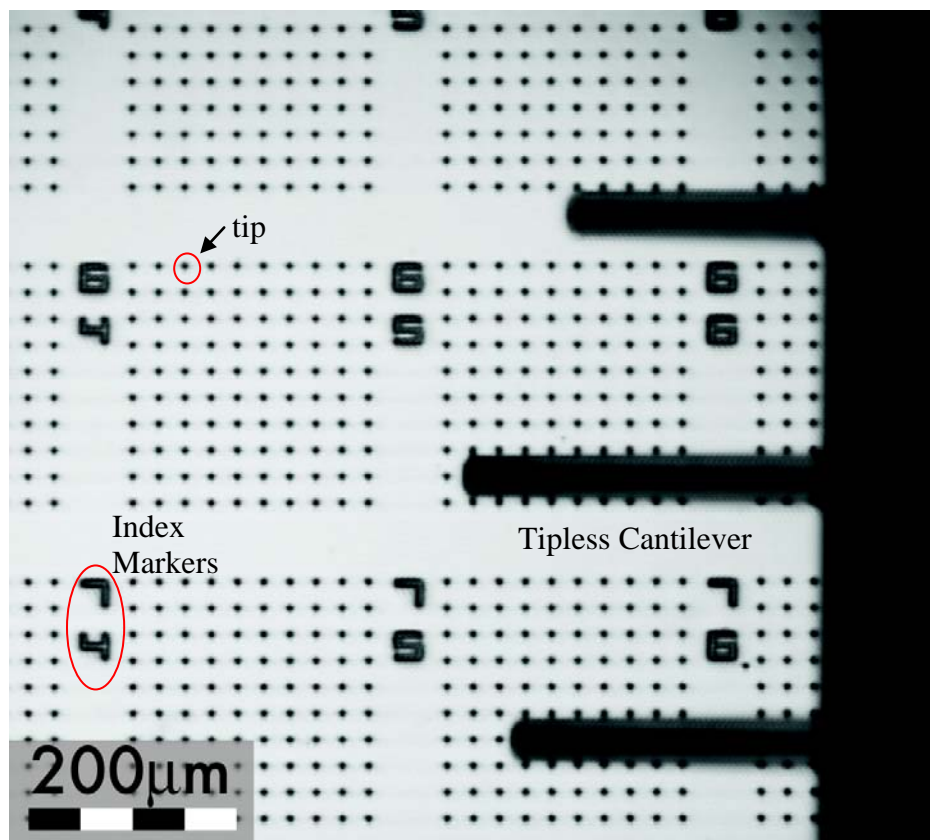


Figure 5.1 Micrographs of tip arrays: This optical micrograph (A) shows the arrangement of tips in the tip array when in use with tipless cantilevers. The index markers provide unique location identifiers for each of the 10's of thousands of substrate supported tips.

such as dip pen nanolithography^{15, 16} and carefully controlled microcontact printing.¹⁷ While there have been some successes in this regard, the infrastructure and expertise required to pattern a cantilever with these methods have posed substantial limitations to the accessibility and ease of use for this technique.

In the work described herein, a procedure was developed to pattern a cantilever with a substantial number of chemically modified nanorods, however one can envision extending this procedure to include nanoparticles of different sizes and shapes. The principles of nanorod based combi-AFM are illustrated in Figure 5.2, and involve five steps: 1) chemical modification of a library of nanorods each chosen for unique identifiable characteristics; 2) immobilization of these rods onto a tipless cantilever; 3) chemical patterning of a tip array; 4) identification of modified nanorods on tipless cantilever; and 5) measurement of interaction forces between opposing chemical libraries.

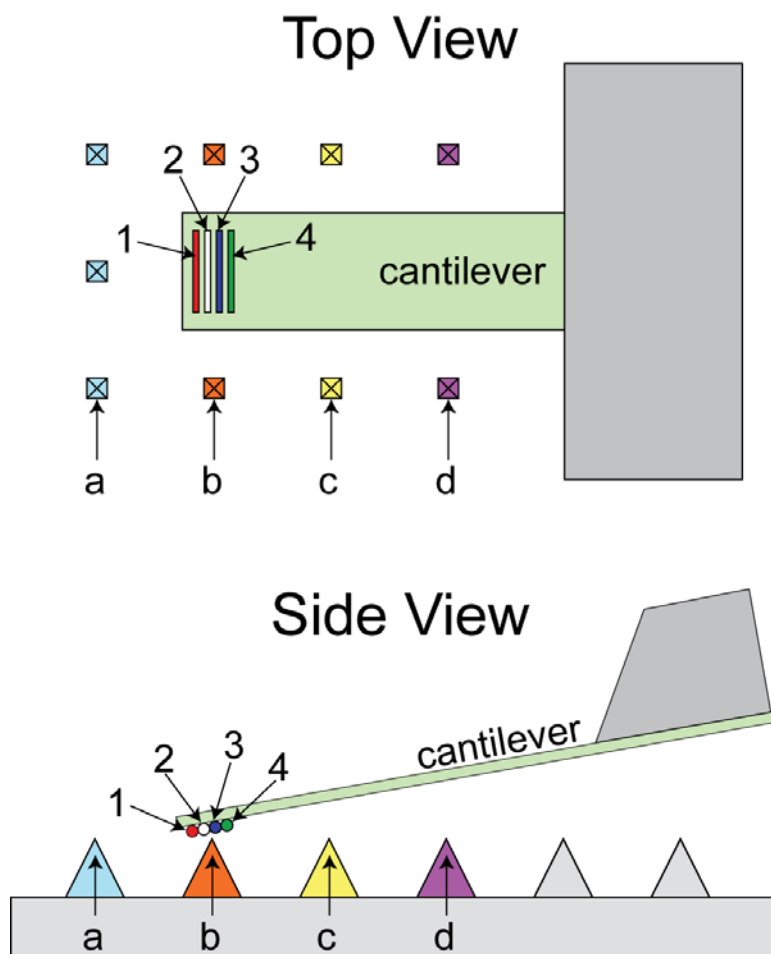


Figure 5.2 Cartoon representing the concept of nanoparticle based combinatorial AFM. The nanorods 1-4 and the tips a-d are each chemically modified with distinct chemistries, and the interaction measurements between each of the 16 combinations may be measured.

5.2 Experimental

Nanorod modification

Ag and Au bar-coded nanorods were purchased from Oxonica Inc. The gold nanorods were synthesized and kindly donated by Keating and coworkers.¹⁸⁻²² The coded and uncoded rods used in these experiments were initially coated with a monolayer of mercaptoundecanoic acid (MUA) as a passivation layer during synthesis. Chemical modification of the uncoded rods involved placing a solution of the MUA modified rods into a homebuilt 100W deep-UV reactor. Following 30 minutes of exposure the rods were transferred to a 1mM ethanolic solution of one of the following replacement thiols: benzenethiol (BT), p-aminothiophenol (ATP), p-mercaptanitrobenzene (MNB) and p-mercaptobenzoic acid (MBA), where they remained until required for use. These replacement thiols were chosen for their diverse chemical functionality and their strong Raman activity.

Tip array modification

The initial tip arrays were cleaned by immersion in fresh piranha solution for 25 minutes followed by rinsing with water. *Piranha consists of 1 part hydrogen peroxide to 3 parts concentrated sulfuric acid. Extreme care should be taken due to the exothermic nature of this reaction.* Following this the protective silicon dioxide layer was etched away by immersing the tip array in 48% HF for 5 minutes followed by rinsing with 0.2 μ m filtered 18M Ω ·cm water (Barnstead-Thermolyne, Nanopure water filtration unit) water. *HF is extremely hazardous.*

Personal protective equipment must be worn at all times and calcium gluconate must be nearby in case any minute amount of HF comes in contact with the skin.

The tip arrays were then again cleaned in piranha again for 25 minutes followed by rinsing with 0.2 μ m filtered 18M Ω -cm water and dried with nitrogen gas. Once clean, the tip arrays were coated with 5nm Cr followed by 45nm Au in a thermal evaporator. The freshly prepared Au coated tip arrays were once again cleaned in piranha, rinsed in 0.2 μ m filtered 18M Ω -cm water and dried with nitrogen gas. The clean Au coated tip arrays were chemically patterned with dodecanethiol (methyl), mercaptoundecanoic acid (acid), aminoundecanethiol (amine), and mercaptoundecanol (alcohol). Patterning of the alkylthiols occurred by micropipetting drops of 1mM alkylthiol/ethanol solutions onto the gold surface. Immobilization of the alkylthiols occurred overnight in an ethanol vapor rich humidity chamber. The chemically patterned tip arrays were then rinsed with ethanol and dried with nitrogen gas.

Cantilever modification

Tipless cantilever modification first proceeded by cleaning the cantilever in soapy water, rinsing with tap water, followed by rinsing with distilled water. The cantilever was then immersed in freshly prepared piranha for 25 minutes, followed by rinsing with 0.2 μ m filtered 18M Ω -cm water and dried with nitrogen gas. Poly(dimethylsiloxane) (PDMS) was chosen to modify the tipless cantilever to make it universally adhesive. The PDMS was formed by mixing 10 parts of Sylgard 184 elastomer with 1 part of Sylgard 184 curing agent (Dow Chemical).

A microscopic droplet of the reaction mixture was transferred to the end of the cantilever and allowed to cure in an oven at 65°C for 3 hours. Microscopic inhomogeneity in the reaction mixture will likely produce materials that can act as surface contaminants, and as a result PDMS films are well-known contamination sources.²³ For this reason, the PDMS modified cantilevers were rigorously cleaned via three cycles alternating between boiling hexane for 10 minutes and a vacuum furnace at 65°C for 30 minutes. Modified nanorods could then easily be attached to the modified adhesive cantilever by a variety of different methods.

Nanorod Characterization

The morphology of the nanorod's size and shape were determined by reflective optical microscopy and scanning electron microscopy. Due to the reflective differences between gold and silver, the sequences intrinsic to the bar-coded nanorods could be observed using reflection optical microscopy. This was performed using an Olympus IX 70/71 (Carsen) inverted optical microscope. The reflective optical properties of the bar-coded nanorods could best be observed using blue light. Scanning electron micrographs were collected using a JEOL model 6301F field emission SEM to assess length dispersion within the nanorod batches. Nanorod modification was assessed using Raman spectrometry. Raman spectra were collected on a Renishaw inVia Raman microscope equipped with a 400mW diode laser $\lambda = 785\text{nm}$, a 50x objective, 10s exposure time and a laser power of 2mW distributed over a $40\mu\text{m} \times 2\mu\text{m}$ spot.

Atomic force microscopy

Following PDMS modification and manual placement of the four modified uncoded nanorods, the cantilever (MikroMasch NSC12) had a resonant frequency in water of 9.1kHz, and a force constant of 0.13N/m, as determined from analysis of the thermal noise.²⁴ This cantilever was mounted above the patterned tip array in a Digital Instruments Multimode AFM equipped with a 140 μ m scanner, wherein the cantilever-supported nanorods were imaged with inverted tapping mode in Nanopure water (Barnstead/Thermolyne). The force measurements were performed in the same solution immediately following the imaging. The force curves were performed at a rate of 3Hz with a ramp size of 250nm and a trigger setpoint of 15nm (2nN). The cantilever deflection and piezoelectric scanner signals were acquired on a Tektronix TDS5034B oscilloscope, in a stream of data that corresponded to ~900 force curves for each tip-rod combination.

5.3 Results and Discussion

The inherent bottle-neck intrinsic to conventional AFM has limited investigations to a small number of interactions within a single experiment.²⁵⁻²⁷ The inverted AFM design aims to circumvent this bottle-neck by interrogating a tipless cantilever supported sample with any one of tens of thousands substrate supported AFM tips. In this design the tip array may be chemically patterned using conventional microcontact printing,¹⁴ robotic spotting as well as microfluidics. Placement of an opposing chemical library onto the tipless cantilever has posed to be challenging due to the limited size of the cantilever.

Initial efforts have restricted patterning of the tipless cantilevers to more complex methods such as dip pen nanolithography^{15, 16} and carefully controlled microcontact printing.¹⁷ Although successful, these methods require extensively experienced user and the success rate is low. The present work proposes the use of chemically modified nanorods, using size, position and intrinsic bar-codes as chemical identifiers once immobilized onto the tipless cantilever. This method could be extended for the general use of nanoparticles, where size and shape would be used as surface modification identifiers. It should be noted that the pull-off forces are dependent upon the tip-particle contact area^{28, 29}, which in turn depends upon the particle radius of curvature. For this reason, it is inadvisable to use particles with different diameters for contact mechanics based combi-AFM. However, the use of modified nanoparticles would be quite advantageous for combinatorial single molecule force spectroscopy investigations.

Characterization of Nanorods

Nanorods were chosen as supports for chemically patterning the tipless cantilever. This is a viable method so long as the particles present a consistent curvature to the tip, thereby enabling the forces to be independent of the lateral shape of the particle. These experiments made use of pure gold nanorods of the same diameter (200 nm) but different lengths (3 μm and 9 μm) were modified with different chemistries, and immobilized from solution onto cantilevers. As is

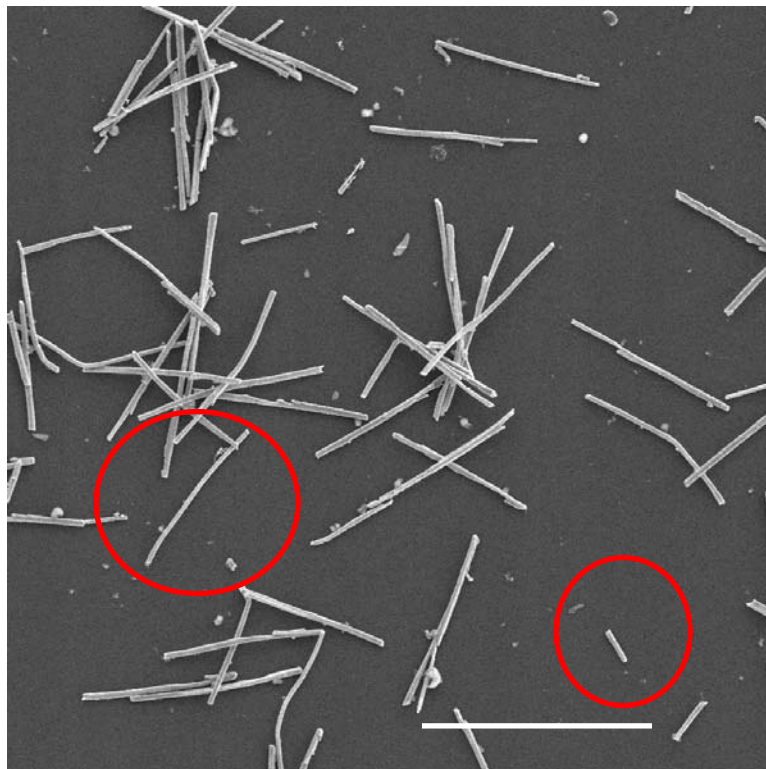


Figure 5.3 Scanning electron micrograph of gold nanorods demonstrating length dispersion within a given batch. Scale bar represent 10 μm .

evident from the encircled rods, in Figure 5.3, both short and long rods are present in our stock of nanorods. The nanorods were not sufficiently monodisperse

within a given nanorod population, and while no long rods were modified with the “short” chemistry, there were usually some short fragments found in the distribution of long rods as seen in the scanning electron micrograph in figure 5.3.

The scanning electron micrograph is taken of a single batch of gold nanorods synthesized to have a length of 8 μm . In this micrograph small fragments of the larger gold nanorods are observed. This polydispersity led to the ineffective discrimination of the chemistry on the short rods. If the nanorods can be synthesized with sufficiently distinct lengths, or if the initial distribution can be effectively fractionated, then nanorods of different lengths may be unambiguously discriminated, and this method would be suitable. Even so, the number of chemistries will be limited by the number of reliably distinguishable lengths.

In an alternate approach we used encoded particles which can be differentiated via optical reflectivity. The silver-gold coded nanorods used in our experiments were 200nm diameter and 9 μm long. The banded silver and gold nanorods can be discriminated based upon the patterns in a scanning electron micrograph as seen in figure 5.4 or a reflection optical micrograph as presented on figure 5.5. Once these rods are immobilized onto the cantilever their reflection micrographs can be used to identify the rods and thereby decode where each of the different chemistries are located. The number of potential unique codes is massive, and more than adequate for large libraries of particles.

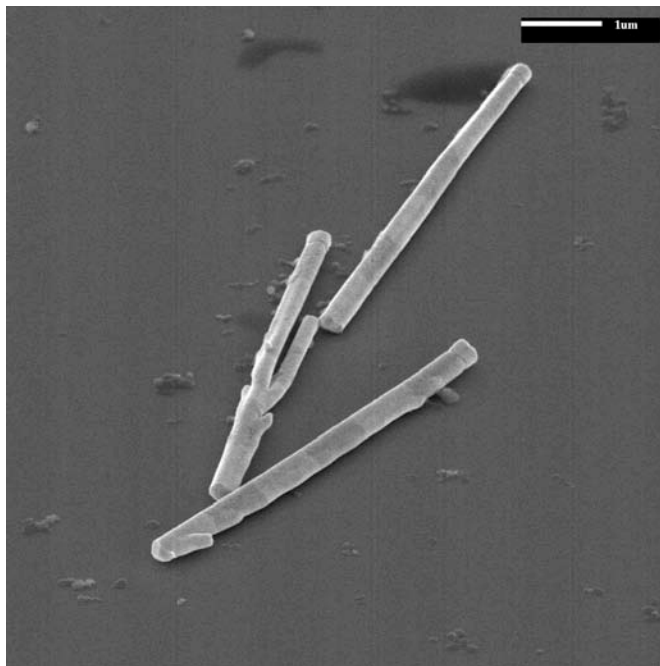


Figure 5.4 Scanning electron micrograph of gold/silver barcoded nanorods. The visual contrast in materials may be used as an identifier of nanorod modification chemistry.

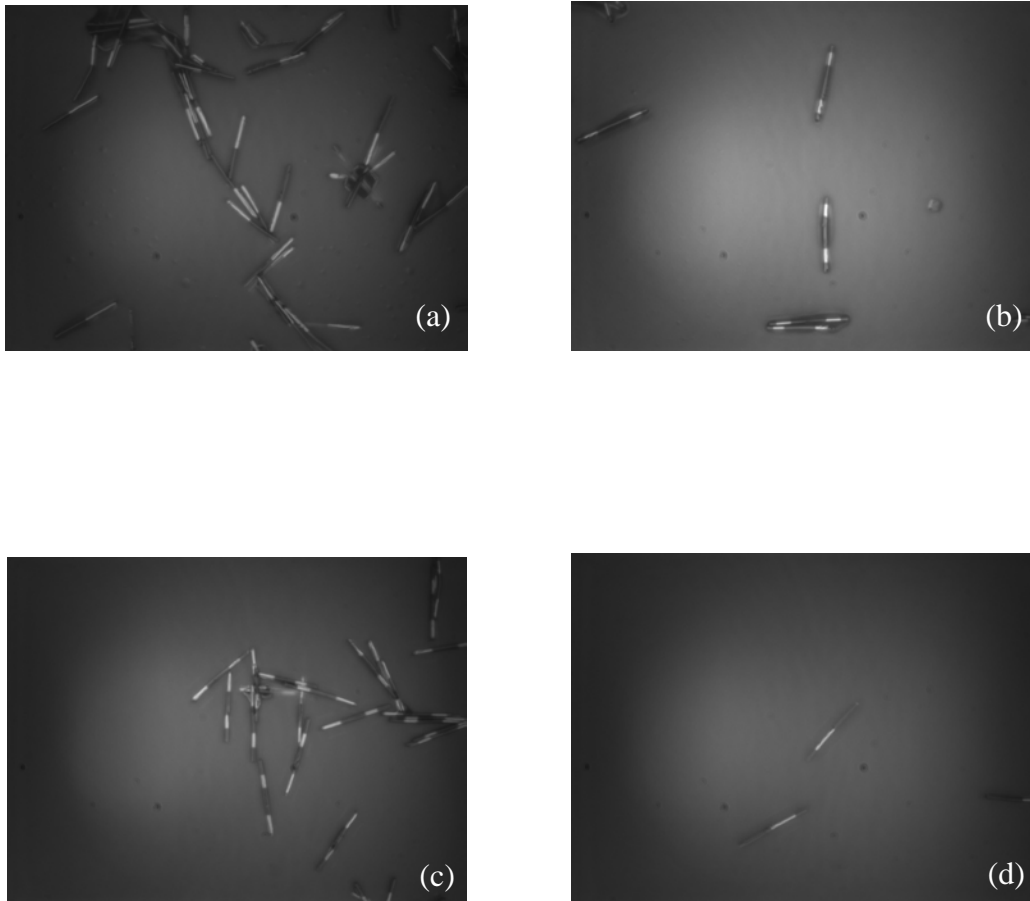


Figure 5.5 Reflection optical micrographs 4 different gold/silver barcoded nanorods illuminated by blue light. The visual contrast due to reflective property differences between gold and silver may be used as an identifier of nanorod modification chemistry.

Immobilization of Chemically Modified Nanorods

By the nature of combi-AFM, the rods on the cantilever may support radically different chemistries e.g., hydrophobic, polar, basic or acidic. Successful immobilization of these chemically disparate rods requires a *universally* adhesive cantilever. We used poly(dimethylsiloxane) (PDMS) to coat tipless cantilevers. The highly adhesive property of the PDMS made modification of the cantilever with wildly different chemistries possible, and at this time we have used these PDMS-levers to support nanorods modified with oligonucleotides and alky, as well as arylthiols. Figure 5.6 contains reflective optical micrographs of nanorods immobilized onto a PDMS modified cantilever. Initial efforts focused on spontaneous attachments of the nanorods onto the adhesive cantilevers. However, when the particle spacing approaches the wavelength of the light, the optical discrimination will suffer, and misidentification may result.

Although these methods of discrimination are effective even when the particles are randomly arranged on the cantilever; confidence in the identification can be markedly improved by manually placing each rod onto the cantilever. One result of manual placement is that identical particles may be used, and the chemistries can then be identified simply by their location. This manual immobilization can be performed simply and rapidly by using an optical microscope equipped with a micromanipulator. Furthermore, this could be automated with machine vision for truly HT applications. The coded and uncoded nanorods shown in Figures 5.6c and 5.6d respectively, were immobilized by this

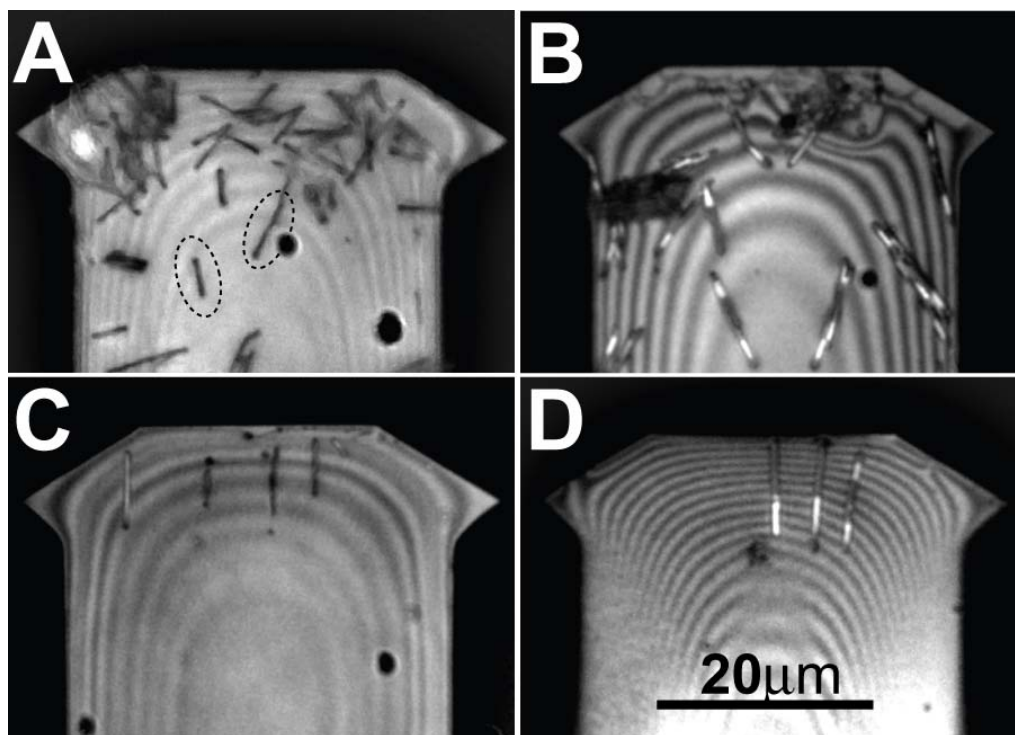


Figure 5.6 Optical micrographs of nanorod modified cantilevers representative of solution phase deposition of (A) uncoded and (B) coded nanorods, as well as manual deposition of (C) uncoded and (D) coded nanorods. The oscillatory pattern is due to optical interference through the PDMS film used for adhesion.

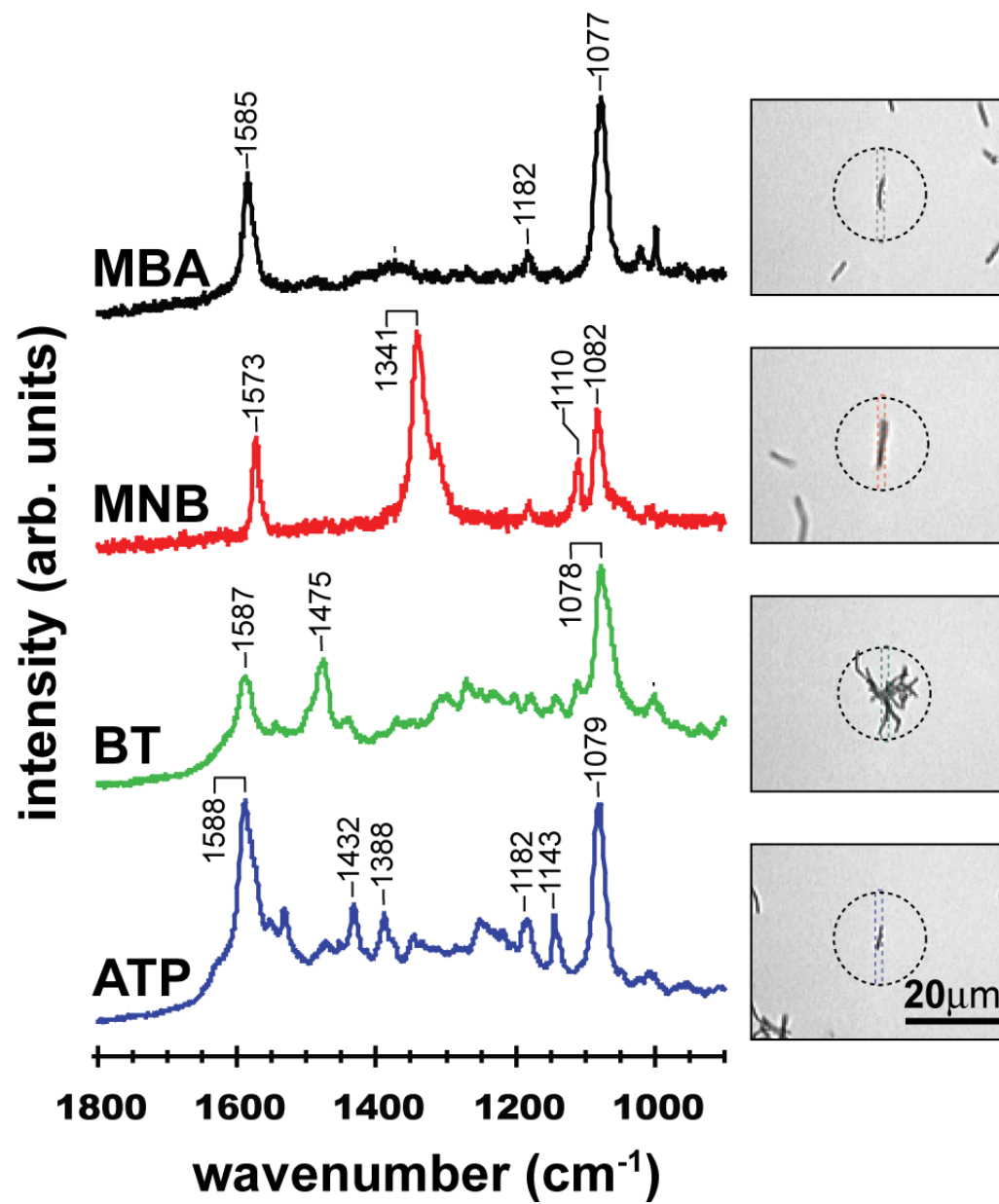


Figure 5.7 Raman spectra and corresponding optical micrographs of nanorods modified with (MBA) p-mercaptopbenzoic acid, (MNB) p-mercaptanitrobenzene, (BT) benzenethiol and (ATP) p-aminothiophenol. The dotted rectangles enclose the regions illuminated by the diode laser and correspond to the samples for the Raman spectra.

Molecule	Assignment	Band (cm ⁻¹)
MBA	C=C ring stretch	1585
	CH bend	1182
	CS stretch	1077
MNB	C=C ring stretch	1573
	NO ₂ stretch	1341
	Phenyl- NO ₂ stretch	1110
	CS stretch	1077
BT	C=C ring stretch	1587
	CCstretch + CH bend	1475
	CS stretch	1078
ATP	C=C ring stretch	1588
	CCstretch + CH bend	1432
	CCstretch + CH bend	1388
	CH bend	1182
	CH bend	1143
	CS stretch	1079

Table 5-1 Summary of peaks positions for the MBA, MNB, BT and ATP Raman active reporters.

manual placement method. Of course for this method to be effective, the particles must remain firmly affixed throughout the entire experiment.

To assess chemical modification of the nanorods Raman active reporters benzenethiol (BT), p-aminothiophenol (ATP), p-mercaptanitrobenzene (MNB) and p-mercaptopbenzoic acid (MBA), were used to derivatize the nanorods. Figure 5.7 shows Raman spectra from modified nanorods along with the corresponding optical micrographs. The rods in question, circled for clarity, were centered and aligned with the narrow laser “spot” shown as dashed rectangles. Variability in the Raman spectra of individual BT modified rods led us to obtain spectra from a cluster of rods. The peak positions were consistent with literature reported values characteristic for the four molecules used in this study³⁰⁻³² suggesting that the rods were properly modified. Table 5.1 contains a summary of peaks positions for the various Raman active reporters.

Combinatorial Atomic Force Microscopy

In combi-AFM, the cantilever and the tip array each support opposing libraries. For these proof of principal experiments, gold-coated tip arrays were manually spotted with four different alkylthiols: dodecanethiol (methyl), mercaptoundecanoic acid (acid), aminoundecanethiol (amine) and mercaptoundecanol (alcohol).

As a test of these particle based combi-AFM methods we assembled our two libraries for force measurements in water. The tip array was composed of tips modified with four different alkylthiolates, and the cantilever supported four

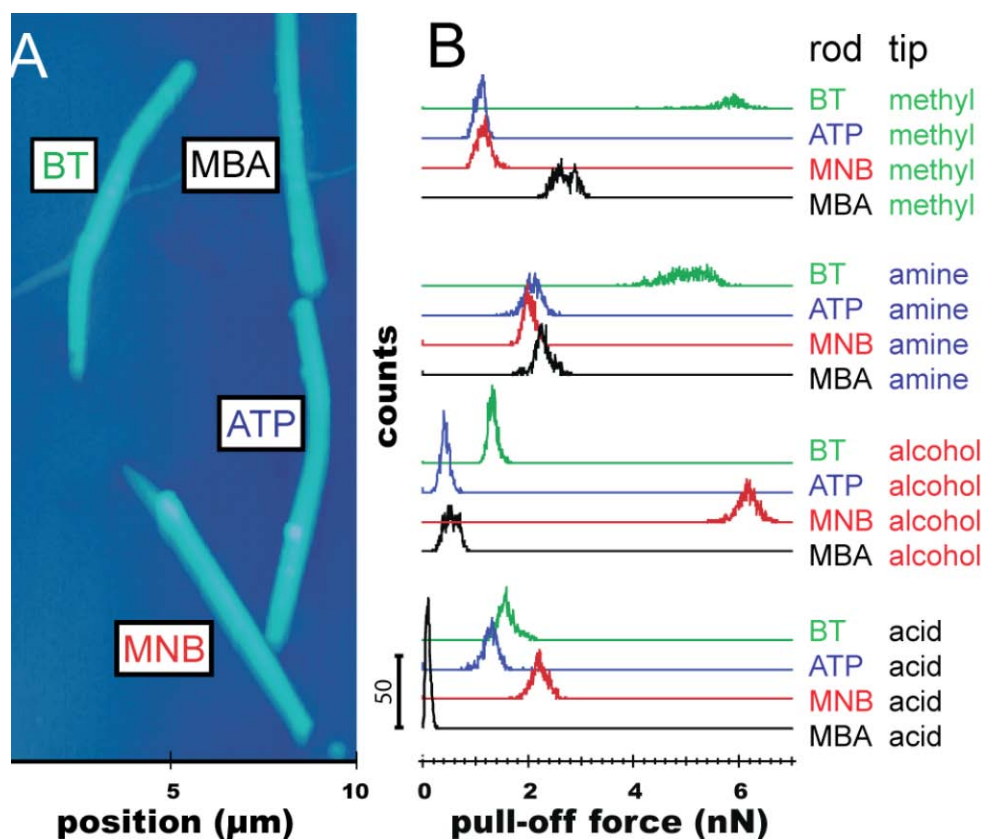


Figure 5.8 (A) Inverted tapping AFM topography image and (B) corresponding histograms of four chemically different tips octadecanethiol (methyl), aminoundecanethiol (amine), mercaptoundecanol (alcohol), mercaptoundecanoic acid (acid), interacting with four chemically different nanorods benzenethiol (BT), p-aminothiophenol (ATP), p-mercaptanitrobenzene (MNB), and p-mercaptobenzoic acid (MBA) immobilized onto a PDMS cantilever. The scale bar represents 50 measurements

arylthiolate modified uncoded nanorods. Together these were used to measure all 16 tip-rod interactions. Figure 4A shows the resulting topographic image which demonstrates that the manually assembled nanorods can be readily discriminated, and that the resolution of the AFM is more than adequate to allow a single tip to probe a single rod without potential interactions with neighboring rods or tips. All sixteen of the interactions between these four rods and the four tips were measured, and the analysis of these force curves with IgorPro routines produced the histograms of pull-off forces shown in Figure 5.8b. The IgorPro routines are found in appendix 8.1.

As expected, the pull-off forces depend markedly upon both the tip and nanorod surface chemistries. These differences in forces may be understood from free energy arguments,²⁶ and to that end, contact angles of water and diiodomethane were used to calculate works of adhesion for each of the combinations of alkyl and arylthiolate monolayers. Although these tips are from a population with tip radii of ~20 nm, the exact tip radii were not determined for these specific tips, and thus we cannot directly compute the works of adhesion from the pull off forces; however, upon examination of each tip independently the trend of forces agreed with contact angle measurements. With two exceptions the trends in the measured pull-off forces were consistent with the trends in the calculated works of adhesion. The methyl-MBA interaction was much larger than calculated, and instead of being the weakest interaction for the methyl tip, it was the second largest. The amine-MNB pull-off force was weaker than expected. It should have been comparable to the amine-BT force, but instead it was

comparable to the amine-ATP pull-off force. While the precise nature of this anomaly is unknown, the amine-MNB measurements were one of the last combinations measured, and so the MNB rods were exposed to the cantilever deflection laser for the longest time. The photoreduction of MNB to ATP on silver has been reported,⁸ and although the photoreduction on gold is much slower than on silver⁸ this is one possible explanation for this anomalous measurement. Additional experiments to clarify the source of these results are clearly required. Nonetheless, this patterning methodology is capable of placing several different chemistries on a cantilever with relative ease, and thus enables more facile combinatorial force measurements.

This method can successfully pattern tipless cantilevers with a wide range of oligonucleotide, alkylthiol and arylthiol modified nanorods, and there is every reason to expect that a host of different chemistries can be immobilized in a similar fashion. In principle, one hundred of these nanorods could be packed right next to each other across a 20 μm wide cantilever. To further optimize the performance of the nanoparticle based combi-AFM we foresee the following changes: 1) including well studied molecular interactions as internal standards within the opposing chemical libraries; 2) including in situ tip characterizers on the cantilever for immediate tip geometry characterization; 3) increasing the number of rods as well as packing density on the cantilever; and perhaps most importantly 4) incorporating computer assisted automatic data collection and analysis. This last point is absolutely crucial when considering the already massive amount of data produced, and how the data processing will scale as the

number of library elements increases.

5.4 Conclusions

In conclusion, this work has demonstrated the successful attachment of a wide variety of chemically modified nanoparticles onto a tipless cantilever using manual and solution based immobilization techniques. The manual attachment method appears to be the most promising of these techniques and can potentially yield a cantilever-supported library containing ~10-20 different chemistries. Upon comparison to the previously reported methods for cantilever patterning, this procedure is substantially simpler, inexpensive and produces unambiguous patterns, which are free from cross contamination issues. The force curves acquired between the four chemically modified nanorods and the four modified tips within the same tip array, demonstrate for the first time sixteen different combinations of interactions during the same experiment, within the same solution. This work has provided an excellent validation that combi-AFM can be used to interrogate moderately sized chemical libraries, and is a substantial advancement of this technique.

REFERENCES:

1. Minne, S. C.; Yaralioglu, G.; Manalis, S. R.; Adams, J. D.; Zesch, J.; Atalar, A.; Quate, C. F. *Applied Physics Letters* **1998**, 72, (18), 2340-2342.
2. Saya, D.; Fukushima, K.; Toshiyoshi, H.; Hashiguchi, G.; Fujita, H.; Kawakatsu, H. *Sensors and Actuators a-Physical* **2002**, 95, (2-3), 281-287.
3. Durig, U.; Cross, G.; Despont, M.; Drechsler, U.; Haberle, W.; Lutwyche, M. I.; Rothuizen, H.; Stutz, R.; Widmer, R.; Vettiger, P.; Binnig, G. K.; King, W. P.; Goodson, K. E. *Tribology Letters* **2000**, 9, (1-2), 25-32.
4. Kawakatsu, H.; Saya, D.; Kato, A.; Fukushima, K.; Toshiyoshi, H.; Fujita, H. *Review of Scientific Instruments* **2002**, 73, (3), 1188-1192.
5. Kakushima, K.; Watanabe, T.; Shimamoto, K.; Gouda, T.; Ataka, M.; Mimura, H.; Isono, Y.; Hashiguchi, G.; Mihara, Y.; Fujita, H. *Japanese Journal of Applied Physics Part I-Regular Papers Brief Communications & Review Papers* **2004**, 43, (6B), 4041-4044.
6. Manalis, S. R.; Minne, S. C.; Quate, C. F. *Applied Physics Letters* **1996**, 68, (6), 871-873.
7. Humphris, A. D. L.; Miles, M. J.; Hobbs, J. K. *Applied Physics Letters* **2005**, 86, (3).
8. Picco, L. M.; Bozec, L.; Ulcinas, A.; Engledew, D. J.; Antognozzi, M.; Horton, M. A.; Miles, M. J. *Nanotechnology* **2007**, 18, (4).
9. Miyatani, T.; Horii, M.; Rosa, A.; Fujihira, M.; Marti, O. *Applied Physics Letters* **1997**, 71, (18), 2632-2634.

10. Viani, M. B.; Schaffer, T. E.; Chand, A.; Rief, M.; Gaub, H. E.; Hansma, P. K. *Journal of Applied Physics* **1999**, 86, (4), 2258-2262.
11. Green, J. B. D.; Lee, G. U. *Langmuir* **2000**, 16, (8), 4009-4015.
12. Green, J. B. D.; Novoradovsky, A.; Park, D.; Lee, G. U. *Applied Physics Letters* **1999**, 74, (10), 1489-1491.
13. Lillehei, P. T.; Poggi, M. A.; Polk, B. J.; Smith, J. A.; Bottomley, L. A. *Analytical Chemistry* **2004**, 76, (13), 3861-3863.
14. Mabry, J. C.; Yau, T.; Yap, H. W.; Green, J. B. D. *Ultramicroscopy* **2002**, 91, (1-4), 73-82.
15. Piner, R. D.; Zhu, J.; Xu, F.; Hong, S. H.; Mirkin, C. A. *Science* **1999**, 283, (5402), 661-663.
16. McCreery, R. L.; Wu, J.; Kalakodimi, R. P. *Physical Chemistry Chemical Physics* **2006**, 8, (22), 2572-2590.
17. Quist, A. P.; Pavlovic, E.; Oscarsson, S. *Analytical and Bioanalytical Chemistry* **2005**, 381, (3), 591-600.
18. Reiss, B. D.; Freeman, R. G.; Walton, I. D.; Norton, S. M.; Smith, P. C.; Stonas, W. G.; Keating, C. D.; Natan, M. J. *Journal of Electroanalytical Chemistry* **2002**, 522, (1), 95-103.
19. Keating, C. D.; Natan, M. J. *Advanced Materials* **2003**, 15, (5), 451-454.
20. Nicewarner-Pena, S. R.; Carado, A. J.; Shale, K. E.; Keating, C. D. *Journal of Physical Chemistry B* **2003**, 107, (30), 7360-7367.
21. Keating, C. D. *Abstracts of Papers of the American Chemical Society* **2005**, 229, 525-PHYS.

22. Sioss, J. A.; Stoermer, R. L.; Sha, M. Y.; Keating, C. D. *Langmuir* **2007**, 23, (22), 11334-11341.
23. Graham, D. J.; Price, D. D.; Ratner, B. D. *Langmuir* **2002**, 18, (5), 1518-1527.
24. Hutter, J. L.; Bechhoefer, J. *Review of Scientific Instruments* **1993**, 64, (7), 1868-1873.
25. Pierres, A.; Benoliel, A. M.; Bongrand, P. *Cell Adhesion and Communication* **1998**, 5, (5), 375-395.
26. Noy, A.; Vezenov, D. V.; Lieber, C. M. *Annual Review of Materials Science* **1997**, 27, 381-421.
27. Vezenov, D. V.; Noy, A.; Ashby, P. *Journal of Adhesion Science and Technology* **2005**, 19, (3-5), 313-364.
28. Johnson, K. L.; Kendall, K.; Roberts, A. D. *Proceedings of the Royal Society of London Series a-Mathematical and Physical Sciences* **1971**, 324, (1558), 301-&.
29. Derjaguin, B. V.; Muller, V. M.; Toporov, Y. P. *Journal of Colloid and Interface Science* **1975**, 53, (2), 314-326.
30. Zhou, Q.; Li, X. W.; Fan, Q.; Zhang, X. X.; Zheng, J. W. *Angewandte Chemie-International Edition* **2006**, 45, (24), 3970-3973.
31. Michota, A.; Bukowska, J. *Journal of Raman Spectroscopy* **2003**, 34, (1), 21-25.
32. McCreery, R. L.; Viswanathan, U.; Kalakodimi, R. P.; Nowak, A. M. *Faraday Discussions* **2006**, 131, 33-43.

Chapter VI

Tip characterization for inverted atomic force microscopy

6.1 Introduction

Atomic force microscopy (AFM) has been used for measuring interaction forces almost since its inception¹⁻³, and there have been several key advancements over the years.⁴⁻⁷ When measuring contact forces between interacting interfaces, chemical functionality as well as the geometry of the opposing surfaces is of critical importance. A number of contact mechanics models have been developed relating the radius of curvature, R , between two surfaces to the pull-off force, F , the force required to separate two surfaces.⁸⁻¹⁰ Specifically, the JKR model⁸ predicts the force to separate a sphere, having a radius R , from a flat plane and is given by equation 6.1;

$$F=3/2\pi W_{ad} R \quad (6.1)$$

W_{ad} is the work of adhesion between the two surfaces in a given solvent. This can be interpreted as the change in free energy required to separate two surfaces within a medium and is further defined by Young's equation;¹¹

$$W_{ad} = \gamma_S + \gamma_L - \gamma_{SL} \quad (6.2)$$

where γ_S , γ_L and γ_{SL} are the interfacial surface energy's of the solid interface, liquid interface and the solid-liquid interface. Knowing the tip radius, W_{ad} can be determined by measuring the pull-off force between the AFM tip.^{6,12,13} However,

W_{ad} can also be found using contact angle measurements and the Young-Dupre equation relating W_{ad} to surface tension of the liquid medium, γ_{lv} ; ¹¹

$$W_{ad} = \gamma_{lv} (1 + \cos \theta) \quad (6.3)$$

Due to AFM's capability to probe surfaces with molecular/atomic resolution, researchers have been developing the force measuring capabilities of AFM for high throughput applications.¹⁴⁻¹⁸ The direct measurement of interaction forces, on this high throughput scale, would potentially offer a wealth of information and potentially provide revolutionary insights into the areas of molecular biology and medicine.

One platform currently being explored for such force measurements is combinatorial AFM, combi-AFM, which is based on an inverted AFM design, which has been discussed in Chapter 5. In this inverted design the sample, which is located on the end of a tipless cantilever, is interrogated by any one of the tens of thousands of substrate-supported tips from within a tip array. The strengths of this technique are the ability to measure a large number of chemical interaction combinations and redundancy for statistical purposes. This is achieved by patterning of opposing chemical libraries on the tip array as well as the cantilever. In a given experiment in which the tip array is patterned with N different chemistries and the cantilever is patterned with M different chemistries, NxM different combinations of interactions may be probed in a relatively short period of time, without the need for disassembly.¹⁹ It is the potentially massive numbers of interactions that lends combi-AFM to be a truly high-throughput technology. Also another advantage of the inverted design is that by using the same cantilever

for all of the measurements in combi-AFM, cantilever-to-cantilever force constant variations are avoided, allowing for interaction forces to be easily compared.

There are also some disadvantages and obstacles to this technique. Patterning of the micron-sized cantilever with even moderate sized chemical libraries has proved to be a substantial impediment, although recent advances have dealt with this difficulty. Initial efforts involved patterning the tipless cantilever using dip-pen nanolithography²⁰ and micro contact printing. More recently, a chemical patterning technique using modified nanoparticles immobilized onto tipless cantilevers has been developed and has been discussed in Chapter 5.¹⁹ Another major obstacle for the widespread adaptation of combi-AFM derives from the need to know the tip shape and radius for quantitative analysis. The large number of tips in a single array leads to the unique difficulty of having to characterize each tip in an efficient manner for quantitative interpretation of the interaction forces.

The work described in this chapter addresses the latter by applying three conventionally used methods for AFM tip characterization and adapting them for the inverted AFM design. These methods are: 1) the imaging of a known standard particles²¹⁻²³; 2) direct imaging with SEM^{10,24}; and 3) blind reconstruction of the tip's geometry following imaging an unknown surface.^{10,23,25-28} To test the effectiveness of the tip characterization methods we measured pull-off forces with chemically modified tips and tipless cantilever with dimethyloctadecylchlorosilane. For all these characterization methods we found that the pull-off forces correlate well with the measured tip radii, thereby enabling

calculation of the work of adhesion of this system. We found these results to agree well with the results obtained by contact angle measurements and provide a means to quantitatively characterize tips used in inverted atomic force microscope force measurements.

6.2 Experimental

Chemicals and Materials

The following chemicals were used as received: hexane (EMD Chemicals Inc., ACS certified) or (Fisher, ACS certified), 2-propanol (IPA, Fisher, certified ACS grade, suitable for electronics use), hydrofluoric acid (Aldrich, 48wt.% HF in water, >99.99%), dimethyloctadecylchlorosilane (DMS, United Chemicals Technologies), aminopropyltrimethylethoxysilane (APDMES, United Chemicals Technologies). Peroxysulfuric acid (piranha) was prepared by mixing 1 part 30% hydrogen peroxide (EMD, ACS certified) with 3 parts concentrated sulfuric acid (EMD, ACS certified). 5nm diameter colloidal gold solutions were purchased from BBInternational, and used as received. Except where noted, all rinsing steps used 0.2 μ m filtered 18M Ω ·cm water (Barnstead-Thermolyne, Nanopure water filtration unit), and all drying steps used 0.2 μ m filtered nitrogen gas from liquid nitrogen boil-off.

Tip array

Two different tip arrays were used for this study; one array contained tall, 7 μ m, dull tips, $R_t \sim 100$ nm. These are referred to as “dull” tips for the remainder

of the Chapter. The other tip array was composed of tips with moderate height, $5\mu\text{m}$ and, $R_t \sim 20\text{nm}$. These are referred to as “sharp” tips for the remainder of the Chapter. Modification of the tip arrays began with immersion in fresh piranha solution for 25 minutes followed by rinsing with water. The protective silicon dioxide layer was then removed by immersing the tip array in 48% HF for 5 minutes followed by rinsing with large amounts of water. The tip arrays were subsequently immersed again in piranha for 25 minutes followed by rinsing with water and drying with nitrogen gas. The tip arrays were then immersed in a solution of $\sim 1\text{mM}$ DMS in hexane overnight followed by rinsing with hexane, drying with nitrogen gas and baking at 105°C , in a covered glass container, for 40 minutes.

Colloidal gold tip characterization

The cantilevers for tip characterization began as tipless silicon cantilevers (MikroMasch, Model NSC12/tipless/noAl). The cantilevers were first cleaned by immersion in fresh piranha for 25 minutes, followed by extensive rinsing, and drying. The cantilever surface was modified by immersion for 25 minutes in a 1mM solution of APDMES dissolved in IPA, followed by rinsing with IPA, drying with nitrogen gas, and baking at 105°C for 40 minutes in glass covered containers. The cantilevers were then immersed in a solution that contained colloidal gold particles ranging in particle diameter from 2-30nm. Following 5 minutes of immersion in the colloidal gold solution, the cantilevers were removed, rinsed and dried. Images of colloidal gold particles were collected

while operating the AFM in inverted tapping mode. All AFM measurements were acquired using a Nanoscope IIIa multimode SPM (Veeco Inc., MultiMode) equipped with a 15 μ m scanner.

SEM tip characterization

Tip radii were determined from analysis of SEM images produced by a JEOL model 6301F field emission SEM. These SEM images were acquired at an angle of 85° with the surface normal, and the tip arrays were viewed along two perpendicular directions (x and y). Analysis of SEM images made use of ImageJ software to digitize the border of the tip. The border was fit to a sixth order polynomial to determine the radius of curvature.

Evaporated niobium tip characterization

The cantilevers for tip characterization began as tipless silicon cantilevers (MikroMasch, Model NSC12/tipless/noAl). The cantilevers were first cleaned by immersion in fresh piranha for 25 minutes, followed by extensive rinsing and drying. The evaporated niobium tipless cantilevers were kindly donated by Aurora Nanodevices Inc. Four topographic images were collected at various locations and scan angles of an evaporated niobium tipless cantilever. The topographic images were recorded at a scan rate of 0.5Hz, and scan size of 500nm. To ensure adequate resolution of the reconstructed tip model, a resolution of 512x512 was used. SPIP was used to generate a 3D model of the c-AFM tip's geometry. Upon constructing a three-dimensional model of the tip's apex, the first

1nm of the tip's apex was fit to a parabola to determine the radius of curvature. This process occurred for the four topographic images to determine an average and standard deviation of the tip's radius of curvature.

Cantilevers for force measurements

Modification of tipless silicon cantilevers (MikroMasch, Model CSC12/tipless/noAl) began by immersion in fresh piranha solution for 25 minutes followed by rinsing and drying. The cantilevers were then immersed in a solution of DMS in hexane overnight, followed by rinsing with hexane, drying with nitrogen gas, and baking at 105°C in a covered glass container for 40 minutes.

Cantilever force constant determination

The thermal method was used to determine the cantilever spring constant.^{29,30} The thermal power density plot of the tipless cantilever's thermal noise was acquired using a Stanford Research Systems model SR785 spectrum analyzer while averaging 1000 scans. The thermal spectra were fit using the quality factor, Q , the amplitude at zero frequency, A_0 , and the resonant frequency, f_0 , as fitting parameters. The cantilever deflection sensitivity was found from the slope of the deflection signal, captured using a Tektronix TDS5034B digital phosphor oscilloscope, while the cantilever was in contact with the tip.

Force measurements

The same AFM used for imaging was also used to measure the pull-off forces. The control software was operated in a mode known as Force Volume with the scan size minimized to correspond to a single point on the cantilever and at a rate of 9.33Hz. In addition to the force volume data, the cantilever deflection and z piezo signals were captured using the oscilloscope at a rate of 20,000 samples per second to a total of 2 million samples. The deflection and z piezo signals were analyzed using custom procedures written in IgorPro, and are freely available upon request from the authors.

Contact angle measurements

Silicone wafers were first cleaned by immersion in fresh piranha solution for 25 minutes followed by rinsing with water and dried with nitrogen gas. The wafers were then immersed in a solution of ~1mM DMS in hexane overnight followed by rinsing with hexane, drying with nitrogen gas and baking at 105°C, in a covered glass container, for 40 minutes. Contact angle measurements were made using water, diiodomethane and ethanleneglycol on a home build gonimeter.

6.3 Results and Discussion

Force curves were acquired in water between DMS modified tip arrays and a tipless cantilever. A set of ~900 force curves were acquired and the force required to break the two surfaces apart was determined using an in-house IgorPro software routine. A typical set of force curves and corresponding histograms is

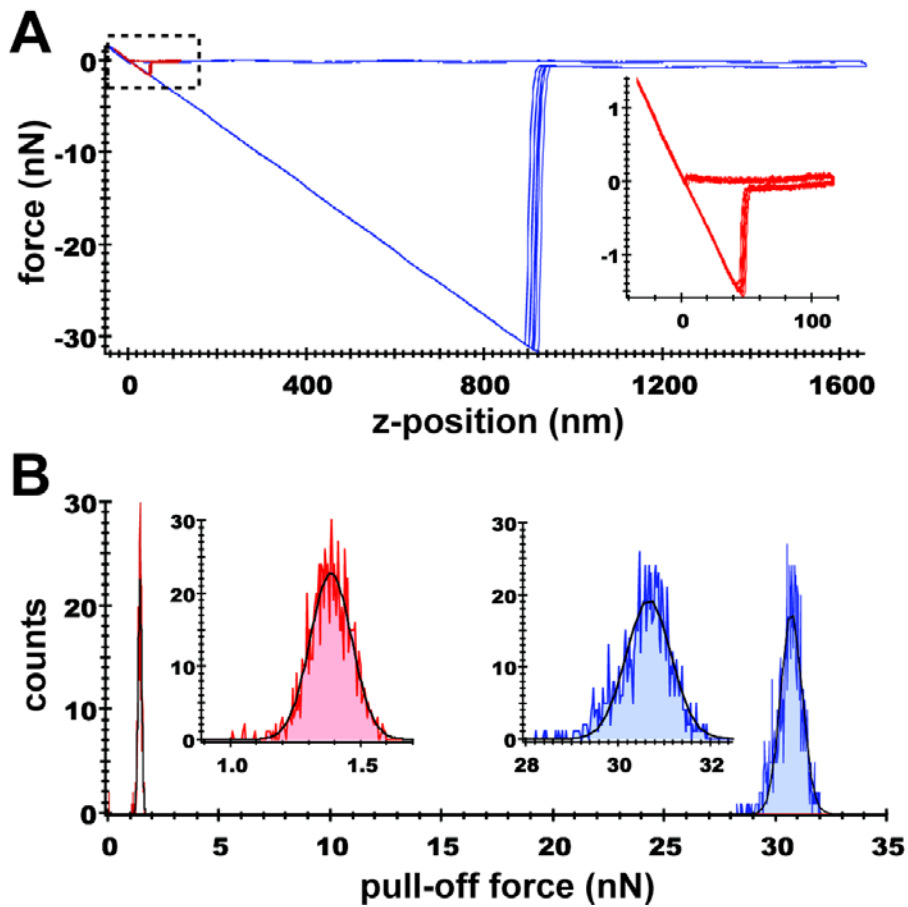


Figure 6.1 A. Force curves in water between octadecyl modified tip and cantilever for a “dull” tip, shown in blue and a “sharp” tip shown in red. B Histograms of the measured pull-off forces from the force curves. Insets are expanded views of the two histograms.

presented in Figure 6.1 for both a sharp tip and a dull tip. Qualitatively, it can be seen that tips having the same surface modification, but different sizes, have drastic effects on the pull-off forces of the two surfaces, verifying the need for quantitative characterization of the tip's geometry. Knowledge of the tip geometry is very important when interpreting AFM measurements, especially those that involve tip-sample interactions. While some researchers have reported accurate geometric and mechanical characterization of AFM tips, it is not common for researchers to routinely characterize the tip shapes. To date there are relatively few methods available for tip characterization, and fewer still that are routine enough to apply to the vast number of chemically modified tips used for combi-AFM. Three methods are compared in this Chapter, a) SEM imaging, b) imaging of unknown samples (niobium crystallites) combined with blind reconstruction and c) imaging of *known* standard samples (colloidal gold particles).

Contact Angle Discussion

The tip radii determined by each of the three methods will be assessed by a force measurements application. Force curves for a hydrophobic cantilever-tip interaction will be collected. Both the tip and cantilever will be modified with DMS. The measured adhesion force and determined tip radii will be used to calculate W_{ad} using the JKR model, equation 6.1. The AFM determined W_{ad} will be compared with the W_{ad} value determined by contact angle measurements.^{11,12,31} Typical images recorded during contact angle measurements are given in

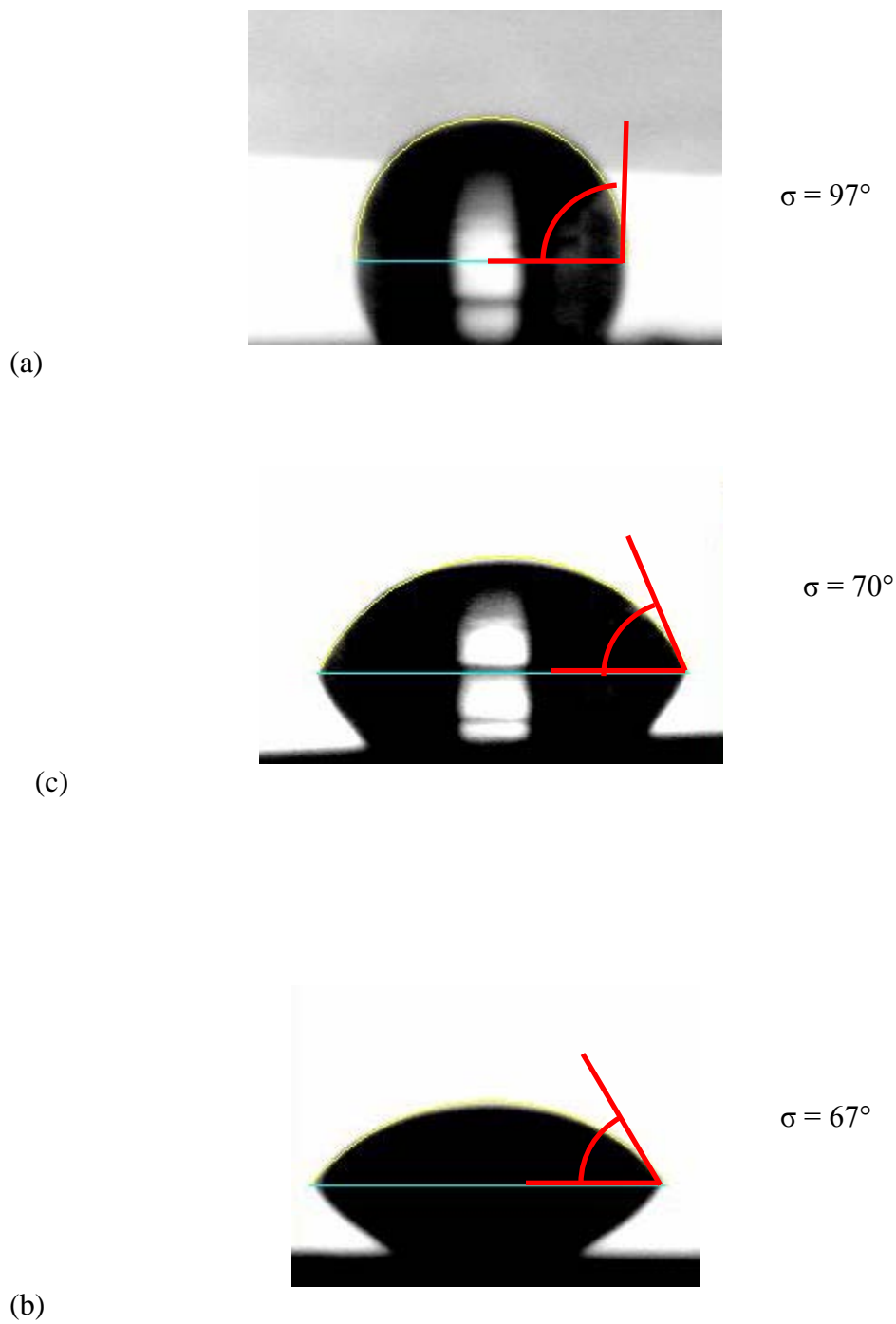


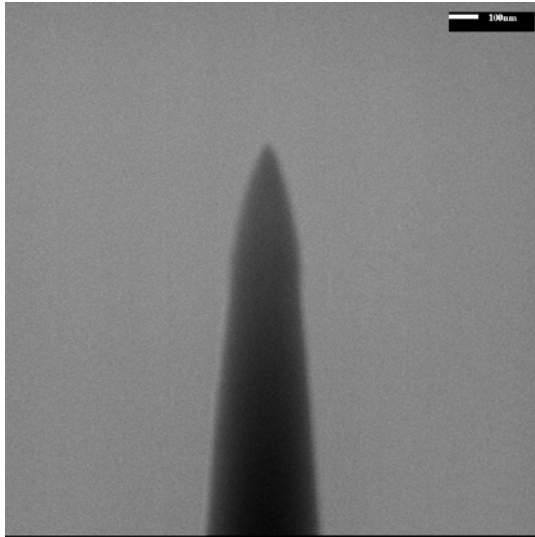
Figure 6.2 Typical images collected during contact angle measurements using water (a), diiodomethane (b) and ethanleneglycol (c) on an octadecyl modified silicon wafer.

Figure 6.2. The contact angles made in triplicate for water, diiodomethane and ethanleneglycol were delivered to 1cm² silicon wafers modified with DMS. The corresponding means and standard deviations are $95^{\circ}\pm 4$, $70^{\circ}\pm 1.3$, $67^{\circ}\pm 2$, respectively. These values were used to calculate the work of adhesion, using equation 6.3, for the system to be 33.6 ± 1.3 mJ/m².

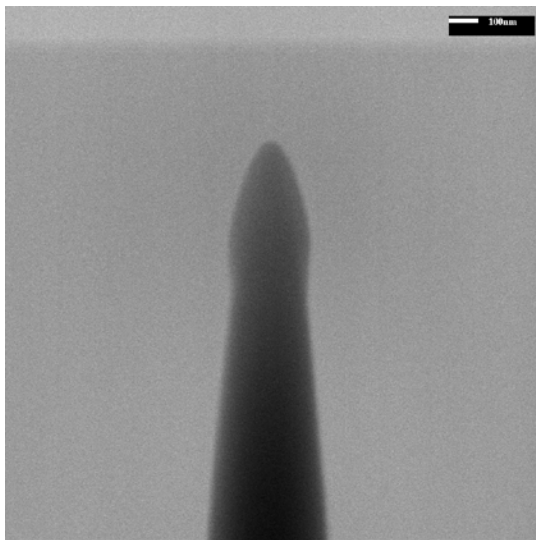
Scanning Electron Microscopy Characterization

Of the three tip characterization methods SEM imaging is routinely used for characterization of commercial tips.^{10,24} There are, however, some problems with using a SEM to measure tip radii within the inverted AFM design. One issue is that the application of SEM imaging to hundreds of AFM tips for a single experiment would be both expensive, time consuming and without substantial additional effort, SEM images at best produce a cross section of the tip geometry along a single direction, thereby losing information parallel to the focal axis. Finally, impurities within the e-beam vacuum chamber may produce a unwanted amorphous carbon film on surfaces being imaged. For combi-AFM applications, this would jeopardize the accuracy of the SEM image and render the tip useless thereafter. It should be noted that hydrocarbon contamination from the SEM imaging process can be rather drastic, rendering the tips useless for conventional adhesion measurements. It was found a tip radius could increase by 19.4nm with just 1 minute of 5kV beam exposure as demonstrated in Figure 6.3.

To limit the amount of hydrocarbon contamination all beam optimization was performed elsewhere on the tip array prior to imaging. During imaging the



(a)



(b)

Figure 6.3 Scanning electron micrograph of AFM tip before (a) and after (b) exposure to a 5kV electron beam for 1 minute.

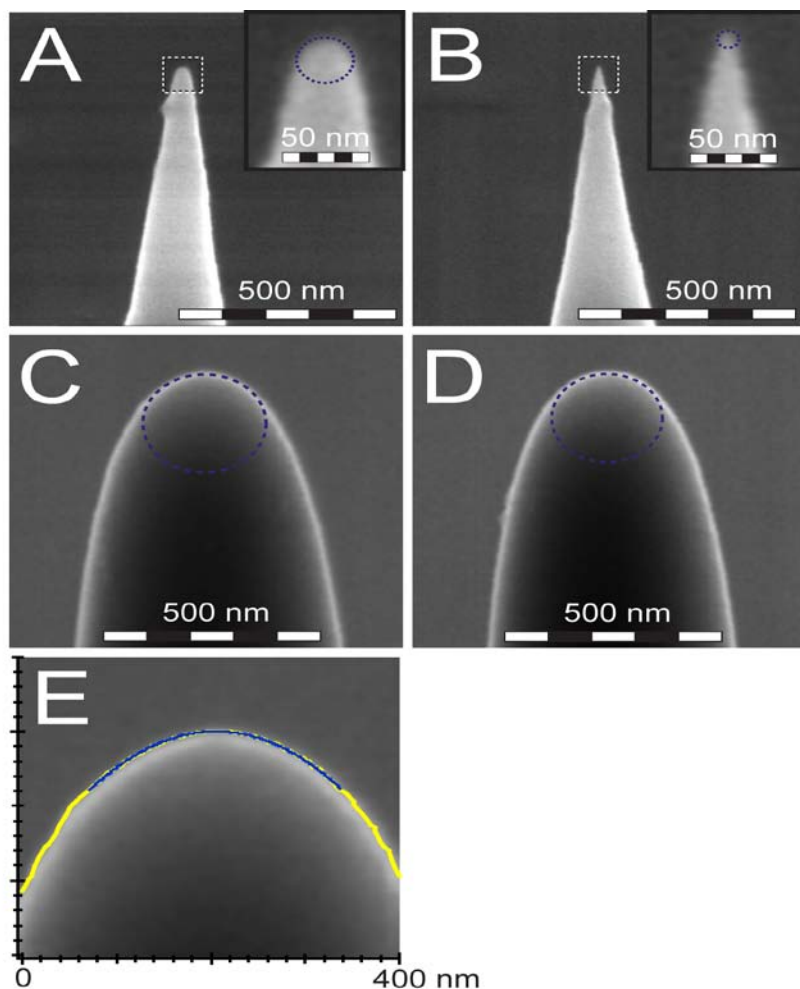


Figure 6.4 Scanning electron micrographs of tips. These SEM images (A) and (B) show a tip representative of a sharp tip array imaged along the x and y directions respectively. The insets include superimposed circles to determine tip radii. The SEM images (C) and (D) show similar results from a tip representative of a dull tip array. The plot in (E) is the exported data that corresponds to the apparent tip edge, and this curve was used to calculate the curvature at the apex of the tip.

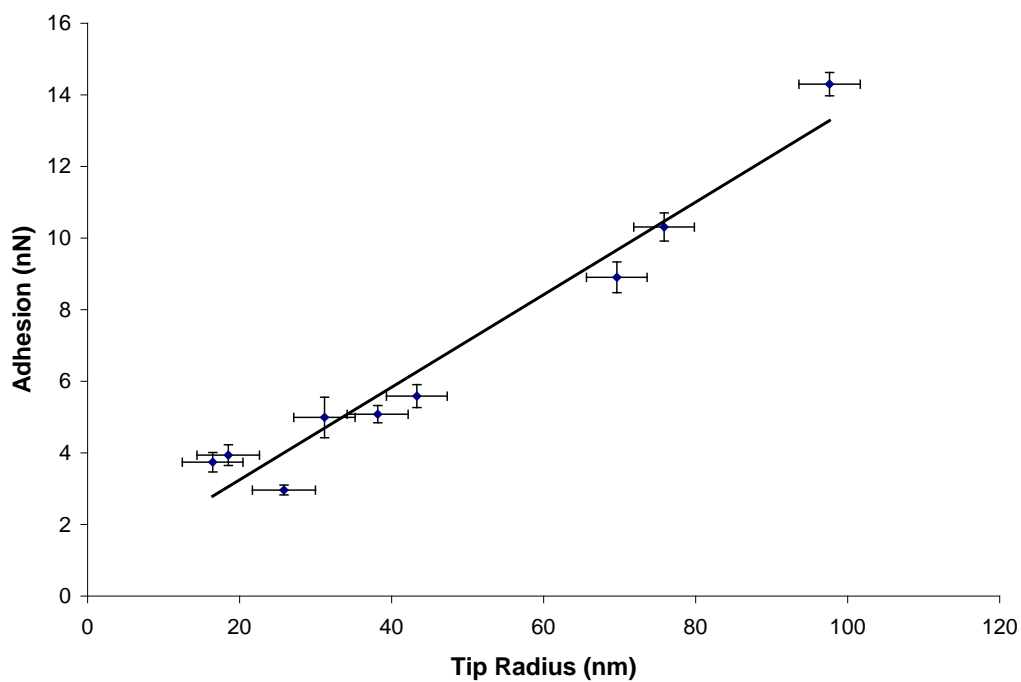


Figure 6.5 Plot of pull-off force as a function of effective tip radius calculated from SEM images. The data points are the mean values of measured pull-off force and determined tip radius. The error bars are the standard deviation of the mean for each parameter. The solid line is the linear least squares fit of the data. The slope of this line was used to determine the work of adhesion of the system to be $28.7 \pm 1.9 \text{ mJ/m}^2$.

tip array was rotated so that SEM images of the tip along the x- and y-directions could be obtained. The SEM images shown in Figure 6.3 are representative of the tips found within the two different tip arrays used in this study. The edges of the tips shown in Figure 6.3 appear to be highlighted in the SEM image contrast. This is due to an increased number of electrons scattered at the edge of the tip, making the edge appear brighter. We exploited this artifact by processing the image data using ImageJ (available at <http://rsb.info.nih.gov/ij/>) which found and exported a trace of the edge of the tip. The trace data was fit to a six order quadratic function to determine the apical tip radius. It should be noted that this method tended to use data that is 10's of nanometers away from the actual tip to determine the tip shape. The effective tip radius, R_{eff} , was determined by;

$$R_{\text{eff}} = 2R_1R_2/(R_1+R_2) \quad (6.4)$$

Where R_1 is the calculated tip radius along the x-direction of the tip and R_2 is the calculated tip radius when the tip array is rotated by 90° . The effective tip radii calculated from SEM images were plotted against their corresponding pull-off forces, presented in Figure 6.5. The work of adhesion for this system was found to be $28.7 \pm 1.9 \text{ mJ/m}^2$, using equation 1 and the slope of the least-squares fit to this data. This value agrees well with the values of 34 mJ/m^2 determined by contact angle measurements.

Colloidal Gold Characterization

A common problem that is intrinsic to AFM is that topography images are a convolution of both substrate topography and tip geometry. Upon imaging particles of known geometry this intrinsic artifact can be exploited to reconstruct the tip's geometry.²¹ For this characterization technique we choose to reconstruct the tips using topographic images of 5nm diameter colloidal gold, which we assumed to be spherical. Gold colloids were immobilized onto a tipless cantilever and tapping mode inverted AFM was used to collect topographic images.²⁴ Figure 6.6 is typical topographic images and corresponding line traces of the same colloidal gold particles for the sharp tip, figure 6.6a, and the dull tip, figure 6.6b. As expected the width of the particles imaged by the dull tip appear to be broader when compared to the image created by the sharp tip. From these images the geometry of the tip being used can be reconstructed. We chose two slightly different methods to characterize our tips in this manner. The first method calculates the tip's radius based on the tip interacting with the particle at half the particle's height, R_p , and the calculated radius of the tip, R_t , may be given by equation 6.5;

$$R_t = w^2/8h \quad (6.5)$$

where w and h are the width at the base, and height of the particle respectively. A geometric model of this method is given in Figure 6.7a.

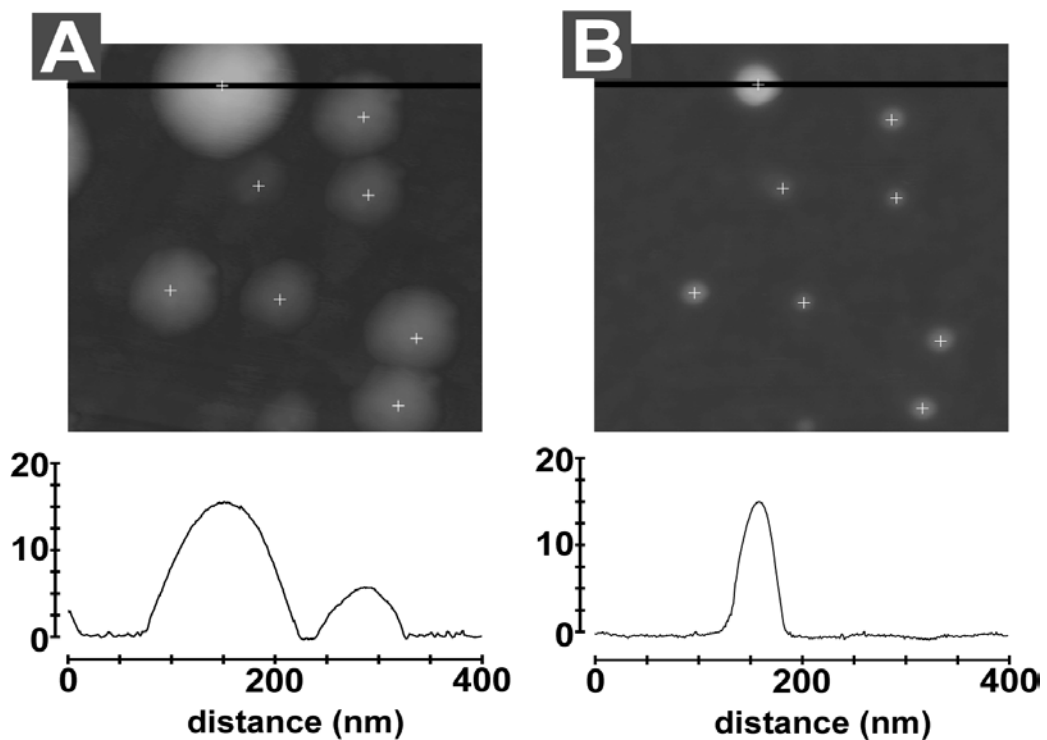


Figure 6.6 Inverted tapping mode AFM topography image of a group of colloidal gold particles on a cantilever imaged with the sharp and dull tips shown in Figure 1B and 1C. Cross-sectional profiles below each image correspond to the line drawn on the image.

Topographic images of nine colloidal gold particles were used to calculate a single tip's radii. The mean of each set of calculated tip radii was determined, and plotted against the corresponding pull-off forces, presented in figure 6.8. The work of adhesion for this system was found to be 28.4 ± 3.3 mJ/m², using the slope of the least-squares fit to this data. The tip reconstruction method calculates the tip's radius based on fitting a sphere up to R_p from the apex of the tip.

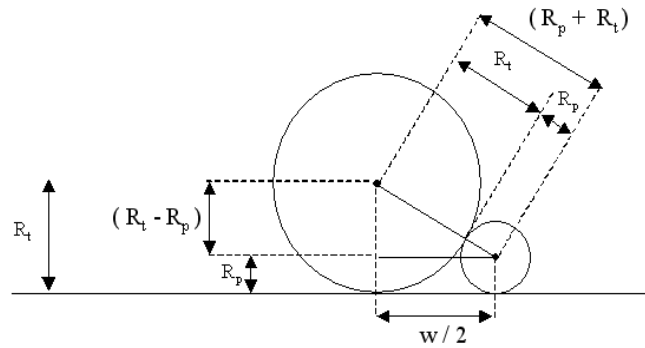
When considering use of these tips for force measurements, only the molecules in first few nanometers from the apex of the tip are involved in pull-off force contact mechanics. Therefore, we also chose to calculate the tip's radius based on information within the first nanometer of the apex. The tip's radius may be calculated by;

$$R_t = w^2/8h + h/2 - h_p/2 \quad (6.6)$$

where h is the vertical distance from the tip's apex measuring the width, w , and h_p is the height of the particle from the base to the apex. A geometric model of this method is given in Figure 6.7b. Using the same topographic images of colloidal gold as the previous method the means of the tip radii were calculated and plotted against their corresponding pull-off forces, presented in figure 6.9. The work of adhesion for this system was found to be 29.3 ± 2.4 mJ/m², using equation 6.1 and the slope of the least-squares fit to this data, which agrees well with the values of 34 mJ/m² determined by contact angle measurements.

$$(R_t - R_p)^2 + (w/2)^2 = (R_p + R_t)^2$$

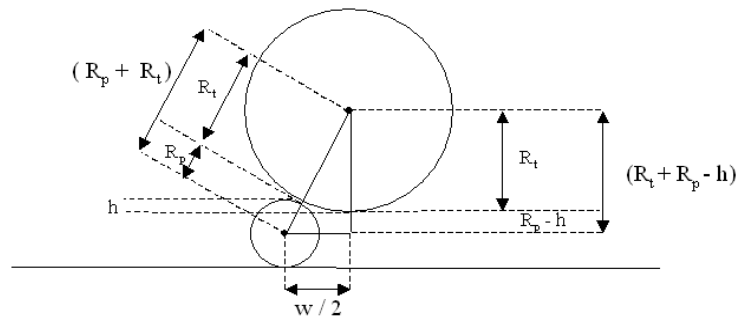
$$R_t = \frac{w^2}{8h}$$



(a)

$$(R_t + R_p - h)^2 + (w/2)^2 = (R_p + R_t)^2$$

$$R_t = \frac{w^2}{8h} + \frac{h}{2} - R_p$$



(b)

Figure 6.7 Geometric models of the methods used to calculate an inverted AFM tip's radius based on imaging colloidal gold nanoparticles. (a) corresponds to calculating the tip's radius using the width at half max in the topography image, and (b) corresponds to calculating the tip's radius using height information within the first 1nm of the tip's apex.

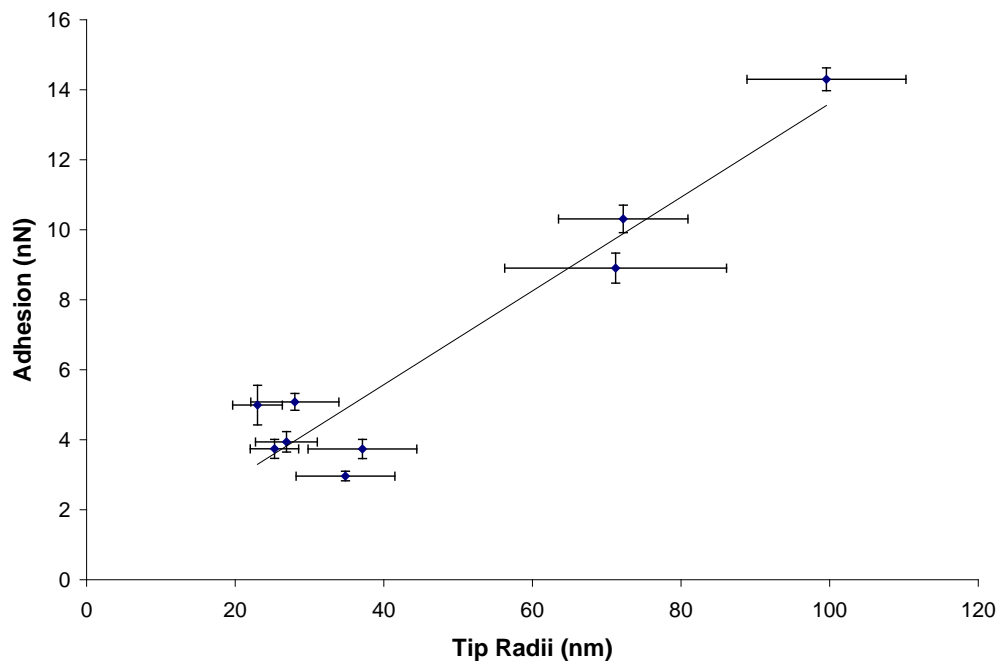


Figure 6.8 This plot of the adhesion versus tip radius is a result of different inverted AFM tips where the tip radii were calculated using the method given in figure 6.7a. The error bars represent standard deviations of the mean values and the solid line is the linear least squares regression through the data which was used to calculate the work of adhesion of the system to be $28.4 \pm 3.3 \text{ mJ/m}^2$.

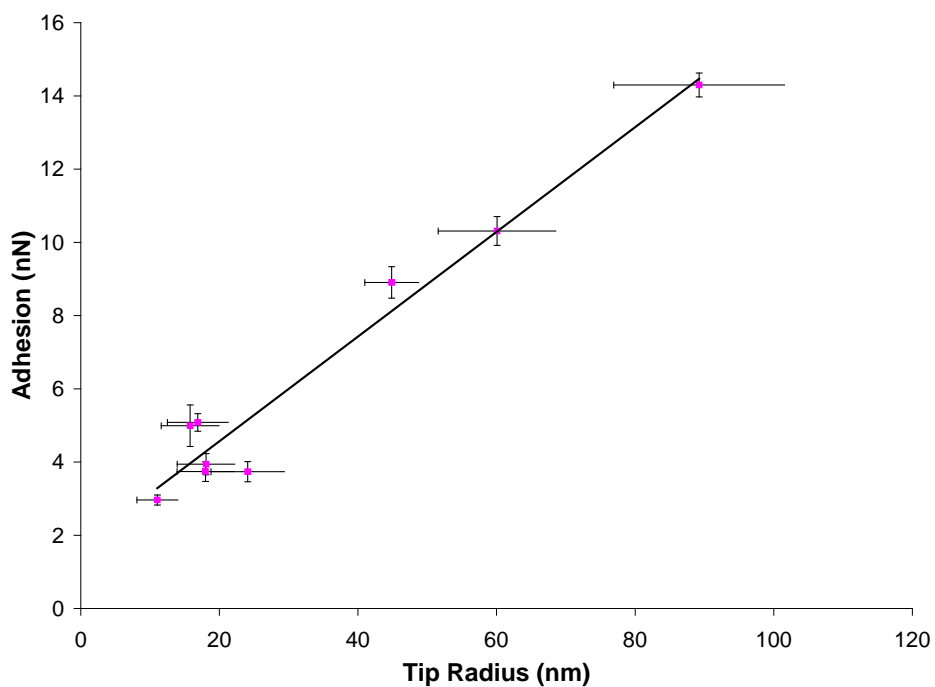


Figure 6.9 This plot of the adhesion versus tip radius is a result of different inverted AFM tips where the tip radii were calculated using the method given in figure 6.7b. The error bars represent standard deviations of the mean values and the solid line is the linear least squares regression through the data which was used to calculate the work of adhesion of the system to be $29.3 \pm 2.4 \text{ mJ/m}^2$.

The benefit of the previous method is that colloidal gold can be immobilized onto a combi-AFM cantilever for immediate tip characterization during an experiment. This would allow users to monitor tip changes during an experiment and allow for discrimination between “good” tips and non-uniform tips prior to being used for pull-off experiments. However, the geometries of the gold particles are not actually known and they are assumed to be spherical. It is possible that colloidal gold particles are not simply spherical particles, but instead may adopt a wide range of crystalline geometries. Furthermore, it is common for smaller particles to aggregate or cluster around larger diameter particles. While it is therefore inappropriate to assume that each particle is spherical, it may be reasonable to assume that the top of each particle presents an ellipsoid to the tip. With this assumption, the measured curvature of each particle can be used to determine the curvature of the tip.

Blind Reconstruction Characterization

Blind reconstruction of a tip’s geometry uses topographic information collected on a relatively sharp sample to reconstruct the curvature of the tip. To this effect, the sample must present topography that is sharper than the tip itself. Tip characterization with blind reconstruction does not actually produce an image of the tip geometry so much as an envelope. Thus, the tip radius determined by this method is an upper limit. While the surface topography does not need to be known, the surface must have sufficiently sharp features to resolve the relevant features on the tip. Niobium crystallites are routinely used for blind

reconstruction, and in fact they are commercially sold as tip characterizers under the name of nioprobe (Aurora Nanoprobe Inc.). Given that we are operating in an inverted design, we cannot affix the commercial 1cm^2 sized sample to our cantilever. Niobium coated tipless cantilevers, supplied by Aurora Nanoprobe Inc., and were used in this study. The performance of two different software packages for the blind reconstruction was examined: 1) Scanning Probe Imaging Processor, SPIP; and 2) a MATLAB routine. Although each of these analysis packages are based on the landmark paper of Villirubia²³, there was substantial difference in performance.

We were easily able to import and process native AFM images in SPIP as well as the MATLAB routine and found that they produced comparable results. However, one of the key differences between these software was that the MATLAB routine allowed the user to select the peaks to be included in the analysis. Although this made the analysis laborious, areas within the image containing noise could easily be avoided. The SPIP software requires that the user exclude areas within the image that contain noise.

The MATLAB tip reconstruction process began by first collecting a tapping mode inverted AFM image of evaporated niobium. A typical topographic image of the niobium-coated cantilever is presented in Figure 6.10a, and the corresponding reconstructed tip envelope is shown in Figure 6.10b. This particular envelope was produced from ~30 different local maxima (marked by small blue crosses in Figure 6.10 a). Inclusion of additional crystallites produced no substantial changes in the tip shape. The three-dimensional reconstruction of

the tip is used to determine an effective radius. Traces taken across the tip image were fitted with polynomial functions, with the peak centered at zero. The curvature of the tips at the peak was used to determine the radius. In this manner, the apex of this tip can be fit with an ellipsoid having the two primary radii of $R_1 = 16.4\text{nm}$ and $R_2 = 12.4\text{nm}$, these can be combined by Equation 6.4 to give an effective tip radius $R_{\text{eff}} = 14.1\text{nm}$.

Tip reconstruction using the SPIP software proceeded in much similar manner as the MATLAB routine, using the same topographic images of evaporated niobium. Rather than selecting peaks to be included in the reconstruction analysis the entire area selected within the image was used for the reconstruction process. Areas of the image that appeared to contain noise were excluded from the reconstruction process.

In our experience, to make this method reliable, there are some substantial constraints on the data acquisition conditions. First, the image must be completely free of drift artifacts. Secondly, noise along the slow scan axis can be a serious problem, which can at times render an image useless for reconstruction. Finally, the choice of drive amplitude and amplitude setpoint parameters are very important and inappropriate choices can lead to dramatically different tip radii. Given that we are primarily concerned with the tip shape at the apex, these considerations are extremely important, and need to be fully understood. For these reasons we took extreme care to minimize noise and drift during the

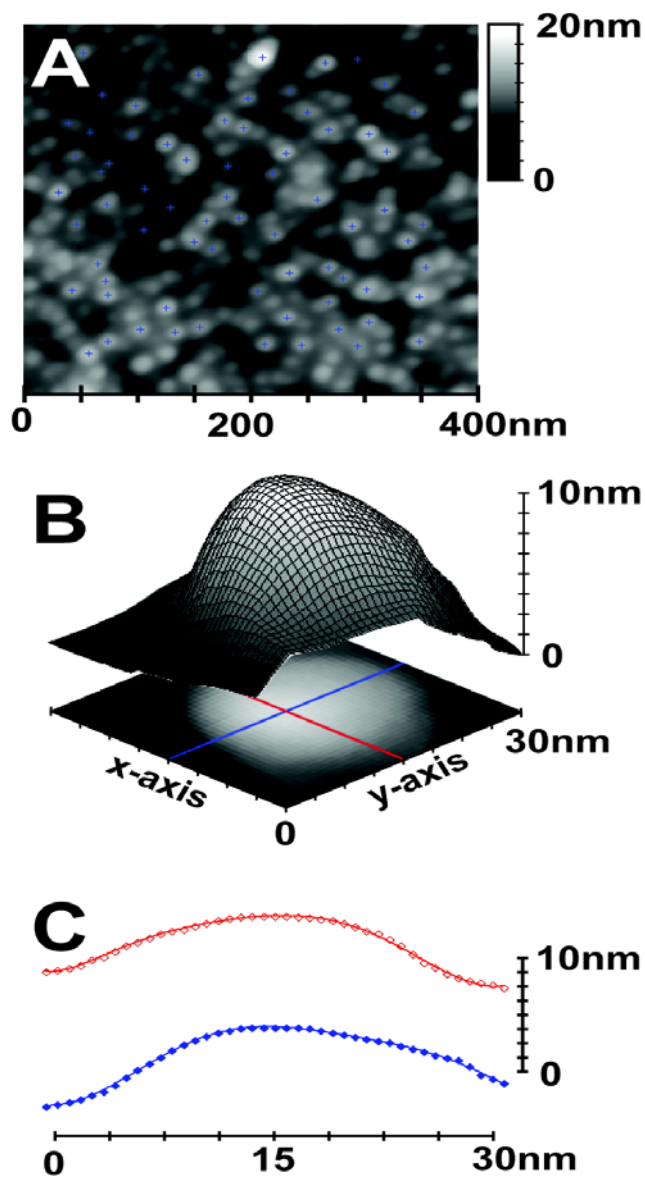


Figure 6.10 Blind reconstruction of the tip shape using a MATLAB routine. (a) Inverted tapping mode image of a niobium coated cantilever showing the local maxima that were used for reconstructing the tip shape. (b) Tip shape generated by blind reconstruction process. (c) Cross sectional traces along the x (red-open diamonds) and y (blue-filled diamonds) axes are shown. The solid lines represent polynomial fits used to determine the radius of curvature along each direction and at the apex.

imaging process; however, noise along the slow scan axis would sometimes still remain. We thus chose the x-axis fit, parallel to the fast axis scan, to be most representative of our tip shape.

The values measured on several tips by the MATLAB routine and from the SPIP tip reconstruction process were plotted against their corresponding pull-off forces, as presented in figure 6.11. The work of adhesion obtained from both the MATLAB routine and SPIP was $30.9 \pm 1.7 \text{ mJ/m}^2$. Based upon this result it is concluded that data analysis with either of these software packages is adequate and will give similar results.

In summary, each of the tip characterization methods employed in this study worked well to determine the tip radii. When used to determine the work of adhesion for analysis of force curves between DMS modified tips and cantilevers, all the methods gave similar values of W_{ad} to the contact angle measured value of 34 mJ/m^2 . A summary of these values are given in table 6.1.

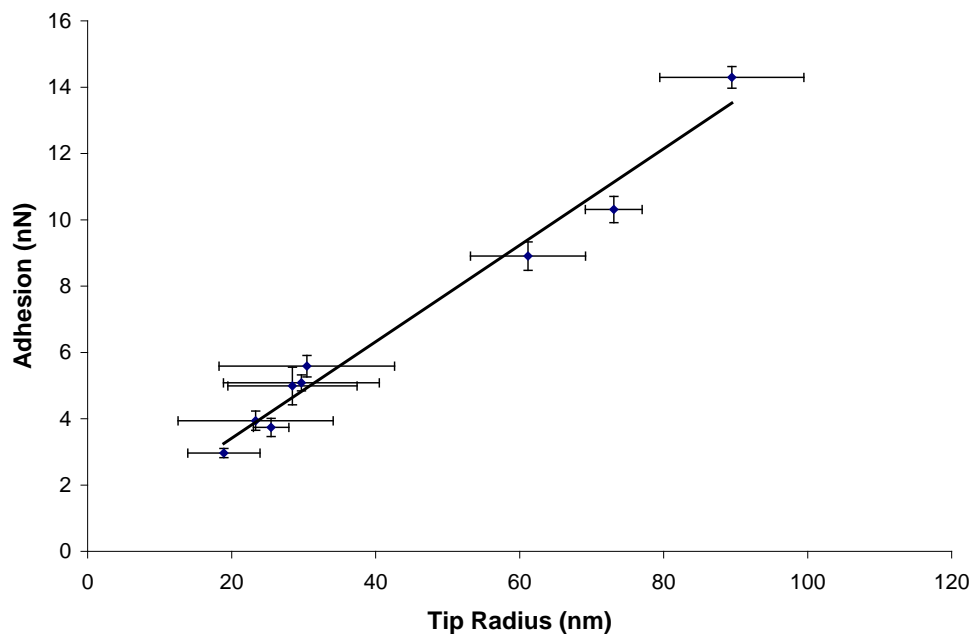


Figure 6.11 This plot of the adhesion versus tip radius is a result of different inverted AFM tips where the tip radii were calculated using blind reconstruction algorithms. The error bars represent standard deviations of the mean values and the solid line is the linear least squares regression through the data, which was used to calculate the work of adhesion of the system to be $30.9 \pm 1.7 \text{ mJ/m}^2$.

Method	W_{ad} (mJ/m ²)	Uncertainty
Contact Angle	33.6	1.3
SEM	28.7	1.9
Gold Colloids	29.3	2.4
Blind Reconstruction	30.9	1.7

Table 6.1 Summary of determined work of adhesion mean values and corresponding uncertainty for the different characterization methods.

6.4 Conclusions

In conclusion, SEM imaging of tips in a tip array, while adequate for the coarse structure, does not clearly determine the curvature within the last few nm of the tip, nor does it allow in situ measurements, nor does it allow 3-dimensional tip structure to be easily determined. Blind reconstruction of a tip's geometry from topographic images of niobium appears to agree best with the expected geometry, based on contact angle measurements; however, imaging time is long and analysis time is laborious. With the advent of "smarter" tip reconstruction software analysis time may be decreased, but this procedure still requires the user to image the evaporated niobium independently from the in situ experiment. The method of reconstructing a tip's geometry from images of gold colloids appears to be most promising for immediate, in-situ tip characterization. This would enable tip damage, as well as irregularities, to be monitored during the course of an experiment, thereby rapidly determining if a tip is "good" for force measurements. This work has demonstrated a means of adapting conventional AFM tip characterization techniques for the characterization of inverted AFM tips. This now allows for the use of the inverted AFM design for quantitative force measurements, measuring hundreds of interactions in a short period of time, within one single experiment. Thus, making combi-AFM a truly quantitative high-throughput technology.

References

- (1) Albrecht, T. R.; Quate, C. F. *Journal of Applied Physics* **1987**, *62*, 2599-2602.
- (2) Moiseev, Y. N.; Mostepanenko, V. M.; Panov, V. I.; Sokolov, I. Y. *Physics Letters A* **1988**, *132*, 354-358.
- (3) Weisenhorn, A. L.; Hansma, P. K.; Albrecht, T. R.; Quate, C. F. *Applied Physics Letters* **1989**, *54*, 2651-2653.
- (4) Vezenov, D. V.; Noy, A.; Ashby, P. *Journal of Adhesion Science and Technology* **2005**, *19*, 313-364.
- (5) Joyce, S. A.; Houston, J. E. *Review of Scientific Instruments* **1991**, *62*, 710-715.
- (6) Noy, A.; Vezenov, D. V.; Lieber, C. M. *Annual Review of Materials Science* **1997**, *27*, 381-421.
- (7) Porter, M. D.; Green, J. B.; McDermott, M. T.; Alves, C. A.; Siperko, L. M. *Abstracts of Papers of the American Chemical Society* **1994**, *207*, 240-COLL.
- (8) Johnson, K. L.; Kendall, K.; Roberts, A. D. *Proceedings of the Royal Society of London Series a-Mathematical and Physical Sciences* **1971**, *324*, 301-&.
- (9) Derjaguin, B. V.; Muller, V. M.; Toporov, Y. P.; Aleinikova, I. N. *Progress in Surface Science* **1994**, *45*, 192-198.
- (10) Dongmo, L. S.; Villarrubia, J. S.; Jones, S. N.; Renegar, T. B.; Postek, M.; Song, J. F. *Ultramicroscopy* **2000**, *85*, 141-153.

- (11) Van Oss, C. J. *Interfacial Forces in Aqueous Media, 2nd edition* **2006**, 28.
- (12) Green, J. B. D.; McDermott, M. T.; Porter, M. D. *Journal of Physical Chemistry* **1996**, *100*, 13342-13345.
- (13) Skulason, H.; Frisbie, C. D. *Langmuir* **2000**, *16*, 6294-6297.
- (14) Minne, S. C.; Yaralioglu, G.; Manalis, S. R.; Adams, J. D.; Zesch, J.; Atalar, A.; Quate, C. F. *Applied Physics Letters* **1998**, *72*, 2340-2342.
- (15) Spisz, T. S.; Fang, Y.; Bankman, I. N.; Reeves, R. H.; Hoh, J. H. *Johns Hopkins Apl Technical Digest* **1999**, *20*, 135-142.
- (16) Sulchek, T.; Minne, S. C.; Adams, J. D.; Fletcher, D. A.; Atalar, A.; Quate, C. F.; Adderton, D. M. *Applied Physics Letters* **1999**, *75*, 1637-1639.
- (17) Neffati, R.; Alexeev, A.; Saunin, S.; Brokken-Zijp, J. C. M.; Wouters, D.; Schmatloch, S.; Schubert, U. S.; Loos, J. *Macromolecular Rapid Communications* **2003**, *24*, 113-117.
- (18) Durig, U.; Cross, G.; Despont, M.; Drechsler, U.; Haberle, W.; Lutwyche, M. I.; Rothuizen, H.; Stutz, R.; Widmer, R.; Vettiger, P.; Binnig, G. K.; King, W. P.; Goodson, K. E. *Tribology Letters* **2000**, *9*, 25-32.
- (19) Chisholm, R. A.; Qiu, W.; Green, J. B. D. *Langmuir* **2007**, *23*, 7891-7894.
- (20) Wu, S. Y.; Berkenbosch, R.; Lui, A.; Green, J. B. D. *Analyst* **2006**, *131*, 1213-1215.
- (21) Vesenka, J.; Manne, S.; Giberson, R.; Marsh, T.; Henderson, E. *Biophysical Journal* **1993**, *65*, 992-997.

- (22) Ramirez-Aguilar, K. A.; Rowlen, K. L. *Langmuir* **1998**, *14*, 2562-2566.
- (23) Villarrubia, J. S. *Journal of Vacuum Science & Technology B* **1996**, *14*, 1518-1521.
- (24) Chan, S. S. F.; Green, J. B. D. *Langmuir* **2006**, *22*, 6701-6706.
- (25) Sheng, S.; Czajkowsky, D. M.; Shao, Z. *Journal of Microscopy-Oxford* **1999**, *196*, 1-5.
- (26) Bonnet, N.; Dongmo, S.; Vautrot, P.; Troyon, M. *Microscopy Microanalysis Microstructures* **1994**, *5*, 477-487.
- (27) Tian, F.; Qian, X. P.; Villarrubia, J. S. *Ultramicroscopy* **2008**, *109*, 44-53.
- (28) Villarrubia, J. S. *Journal of Research of the National Institute of Standards and Technology* **1997**, *102*, 425-454.
- (29) Hutter, J. L.; Bechhoefer, J. *Review of Scientific Instruments* **1993**, *64*, 1868-1873.
- (30) Levy, R.; Maaloum, M. *Nanotechnology* **2002**, *13*, 33-37.
- (31) Nietz, A. H. *Journal of Physical Chemistry* **1928**, *32*, 255-269.

Chapter VII

Conclusions and Future Work

7.1 Overall Conclusions

With the growing need to understand and characterize nanoscale properties of surfaces, atomic force microscopy has become a unique tool used for academic and industrial applications. This dissertation has detailed the use of atomic force microscopy to investigate charge transport through molecular films and development of combinatorial force microscopy. The initial studies of charge transport through aryl films demonstrated that molecular layer compression and deformation play a key role in the overall charge transport properties of a molecular junction. Under low applied loads, the molecular junction charge transport can be estimated using the work function of the electrodes and the lowest unoccupied molecular orbital of molecular layer. Upon greater loads, the layer will compress and deform and the charge transport through the junction resembles field emission.

This work also addressed the low degree of reproducibility between micro and nanoscale charge transport measurements observed within the molecular electronic field.¹ Using a Cu coated AFM tip as top contact in a PPF/NAB/Cu molecular junction the electronic properties were compared to a micro-sized PPF/NAB/Cu molecular junction formed by metal deposition of the top contact. It was found that the JV curves of the micro-sized molecular junctions overlapped well with the current densities measured on the c-AFM with an applied force of

~60 nN providing evidence that charge transport scales with contact area within this size range. The findings from this work are directly being used for the integration of aryl films into the microelectronics industry which uses metal deposition to form micro-sized top contacts.

This thesis also explored the methodology to quantitatively interrogate the interactions between opposing chemical libraries involved in combinatorial inverted atomic force microscopy was developed. In this, a means to chemically pattern a tipless cantilever to support a meaningful chemical library was required. This was achieved by the use of chemically modified nanorods as chemical identification. A chemical library of four aryl thiols was immobilized onto a tipless cantilever in this manner and was interrogated by an opposing library of four alkylthiols within a single experiment. To truly obtain a quantitative interpretation of AFM force spectroscopy results one must accurately determine the tip's geometry. Inherently, a large number of tips can be used during a single combinatorial AFM experiment involving the inverted AFM. To address this hurdle three techniques of tip characterization were explored with respect to the inverted AFM design. In this we found that colloids of known geometries could be used to assess tip wear during an experiment. However it was determined that characterization of the inverted AFM tips was best determined post experiment using a niobium coated tipless cantilever. The crystallites of niobium are sharper than the AFM tips and in effect image the tip. Using blind reconstruction algorithms, a three-dimensional model of the tip's shape can be

generated. Although this is time consuming and does not have a high throughput, it was found that this method contained the smallest uncertainties.

With the advent of automation and self-correcting software atomic force microscopy is evolving into a mainstream tool for nanoscale characterization of surfaces. The work in this thesis expands the use of AFM to understand charge transport industrial relevant molecular junctions and that these properties scale with size. The later part of the thesis demonstrates AFM to be a unique tool to perform high throughput chemical force microscopy that may have vast implications in drug discovery, medical and molecular biology fields.

7.2 Future Work

Ongoing Investigations of Charge Transport Through Molecular Layers

The work in this thesis has provided the initial insights into charge transport through diazonium salt derived molecular layers and how molecular layer compressibility can play a key role. Presently, ongoing efforts are underway to address the issue of how molecular layer thickness will affect the compressibility and charge transport through such a junction? McCreery and coworkers have found that current decreases as a function of molecular layer thickness using micro-sized molecular junctions formed by metal deposition of the top contact.^{2,3} Findings in Chapter 2 demonstrated a transition of charge transport properties associated with film alteration during top contact formation. Efforts are underway to vary the molecular layer thickness of nitroazobenzene and collect J/V curves at various applied loads. The molecular layer thickness can

be controlled by concentration of diazonium salt, and electrochemical deposition time. Efforts are also underway to measure the charge transport through a single aryl molecule grafted to an electrode. Recent findings from Shewchuk and McDermott are being used to decrease the concentration of aryl groups grafted to a gold electrode in a sea of non-conducting alkyl thiols.⁴ Initial studies have demonstrated great promise and an IV curve for a mixed layer of NAB and dodecane thiol is provided in Figure 7.1 and can be contrasted to a solely dodecane thiol on gold in Figure 7.2. The results indicate an increased efficiency for charge transport in the mixed molecular layer films as compared to the solely thiol counterpart. This suggests that mixed layer molecular junctions may provide a robust system for fabrication of molecular junctions, however further work is underway to fully understand these observations. Another experiment that has been proposed from findings within this dissertation is a comparison of charge transport between a nitrobenzene layer and a nitrobenzene thiol layer on a gold electrode. In this work a near monolayer nitrobenzene layer will be grafted to a gold electrode. Current/voltage curves will be collected and compared to measurements made on a nitrobenzene thiol layer. It is assumed that aryl films derived from diazonium salts have a higher degree of electronic coupling with the underlining electrode compared to thiol counterparts. The results will provide insights into the effect of electronic coupling have on charge transport.

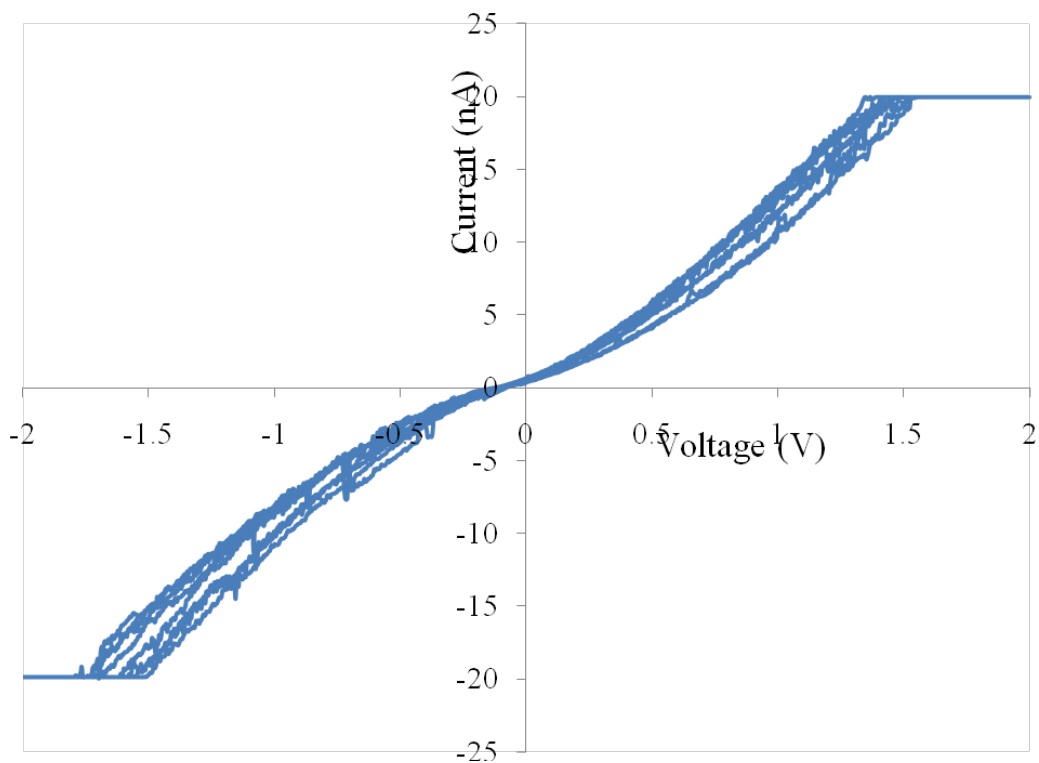


Figure 7.1 Overlay of five IV curves of a Au/0.5NAB(0.5C12-thio)/Au-tip molecular junction.

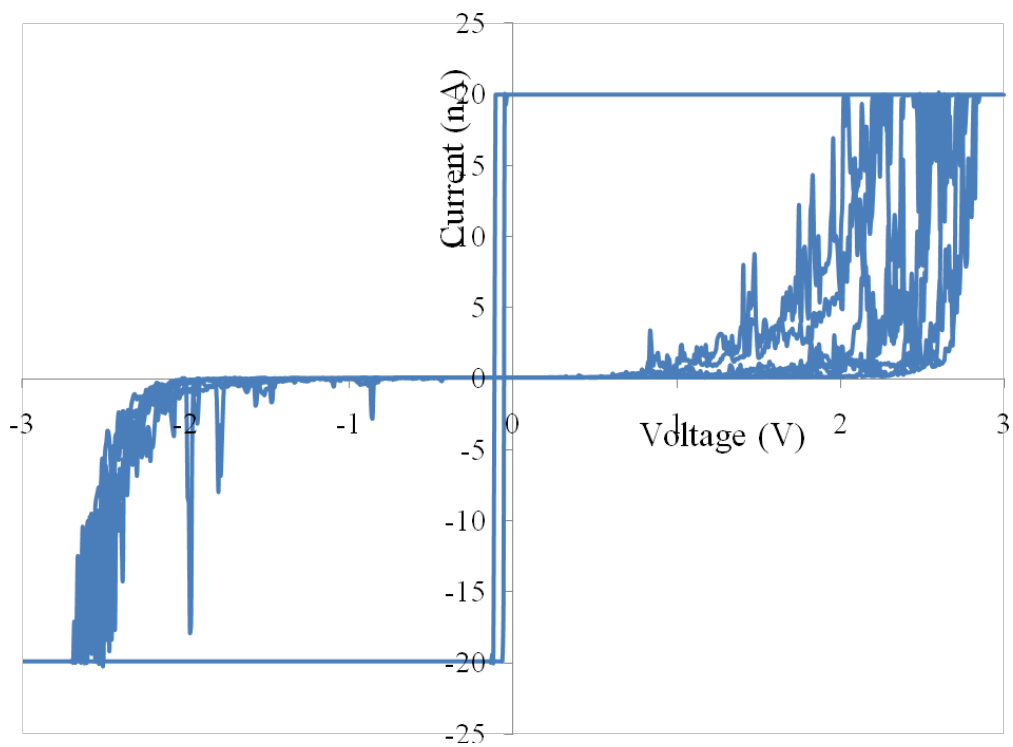


Figure 7.2 Overlay of five IV curves of a Au/C12-thio/Au-tip molecular junction.

Due to the flexibility of molecular layer immobilization to a wide variety of surfaces,⁵⁻⁷ molecular films derived from diazonium salts may provide an advantageous means of modifying surfaces for industrial and biomedical applications. Efforts are underway within the McDermott group to exploit the attachment chemistry for modification of Au and Ag nanoparticles for expanding their use for cellular biology and medical diagnosis applications.

Future Prospects for Combinatorial Atomic Force Microscopy

The work in Chapters 5 and 6 developed the methodology to quantitatively interrogate opposing chemical libraries of substantial numbers of molecules. Ligand-receptor and single molecule protein pulling experiments will benefit from the methodology developed within this dissertation. Despite these gains the use of nanorods as chemical discriminators is practically limited to ~10-20 different chemistries and nanorod aggregation can influence chemical modification. One potential avenue that may circumvent this issue is the use of aptomers linked to DNA super structures.^{8,9} The monomer units of the DNA structure spontaneously attach and form well ordered structures. The placement of aptomer tags can be coded into the DNA structure allowing for a high degree of confidence of aptomer location. Proteins will attach to the aptomers creating a patterned structure of proteins.^{8,9} The DNA superstructures can be immobilized onto a tipless cantilever greatly enhancing the number and density of components within the library.

References

- (1) Akkerman, H. B.; de Boer, B. *Journal of Physics-Condensed Matter* **2008**, *20*.
- (2) Kalakodimi, R. P.; Nowak, A. M.; McCreery, R. L. *Chemistry of Materials* **2005**, *17*, 4939-4948.
- (3) McCreery, R. L.; Wu, J.; Kalakodimi, R. P. *Physical Chemistry Chemical Physics* **2006**, *8*, 2572-2590.
- (4) Shewchuk, D. M.; McDermott, M. T. *Langmuir* **2009**, *25*, 4556-4563.
- (5) Stewart, M. P.; Tour, J. M.; Kosynkin, D. V.; Allara, D. L.; Dirk, S. M.; Maya, F. M. *Abstracts of Papers of the American Chemical Society* **2003**, *225*, 2-INOR.
- (6) Chen, B.; Lu, M.; Flatt, A. K.; Maya, F.; Tour, J. M. *Chemistry of Materials* **2008**, *20*, 61-64.
- (7) Bernard, M. C.; Chausse, A.; Cabet-Deliry, E.; Chehimi, M. M.; Pinson, J.; Podvorica, F.; Vautrin-Ul, C. *Chemistry of Materials* **2003**, *15*, 3450-3462.
- (8) Park, S. H.; Yin, P.; Liu, Y.; Reif, J. H.; LaBean, T. H.; Yan, H. *Nano Letters* **2005**, *5*, 729-733.
- (9) Liu, Y.; Lin, C. X.; Li, H. Y.; Yan, H. *Angewandte Chemie-International Edition* **2005**, *44*, 4333-4338.

- (1) Akkerman, H. B.; de Boer, B. *Journal of Physics-Condensed Matter* **2008**, *20*.
- (2) Kalakodimi, R. P.; Nowak, A. M.; McCreery, R. L. *Chemistry of Materials* **2005**, *17*, 4939-4948.
- (3) McCreery, R. L.; Wu, J.; Kalakodimi, R. P. *Physical Chemistry Chemical Physics* **2006**, *8*, 2572-2590.
- (4) Shewchuk, D. M.; McDermott, M. T. *Langmuir* **2009**, *25*, 4556-4563.
- (5) Stewart, M. P.; Tour, J. M.; Kosynkin, D. V.; Allara, D. L.; Dirk, S. M.; Maya, F. M. *Abstracts of Papers of the American Chemical Society* **2003**, 225, 2-INOR.
- (6) Chen, B.; Lu, M.; Flatt, A. K.; Maya, F.; Tour, J. M. *Chemistry of Materials* **2008**, *20*, 61-64.
- (7) Bernard, M. C.; Chausse, A.; Cabet-Deliry, E.; Chehimi, M. M.; Pinson, J.; Podvorica, F.; Vautrin-UI, C. *Chemistry of Materials* **2003**, *15*, 3450-3462.
- (8) Park, S. H.; Yin, P.; Liu, Y.; Reif, J. H.; LaBean, T. H.; Yan, H. *Nano Letters* **2005**, *5*, 729-733.
- (9) Liu, Y.; Lin, C. X.; Li, H. Y.; Yan, H. *Angewandte Chemie-International Edition* **2005**, *44*, 4333-4338.

Appendix

8.1 Igor Pro Rountine for Analysis of Force Curves

```
#pragma rtGlobals=1          // Use modern global access method.
#include <Multi-peak fitting 1.4>
//
Function Adhesion(voltagewave0,deflectionwave0,raw_adh, adh)
//
//           Program calculates adhesion measurements from cantilever
//           deflection and z - piezo data
//           collected via Oscilloscope.  The number of increments, i, and
//           increment step size is set-up for
//           data collected at 20kS/sec, 2 M resolution, and force curve
//           frequency of 9.30 Hz.
//           Small modifications may be required if these parameters are
//           changed.
//
//           User must Kill (data - kill waves) deflection and voltage waves and
//           load (data - loadwaves - load general binary file) deflection and
//           voltage waves that are going to be analyzed.  The names of
//           deflection (cantilever deflection signal) and voltage (Z-piezo
//           signal) waves must be deflection0
```

```

//          and voltage0 respectively.
//
//  define the waves, variables and parameters
wave voltagewave0, deflectionwave0
wave raw_adh, adh
variable xmin, xmax, ramp, ow1, ow2, ow3, ow4, ow5, ow6, ow10, ow11,
variable ow12
variable v_avgdef, delta, K1, Kf
variable i=0, n=0
wave W_coef

//
//          set output variable waves initially to zero
//
raw_adh = 0
adh = 0
//-----
//          User is prompt to input variables
//          xmin and x max should creat a range that a minimum occurs to the
//          right of the maxium
//          The ramp size is the same as when acquiring the force curves
//
•Display voltagewave0
•SetAxis bottom 0,4000;DoUpdate

```

```

xmax = 4000

xmin = 2000

ramp = 500

Kf = 0.1522

prompt xmin, "enter xmin (nm)"

prompt xmax, "enter xmax (nm)"

prompt ramp, "enter ramp size (nm)"

Prompt Kf , "enter force constant of cantilever (nN/nm)"

DoPrompt "Super Cool Science Geek", xmin,xmax, ramp, Kf

    delta = xmax -xmin

//-----

-----

//    Looking at the piezo data between xmin and xmax to find the maximum
//    and minimum

    Wavestats /Q/R = [xmin,xmax] voltagewave0

silent 1

//

//-----

//    The user may have to adjust the number of increments, i, to analysis all the
//    force curve data

//

for (i=0;i<1000;i+=1)

    ow1 = v_min    //what is the minimum piezo voltage in this region

```

```

ow2 = v_minloc //data point where minimum piezo voltage
ow3 = v_max //what is the maximum peizo voltage in this region
ow4 = v_maxloc //data point where maximum peizo voltage occurs
delta = 2* (ow2-ow4) // calculate number of data points in one force curve

//
//-----
// inputs variables,.... user may need to change according to data collection
//
//          K1= delta / (2*ramp ) // time traveled per nm (point/nm)
//
//-----
//          Analysis cantilever Deflection data to find adhesion force
//
//          finds minimum and subtracts baseline
//
//          if (v_minloc>v_maxloc)
//
//          wavestats /Q/R = [ow4-100, ow2+100 ] deflectionwave0
//          ow6 = v_min
//
//          The next two lines find a maximum baseline of the deflection data
//          right after the snap out
//          This procedure is good when the baseline of the deflection data is wavy
//

```

```

        wavestats /Q/R = [v_minloc+100, v_minloc+200 ]
deflectionwave0 // (line 6)

        ow5 = v_avg
        // (line 7)

        n=n+1 // number of force curves

        raw_adh[i] = ow5 - ow6

//-----
// incorporation of force constant,... force constant is required to be inputted in
// program
//
wavestats /Q/R = [ow4-100, ow2+100 ] deflectionwave0

        ow10 = -(v_minloc - v_maxloc) / (v_min - v_max) // (point/dat)
        ow12 = raw_adh[i] // (dat)
        ow11 = ow10*(1/K1) * (ow12) // (nm)
        adh[i] = Kf * ( ow11 ) // Adhesion force (nN)
        v_avgdef = faverage (ow10, 1,n)

//-----
// Increments analysis to next force curve
//
        endif

wavestats /Q/R = [ow2 + 100, ow2+ 100 + delta ] voltagewave0

endfor

//-----

```

```

//
//
//          display results to screen
print v_avgdef
//
//          Making and fitting histogram of adhesion data
//
•Make/N=1000/D/O adh_Hist;DelayUpdate
•Histogram/B={0,0.05,1000} adh,adh_Hist
CurveFit gauss adh_Hist /D
Display fit_adh_Hist, adh_Hist
Label bottom "Adhesion Forces (nN)"
ModifyGraph lsize(fit_adh_Hist)=1.5,rgb(fit_adh_Hist)=(0,34816,52224)
•TextBox/C/N=text0 "\\{"Yo = %g, +/- %g \",W_coef[0],W_sigma[0]}r\\{"A =
%g, +/- %g \",W_coef[1],W_sigma[1]}r\\{"Xo = %g, +/- %g
\",W_coef[2],W_sigma[2]}";DelayUpdate
•AppendText/N=text0 "\\{"Width = %g, +/- %g \",W_coef[3],W_sigma[3]}"
TextBox/C/N=text0/A=RB/X=-6.05/Y=71.90
//-----
end

```

Analyze your life closely. You will eventually find it difficult to misuse it by becoming machinelike or by merely seeking money as a surrogate for happiness.

Tenzin Gyatso